Metallogenic Modeling and Mineral Potential Mapping in the Takab District, NW Iran

Dissertation

zur Erlangung des akademischen Grades
Doctor rerum naturalium (Dr. rer. nat.)

vorgelegt der

Mathematisch-Naturwissenschaftlich-Technischen Fakultät
(mathematisch-naturwissenschaftlicher Bereich)

der

Martin-Luther-Universität Halle-Wittenberg

von

Mohammad Sadeghi, geb. am 18.06.1973 in Jahrom

Gutachter:

1. Prof. Dr. Gregor Borg (Institut für Geowissenschaften, Martin-Luther-Universität Halle-Wittenberg)

Prof. Dr. Cornelia Gläßer (Institut für Geowissenschaften, Martin-Luther-Universität Halle-Wittenberg)

2. Prof. Dr. Bernd Lehmann (Institut für Mineralogie und Mineralische Rohstoffe, Technische Universität Clausthal)

Verteidigt in Halle/Saale, 30.11. 2009

MARTIN-LUTHER-UNIVERSITY HALLE-WITTENBERG
INSTITUTE FOR GEOSCIENCE

Metallogenic Modeling and Mineral Potential Mapping in the Takab District, NW Iran

Dissertation submitted for the academic degree as
Doctor rerum naturalium (Dr. rer. nat.)
at the Faculty of Science III of the
Martin-Luther-University Halle-Wittenberg
by

Mohammad Sadeghi
born (18/06/1973), (Jahrom), (Iran)

(Halle/Saale, June 2009)

Thesis supervisors:

Prof. Dr. Gregor Borg (Petrology and Economic Geology, Martin-Luther-University Halle-Wittenberg)

Prof. Dr. Cornelia Gläßer (Remote Sensing and Cartography, Martin-Luther-University Halle-Wittenberg)

Acknowledgements

First of all I would like to thank my PhD supervisors Prof. Dr. Gregor Borg and Prof. Dr. Cornelia Gläßer for supporting me during these past four years.

Prof. Borg has been supportive and has given me the freedom to pursue various projects without objection as well as his encouragements during my work been the most important factor in my promotion. I am also very grateful to him for his scientific advice, knowledge and many insightful discussions and suggestions and also for the facilities.

I am most grateful to Prof. Gläßer for supporting this thesis with her ideas and her helpful suggestions offered. She has also provided insightful discussions about the research.

I would like to express my heartfelt thanks to Andreas Kamradt and his family members for their kindness and affection, and for never letting me feel that I am away from my family and country. He has helped me in my different problems during my habitancy in Germany.

Many thanks go to Thomas Degen for his useful guidance.

This study would not have been possible without the general support of group manager of GIS, Dr. M. Zareinejad. She has provided a proper environment and adequate facilities for my work.

Many thanks also to Dr. P. Giahchi for her efforts to arrange the administrative process.

I would like to thank general director (Mr. M.T. Korehie) of Geological Survey of Iran (GSI), management of Geomatics department (Mr. V. Fotovvati), and the Geoscience Department of the Martin Luther University Halle-Wittenberg (MLU). I would also like to thank the Carl Duisberg Centern (CDC) and the Geological survey of Iran (GSI) for financial support.

My special thanks go to my friends, M. Heydari, M. Moradi, S.T. Delavar, S.A. Moosavi and S.A. Meshkani who accompanied me during the fieldwork in Takab region. Furthermore, I am deeply indebted to my colleagues at Geological Survey of Iran that have provided the environment for sharing their experiences about the problems.

I would like to express special thanks to my beloved wife, Behnoush. She helped me to concentrate on completing this research and supported mentally during the course of this work. Without her helps and encouragements, this study would not have been completed.

A special thought is devoted to my parents for a never-ending support and encouragement to pursue my interests.

Finally, my deepest love goes to my son, Behrad, who is now almost five years old.

Sadeghi, June 2009

Table of Contents

List of Abbreviations

AAS = Atomic Absorption Spectrophotometry

ASD = Analytical Spectral Devices Inc.

ASTER = Advanced Spaceborne Thermal Emission and Reflection Radiometer

CRD = Carbonate Replacement Deposit

DEM = Digital Elevation Model

ETM^{+} = Enhanced Thematic Mapper Plus

GCPs = Ground Control Points

GIS = Geographic Information Systems

GSI = Geological Survey of Iran

IDL = Interface Description Language

IOCG = Iron Oxide Copper Gold

IZMDC = Iran Zinc Mines Development Company

JPL = Jet Propulsion Laboratory

Ma = Million years

Mt = Million tones

MVT = Mississippi Valley Type

NASA = National Aeronautics and Space Administration

NGDIR = National Geoscience Database of Iran

PC = Principle Component

ppm = parts per million

RBD = Relative Band Depth

RGB = Red, Green, Blue

RMS = Root Mean Square

SDM = Spatial Data Modeller

SWIR = Shortwave Infrared

TIR = Thermal Infrared

USGS = United States Geological Survey

UTM = Universal Transverse Mercator

VNIR = Visible Near Infrared

XRD = X-Ray Diffraction

XRF = X-Ray Fluorescence

3D = Three-Dimensional

Abstract

Modern regional exploration of ore deposits requires high-quality spatial data and the integration of geographic information systems (GIS) and remote sensing methods.

The northwestern part of Iran is host to several active and abandoned lead-zinc and gold deposits and occurrences. The biggest of these deposits are Angouran Mine, a high-grade carbonate-hosted Zn-Pb deposit (Mississippi Valley type) and Zarshouran, a Carlin type Au-As deposit.

The main objective of this research` is delineation of relationship between structures and mineral occurrences and producing of mineral potential maps by the integration of geological information, remote sensing data (satellite data, airborne magnetic and radiometry) and geochemical data in a GIS environment.

A set of spatial geological data has been gathered, processed, and integrated within a GIS in order to produce mineral potential maps for carbonate-hosted deposits in the Takab region, NW Iran, covering some 15.000 km².

The data sets used for this study comprise geological maps (1:100.000 scale), Landsat 7 ETM^+, and Aster data, airborne magnetic and radiometric grid, as well as geochemical stream sediment data.

The remote sensing data have been interpreted jointly with geological field information and formed the base for a lithological, structural and alteration mapping exercise. The results revealed several circular structures and lineaments of various sizes. These circular and linear structures appear to be the main spatial control on ore deposits and occurrences, especially of Pb-Zn, Au, Cu and Fe. Geophysical data indicate several shallow intrusive and subvolcanic bodies and structural features. Geochemical stream sediment samples show marked anomalies that also follow these circular structures and lineaments and delineate distinct trends of mineralization.

Additionally, a fuzzy-logic (knowledge driven method) approach has been adopted for prospectivity analysis, where each data layer has been assigned a weighting between 0 and 1, based on metallogenic importance. The results have been integrated in the GIS environment for the selection of the best new target areas for carbonate replacement deposits (Mississippi Valley type Pb-Zn and Carlin type gold deposits). Furthermore this method was compared with index overlay method. Fuzzy logic and index overlay method comparison indicated some differences in the patterns but almost all of the most important deposits in the district were predicted satisfactorily.

Regional structural zones are believed to represent the main tectonic and magmatism phases which control the spatial distribution of mineralization events. The Late Cenozoic magmatism (Pliocene and Quaternary) and related hydrothermal activities, the distribution pattern of structural features and ore occurrences and especially gold mineralization in the NW of Iran demonstrate that mineralization events can occur along deep strike-slip faults.

Chapter 1 Introduction

1.1 Background to the Research

Optimization of land use is a major policy objective in most countries. It is every government's wish, especially in developing countries, to explore and exploit its natural resources to provide economic and social development for its people. Socioeconomic development, however, is hampered due to under-utilization of their natural resources mostly because of lack of sufficient and appropriate geosciences data. Another factor that hampers socioeconomic development is giving much emphasis to one mineral commodity as a source of revenue and gives less significance to other potential resources (Chikambwe, 2002).

Generally ore deposits occur below the earth's surface and cannot, therefore, be mapped directly. However, it is possible to map mineral potential by new exploration techniques. Systematic regional exploration programs based on geo-exploration datasets in GIS environment by new data integration methods cause to convert large volumes of raw data to beneficial and applicable information. Exact selection of generic models related to mineral potential in different regions can help to develop the critical factors associated with the genetic models and the recognition criteria from a data analysis that are used to form the structures and weightings of that model in target areas.

1.1.1 Definition of Mineral Potential

Mineral potential, as used in this research, is the set of characteristics attributed to a particular area that describes the probability for the presence of mineral deposits or existence of mineralization (Carranza, 2002). The term 'mineral potential' describes the possibility of the presence of mineral deposits or mineralization. Mineral potential does not take into account economic factors such as deposit grade, tonnage, physical, chemical and mineralogical characteristics, nature and thickness of overburden, availability of man power and technology, market demand, etc., as these are typically unknown during mineral potential mapping. Mineral potential mapping of an area involves demarcation of potentially mineralized zones based on geologic features that exhibit significant spatial association with target mineral deposits. These features, which are termed recognition criteria, are spatial features indicative of various genetic earth processes that acted conjunctively to form the deposits in the area. Recognition criteria are sometimes directly observable; more often, their presence is inferred from their responses in various spatial datasets, which are appropriately processed to enhance and extract the recognition criteria to obtain evidential or predictor maps (Porwal, 2006).

1.1.2 Fuzzy Model for Mineral Potential Mapping

It is possible to use mathematical models of the relation between recognition criteria and target mineral deposits for mineral potential mapping. The most important factor is the selection of appropriate model for each type of ore deposits. One of the knowledge-driven models is fuzzy logic. Variables of fuzzy models for mineral potential mapping consist of the recognition criteria for the target mineralization. These are selected either by using (a) empirical methods based on a statistical (or heuristic) evaluation of geological characteristics of known mineral deposits or by using (b) an appropriate genetic mineral deposit model. Spatial data sets that provide evidence for the recognition criteria then are processed to generate multiclass evidential maps for modeling.

The most significant procedures in approaches to fuzzy modeling are the definition of fuzzy membership values of multiclass evidential maps and the selection of appropriate inference network and fuzzy set operators for combining the evidential maps (Porwal et al., 2003).

1.2 Rationale for the Research

In a traditional mineral exploration approach, each data set collected is processed, modeled and interpreted individually but geologists now routinely use geographic information systems (GIS) for their fieldwork and a typical mineral exploration project employs several exploration methods and collects multiple sets of exploration data (Choi et al., 2000).

The geological features especially a proper host rock in an area is the initial most important factor in mineral potential. Comparing the geology of a particular area with conceptual mineral deposit and exploration models is among the initial steps undertaken to evaluate and classify its mineral potential. Also, recognition of the spatial associations of discovered mineral deposits with the different geological features in well-explored regions is a main factor in most exploration projects.

Geographic information systems are computer-based environments designed for the efficient storage of diverse spatial and non-spatial datasets and allow the effective visualization, analysis, and integration of data (Knox-Robinson, 2000).

One of the major applications of a GIS is the ability to integrate and combine multiple layers of lithology, structure, remote sensing, geophysical and geochemical characteristics to delineate mineral prospectivity maps (Chung and Agterberg, 1980; Bonham-Carter et al., 1988; Harris, 1989; Moon et al., 1991; Bonham-Carter, 1994; Rencz et al., 1994; Wright and Bonham-Carter, 1996; Raines, 1999; Harris et al., 2000).

Mineral potential mapping is an important type of geologic mapping activity and usually covers a great part of varied studies, focused on spectral analysis (e.g. Longhi et al., 2001), geological mapping (e.g. Harris, 1991), structural mapping (e.g. Liu et al., 2000), identification of hydrothermal alteration zones (e.g. Podwysocki et al., 1983), mineral alteration mapping (e.g. Tangestani and Moore, 2002), hyperspectral imagery (e.g. Neville et al., 2003), integration with GIS (e.g. Akhavi et al., 2001) and other methods.

Locating mineral resources relies primarily on knowledge of the general geological make up of an area (Rajesh, 2004). Therefore, a basic geological understanding of the formation of mineral deposits is relevant:

- Particular mineral deposits occur in particular rock types (e.g. magmatic diamond usually occurs in kimberlite).
- Mineral deposits in very many occur along or adjacent to geologic/tectonic structures.

- Mineral deposits usually show (strong) alteration of wall rocks on the earth's surface.
- Mineral deposits usually occur near the contact between favourable rock types (e.g. porphyry copper deposits have a direct spatial association with the contact of granitic to intermediate intrusive rocks; Guilbert and Park, 1996).

The genesis of mineral deposits is a good example for situations where the high complexity of physical and chemical processes can lead to an incomplete understanding of the deposit formation. In fact, Bonham-Carter (1994) mentioned that these processes are often too complex for a direct prediction of a mathematically-expressed theory; thus it is necessary that the prospecting process for exploring favourable areas rely mainly on empirical relies defined by "ore deposit models".

1.3 Main Research Objectives

The objectives of the current research and PhD thesis are as follows:

- Development of a GIS-based exploration model for predictive mapping of areas with a potential for Carbonate Replacement Deposits (CRD).
- Determination of spatial relationships between geological and especially tectonic structures and known ore deposits in such as this area and extraction of these structures from the data-sets used in this study.
- To develop and successfully demonstrate the applicability a methodology for remote-detection of indications of mineralization.

1.4 Methodology

A flowchart of the generalized methodology used in this research for spatial GIS-based mineral potential mapping is shown in figure 1.1.

1.5 Software

The software programs used in this study are listed in table 1.1.

Geosoft software was used for the processing of geophysical data (extraction of geophysical structural features and magnetic shallow bodies) and ENVI and PCI Geomatica were applied for the processing and spatial analysis of satellite data (extraction of structural features and hydrothermally altered rocks). Fry plots were produced by DotProc software and ArcGIS and ArcSDM were used for the processing, integration and GIS modeling of geo-exploration datasets.

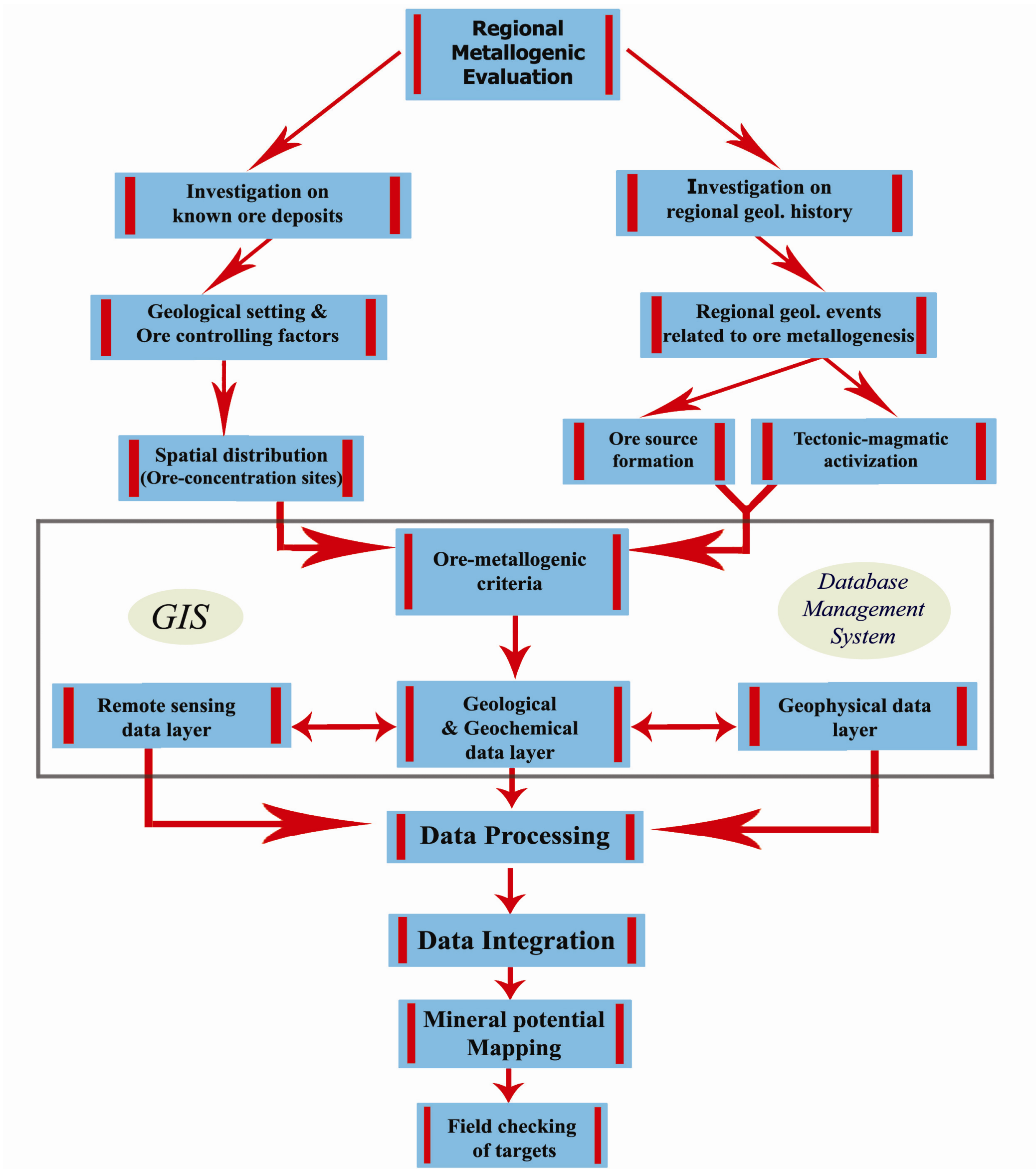

Fig. 1.1 Flowchart of the methodology for predictive mapping of the CRD mineral potential of a region (modified from Pan and Harris, 2000).

Data Capture	ArcGIS, ArcView, AutoCAD Map
Data Processing	ArcGIS, ArcView, Geosoft, ENVI, PCI Geomatica, DotProc
Data Integration & Modeling	ArcGIS, ArcSDM

Tab. 1.1 Software used in this study for processing, integration and modeling of geo-exploration datasets.

Chapter 2 The Study Area

2.1 Geography

The study area, the Takab 1:250.000 map quadrangle, is located in the NW of Iran, between longitude 46° 30′ - 48° 00′ E and latitude 36° 00′ - 37° 00′ N in the Zanjan, Kurdistan and North and West Azarbaijan Provinces. Takab with a population of about 80.000 is the largest town in this area and is situated almost in the middle part and about 266 km from Tehran (Fig. 2.1)

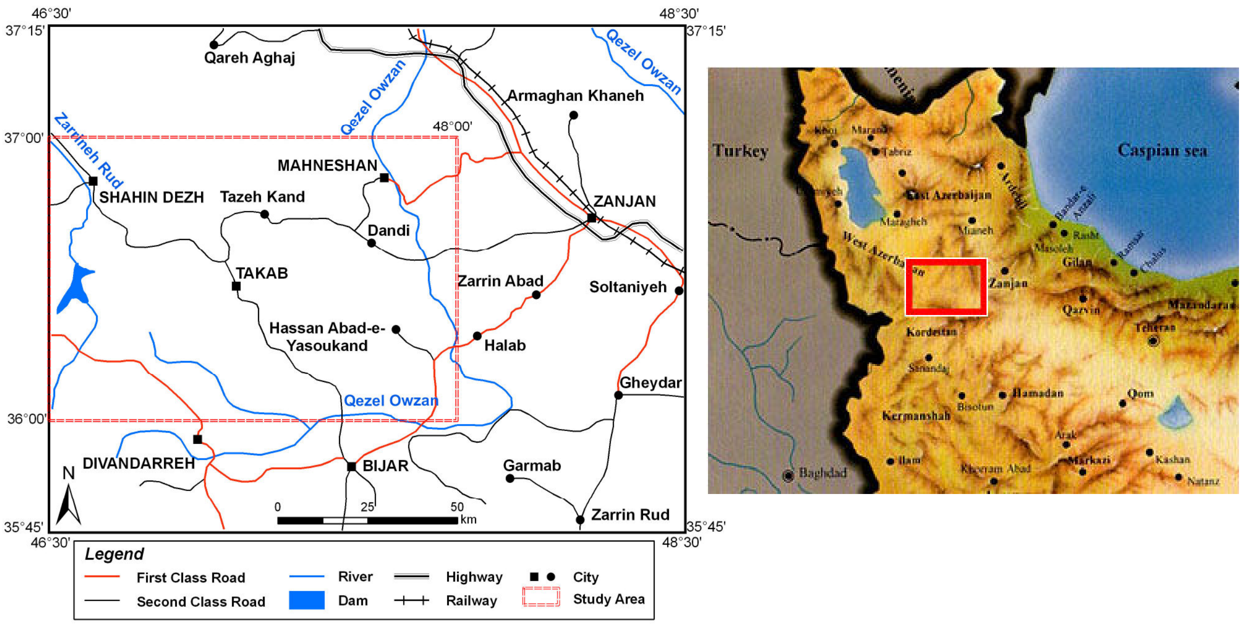

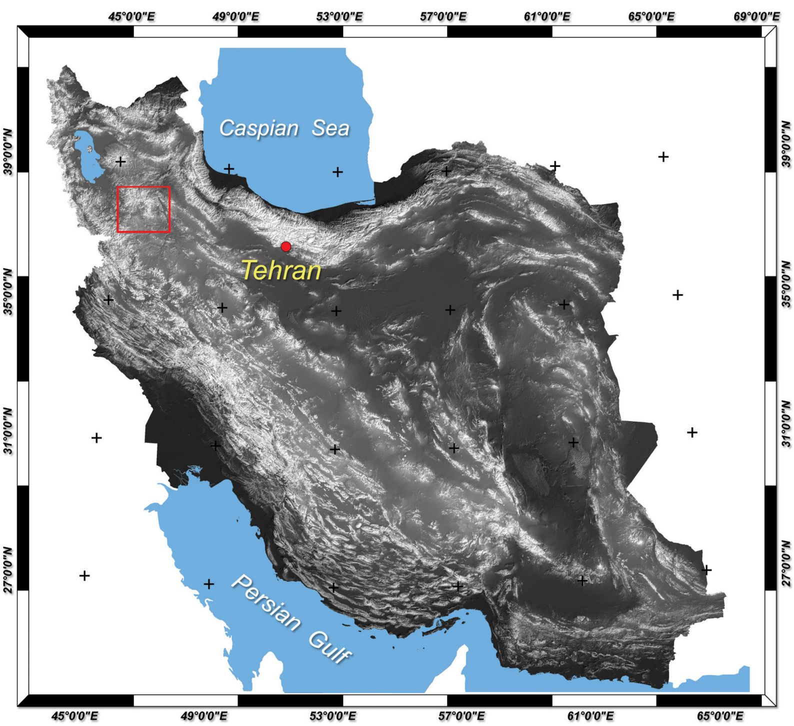

Fig. 2.1 Location map of the study area (Takab region), northwest Iran.

The area is generally mountainous, especially in the central and western part. The Belghais Mountain, with an elevation of 3330m above level sea is the highest peak in the NE of Takab. Other major mountains are Ghebleh Dagh (3208m), Abdolghasem (3090m), Gor Gor (2930), Okoz Olan (2917m), Jangutaran (2875m) and Eiman Khan (2862m).

Two main rivers carry the drainages northwards to the Caspian Sea and to the Urumiyeh Lake. The Qezel Owzan River enters the area from the southeast and flows northwards to the Caspian Sea and the Zarrineh Rud River flows from the west and drains into the Urumiyeh Lake.

The inhabitants of this area are Turkish in the north, east and southeast and Kurdish in the west and southwest. The people's main occupation is in agriculture and animal husbandry.

The main roads in this quadrangle are the routes Zanjan - Takht-e-Soleyman - Takab, Bijar - Takab - Shahindezh and Sanandaj - Saqez.

The climate of this district is largely influenced by the rainy winds of the Atlantic Ocean and Mediterranean. Cold northern winds affect the area during winter and cause heavy snow. The highest average temperature in the Takab reaches 31.4℃ in August, and the lowest temperature is –9.1℃ in January. The average of Temperature, precipitation and humidity is shown in figure 2.2 (Meteorological Organization of Iran).

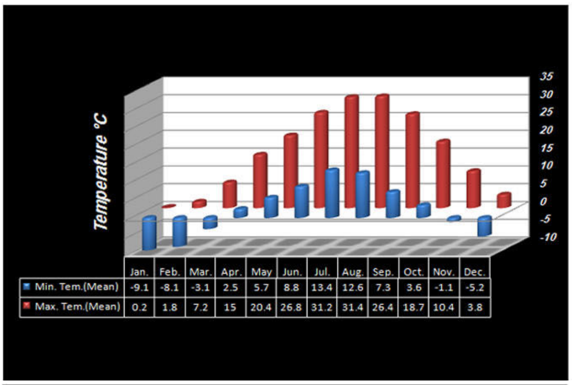

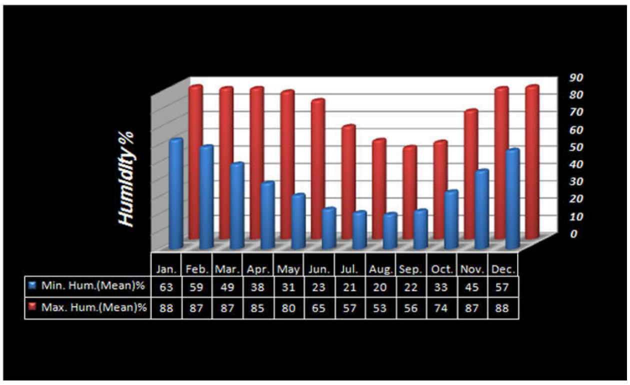

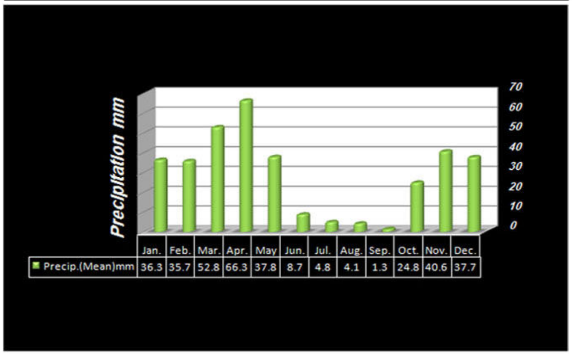

Fig. 2.2 Average of temperature, humidity and precipitation of Takab district (Meteorological Organization of Iran).

The famous historical complexes, Takht-e-Soleyman and Zendan-e-Soleyman are situated to the North-East of Takab. Takht-e-Soleyman was one of Takab's oldest Zoroastrian fire temples during the Sassanid Dynasty and had the name Azargoshasb. Another historical place, Karaftoo, is an ancient cave and situated in the southwest of Takab near the Gur-e-Baba Ali village in the Oligomiocene Limestone (Qom Formation). The structure of the cave dates back to Arcasid Dynasty about 3 BC. The dwellings of this cave, 2000 years ago were reputed temples of Heraclees (the Greek deity) (Fig. 2.3).

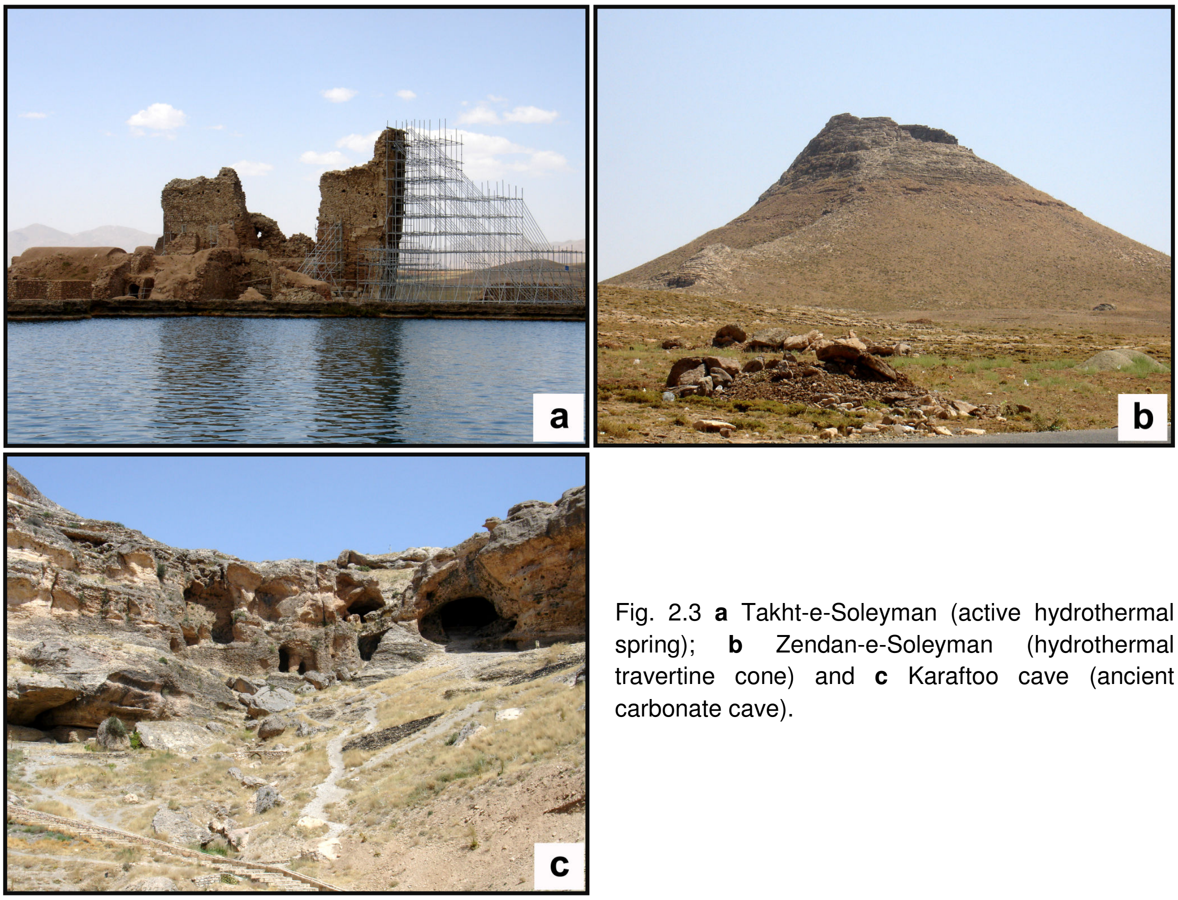

Fig. 2.3 **a** Takht-e-Soleyman (active hydrothermal spring); **b** Zendan-e-Soleyman (hydrothermal travertine cone) and **c** Karaftoo cave (ancient carbonate cave).

2.2 Geological Setting

2.2.1 General Remarks

In the northern part of study area, a sedimentary sequence, more than 13.000 m thick is exposed, ranging in age from Precambrian to Recent. Volcanic rocks within this sequence are the result of magnetic activity in the Late Precambrian, Cretaceous, Eocene, Oligo-Miocene and Post-Miocene times. Besides the long time-gaps from the Silurian to Permian, a few short breaks have also occurred, namely in the Late Cambrian, Early Permian, Early Jurassic, Early Cretaceous, Eocene, Oligo-Miocene, Plio-Pleistocene and Quaternary. Epicontinental and shallow marine rocks characterize the Late Precambrian to Ordovician, Permian, Triassic and Lower Jurassic formations, where marine rocks constitute the Middle and Upper Jurassic, Cretaceous and Lower Miocene formations and terrestrial and continental beds are confined to the Oligocene, Middle and Upper Miocene and Pliocene (Alavi et al., 1982).

2.2.2 Stratigraphy

A stratigraphic column is shown in table 2.1.

Precambrian

A. Metamorphic Rocks (Basement?)

Tab. 2.1 Stratigraphy sequence in the Takab Quadrangle (1:250.000 scale; after Alavi et al., 1982).

Litological Unit	*Lithology*	*Age*	*Thickness (m)*
	Teracces & travertine deposits	Quaternary	250
	Pinkish clayeybeds with conglomerate & fresh water limestone localy	Pliocene, pleistocene	± 150
Upper Red Formation	Red, grey & green sandy marls with gypsum in lower part	Middle to Late Miocene	700-2000
Qom Formation	Carbonatic shallow marine beds & detritic with intercalated volcanics	Oligocene, Miocene	600-350-870
Lower Red Formation	Red conglomerate & sandy marl	Oligocene, Miocene	1200
Karaj Formation	Agglomerate, volcanics, green tuff, tuffaceous shale, marl	Eocene	± 2000
Ziarat Formation	Nummulitic limestone	Eocene (Lutetian)	60
Fajan Formation	Red conglomerate & sandstone	Eocene	200
	Grey shale & limestone with Globotruncana & volcanic	Late Cretaceous	± 500
	Grey limestone with orbitolinas	Early Cretaceous	± 300
Lar limestone	Limestone with ammonites & belemnites	Late Jurassic	300
Dalichai Formation	Green marl ammonites bearing	Calluvian	± 100
Shemshak Formation	Green & grey shale & sandstone with plantremains and coal locally	Early Jurassic	± 1000
Elika Formation	Dolomite & vermicular limestone	Triassic	± 150
Ruteh Limestone	Grey limestone & dolomite with fusulinids	Late Permian	250
Dorud Formation	Red to wine-coloured sandstone & shale	Permian	100
Mila Formation	Limestone with trilobites (Obolus)	Cambrian, Ordovician	300
	Graptolite-bearing black shale & nodular limestone	Cambrian, Ordovician	550
Lalun Sandstone	Quartzitic red sandstone with white "top quartzite"	Early Cambrian	500
Zagun Formation	Red to purple shale (Micaceous)	Late Precambrian	500
Barut Formation	Red & green shale with dolomite	Late Precambrian	400
Soltanieh Dolomite	Dolomite (with Chopoqlu shale member)	Late Precambrian	1300
Bayandor Formation	Red sandstone & shale	Late Precambrian	300
Qareh Dash Formation	Rhyoloites, tuff & lapili tuff	Late Precambrian	± 1000
Kahar Formation	Green shale, dolomite, phyllite	Precambrian	± 1200
Metamorphic Rocks	Complexes of kheyrabad, Mahneshan, Amirabad & Kuh-e- Sursat	Precambrian	± ? 3000

Precambrian rocks are exposed mainly in the central part of this area. They consist of (1) highly metamorphosed rocks (2) slightly metamorphosed to non-metamorphosed rocks, and (3) intrusive rocks. The Precambrian metamorphic complexes can be described as follows (Alavi and Amidi, 1968): The complex of Kuh-e-Sursat, complex of Amirabad, complex of Mahneshan and the complex of Kheyrabad (Fig. 2.4).

Complex of Kuh-e-Sursat

This complex is exposed in the western part of the study area and overlain by Late Precambrian rocks. It is subdivided into the Incheh and Main Bolagh unites (Pelissier et al., 1967). The rocks are regionally metamorphosed to amphibolite facies grade.

Complex of Mahneshan

Mahneshan complex is exposed in the eastern part and interfingers with the complex of Kheyrabad. It is divided into two unites, the Aq Kand gneiss and Poshtuk schist and marble.

Complex of Kheyrabad

This complex consists of metamorphosed rocks and is exposed in the northern part of the area. It comprises the Daveh Yataqi Gneiss, Alam Kandi Amphibolites and Angouran Schist.

Complex of Amirabad

The Amiabad Complex consists of gneiss and migmatite and overlying schist and marble (Pelissier et al., 1967). The complex is in the southern part of metamorphic rocks area. The grade of metamorphism is quite low.

B. Kahar Formation

The oldest formation consists of micaceous shale, green-grey shale, and in some places slightly tuffaceous shale. This Formation is exposed in the western and eastern part of the area.

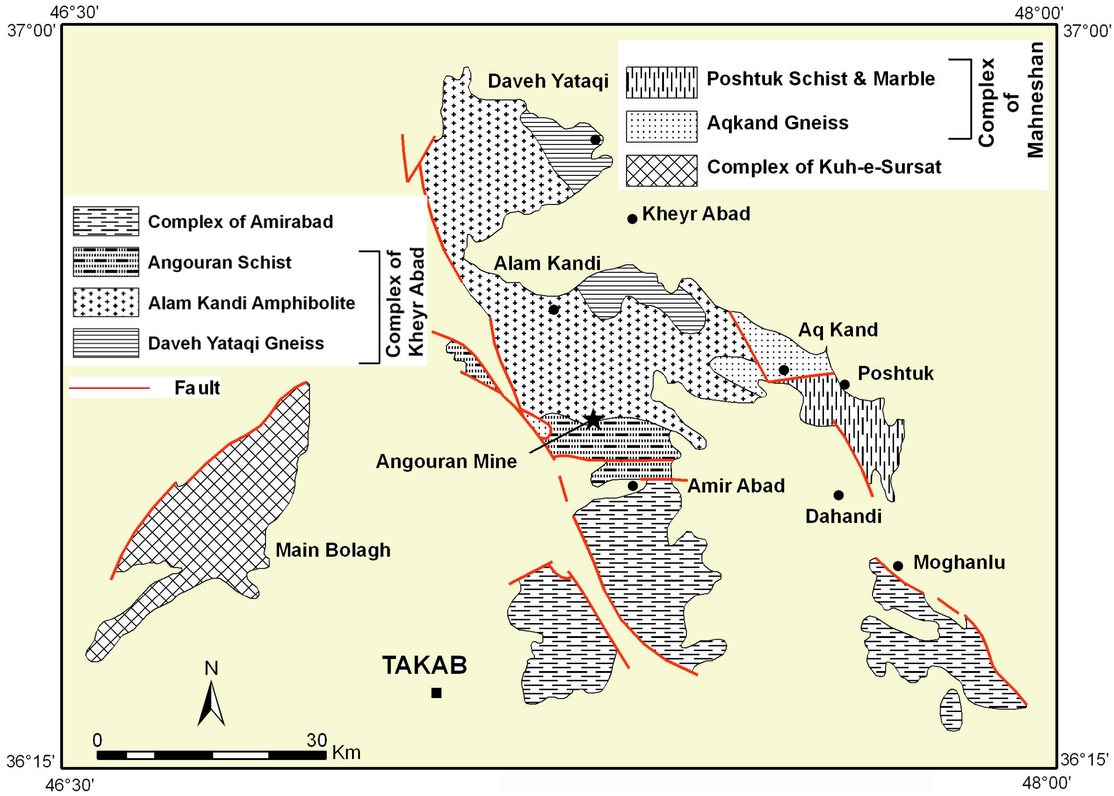

Fig. 2.4 Distribution map of Precambrian metamorphic complexes (modified after Alavi et al., 1982).

Late Precambrian

The late Precambrian non-metamorphic sequence comprises, from bottom to top, Qareh Dash Formation, Bayandor Formation, Soltanieh Dolomite, Barut Formation and Zagun Formation.

Qareh Dash Formation

This formation consists of a sequence of rhyolite tuffs, lava and tuffaceous sediment, with a thick dolomite band in the middle. Outcrop areas are in the western part and generally small.

Bayandor Formation

The Bayandor Formation consists of purple sandstone, coarse-grained sandstone and sandy shale with intercalations of cherty dolomite. It occurs only in the west and northwest of the area.

Soltanieh Dolomite

The Soltanieh Formation consists of dolomite with nodules and bands of chert and a few horizons of thin-bedded limestone and is exposed in the northwestern part of the area.

Barut Formation

This formation consists of dolomite, limestone and micaceous shale in the eastern and western part of the area. In the eastern part, the lowermost beds are in contact with the Doran Granite.

Zagun Formation

Red and violet micaceous shale with thin intercalations of sandy shale overlies the Barut Formation transitionally. The distribution map of Precambrian rock units is shown in figure 2.5.

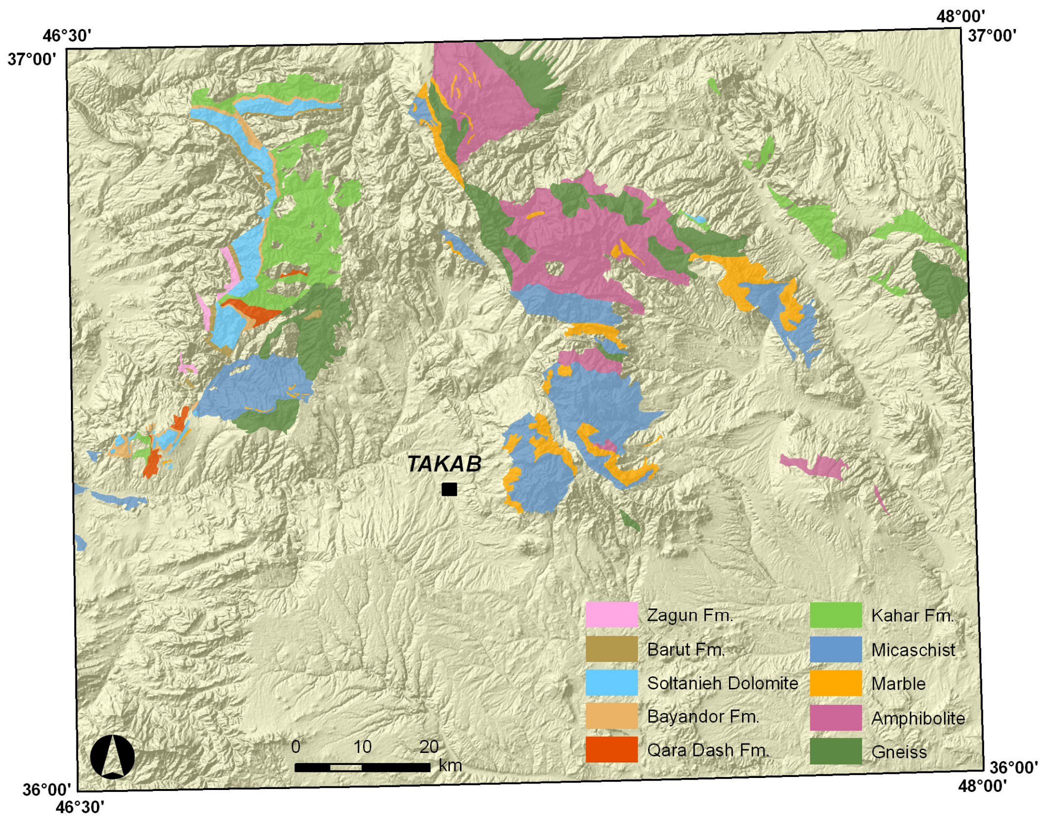

Fig. 2.5 Distribution map of Precambrian rock units (extracted and GIS-ready from 1:250.000 geological map of Takab, Geological Survey of Iran).

Paleozoic

Cambrian

The Cambrian deposits consist of the Lalun sandstone and Mila Formation.

Lalun Sandstone

Red sandstone with intercalations of red sandy shale, overlying the Zagun Formation in places.

Cambrian-Ordovician

Mila Formation

Dolomite and limestone resembling the lower and middle parts of the Mila Formation in the Zanjan area conformably overlie the Lalun Sandstone.

Permian

The Permian rocks are found mainly in the eastern and western parts of the area (Fig 2.6).

Dorud Formation

This formation consists of quartzite, sandstone and sandy shale. In the northwestern part of this area, the Dorud Formation overlies the Zagun and Lalun Formations directly and in the western part it rests directly on the black dolomite of the lower part of the Mila Formation.

Ruteh Limestone

A sequence of carbonate beds conformably overlies the shale and sandstone of the Dorud Formation. They are exposed in the northeast and western parts of the study area.

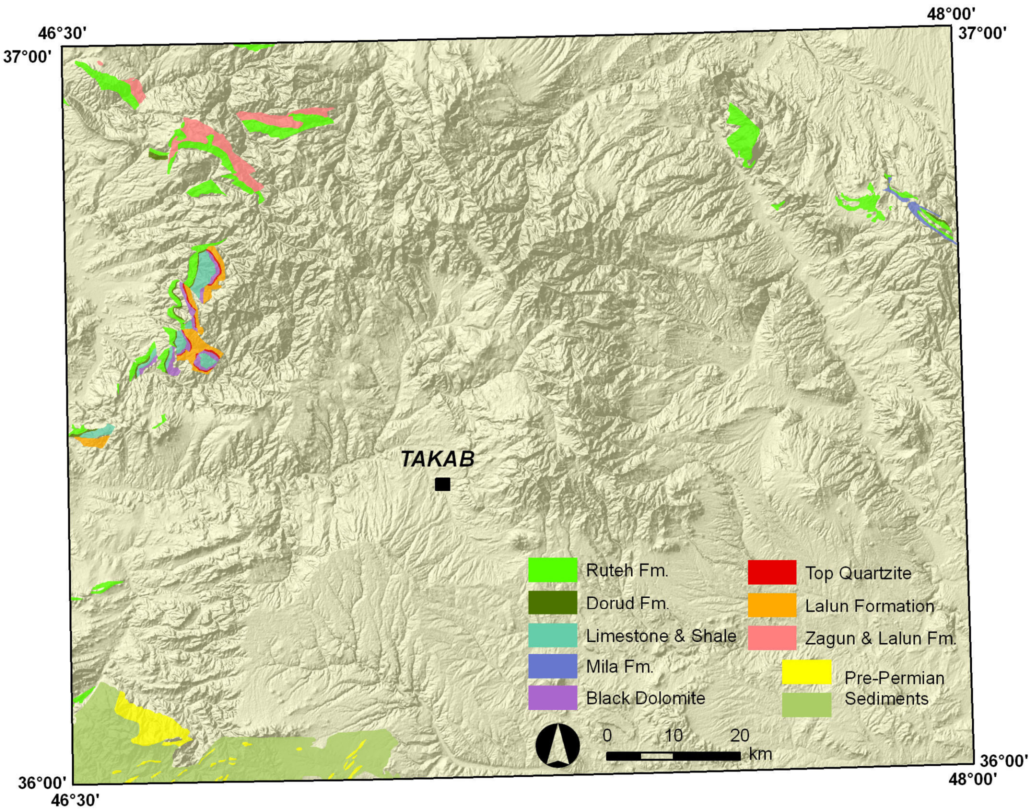

Fig. 2.6 Distribution map of Paleozoic rock units (extracted and GIS-ready from 1:250.000 geological map of Takab, Geological Survey of Iran).

Mesozoic

Mesozoic rocks are exposed in the eastern and western parts of the area (Fig. 2.7) and range in age from Triassic to Upper Cretaceous.

Triassic

Triassic beds are exposed in the northwestern part of the area. They are represented by limestone and thick dolomitic layers overlying the Permian Ruteh Limestone.

Jurassic

The most complete section of Jurassic beds is exposed in the western part of the area, where three different units are present:

Shemshak Formation

The Shemshak Formation in this area is composed of blackish and olive green shale, alternating with grey green sandstone and rare thin sandy limestone.

Dalichai Formation

A sequence with green marly to micritic limestone in the lower part and thick-bedded cherty limestone in the upper overlies the Shemshak Formation and is particularly well developed in the western part of the area.

Lar Formation

The upper Jurassic sequence consisting of thin bedded red limestone and thick-bedded light-colored limestone consisting chert concretions overlies the micritic beds conformably and has been equated with the Lar limestone.

The most extensive exposure of Lar Formation is in the northeast of the study area.

Cretaceous

Cretaceous rocks (limestone, shale, and andesitic volcanic) are present mainly in the western part of the area. In the eastern part, the sequences are less complete.

Lower Cretaceous

Alavi and Amidi, 1968, described the Lower Cretaceous limestone as light-grey sandy limestone. In places it overlies the shale of Jurassic Shemshak Formation.

Upper Cretaceous

Upper Cretaceous black shale overlying the Orbitolina limestone contains intercalated micritic Globotruncana bearing limestone of Coniacian age in the eastern part. In the southwest of the area, Alavi and Amidi, 1968, found extensive exposure of possibly Cretaceous rocks metamorphosed in the lower greenschist facies.

Cenozoic

Tertiary

Tertiary rocks cover a wide area (Fig. 2.8) and its major subdivisions are:

Eocene

Eocene beds are characterized by the presence of sandy limestone, lavas and tuffs resulting from sub-marine volcanic activity. The main lithologic units are as follows:

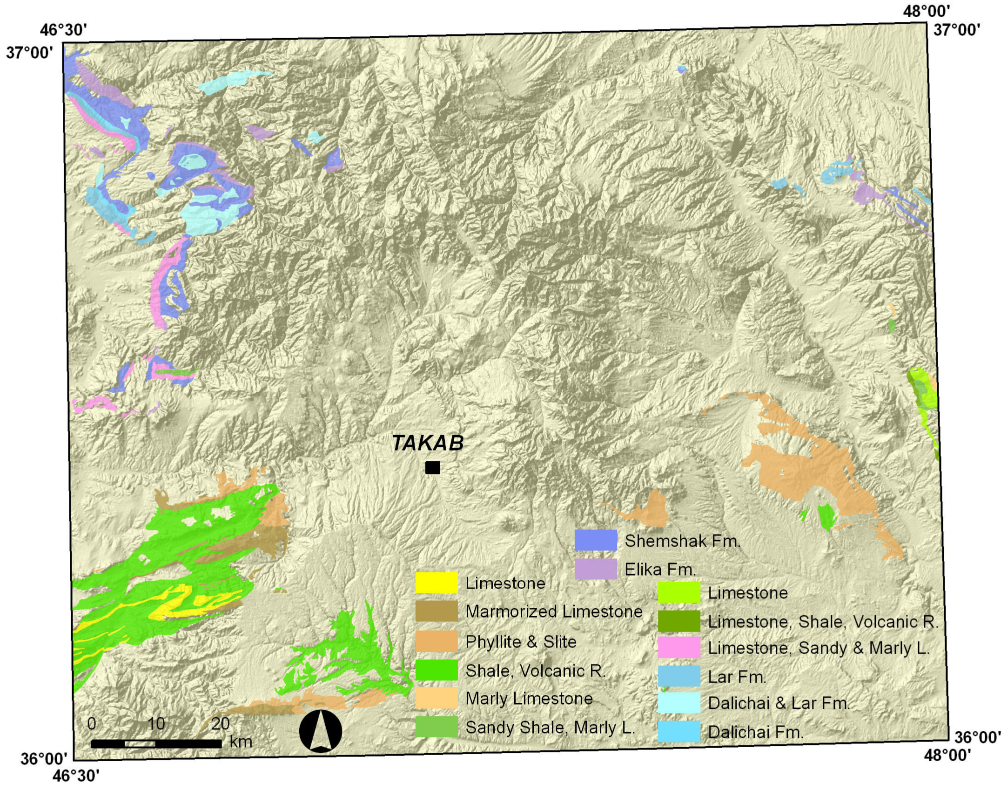

Fig. 2.7 Distribution map of Mesozoic rock units (extracted and GIS-ready from 1:250.000 geological map of Takab, Geological Survey of Iran).

Basal beds (Fajan Formation)

These consist of conglomeratic beds 10-100 m thick, attributed to the Fajan Formation.

Nummulitic beds (Ziarat Formation)

This formation consists mainly of sandy limestone and in places tuffaceous limestone and shale, overlying the basal conglomerate beds. Alavi and Amidi, 1968, described them as forming lenses in the conglomerate and in the Eocene green tuffs.

Greenish tuff, lava breccias, andesitic lava, dacitic tuff and lava (Karaj Formation)

These rocks consist of two distinct parts. The lower part consists of green tuff and tuffaceous shales. The upper part of sequence consists of green dacitic tuff, andesitic crystal tuff, agglomerate and lava breccias referred by Alavi and Amidi, 1968, to the Karaj Formation.

Oligocene (?)-Miocene

Lower Red Formation

A sequence of coarse-grained detritic red-brown layers is found below the marine Miocene beds. In places they can be seen to overlie the fine-grained detritic Eocene sediments but it is not easy to define a limit between Eocene and Oligocene. Their presence immediately below marine Miocene beds suggests epeirogenic uplift following Upper Eocene marine deposition in the area.

Oligocene-Miocene

Qom Formation (Marine beds)

These beds typically consist of a basal conglomerate 10-100 m thick, overlain by yellow limestone (ridge-forming in many places) and marls, sandy at upper levels and passing upwards to continental deposits of the upper formation. In the central part of the area, the volcanic of shallow marine carbonatic beds with intercalated volcanic (lavas and tuffs) are subhorizontal and cover a wide area.

Upper Red Formation

It consists of a continental evaporitic sequence. The change from the marine deposits to the evaporitic continental beds is usually transitional and could be the result of slow positive movement of the basin.

Volcanic rocks such as dacitic or rhyolotic tuff indicate continuation of volcanic activity and gypsum layers and gypsiferous marls are a characteristic feature of this formation.

Pliocene-Pleistocene

A sequence of horizontal to subhorizontal argillaceous beds of yellowish red color overlies unconformably various beds of the Upper Red Formation, Qom Formation and older beds. It is exposed as a light red sheet in the plains in the southern and eastern parts of the area.

Quaternary

Horizontal, poorly consolidated gravel, sand and clayey beds form terraces and alluvial deposits. There are two types of travertine in the study area:

The first type includes travertine cones and terraces, associated with post-volcanic geothermal activity e.g. at Takht-e-Soleyman and other type that occurs e.g. on slopes below the Angouran ore body (Borg, 2005).

Igneous Rocks

Intrusives

Intrusive masses have invaded various formations in different periods ranging from Late Precambrian to Neogene (Fig. 2.9).

Precambrian

Precambrian intrusive rocks in the study area consist of Anatectic Granite and Doran Granite.

Anatectic Granite

This granite is described by Alavi and Amidi, 1968, from the western part of the area. The rock contains as essential minerals muscovite, quartz, orthoclase, microcline and plagioclase. Some whitish pegmatitic gneiss or gratite outcrops are found in the eastern part (Moghanlu area).

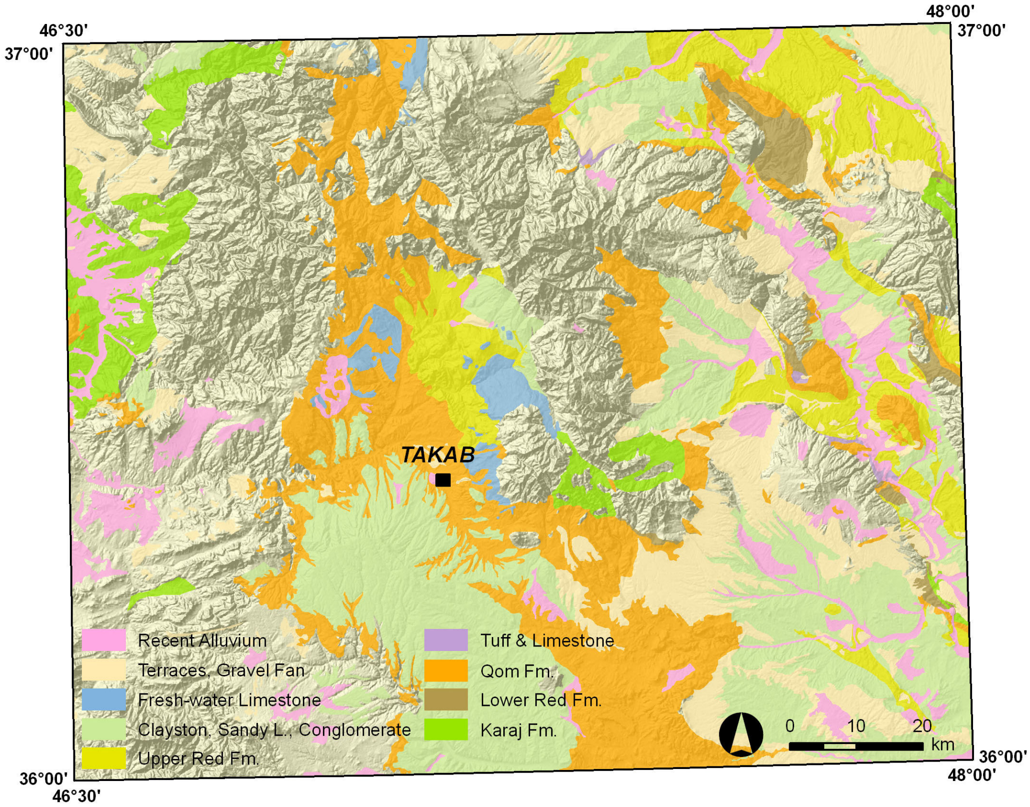

Fig. 2.8 Distribution map of Cenozoic rock units (extracted and GIS-ready from 1:250.000 geological map of Takab, Geological Survey of Iran).

Doran Granite

The largest exposures are in the western part of the area and other scattered small exposures occur in the eastern part.

Late Jurassic to Early Cretaceous (Mahmudabad granite)

A granitic mass occurs near Mahmudabad village (Alavi and Amidi, 1968) and cut the Jurassic beds. The rock is mozonite biotite granite and the texture is hypodiomorphic granular. Essential minerals are quartz, K-feldespars, plagioclase and biotite.

Post Cretaceous to Pre-Oligocene (Porphyritic granite)

Granite with large pink feldspars forms several intrusive bodies in Early and Late Cretaceous shale and limestone in the western part of the area.

Late Miocene or Post-Miocene

The youngest intrusion, of dioritic composition, invaded Lower Miocene marine beds in the southeast of the central part. Tonalitic masses are exposed south of Shahrak village and Granodiorite bodies intrude in the metamorphosed beds on the slope of Kuh-e- Shah Neshin.

Extrusives

Extrusive volcanic rocks are found intermingled with sedimentary and metamorphic rocks in almost all formations from Precambrian to Neogene (Fig. 2.9).

Precambrian

In the metamorphosed rocks are found the gneisses formed in the part from volcanic detritus and basic volcanic. The Kahar Formation contains rhyolitic beds and andesitic lava.

Late Precambrian

Acid volcanic are reported by Alavi and Amidi, 1968, from the western part of the area. They are mainly rhyolitic lava and tuff; quartz porphyry occurs in the Kuh-e-Qareh Dash.

Mesozoic

Volcanic layers and tuffs occur in the Mesozoic sedimentary sequence (Late Jurassic?).

Cretaceous

There are exposures of shale and schist containing intercalations of volcanic of various compositions but mainly andesitic.

The largest exposure is in Kuh-e-Shah Neshin. In the eastern part, andesitic lavas and tuffs are intercalated in Cretaceous limestone and shale and in the southwestern part, somewhat metamorphosed Cretaceous beds contain altered volcanic.

Cenozoic

Eocene

The composition of the Eocene volcanic rocks in the study area is mainly andesitic.

Oligocene (?)-Miocene

In the Oligo-Miocene marine, the volcanic appear at different composition such as andesitic and dacitic-rhyolitic lavas and related tuffs.

The Burdigalian igneous age of the rhyodacite of 18.42±0.18 Ma dates (Early Miocene) the volcanic activity of this period and gives a minimum age to the emplacement of the thrust sheet overlying these volcanic rocks (Daliran et al., 2009).

Quaternary

The young volcanic activity in the area produced olivinbasalt flows, to be seen in small exposures in the southern and southeastern part.

The youngest magmatic rock of the area is tholeiitic basalt dyke, cross-cutting rhyodacitic tuff (Angouran, SE of the open pit). This dyke is considered to be Tertiary-Quaternary in age (Daliran et al., 2009).

Figure 2.10 shows simplified geological map of the study area.

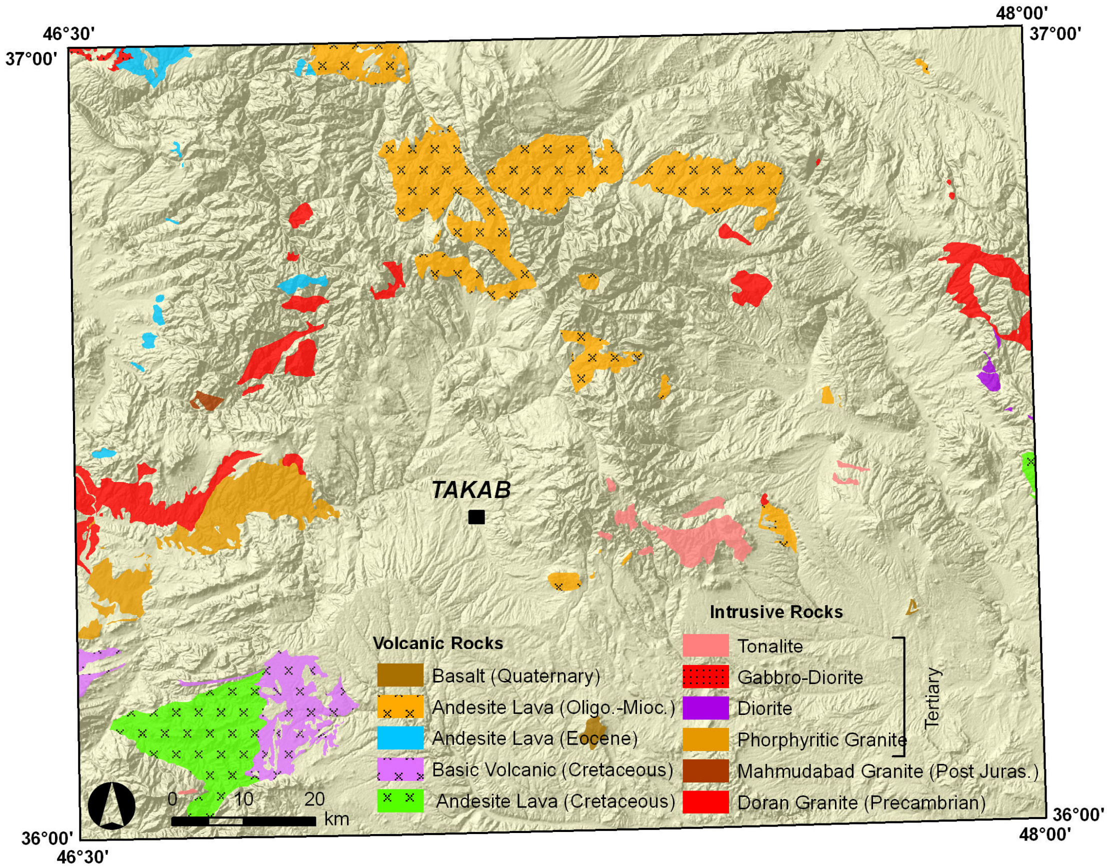

Fig. 2.9 Distribution map of igneous rocks (extracted and GIS-ready from 1:250.000 geological map of Takab, Geological Survey of Iran).

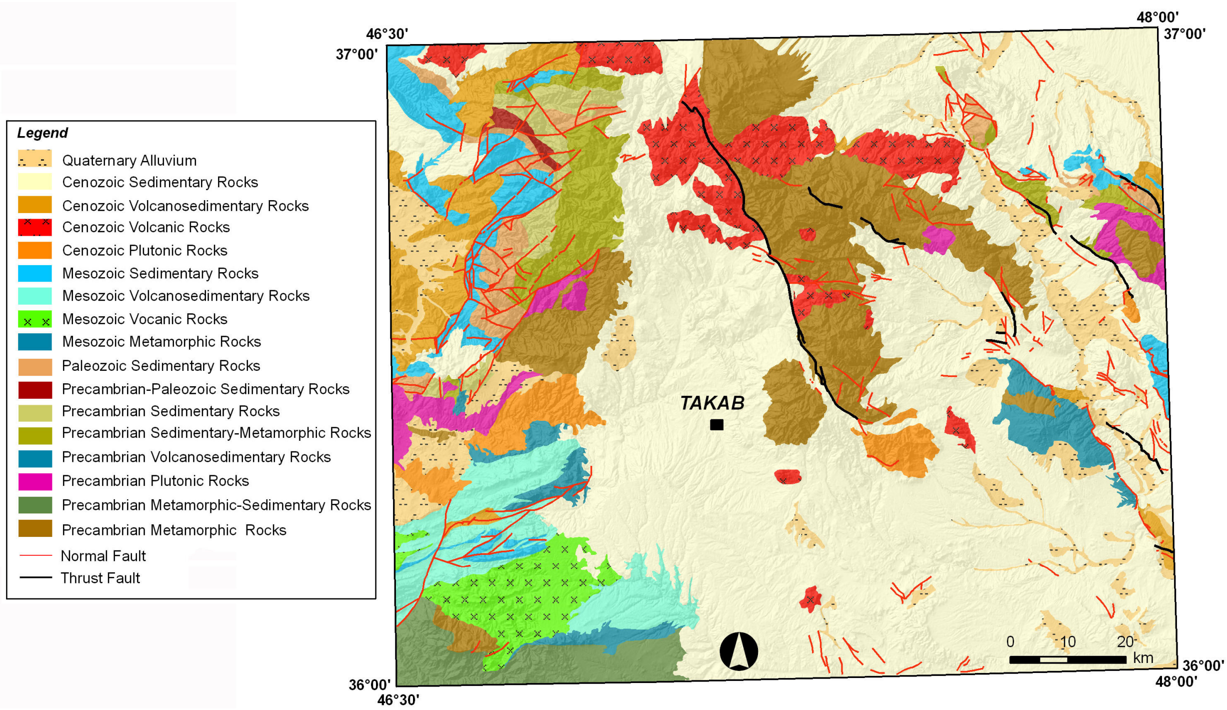

Fig. 2.10 Simplified geological map of the study area (modified and GIS-ready from 1:250.000 geological map of Takab, Geological Survey of Iran).

2.3 Tectonic Setting

2.3.1 Generalized Tectonic Setting

There are different opinions for the structural zones in the study area, for example; the Alborz-Azarbaijan structural zone of the Alpine-Himalayan chain (Nabavi, 1976), Sanandaj-Sirjan and Central Iran structural zones (Berberian, 1981), and Sanandaj-Sirjan structural zone (Stocklin, 1968; fig. 2.11).

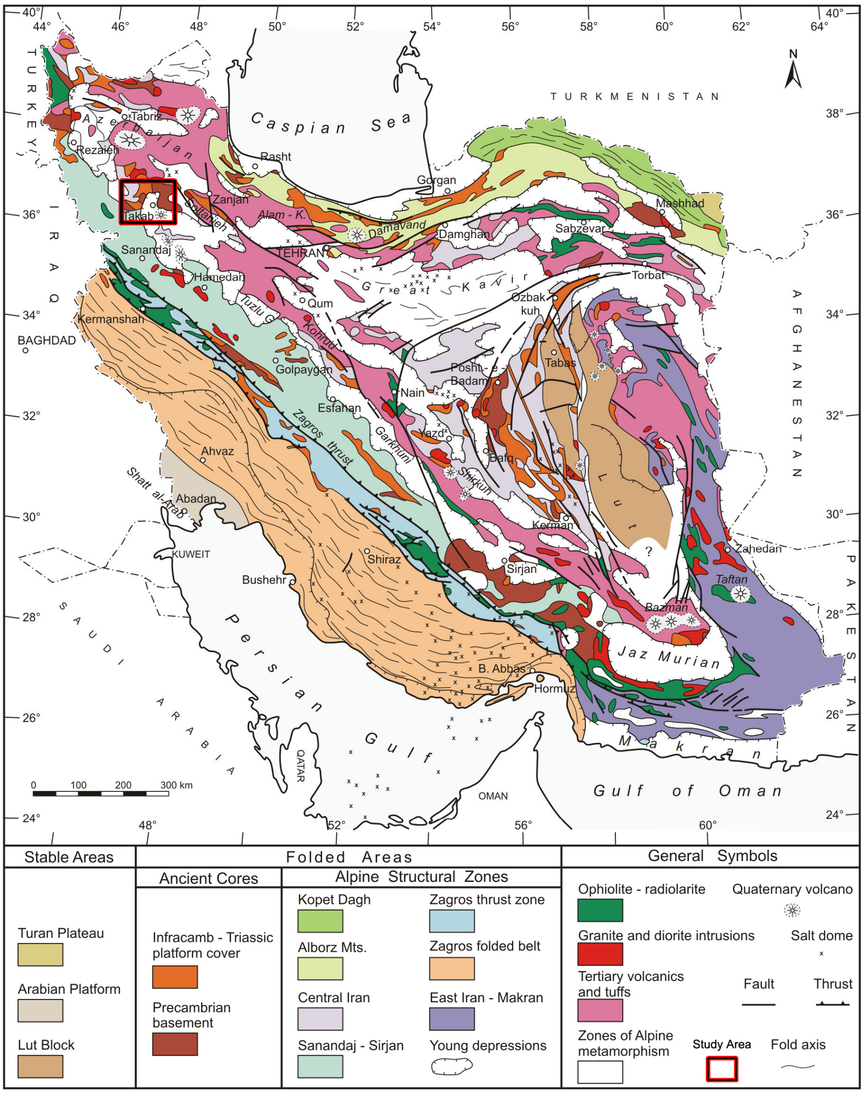

Fig. 2.11 Generalized tectonic map of Iran (map by M. Frotzscher, redrawn after Stöcklin, 1968) and location of the study area.

The Sanandaj-Sirjan metamorphic zone is a part of Zagros Orogenic Belt. The Zagros Orogen of western Iran consists of four parallel tectonic zones from the northeast to southwest (1) the Urumieh-Dokhtar Magmatic Arc, (2) the Sanandaj-Sirjan Zone, (3) the Zagros Fold-Thrust Belt, and (4) the Mesopotamian-Persian Gulf foreland basin (Berberian and King, 1981; Alavi, 1994).

The Zagros orogeny provides a unique opportunity within the Alpine system to evaluate the interplay between a young Tertiary collision and earlier subduction/ obduction processes. Within the Crush zone and the Sanandaj–Sirjan (internal) zone separating the Zagros Fold belt from Central Iran, there are several major tectonic events taking place at the end of the Cretaceous, of the Eocene and from the Mio–Pliocene onwards (Agard et al., 2005).

The Sanandaj-Sirjan Zone extends for 1500 km along strike from northwest (Sanandaj) to southeast (Sirjan) in the western part of Iran and has a width of 150-200 km (Mohajjel and Fergusson, 2000). The rocks in this zone are the most highly deformed in the Zagros orogen and share the NW-SE trend of its structures (Ghasemi and Talbot, 2005). It consists of Paleozoic strata formed in an epicratonic setting that were subsequently overlain by a volcanic and sedimentary succession deposited during the Triassic opening of Neo-Tethys (e.g. Sengör et al., 1988).

The orogenic belt is the result of closure of Neo-Tethys by consumption of oceanic crust at a northeast-dipping subduction zone below central Iran and subsequent Cretaceous continental collision between the Afro-Arabian continent and the Iranian microcontinent in Late Cretaceous to Tertiary time (Berberian and King, 1981). Widespread thrusting has been attributed to the collision in the Sanandaj-Sirjan Zone (Alavi, 1994) (Fig. 2.12).

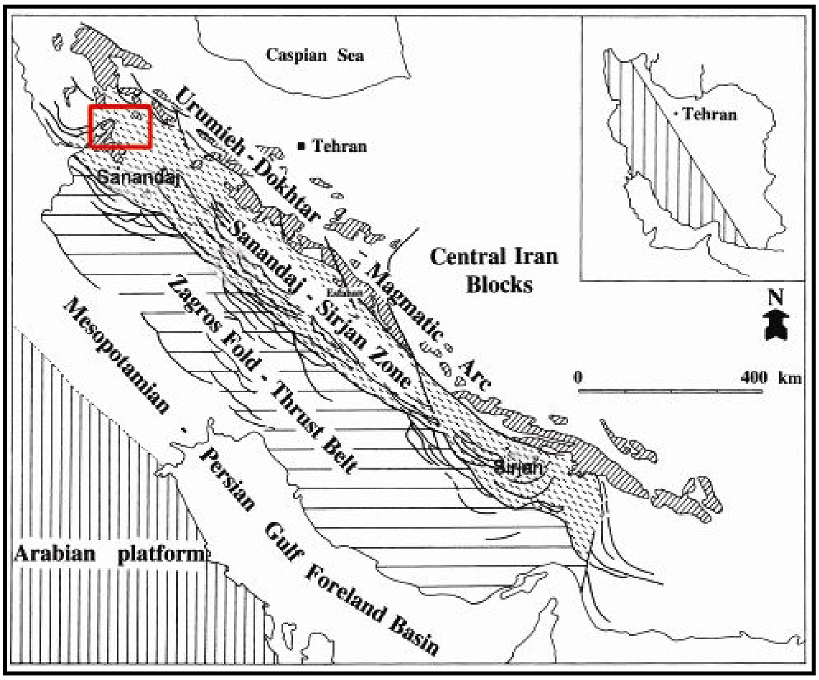

Fig. 2.12 Tectonic zones of the Zagros Orogen in western Iran (after Alavi, 1994) & location of the study area.

Geodynamic evolution of the Sanandaj-Sirjan metamorphic zone is shown in figure 2.13 (Sheikholeslami et al., 2003).

2.3.2 Structural Zones

The study area is divided to four structural zones (A, B, C and D) (Alavi et al., 1982) (Fig. 2.14). The characteristics of these zones are as follows:

Zone A: (1) This zone is located in the central part, comprises highly metamorphosed rocks (micaschist, gneiss, amphibolites, marble), and has a high topographic relief, (2) The Main regional structural trend is NW-SE and (3) A big thrust fault has juxtaposed metamorphic rocks against Miocene volcano-sedimentary rocks.

Zone B: This zone is located toward the east of zone A and has two subzones: Ba & Bb.

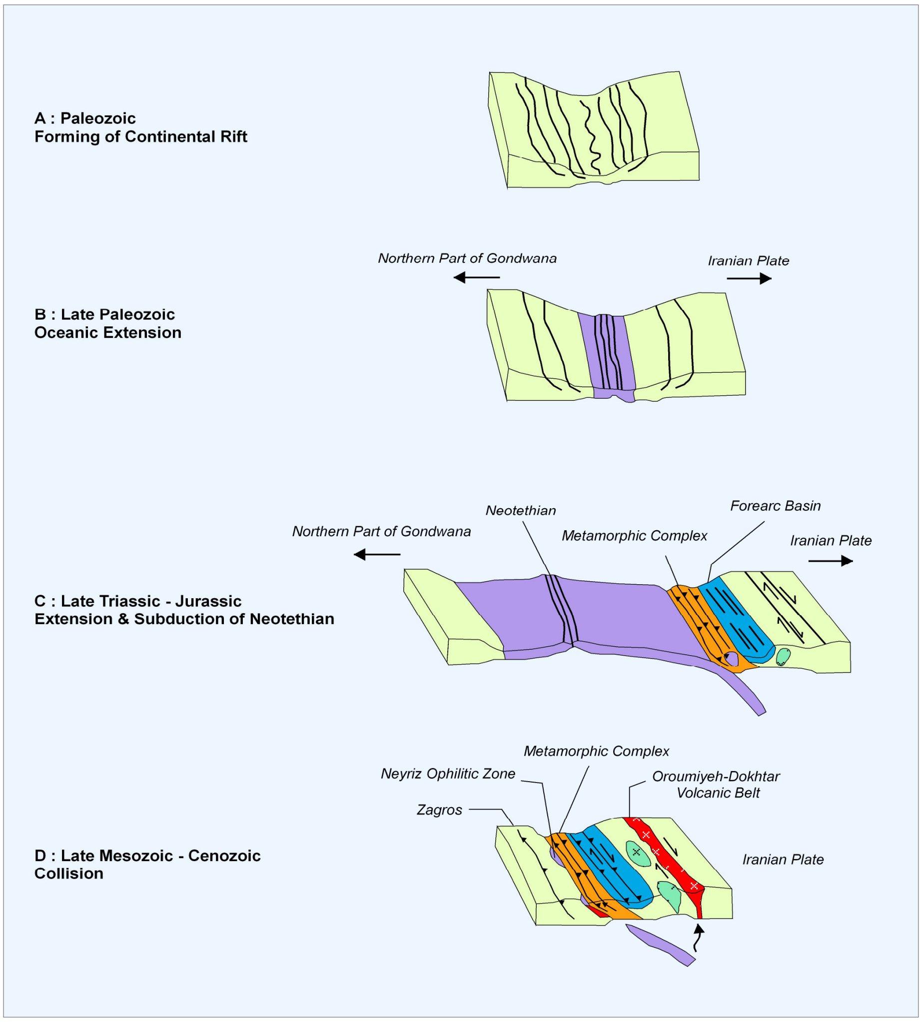

Fig. 2.13 Geodynamic evolution of the Sanandaj-Sirjan metamorphic zone (Sheikholeslami et al., 2003).

Subzone Ba: (1) Located in the northern part of zone B, (2) The subzone is composed of the oldest rock units in the region from Precambrian to Permian, (3) Silurian-Carboniferous rock units and probably Triassic are absent and (4) The main structural trend is NW-SE.

Subzone Bb: (1) Located in the southern part of zone B, (2) The oldest rocks exposed are undifferentiated beds of Mesozoic, Cretaceous limestone and volcanic rocks, (3) The main structural trend is NW-SE and (4) There is a tectonic graben between two reverse faults at the boundary between subzones Ba and Bb.

Zone C: (1) This zone is located in the northwestern part of the Takab quadrangle, (2) Rocks of all stratigraphic periods, except for the Silurian-Carboniferous, occur in this zone, (3) Late Precambrian units are particularly characterized by tectonic faulting, (4) Mesozoic rocks, in contrast, have been deformed mainly by folding, (5) Faults in this zone strike dominantly in SW-NE direction and (6) Two main strike directions prevail in the late Permian to Jurassic beds (NW-SE and E-W in the northern part and N-S in the southern part of this zone).

Zone D: (1) This zone is located on the southwestern part of the study area, (2) All geological units are Permian or younger, (3) The Cretaceous rocks are in the faulted contact with Permian units and are highly folded and faulted, (4) The main strike of structural features is E-W in the northern part & SW-NE in the southern part of this zone and (5) Metamorphism in this zone is related to emplacement of granitic bodies.

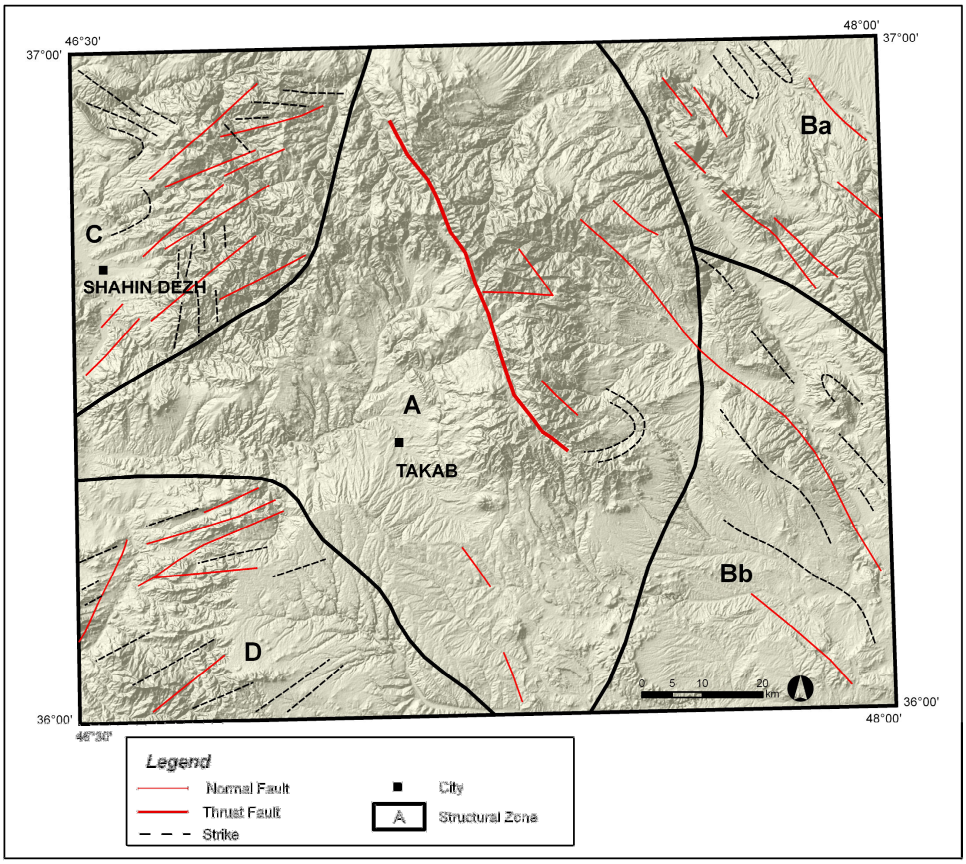

Fig. 2.14 Schematic map of tectonic zones & structural features of the study area (modified after Alavi et al., 1982).

2.3.3 Structural History

The geologic structure of the various zones outlined above probably took shape during the Assyntic and Alpine Orogenies (Alavi et al., 1982).

A Late Precambrian (Assyntic) Orogeny is believed to have been responsible for the foliation and metamorphism of the Precambrian basement rocks. The Doran Granite intrusion and perhaps the Qareh Dasgh extrusive acidic lava and tuff would be consequent on the Assyntic orogeny. The Assyntic movements were probably responsible for uplift of the extensive metamorphic phyllitic complex which forms the crestal part of the mountains in the central part of the area and is variously overlapped by Mesozoic and Miocene sediments.

The apparent absence of Post-Ordovician Pre-Permian beds form the whole of the area is baffling, scince there is no evidence of Paleozoic movement. But regional subsidence around the high land is suggested by the overlapping of Permian beds and Mila Formations. The Alpine orogeny in the area started in Late Triassic or Liassic time. The first movements are indicated by termination of marine Triassic sedimentation and by emergence (and break in sedimentation) in the time interval Upper Triassic-Lower Jurassic. Jurassic time is marked by a cycle of deposition with conglomeratic basal beds, epicontinental sediments and marine beds. Late Jurassic-Early Cretaceous movement is indicated by the presence of red basal beds marking the Cretaceous transgression over the Lar Limestone near the western boundary of the study area (southeast of Marijan).

The Pre-Cretaceous movement was more epirogenic than orogenic. However, such movement was followed by intrusion of Mahmudabad Granite and by volcanic activity in the cretaceous time in the southern part of the area. Another phase of the Alpine orogeny occurred in Post-Cretaceous (or Pre-Eocene) time. It is marked by strong folding and faulting of Mesozoic or older beds and was responsible for metamorphism and lineation of the Cretaceous beds. The presence of Eocene basal conglomerate indicates regional emergence and a period of erosion prior to the Eocene transgression. The Post-Cretaceous granitic intrusions were most probably emplaced during this time. Regional subsidence took place again before the Early Miocene, resulting in transgression of shallow marine beds which even overlie directly the Precambrian basement in the central part of the area. This renewed tectonic movement was followed by igneous extrusion at different times and by volcanic activity during the Early Miocene.

The last major orogenic movements took place in Post-Miocene time, when moderate folding of the Miocene beds provided the basic structural pattern of present-day mountains. Subsequent slight epirogenic movements have reactivated subsidence of Miocene basins and the subsequent transgression of Plio-Pleistocene beds with subhorizontal clayey beds over them is marked by a clear angular unconformity (Alavi et al., 1982).

2.4 Major Ore Deposits

The discovery of various types of mineralization has turned the Takab area into a significant mineralized zone in Iran. There are several deposits and numerous mineral occurrences in this area. The most important of them are Angouran (Zn-Pb), Zarshouran (Au-As), Aqdarreh (Au), Shahrak (Fe) and Baycheh-Bagh (Cu, Ni, Co, As, Bi) deposits.

Angouran (Zn-Pb) deposit

The world-class, high-grade Angouran nonsulfide Zn–Pb deposit (Fig. 2.15), situated in the western Zanjan Province about 450 km northwest of Tehran, is one of the major Zn producers in Iran. The deposit is hosted within an allochthonous-thrust slice of a Neoproterozoic metamorphic complex, mostly marbles and schists that is resting tectonically emplaced on a Tertiary-Quaternary sedimentary and volcanic sequence (Borg, 2005). The Angouran deposit is located within one of a number of metamorphic inlier complexes in the central Sanandaj-Sirjan Zone of the Zagros orogenic belt, close to the Urumiyeh-Dokhtar Magmatic Arc and may represent a new type of low-temperature carbonate-hosted Zn–Pb ore that is distinct from Mississippi Valley type and sedimentary-exhalative deposits (Gilg et al., 2006).

Predominantly supergene nonsulfide ore reserve at Angouran are about 18 Mt of ore at 28% Zn, mainly in the form of Zn carbonates, and 4.5% Pb (Annels et al., 2003; Borg & Daliran, 2004 and Daliran & Borg, 2005a, 2005b). Additional yet unexploited hypogenen sulfide reserves amount to about 5 Mt at 40% Zn (Daliran & Borg, 2005a, 2005b and Gilg et al., 2006). The metamorphic complex at Angouran comprises metagabbros, amphibolites, ultramafics, metapelites, siliciclastics, and carbonates. These lithologies are consistent with an intraoceanic island arc complex (Gazanfari, 1991). The age of the protoliths of the metamorphic rocks are not well constrained but are presumably of

Neoproterozoic (to Cambrian?) age (Hamdi, 1995; Stockli et al., 2004). There is a flat-lying bedded travertine plateau, 500 m east of the Angouran mine (Borg, 2005; Gilg et al., 2006) (Fig. 16). Quaternary sediments in the Angouran area comprise widespread gravel fans, alluvium, and very extensive travertine deposits that are related to numerous low to moderately hot springs in the area (Boni et al., 2007).

Following a descriptive classification by the IZMDC (Iran Zinc Mines Development Company) geologists, seven distinct ore types have been distinguished at Angouran mine (Boni et al., 2007): (1) Predominant hard carbonate ore (in close contact with sulfides), (2) Soft carbonate ore with high clay content, usually overlying the hard carbonate ore, (3) Very porous, vuggy breccia ore with clasts of hard carbonate ore, (4) Creamy white massive calamine ore, (5) Very low grade ore, (6) Sulfide ore and (7) Mixed sulfide-carbonate ore.

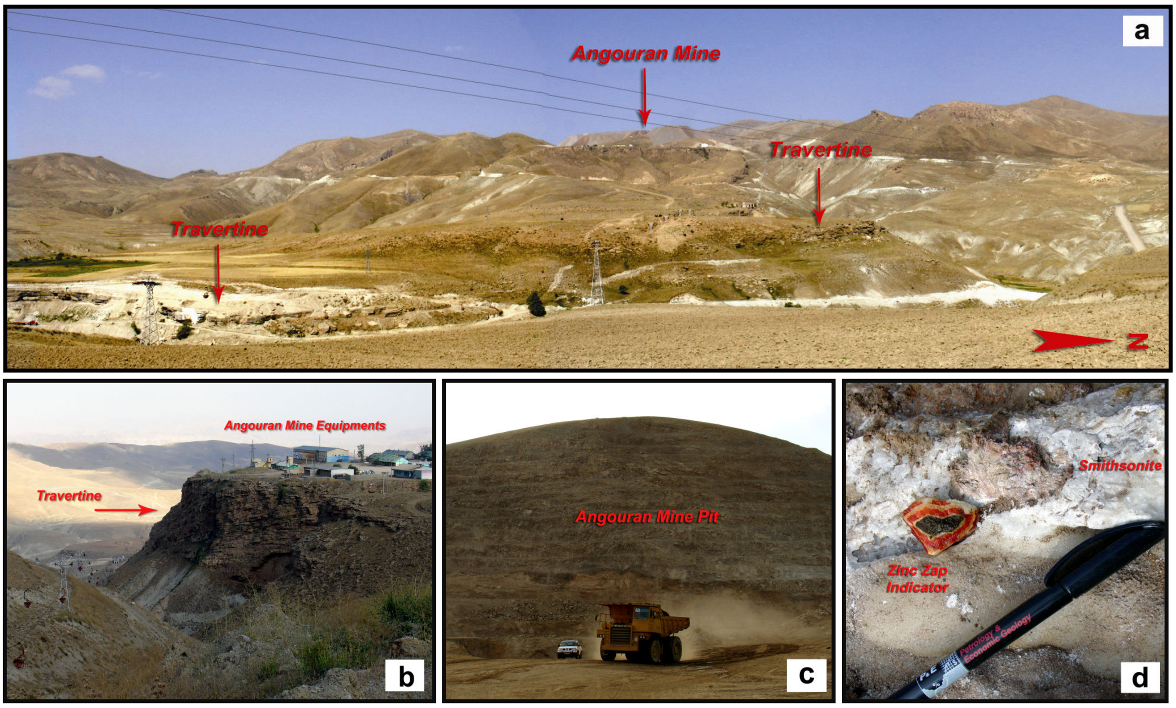

Fig. 2.15 **a** Perspective of Angouran mine; **b** Equipment of mine on the travertine layer; **c** Angouran mine pit and **d** Zoned Smithsonite ($ZnCO_3$) concretion.

Zarshouran (Au-As) deposit

The Zarshouran gold deposit (Fig. 2.16) is located in the north of Takab, in the West Azarbaijan Province. It is hosted by Pracambrian carbonate and black shale formations which have been intruded by a weakly mineralized granitoid. Granitoid intrusion fractured the sedimentary rocks, thereby improving conditions for hydrothermal alteration and mineralization. Silisification is the principle hydrothermal alteration along with decalcification and argillisation (Asadi et al., 2000). The Zarshouran deposit is well known for arsenic mining in Iran. In this area, there are other deposits and prospects of As-Sb-Hg-Tl-Au mineralization, which all seem epithermal in character and exhibit similar genetic features (Mehrabi et.al, 1999). Its mining history dates back hundreds of years and ancient workings for arsenic and gold can still be seen in the area (Modabberi & Moore, 2004). Remnants of gold panning sites (Fig. 17) are also visible along the Zarshuran Stream in an interval of about 500 m (Mohajer et al., 1989). The petrography, mineralogy and trace element geochemistry of Zarshouran gold deposit show that it is a Carlin-like sediment hosted disseminated gold deposit. The association of mineralization at Zarshouran with a magmatic intrusion and the presence of tellurium in concentrations sufficient to precipitate telluride suggest a greater magmatic component in the mineralizing hydrothermal solution than is typical for most Carlin-type deposits (Asadi et al., 2000).

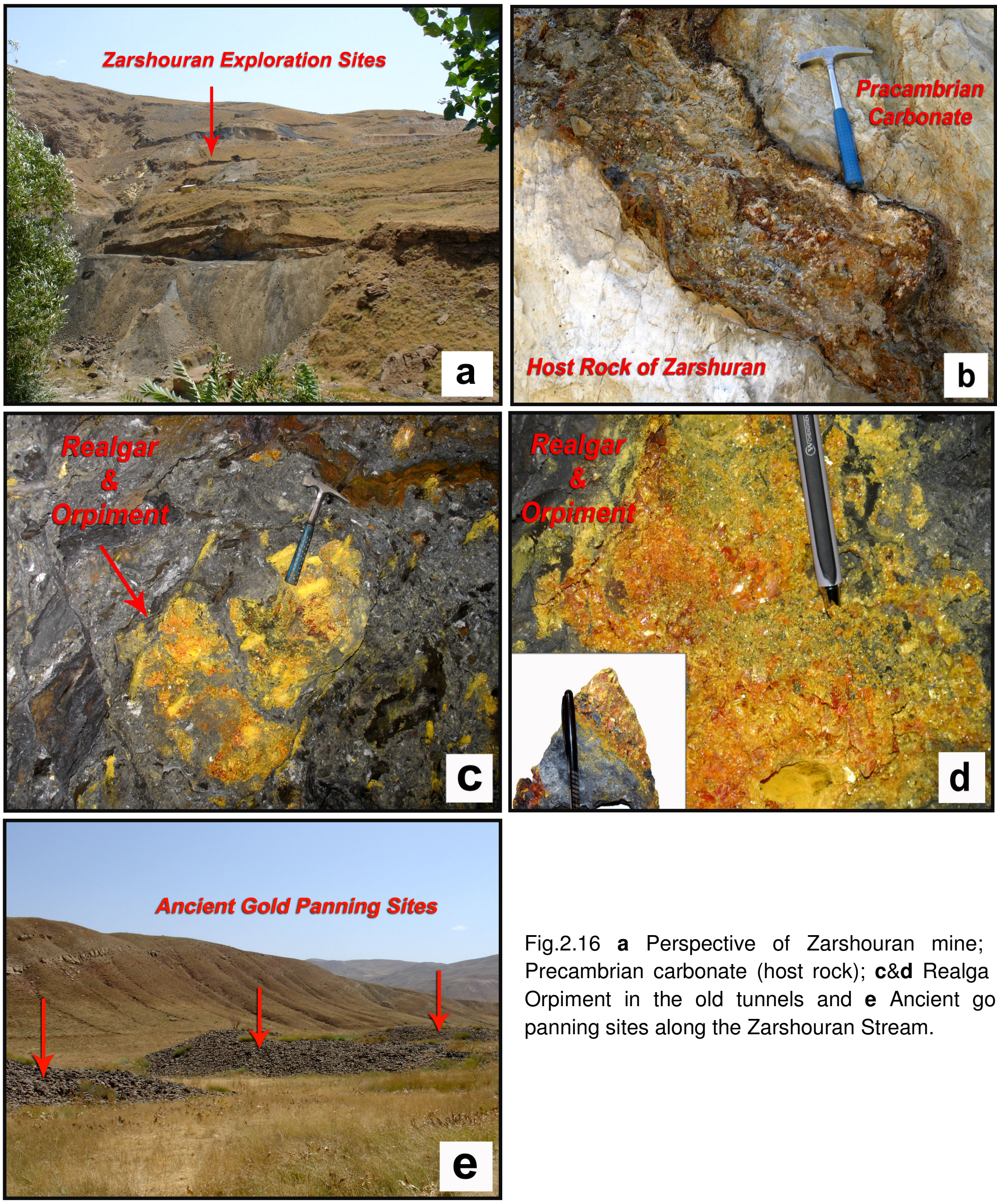

Fig.2.16 **a** Perspective of Zarshouran mine; **b** Precambrian carbonate (host rock); **c&d** Realga & Orpiment in the old tunnels and **e** Ancient gold panning sites along the Zarshouran Stream.

The mineral assemblage includes micron to angstrom-size gold, orpiment, realgar, stibnite, getchellite, cinnabar, thallium minerals, barite, Au-As-bearing pyrite, base metal sulphides and sulphosalts. Most of the gold is detectable only by chemical analysis, but sparse metallic gold has been observed in hydrothermal quartz, orpiment and realgar. Electron microprobe and bulk chemical analysis indicate that gold probably occurs in minerals such as pyrite-arsenian pyrite, orpiment and realgar, although the nature of gold occurrence in these phases is still unknown (Mehrabi et al., 2003).

Final exploration operations confirm the deposits of Zarshouran at four million tons of 5.81 ppm gold ores and seven million tons of 4 ppm gold ores. A total 50 tons of gold can be exploited from this mine.

Aqdarreh (Au) deposit

The disseminated gold deposit of Agdarreh (Fig. 2.17) (24.5 t Au at 3.7 g/t Au) is hosted in hydrothermally leached Miocene reefal limestone in the Takab geothermal field, in the west Azarbaijan Province, which is part of the Cenozoic Urumieh–Dokhtar volcanic arc of NW Iran. Alteration and mineralisation are largely bedding controlled blanket-like and include: (1) pre-ore decalcification; (2) first-stage silicification associated with pyrite (early pyrite with 3–4 wt% As, late pyrite with <1–3 wt% As) and sphalerite; (3) second-stage silicification with precipitation of galena, Pb–Sb–As sulphides, sulphosalts, tellurides and native bismuth; (4) late-stage cinnabar and barite in vugs; (5) oxide ore stage and carbonate alteration (Daliran, 2007).

The Aqdqrreh deposit is within a fault-bounded Tertiary sedimentary basin and a geothermal field. Gold ore is controlled by NW and NE to E striking faults (Daliran et al., 2002). Gold mineralisation is associated with the hydrothermal metal suite of As, Sb, Hg, Te, Se, Tl, Ba, Zn, Ag, Cd, Bi and Pb, and is characterised by very low Cu contents. The hydrothermally altered and mineralised rocks occur in two zones; Agdarreh East and Agdarreh West, which are divided by a structurally controlled NW-trending valley. Zones of silicification at Agdarreh East form NNE-aligned outcrops parallel to the fault system, indicating that the faults served as pathways to the mineralising fluids. At Agdarreh West, the silicified zones occur close to the NW-trending contact between the host limestone and the non-mineralised Upper Red Formation (Daliran, 2007).

The Agdarreh deposit shows many similarities with Carlin-type ore and is interpreted to have resulted from near-surface hydrothermal activity related to the Cenozoic arc volcanism that developed within the extensional Takab graben. The extensive oxidation at Agdarreh may be partly due to the waning stages of hydrothermal activity. Active H_2S-bearing thermal springs are locally depositing extremely high contents of Au and Ag, and travertine is present over large areas, suggesting that ore-forming hydrothermal activity occurred periodically from the Miocene to Recent in the Takab geothermal field (Daliran, 2007). Also the Aqdarreh gold deposit may be referred to as sedimentary rock-hosted disseminated gold (SRHDG) deposits (Hofstra, 2002).

Shahrak (Fe) deposit

The Shahrak iron deposit (Fig. 2.18) is located in the east of Takab, in the Zanjan Province. Cretaceous to Quaternary rocks are exposed in the mine area but Oligomiocene rocks has the most exposure. It is hosted by Oligomiocene rocks (tuff, andesitic tuff and carbonate rocks).

Genesis of the ore mineral is related to volcanic rocks that simultaneously has engendered with Qom Formation. Based on geology and mineralogy evidences, this deposit is attributed to metasomatic iron type (Jafarzadeh et al., 1995).

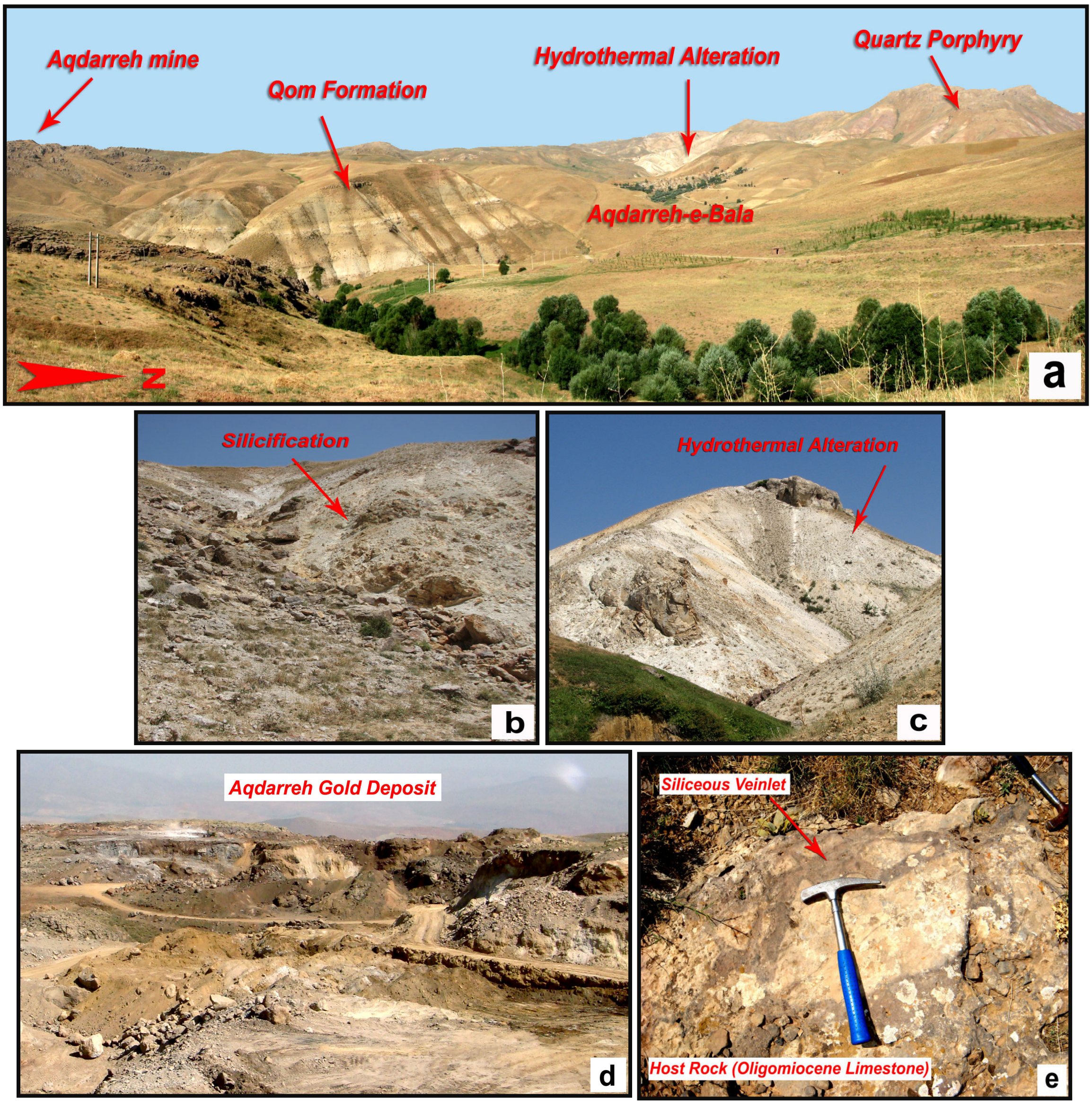

Fig. 2.17 **a** Perspective of Aqdarreh area; **b** Silicification in the north of Aqdarreh mine and **c** Hydrothermal alteration of Quartz porphyry and Microgranit in the north of Aqdarreh mine; **d** Perspective of Aqdarreh mine and **e** Oligomiocene limestone (host rock) of Aqdarreh gold deposit with siliceous vienlet.

The ore body occurs within the carbonate rocks and forms concordant layers. The ore reserve at Shahrak is about 40 Mt of ore at 63% Fe, mainly magnetite. Hematite and limonite are accessory minerals (Jafarzadeh et al., 1995).

*Baycheh-Bagh (*Cu, Ni, Co, As, Bi*) deposit*

The Baycheh-Bagh deposit is located in the north of Takab, in the Zanjan Province. Based on lithostratigraphy point of view includes gneisses and amphibolites of Precambrian, which are unconformably overlain volcanic-volcanoclastic and associated sedimentary rock units of Tertiary and Quaternary age.The volcanic rocks are divided into rhyolitic and andesitic groups in which the rhyolitic group provides the main host-rock of the deposit. Ore parageneses include Cu, Pb, Zn, Ni, Co and Bi minerals (Chalcopyrite ($CuFeS_2$), Tetrahedrite ($Cu_{12}Sb_4S_{13}$), Malachite ($Cu_2(CO_3)(OH)_2$), Azurite ($Cu_3(CO_3)_2(OH)_2$), Galena (PbS), Sphalerite (ZnS), Cobaltite (CoAsS), Skutterudite ($CoAs_3$), Niccolite (NiAs), Bismuthinite (Bi_2S_3) and …) that occurred in nine major veins and several smaller veinlets.

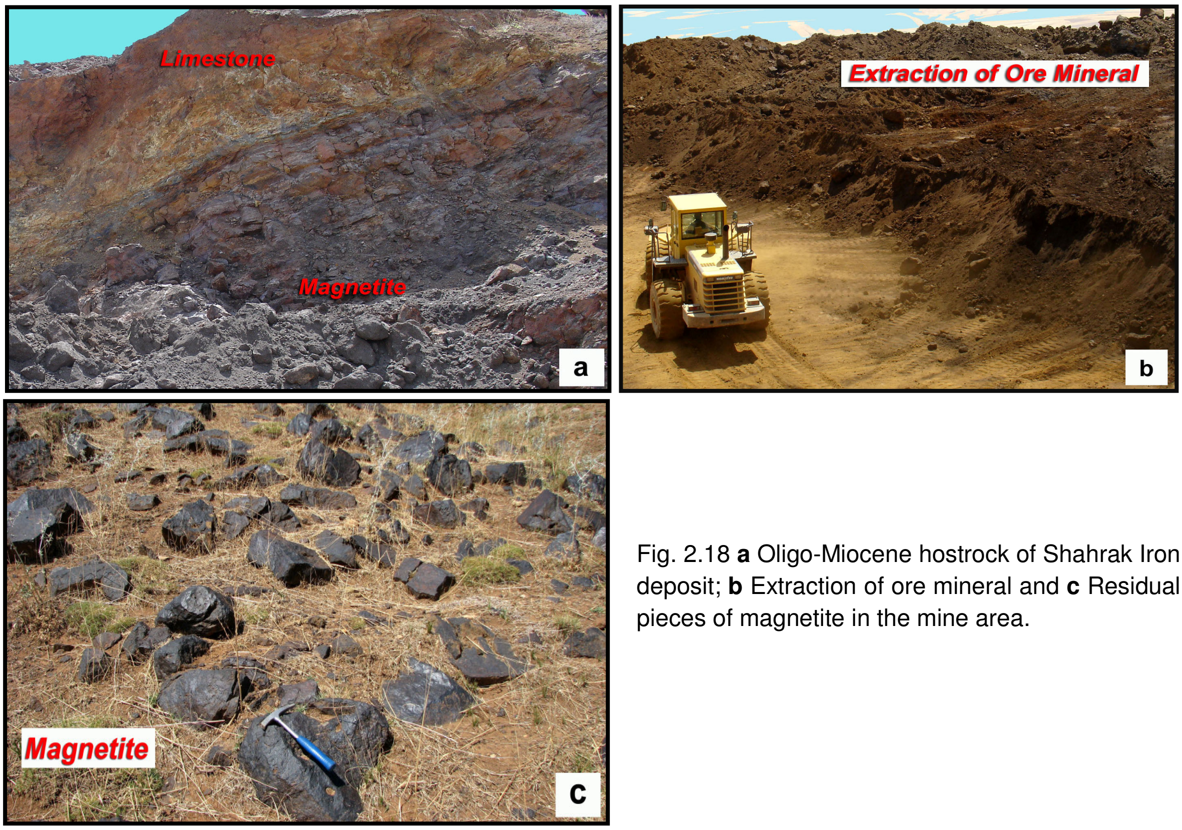

Fig. 2.18 **a** Oligo-Miocene hostrock of Shahrak Iron deposit; **b** Extraction of ore mineral and **c** Residual pieces of magnetite in the mine area.

The ore-generation processes based on the nature of magmatic host rocks, ore assemblages and thermometric data in the Baycheh-Bagh deposit, similar to other hydrothermal five-element vein deposits, seems to have occured in relation to ore-bearing fluids migration. These fluids the metals of recycled the deep-seated basic and ultrabasic rocks of the old basement as also adjacent volcanoclastic hosts and deposited the ore minerals in the fault spaces in under suitable conditions (Lotfi and Karimi, 2004). Figure 2.19 shows the view of mine and a sample of the copper minerals.

There are several smaller mineral occurrences in the study area include: Au-As (Arabshah), Sb (Agdarreh Bala and Moghanlu), Hg (Shirmard and Shakh-Shakh Mountain), Mn (Dabal Kuh), Fe (Kuh Baba), Pb-Zn (Ay Qalehsi and Arpachay) and Zn (Au) (Chichaklou). Figure of some of aforesaid mineral occurrences attached in appendices.

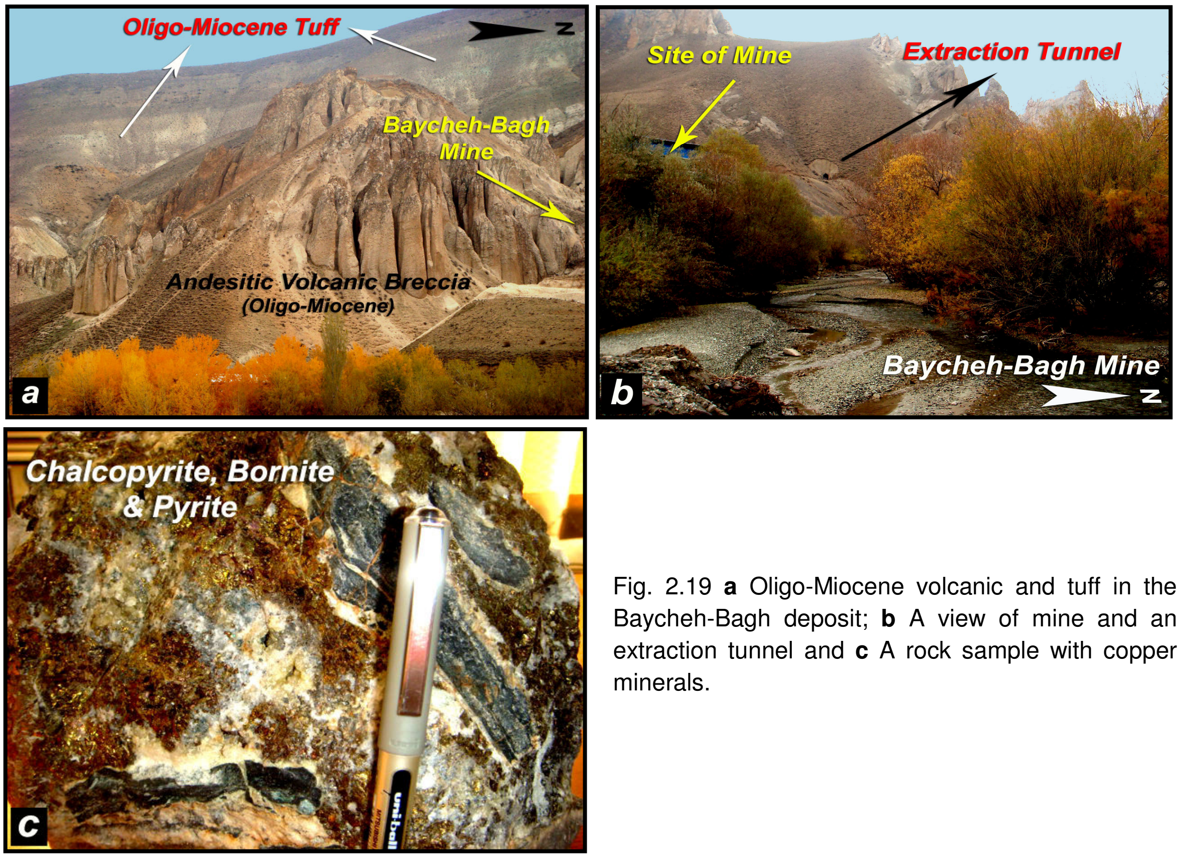

Fig. 2.19 **a** Oligo-Miocene volcanic and tuff in the Baycheh-Bagh deposit; **b** A view of mine and an extraction tunnel and **c** A rock sample with copper minerals.

Chapter 3 Deposits Recognition Criteria and Geo-Exploration Datasets

3.1 Introduction

Mineral deposit models have been defined by (Ludington et al., 1985) as “systematically arranged information that describes the essential attributes of a class of mineral deposit”. An exploration model for a certain area and class of deposit can be generated by customizing a general mineral deposit model for the area under study. The conceptual model implemented in the GIS-based mineral potential mapping, is based on the mineral deposit model applicable to the deposit type of interest and the environment in which the deposit occur. The deposit exploration model is composed of all the deposit model components that provide criteria for exploration and recognition of deposit indicators, from data derived from geological, geophysical and geochemical surveys and other data sources such as remote sensing data. The deposit exploration model therefore guides the choice of data sets, the operations employed to extract useful information for mineral prediction, and, where the expert system methods are used for data combination, the ranking or weighting of data layers (Rojas, 2003). The following paragraphs will outline such ore deposit types that are geologically expected and have an empirically proven track record in the area under investigation.

3.2 Carbonate Replacement Deposits (CRD)

Mississippi Valley type (MVT) Pb-Zn and Carlin type gold deposits are the two most important types of Carbonate Replacement Deposits (CRD). Carbonate-hosted lead-zinc and gold ore deposits are important and highly valuable concentrations of Pb-Zn sulfide and Au ores hosted within carbonate (limestone, dolomite, marl) formations and share a common or similar genetic origin.

3.2.1 General Characteristics of Mississippi Valley Type Pb-Zn Deposits

Mississippi Valley type (MVT) lead-zinc deposits are a varied family of epigenetic ore deposits that form predominantly in dolostone and in which lead and zinc are the major commodities. Most are found in rocks of Cambrian and Ordovician, Devonian and Carboniferous, and Triassic ages. Undeformed orogenic foreland carbonate platforms are the favoured tectonic setting for MVT deposits; some are in carbonate sequences in foreland thrust belts bordering foredeeps and fewer still are associated with rift zones (Leach et al., 1995).

MVT deposits typically occur in metallogenic districts, covering hundreds, or even thousands of square kilometers. Within each district, deposits display remarkably similar features, including mineral assemblages, isotopic compositions, and textures. Ore controls typically are district-specific; examples include shale edges (depositional margins of shale units), limestone-dolostone transitions, reef complexes, solution collapse breccias, faults, and basement topography (Leach et al., 1995).

Some characteristics of MVT Pb-Zn deposits are as follows (Hassanipak and shojaat, 2000; Tab. 3.1).

Tab. 3.1 Characteristics of Mississippi Valley type Pb-Zn deposits (Hassanipak and shojaat, 2000).

Definition	Epigenetic - stratabound ore deposits of sphalerite and galena (mainly sphalerite) in primary or secondary cavities of carbonate rocks
Host Rock	Dolomite and dolomitic limestone
Alteration	Dolomitization, silicification, limestone dissolution and karstification
Age	Generally Cambrian up to Mid. Ordovician, but also from Proterozoic up to Triassic and much younger
Geochemistry	Zinc (Zn), Lead (Pb), Copper (Cu), Arsenic (As), Silver (Ag), Molybdenum (Mo), Cobalt (Co), Nickel (Ni), Cadmium (Cd), Boron (B), Antimony (Sb), Fluorine (F)
Geophysics	Airborne magnetics for underlying basement topography and IP (Galena & Pyrite)
Ore Mineralogy	Sphalerite, galena, chalcopyrite, pyrite, marcasite, fluorite, barite, anhydrite, gypsum
Tectonic Setting	Foreland sedimentary basins and stable continental platforms. MVT is formed under continental compressional conditions

Schematic model of MVT deposit is shown in figure 3.1.

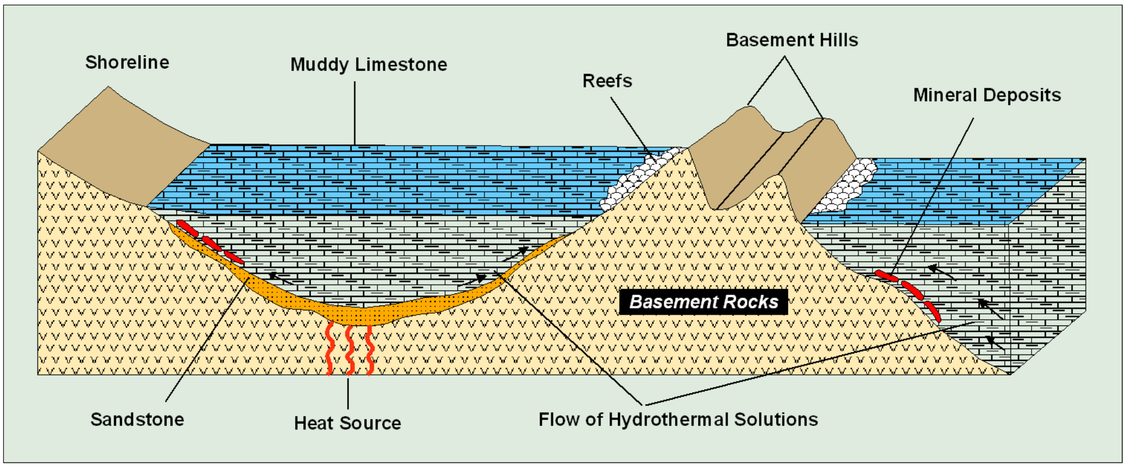

Fig. 3.1 The relationship between Mississippi Valley type deposits, the edges of sedimentary basins, and the flow of hydrothermal solutions (Encyclopedia Britannica, Inc., 1999; www.britannica.com).

3.2.2 General Characteristics of Carlin-Type Gold Deposits

Basically, Carlin-type gold deposits are characterized by:

(1) strong structural control of mineralization by faults and folds, (2) calcareous sedimentary host rocks of diverse lithofacies, types, locally with igneous rocks, (3) decarbonatization, argillization, silicification and sulfidation alterations, (4) the occurrence of submicron-size gold particles (<0.2 μm) in association with pyrite, arsenian pyrite and arsenopyrite, and (5) a geochemical signature of Au, As, Hg, Sb and Tl (Radtke, 1985; Wang et al., 1994; Liu, 1994 and Hofstra and Cline, 2000).

Some characteristics of Carlin-type gold deposits are as follows (Hassanipak and shojaat, 2000; Tab. 3.2).

Tab. 3.2 Characteristics of Carlin-type gold deposits (Hassanipak and shojaat, 2000).

Definition	Finely disseminated native gold (Au) and sulfides in carbonate host rocks
Host Rock	Thinly bedded silty or argillaceous carbonaceous limestone or dolomite, commonly with carbonaceous shale
Alteration	Decarbonatization of carbonate rocks, silicification, (jasperoids), intense argillic alteration in the core of some deposits – which grades outwards into peripheral sericitic alteration
Age	Generally Tertiary but can be seen in every geological period
Geochemistry	Gold (Au), arsenic (As), silver (Ag), mercury (Hg), antimony (Sb), molybdenum (Mo), tungsten (W), thallium (Tl) , fluorine (F), barium (Ba).
Ore Mineralogy	Native gold (micron and sub-micron-size free gold in silica, pyrite, arsenopyrite, stibnite, realgar, orpiment, cinnabar, fluorite, barite
Tectonic Setting	Passive continental margins with subsequent deformation and intrusive igneous activity

Carlin-type gold deposits are a type of hydrothermal deposits (Epithermal; Radtke et al., 1980 & Mesothermal; Evans, 1993).

Schematic illustration of geologic environments in which hydrothermal gold deposits form is shown in figure 3.2. Arrows show sources of water thought to have formed these deposits (Kesler, 1994).

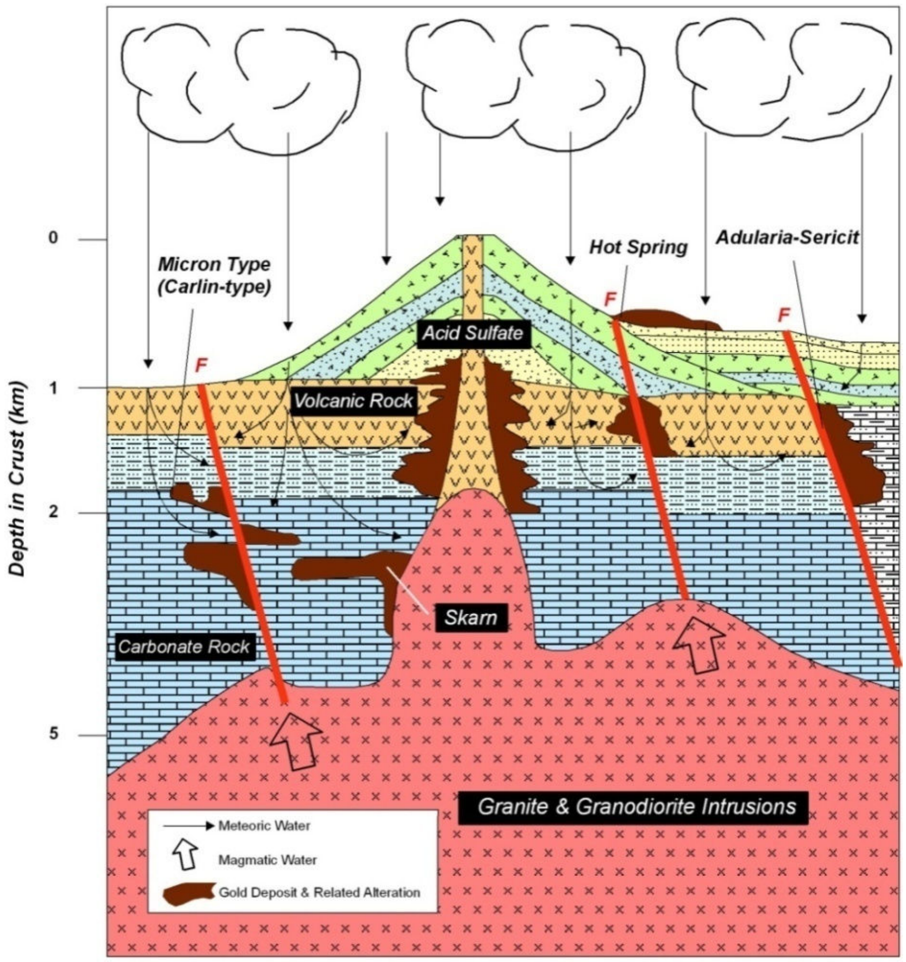

Fig. 3.2 Schematic illustration of geologic environments in which hydrothermal (Carlin-type) gold deposits form (Kesler, 1994).

3.3 Exploration Recognition Criteria

Based on the general characteristics of Mississippi Valley type (MVT) Pb-Zn and Carlin-type gold deposits, both elsewhere and in the study area, the following parameters are considered to act as “recognition criteria” for the exploration of these or similar deposit types in the terrain.

3.3.1 Recognition Criteria for the Exploration of MVT Pb-Zn Deposits

Exploration for MVT deposits is relatively complex in theory and straightforward in practice. During the area selection phase, attention must be paid to the nature of the carbonate sequences, especially if there is specific alteration such as a 'dolomite front' identified within oil exploration wells for hydrocarbons, which are commonly associated with MVT Pb-Zn mineralization.

The facies of the carbonate sequence is critical, as this is controlled mostly by faults, which have acted as conduits for ore fluids and thus are the ultimate target of exploration. Bradley and Leach (2003) examined the tectonic aspects of foreland evolution and concluded that the type of foreland is not a critical control on ore formation. Mississippi Valley-type deposits are located in collisional and transpressional orogens. Also associated with orogens are MVT deposits that occur in fold and thrust belts. Some deposits formed in flat-lying rocks or were later caught up in the thrusting. Others formed synchronously with thrusting and others formed after burial by the thrusts (Leach et al., 2005).

3.3.2 Recognition Criteria for Exploration of Carlin-Type Gold Deposits

Exploration for Carlin-type deposits in some areas (e.g. Great Basin, USA) is focused on the presence of outcropping jasperoids and fundamental geologic mapping. Given the apparent link of the metallogenesis to magmatism in the Great Basin, the presence of igneous rocks is considered positive; however, Carlin-type deposits in other areas of the world (particularly China) do not all have such a strong documented link to magmatic activity. Although Au is the most important trace element indicator, other metals such as As, Sb, Hg, Tl and Ba are utilized as exploration tools.

Abundant geochemical sampling is critical, as all of these elements can have an erratic distribution. On a regional scale, deep crustal structures as indicated by geophysics or geochemistry are also important (Arehart, 2003).

3.4 Distribution Patterns of Mineralization

The spatial distribution of mineralization is the foremost concern in regional exploration and it could be considered as a very important tool in the investigation of mineral deposits (Yaghubpur and Hassannejad, 2006).

The study of spatial distributions of mineralization is an important issue in mineral exploration because it can give an insight about the geological controls responsible for the generation of mineral deposits, and therefore can help to visualize the possible locations of undiscovered deposits. One of the most important controls on the distribution of mineralization in most deposits is faults and fracture systems, along which hydrothermal fluids can move and minerals can be deposited (Palomera, 2004). Mapping at scales relevant to a geological problem and with an emphasis on structural geology is very useful in understanding the directional controls on mineralization. There are several methods, one of which is “Fry analysis” that could be used as a complement to mapping (Yaghubpur and Hassannejad, 2006).

“Fry analysis” is a good method to determine the direction(s) of maximum continuity of the deposits and can be used for different types of deposits. Fry analysis uses a geometrical method of spatial autocorrelation. The method uses all center-to-center spatial relationships (or translations) between every pair of points.

3.4.1 Fry Analysis

Fry analysis is a point pattern analysis method that uses separations between all objects of an object distribution (Fry, 1979) in contrast to the “nearest neighbor methods”. Fry analysis (Fry, 1979) can be applied manually by placing a sheet of tracing paper on which a series of parallel reference lines (typically north pointing on a map) have been drawn, and the location of each data point is recorded. On a second sheet of tracing paper with a center point (or origin), a set of marked parallel lines are kept parallel to those on the first sheet. The origin of the second sheet is placed on one of the data points on the first sheet and the second sheet marked with all the positions of points on the first. Then the origin of the second sheet is placed on a different data point on the first and the position as gain recorded on the second sheet. This is continued, maintaining in the same orientation, until all points on the first sheet have been used as the origin on the second. For “n” data points, there are n^2-n translations. The resulting Fry plot may be further analyzed by construction of a rose diagram, recording joint frequency versus directional sector (Vearncombe and Vearncombe, 1999).

The analytical methods of Fry (1976) and Allison et al. (1997) were developed further by Vearncombe et al. (1999), applying them to the spatial distribution of mineralization and as an alternative to directional variography, to the distribution of mineralization as recognized in drilling. Fry analysis according to Vearncombe and Vearncombe (1999), can produce interpretable results with modest-size data sets that include 14 or more samples. Typically the larger the number of sample data, the more reliable the end results.

3.4.2 Results of Fry Analysis

The Fry analysis for the study area was carried out using 23 Pb-Zn and 16 Au deposits or ore indications, each one represented by a point in the DotProc software (Fig. 3.3).

The occurrences of Pb-Zn and Au in the study area are of different metallogenetic origin. Fry analysis and derivative rose diagrams of the structural terrains were applied for all Pb-Zn and Au mineralizations of the study area according to the method suggested by Vearncombe and Vearncombe, 1999. Therefore the spatial relationships of the mineralizations and the rose diagrams of the major faults were prepared for all of these occurrences. When this analysis is used for mineral exploration, the results can be interpreted by looking at the Fry plot, but also by looking at derivative rose diagrams generated from the Fry plots. If there are regular patterns in terms of spacing and orientation of points, the Fry plot will enhance such patterns allowing an easier visual interpretation of them. High frequencies of orientation observed in the plots can reflect orientations of structures that controlled the mineralization.

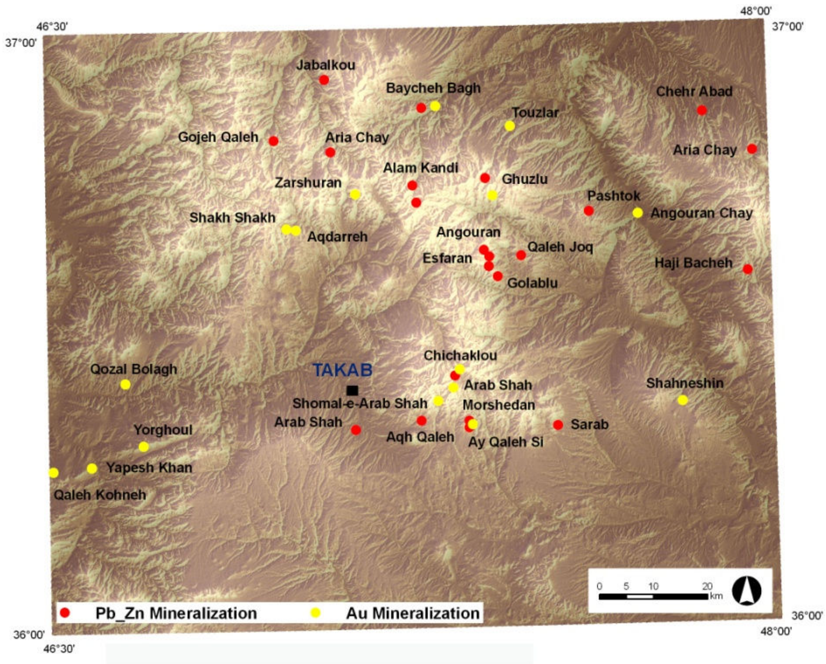

Fig. 3.3 Distribution map of Pb-Zn (23 points) and Au (16 points) occurrences in the study area.

When Fry plots are analyzed, parallel patterns can be separated at a recurrent distance from each other indicating, which could be the spacing between the structural corridors with that orientation that are responsible for the pattern.

In the first Fry analysis, the total population of 23 Pb-Zn mineralization points was used to generate a Fry plot (with 506 translations) and two derived rose diagrams (Fig. 3.4). In one of the rose diagrams all translations plotted and in the other one, just the translations of less than 10 km length (range = 0-10 km) were plotted.

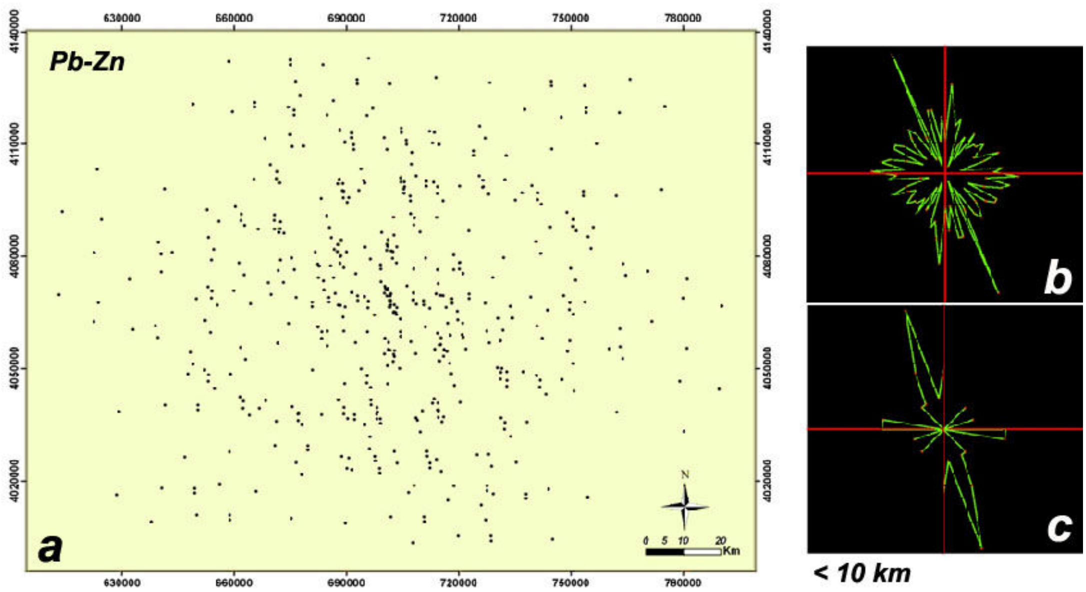

Fig. 3.4 **a** Fry plot with 506 translations obtained using all Pb-Zn occurrences; **b** Rose diagram of all translations. A predominant direction at NNW-SSE and a secondary one at N-S and W-E trends and **c** Rose diagram of translations of less than 10 km length showing possible enhanced local controls at NE-SW trend.

In the rose diagram with all translations, a predominant direction with a NNW-SSE trend and two major trends with N-S and W-E trends respectively, are easily observed (Fig. 3.4 b). In the rose diagram of translations of less than 10 km (Fig. 3.4 c), the same major and two minor directions become even more apparent. The same prominent direction (NNW-SSE, the main trend of the Sanandaj-Sirjan structural zone) are recognized in both rose diagrams and at the short range a new secondary direction at the NE-SW trend appears. This indicates that the NE-SW direction (predominant trend of geological faults) become more important at local scale.

In the second analysis, the total population of 16 Au mineralization points was used to generate a Fry plot (with 240 translations) and two derived rose diagrams (Fig. 3.5). In one of the rose diagrams all translations plotted and in the other one, just the translations of less than 15 km length (range = 0-15 km) were plotted.In the Fry plot and rose diagram with all the translations, a predominant direction with NE-SW trend and a secondary one with NW-SE and W-E trends are observed. In the rose diagram of translations of less than 15 km, two main directions at NW-SE and NE-SW trends were observed. At the short range for Au occurrences, the NE-SW trend is the more important trend (trend of big lineaments) on a local scale.

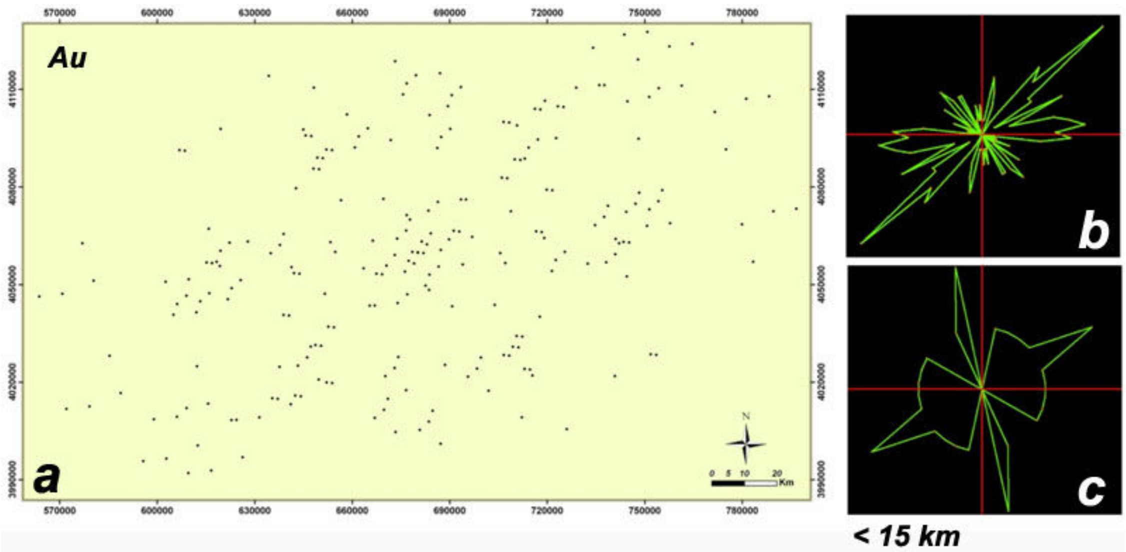

Fig. 3.5 **a** Fry plot with 240 translations obtained using all Au occurrences; **b** Rose diagram of all translations. A predominant direction at NE-SW and a secondary one at NW-SE and W-E trends and **c** Rose diagram of translations of less than 15 km length showing possible enhanced local controls at NE-SW trend.

3.5 Geo-Exploration Datasets

Mineral exploration potential assessment or the classification thereof is a multi-stage process with the ultimate objective of delineating mineralized zones that can be exploited under prevailing economic conditions (Reeves et al., 1990).

Ideally, during each stage, multivariate and multi-source geo-exploration datasets are used to guide the succeeding stages of mineral potential assessment and classification. At the medium-scale stage (i.e., regional to district scale, ranging from 1:50.000 to 1:100.000 scale map coverage), for example, the geo-exploration datasets required should be ideally derived from geological, remote sensing (e.g. spectral), geophysical and geochemical surveys. The increasing need to integrate geo-exploration datasets arises from the fact that most of the easily-recognized mineral deposits have long been known and that more evidence and advanced methods are necessary to accurately assess and classify the subsurface mineral potential of a particular area (Bonham-Carter, 1997; Chinn and Ascough, 1997; Raines, 1997 and Pan and Harris, 2000).

Geo-exploration datasets used in this research include ore occurrences data (mine and ore indication), geological, geochemical, geophysical and remote sensing data (Aster and Landsat 7 ETM$^+$).

3.5.1 Geological Data

The geological maps (six sheets, i.e. sheet Mahneshan, Takht-e-Soleyman, Shahindezh, Chapan (Irankhah), Takab and Qodjour (Yasoukand)) at 100.000 scale (Geological Survey of Iran) were captured in digital format (shp format).

To input the lithological data into the GIS, each geological map was digitized separately and then glued together and slightly modified at the margins using information from ASTER data. The en-bloc map was polygonized to produce areas representing different rock units using the UTM (Universal Transverse Mercator) projection and its lithological and stratigraphic attributes (lithological unit name, formation, geological age and description and …) were recorded in an associated attribute table. In this map, various lithostratigraphic units are classified up to the level of geological “formation” status.

Faults were digitized as segments from six geological maps (1:100.000 scales) and glued together too (Fig. 3.6). The fault properties input in the attribute table.

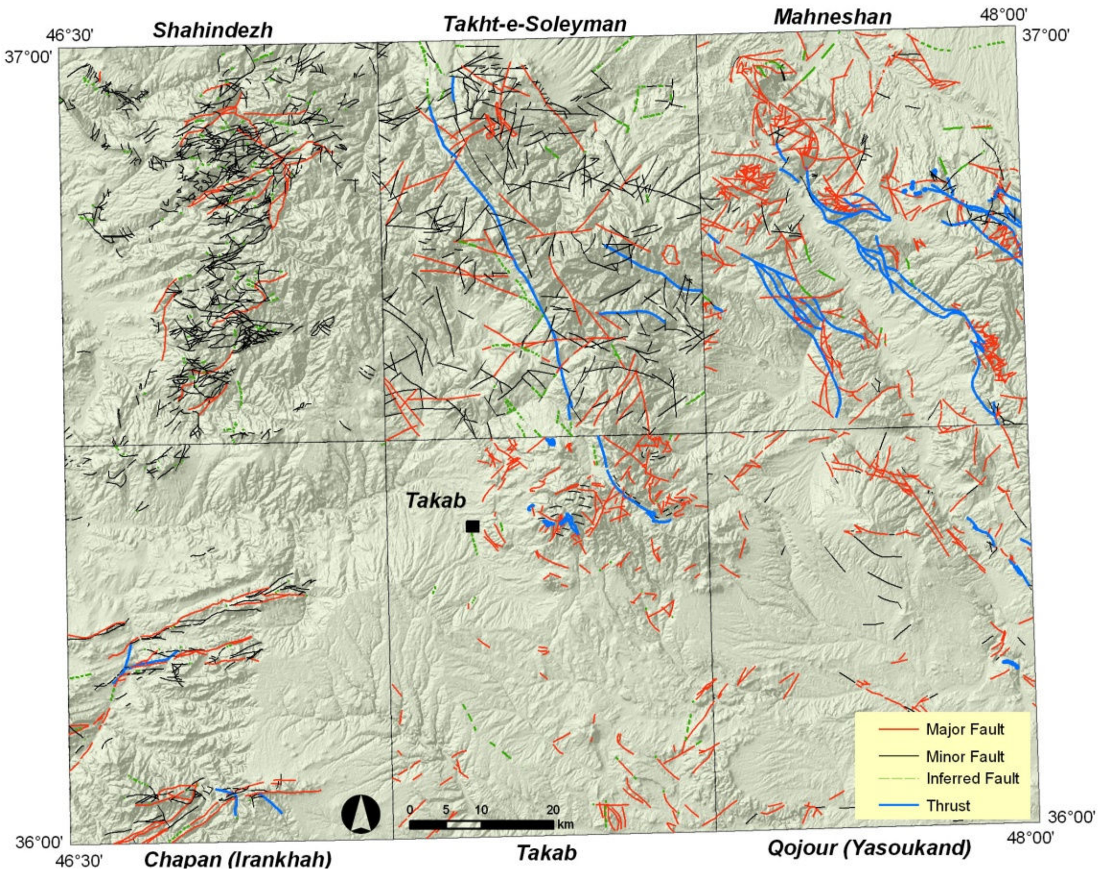

Fig. 3.6 Structural map of the study area (extracted and GIS-ready from six 1:100.000 geological maps, Geological Survey of Iran).

3.5.2 Geochemical Data

Geochemical responses in data sets derived from rock or soil samples can reflect a number of processes that have occurred within the survey area depending on the nature of the material sampled and the method of analysis used to make geochemical determinations.

Geochemical data were obtained from six 1:100.000 scale maps stream sediment survey (Geological Survey of Iran). Geochemical data covers the study area with 4501 samples representing a sampling density of approximately 3 to 4 samples per km^2. The samples were composed of stream sediments of naturally disintegrated rocks. They were air dried and were sieved to obtain the 80 mesh fraction. The samples were analyzed for Au, Ag, Cu, Pb, Zn, As, Sb, Cd, W, Sn, Mo, Ba, Bi, B, Sr, Cr, Co, Ni and … values by AAS (Atomic Absorption Spectrophotometry) and XRF (X-Ray Fluorescence) analysis. Spatial and non-spatial attributes of the geochemical data were interred into the attribute table.

Because the geochemical data pertain to areas are underlain by different lithologies and different detection limits and background values for the various elements in every sheet, the data sets were studied separately for each sheet. For example, table 3.3 shows the elementary statistics of elements concentration of geochemical raw data (stream sediment samples) for the Mahneshan sheet.

Tab. 3.3 Elementary statistics of elements concentration (ppm) of geochemical raw data in Mahneshan sheet.

Element	*Count*	*Mean*	*Median*	*Std. Dev.*	*Variance*	*Skewness*	*Kurtosis*	*Min.*	*Max.*
Ag	816	1.8602623	1.8965	0.31346605	0.098260964	-0.73075703	1.387703	0.52	2.76
As	816	11.607262	11.956	2.248363631	5.055139016	-0.66819099	0.988579	2.54	17.45
Ba	816	691.60916	706.3295	109.7647073	12048.29097	-0.52801196	1.802224	183.22	1053.55
Bi	816	0.147	0.148	0.022319016	0.000498138	-0.97547228	3.858231	0.04	0.24
Cd	816	0.119	0.116	0.022555344	0.000508744	0.595340614	1.080433	0.06	0.23
Co	816	12.8	10.2025	9.885984874	97.73269693	4.399198051	41.21757	0.13	126.78
Cr	816	142.5	138.065	93.9793394	8832.116234	0.931926533	1.543482	3.75	595.35
Cu	816	38.8	38.2325	11.7568771	138.2241592	0.397498002	0.941939	6.28	83.11
Hg	816	0.11	0.068	0.524534087	0.275136009	28.23757124	803.4377	0.002	15
Ni	816	51.01	44.514	44.40273917	1971.603246	1.397678266	2.69286	2.91	290.27
Pb	816	33.9	30.1255	84.85244633	7199.937648	22.90184904	552.7416	2.07	2200
Sb	816	0.68	0.685	0.09832803	0.009668402	-0.43718023	0.615502	0.32	0.99
Sc	816	9.2618701	9.081	4.945865378	24.46158434	0.882914282	1.36954	0.85	32.46
Sn	816	6.3353211	6.4265	0.616593893	0.380188029	-0.89466031	2.523577	2.84	8.27
Sr	816	410.93043	407.6115	59.00410365	3481.484248	0.457923998	0.735757	218.62	673.27
V	816	182.81591	175.7095	115.7213908	13391.44029	0.9529295	1.49579	3.82	736.10
W	816	2.5586949	2.5935	0.573759319	0.329199756	-0.57479912	1.949809	0.16	4.84
Y	816	14.512192	14.409	1.25123791	1.565596308	0.335484799	0.755669	10.91	19.52
Zn	816	87.478011	79.703	112.5854142	12675.47549	19.37806893	398.2876	11.83	2600

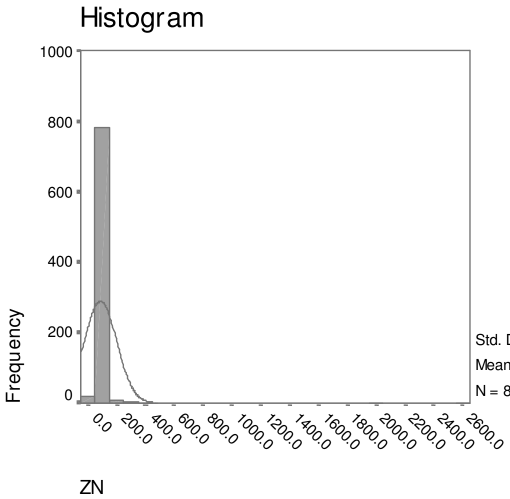

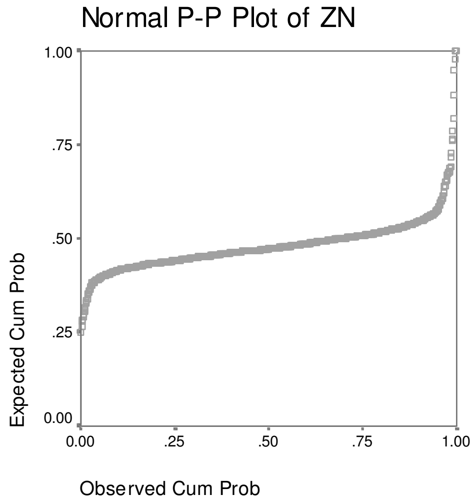

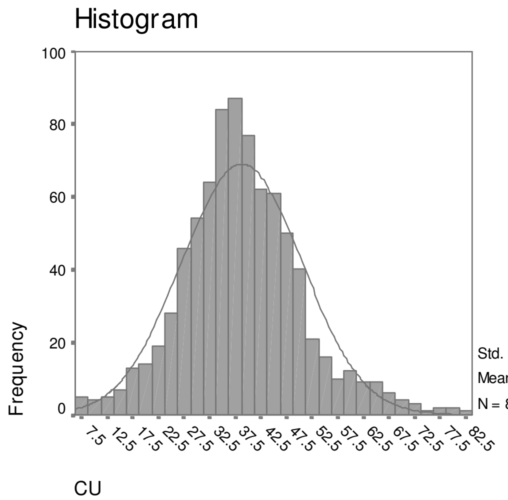

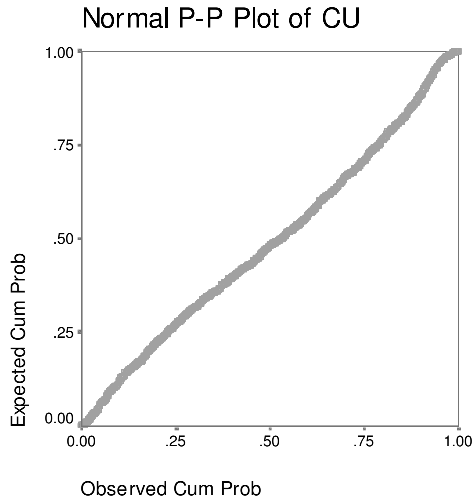

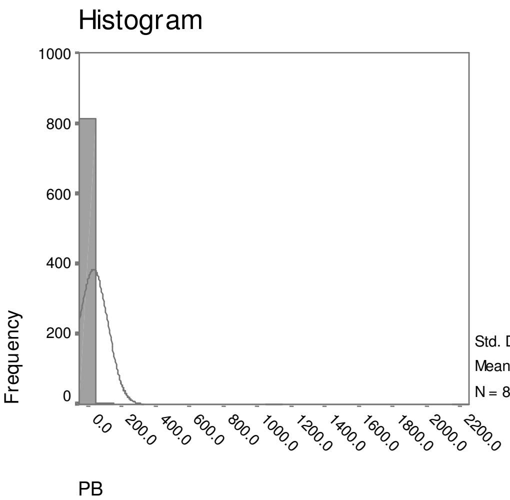

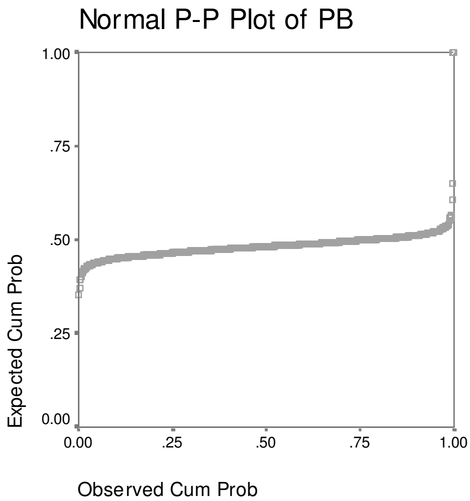

Values that are equal to or less than the mean are considered low background. Values between the mean and mean plus one standard deviation (x + s.d.) are high background. Values between x + s.d. and x + (2 * s.d.) are slightly anomalous. Values greater than x + (2 * s.d.) are highly anomalous. Figure 3.7 shows the geochemical distribution map of Zn in the study area.

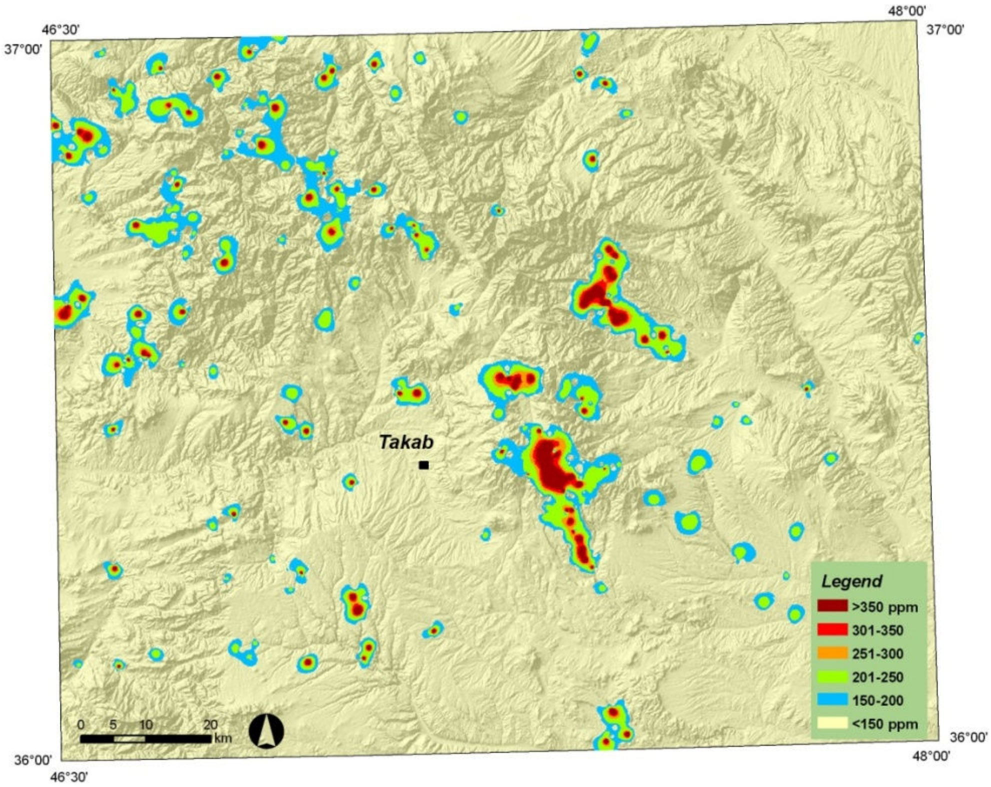

Fig. 3.7 Geochemical distribution map of Zn in the study area.

3.5.3 Remote Sensing Data

Remote sensing data were obtained from Aster (Advanced Spaceborne Thermal Emission and Reflection Radiometer) L1B and Landsat 7 ETM$^+$ (Enhanced Thematic Mapper Plus) data. The Aster and ETM$^+$ images were georeferenced using control points identified both on the images and on 1:25.000 scale topographic maps. They were corrected for atmospheric effects. ETM$^+$ images were joined into a mosaic to create one common scene. Image enhancement was performed to extract structures that would not have been apparent from the images. The lineaments, circular structures and hydrothermal alteration zones were digitized from the ETM$^+$ and Aster data with different techniques. An index map of Aster scenes (7 scenes) for the study area is shown in figure 3.8.

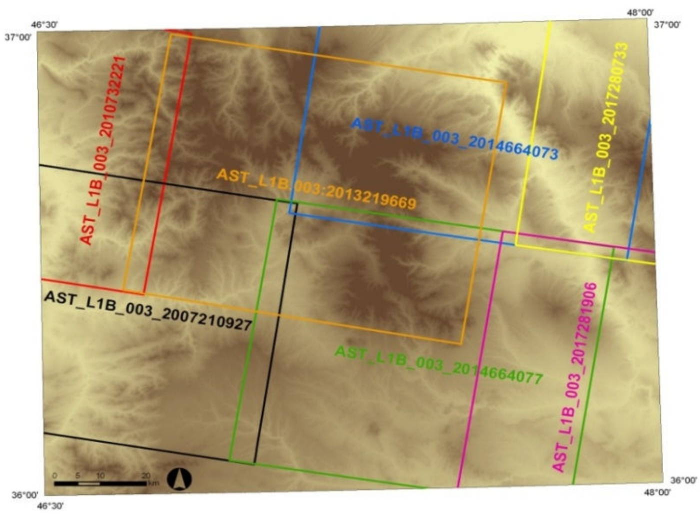

SCENE_ID	DATE
AST_L1B_003_2010732221	28/Apr/01
AST_L1B_003_2007210927	11/Jun/02
AST_L1B_003_2014664073	29/Jul/02
AST_L1B_003_2014664077	29/Jul/02
AST_L1B_003_2017281906	18/Sep/03
AST_L1B_003_2013219669	14/Jul/00
AST_L1B_003_2017280733	18/Sep/03

Fig. 3.8 Index map of Aster scenes in the study area.

Two scenes of Landsat 7 ETM$^+$ cover the study area. Figure 3.9 shows the index map of ETM$^+$ senses in the study area.

SCENE_ID	DATE
ETM_p167_r034	1999
ETM_p167_r035	1999

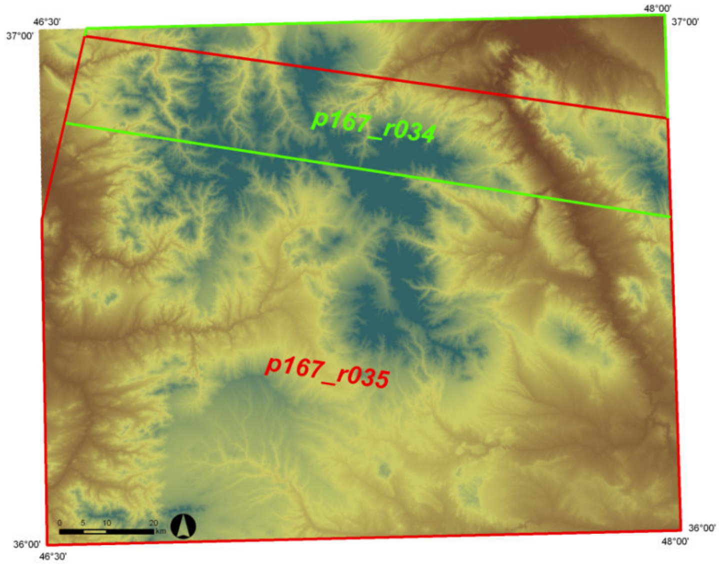

Fig. 3.9 Index map of Landsat 7 ETM$^+$ scenes in the study area.

3.5.4 Geophysical Data

Geophysical data include magnetic and radiometric (K, Th and U) digital grid maps from a 1977-78 airborne geophysical survey (with following of topography elevations) with 500m lines spacing over the study area (Prakla- Seimos GmbH). These data belong to the Atomic Energy Organization of Iran. Table 3.4 shows the characteristics of flights for taking of geophysical data.

Tab. 3.4 Characteristics of flights for taking of geophysical data.

Line spacing	***500 meter***
Line direction	***N-S***
Controlling line	***5 km***
Nominal terrain clearance	***120 meter***
Sample internal	***1 second***
Magnetometer type	***Proton magnetometer (0.5 nT)***
Radiometric spectrometer	***Gama spectrometer (512 channels)***

There are also geophysical data (digital grid map) with 7.5 km line spacing and an aeromagnetic map at a 250.000 scale (Geological Survey of Iran, 1978), which have also been used and integrated into the current study. Figure 3.10 shows the geophysical features in the study area.

3.5.5 Mineral Occurrences Data

The mineral occurrence database was prepared in digital format (shp format) from the NGDIR (National Geoscience Database of Iran) of the Geological Survey of Iran. It contains descriptions of all known mineral occurrences in the study area. This database includes 83 records that are described by string fields: Name, Coordinate, Ore minerals, Host rock, Age of host rock, Stage, Activity, Genesis and Description. The locations of mineral occurrences are indicated on the simplified geological map (Fig 3.11).

Fig. 3.10 Geophysical features from 1:250.000 aeromagnetic map on the 7.5 km line spacing total magnetic grid map in the study area (Geological Survey of Iran, 1978).

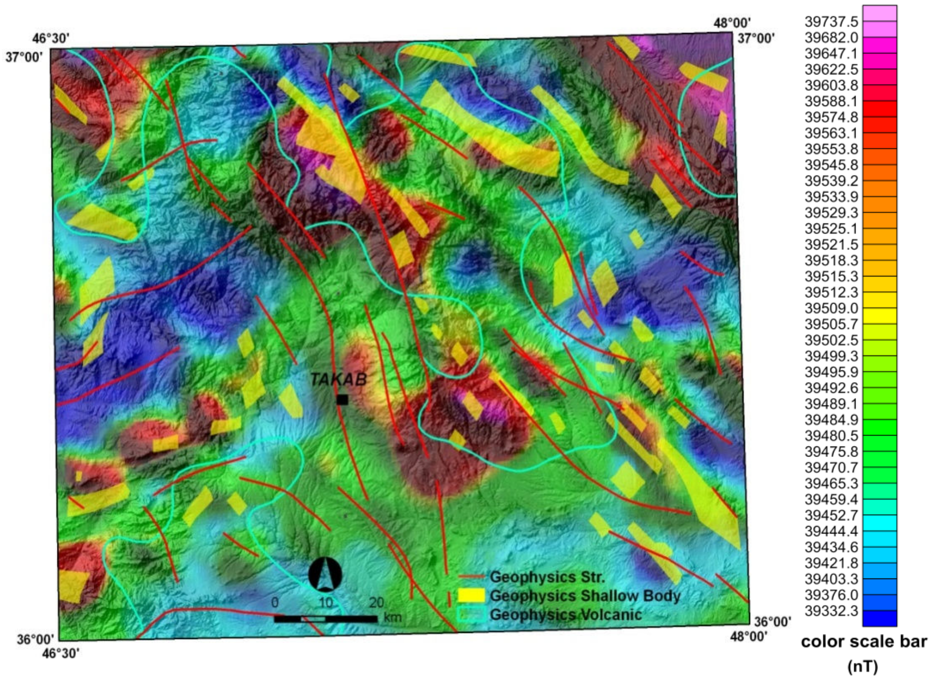

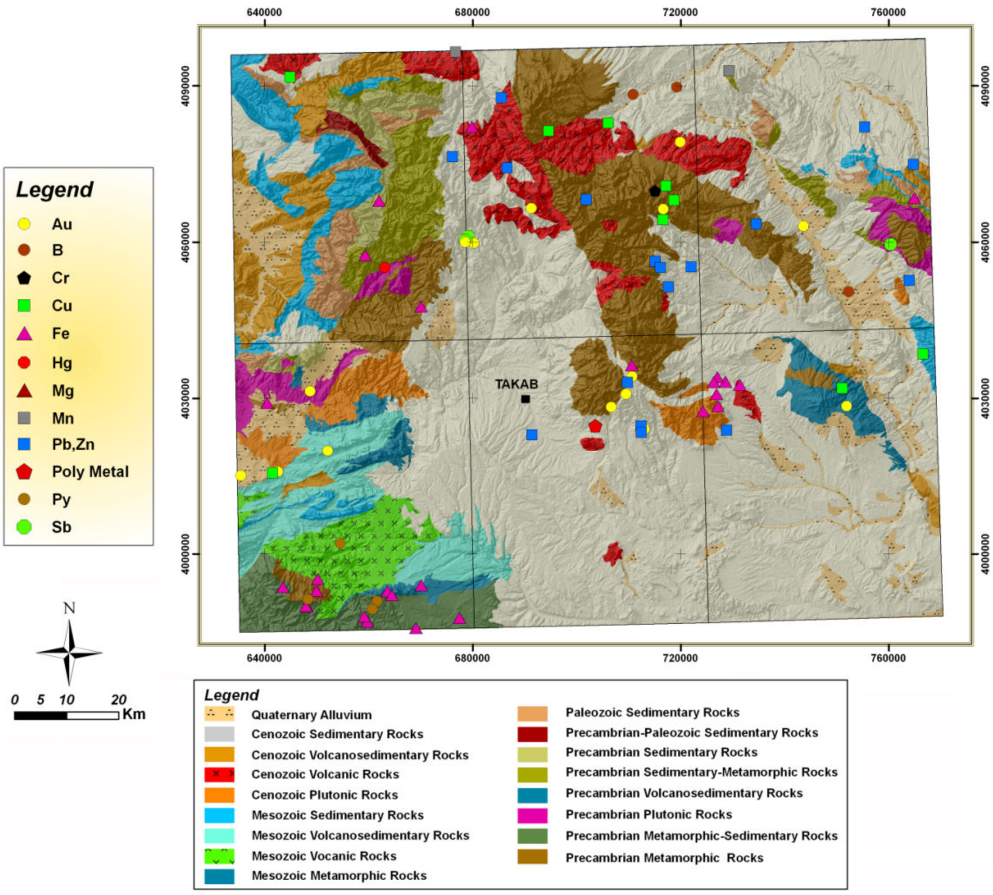

Fig. 3.11 Distribution map of mineral occurrences on the simplified geological map (extracted and GIS-ready from 1:250.000 geological map of Takab, Geological Survey of Iran).

Chapter 4 Remote Sensing of Mineralization Indications

4.1 Introduction

The presence of mineral deposits may be indicated by a lithological, geochemical, or geophysical anomaly (Carranza, 2002). Hydrothermally altered rocks are lithologic anomalies, which result from the chemical attack of pre-existing rocks by hydrothermal fluids (Pirajno, 1992). One of the important factors to locating the main outflow zones of hydrothermal systems is the spatial distribution of hydrothermally altered rocks, which may lead to the recognition of mineral deposits (Lowell, 1991).

Geological, geophysical and remote sensing structures are one of the most important control factors on the spatial location of ore deposits. Structural features are inestimable information for predictive mineral potential mapping. The spatial relationship between structural features (lineament and circular structure) and mineralization is very important in exploration of ore deposits. “Lineament analysis are undertaken to ascertain the regional structural elements at which emplacement of shallow level intrusions may have occurred, in addition to local minor structures that may have been important in controlling ore deposition” (Miyatake, 2002).

Recently, remote sensing data plays an important role in the mineral exploration projects. One of the common applications is extraction of alteration zones and structural features related to mineralization. Remote sensing data were processed for extraction of hydrothermally altered rocks and structural features in the study area. In this study we used two types of remote sensing data, one is Aster data for extraction of alteration zones and local features and the other is Landsat 7 ETM^+ for analysis of regional structural features.

4.2 Aster Data

ASTER (Advanced Spaceborne Thermal Emission and Reflection Radiometer) is an advanced multispectral sensor that is a facility instrument selected by NASA to fly on the Terra polar orbiting spacecraft in December 1999, and by 14 spectral bands with medium spatial, spectral and radiometric resolution covers a wide spectral region from visible to thermal infrared. The characteristics of spectral Aster bands are shown in figure 4.1. Three telescopes cover the wide spectral region, three VNIR (Visible and Near Infrared Radiometer) bands with a spatial resolution of 15 m, six SWIR (Short Wave Infrared Radiometer) bands with a spatial resolution of 30 m and five TIR (Thermal Infrared Radiometer) bands with a spatial resolution of 90 m. In addition one more telescope is used to see backward in the near infrared spectral band (band 3B) for stereoscopic capability (ASTER User’s Guide, 2007).

Two types of Level-1 data are produced by the Aster instrument, Level-1A and Level-1B data. Level-1A data are formally defined as reconstructed, unprocessed instrument data at full resolution. According to this definition the Aster Level-1A data consist of the image data, the radiometric and geometric coefficients without applying the coefficients to the image data to hold the original data values. The Level-1B data are generated by applying these coefficients for radiometric and geometric correction (Arenallo, 2003).

Sub-system	Band No.	Spectral Range (μm)
VNIR	1 2 3N 3B	0.52 – 0.60 0.63 – 0.69 0.78 – 0.86 0.78 – 0.86
SWIR	4 5 6 7 8 9	1.600 – 1.700 2.145 – 2.185 2.185 – 2.225 2.235 – 2.285 2.295 – 2.365 2.360 – 2.430
TIR	10 11 12 13 14	8.125 – 8.475 8.475 – 8.825 8.925 – 9.275 10.25 – 10.95 10.95 – 11.65

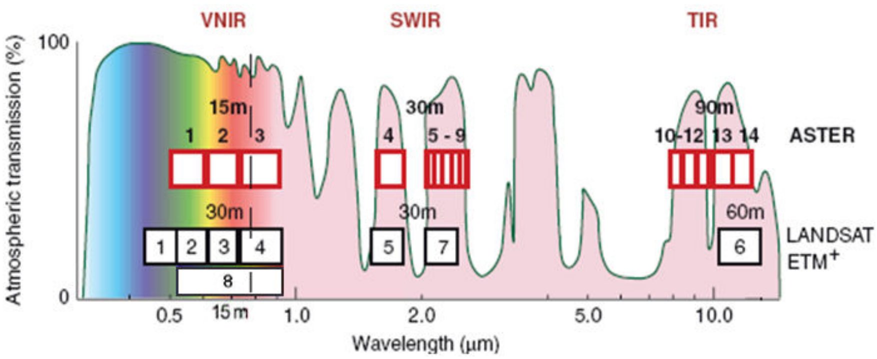

Fig. 4.1 Characteristics of spectral Aster bands (table) (ASTER User's Guide, 2007) and spectral bands of Aster and Landsat ETM^{+} satellite instruments (red and black boxes) (modified from Raupa, et al., 2007).

4.2.1 Pre-processing of Aster Data

Remote sensing data is represented digitally in the form of matrices of pixels or cells, where each cell corresponds to a number. These matrices of cells form raster images where the digital number is displayed by a brightness level in a grayscale image or a color if a color palette is used (Weese, 2002). Before these data can be used, they require a number of pre-processing operations. The two main types of pre-processing for data correction are radiometric and geometric correction.

The removal of distortions in the amount of electromagnetic energy received by the satellite is radiometric correction so that the reading reflects the true intensity reflected or emitted by the surface. It is necessary to do such correction due to atmospheric attenuation of energy before it reaches the sensor, and sensor irregularities such as striping, scans line dropping, and random noise. Before the data is released to the user, generally this kind of correction is done on the satellite or by the data warehouse (Weese, 2002). The process of geometric correction involves identifying the image coordinates (i.e. row, column) of several clearly discernible points, called ground control points (or GCPs) in the distorted image, and matching them to their true positions in ground coordinates (e.g. latitude, longitude). A map such as topography map usually is used for the true ground coordinates. This is image-to-map registration (Ouattara et al., 2004).

"The mosaic is an assemblage of overlapping aerial or space photographs or images whose edges have been matched to form a continuous pictorial representation of a portion of the earth surface" (Singhroy et al., 1996). Sometimes, this process is very important when one needs several image scenes to cover a study zone. The Orthorectification technique was used to convert Aster images into geographically-accurate forms, also the geometric correction was applied for the Aster data of the study area in the PC Geomatica software by using of topography maps (1:25.000 scales) before the main processing (about 80 points for every scene of Aster data by Root Mean Square (RMS) error method). Figure 4.2 shows the Aster false-color composite images (R: 3, G: 2, B: 1) (7 scenes) over the study area.

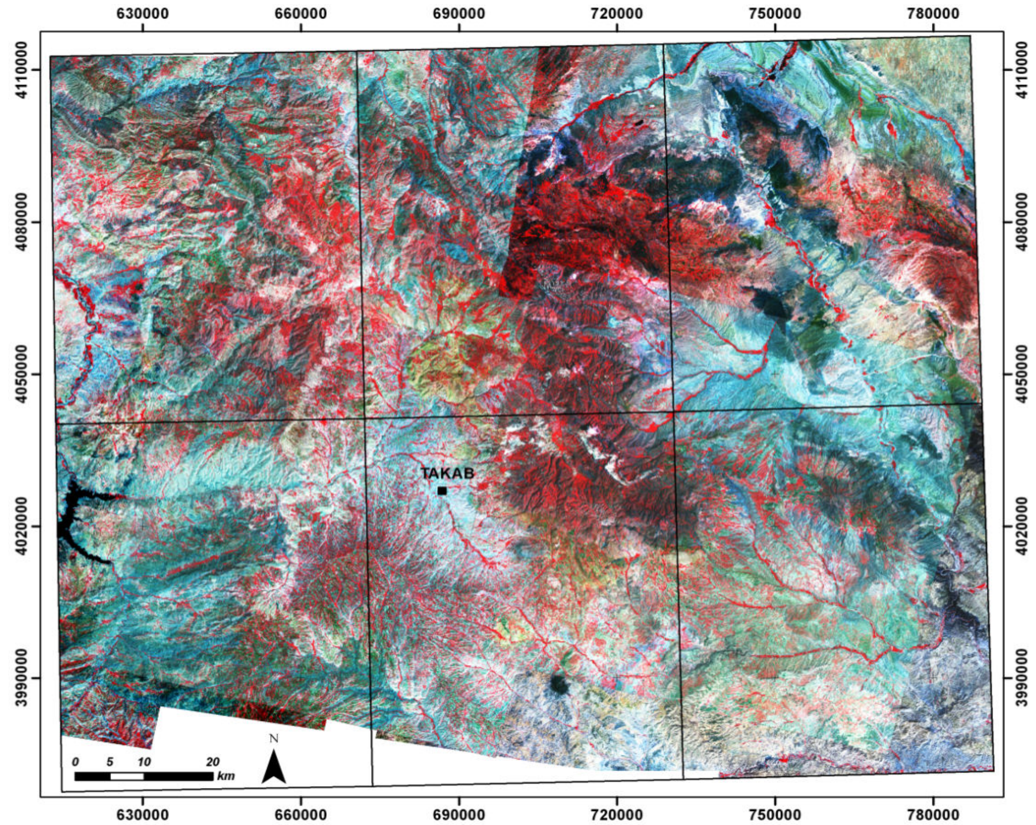

Fig. 4.2 Aster false-color composite image (R: 3, G: 2, B: 1) of the study area.

4.2.2 Remote Detection of Hydrothermally Altered Rocks

SWIR spectroscopy is applied for identification of hydrothermally alteration minerals. The spectral bands of the Aster SWIR subsystem were designed to distinguish Al-OH, Fe, Mg-OH, H-O-H, and CO_3 absorption features by measuring of reflected solar radiation in one band centered at 1.65 µm, and five bands in the 2.10–2.45 µm region (Mars and Rowan, 2006). Figure 4.3 shows the spectra of some hydrothermal alteration minerals and their characteristics.

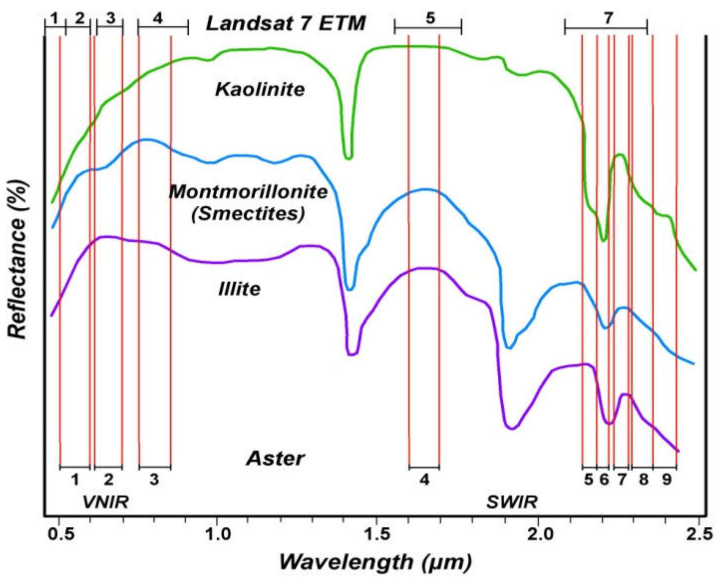

Fig. 4.3 Spectra of some alteration minerals showing their characteristic absorptions pikes, and wavelength intervals of Landsat ETM$^+$ and Aster bands (modified from Sabins, 1999).

Aster data were applied to identify and extract the argillic and sericitic alteration haloes in the study area using the Relative Band Depth (RBD) technique that Crowley et al., 1989 were used for mineral discrimination in the Ruby Mountains, Montana. For each absorption feature, the numerator is the sum of the bands representing the shoulders, and the denominator is the band located nearest the absorption feature minimum (Mars and Rowan, 2006) (Fig. 4.4). RBD5 [(ASTER band 4 + ASTER band 6)/ ASTER band 5] (Fig. 4.6c) and RBD6 [(ASTER band 4 + ASTER band 7)/ ASTER band 6] (Fig. 4.7b) images respectively were used to delineate argillic and sericitic mineral assemblages using Aster SWIR (1.6 to 2.43 μm) data (Rowan and Mars, 2003). Additionally Aster band-ratio (e.g. 5/6 & 7/5, Argillic alteration; 4/5 & 7/6, Sericitic alteration) and RGB color composition image (e.g. 4/5/6 (Fig. 4.6b; Argillic alteration) & 4/5/7 (Fig. 4.7a; Sericitic alteration)) also were applied for extraction of hydrothermally altered rocks. Argillic and phyllic alteration zones derived from the Aster data were converted to vector data. The presence of vegetation in Aster pixels isn't useful for mapping of argillic and phyllic rocks by RBD5 and RBD6 images, because some organic-compound (typically cellulose) absorption features centered near 2.10 and 2.30 μm are near the wavelength of some of the main Al-OH and Fe, Mg-OH absorption features (Mars and Rowan, 2006). The ration of band 3/ band 2 as a digital mask is used and applied to these RBD images to delete pixels containing green vegetation (Rowan et al., 2005). Figure 4.6a shows the argillic and sericitic alteration zones in the middle part of the study area (R: 4, G: 5, B: 6).

Additionally IDL logical operator algorithms (Mars and Rowan, 2007) were applied to map argillic and phyllic-altered rocks (ENVI software). Alunite and kaolinite are common minerals in argillic altered-rocks and muscovite is associated with phyllic-altered rocks (Fig. 4.5). Multiple band ratios are used in the logical operator algorithm to mask dark pixels, green vegetation, and alteration into a single algorithm which streamlines regional mapping and provides a consistent approach for mapping altered rocks in the study area (Mars and Rowan, 2006) (Fig. 4.8).

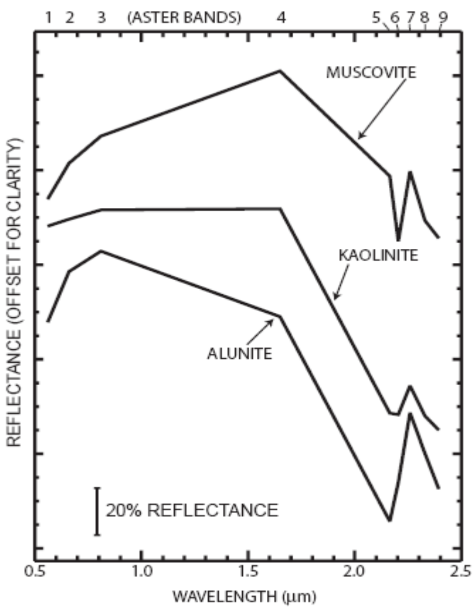

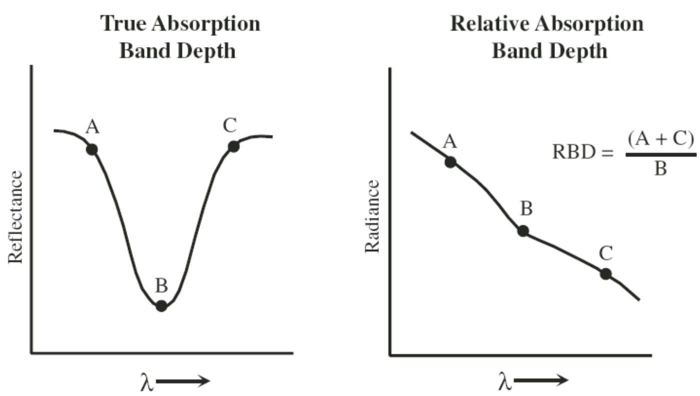

Fig. 4.4 Relative band depth (RBD) ratio schematic (Mars et al., 2006; modified from Crowley et al., 1989).

Fig. 4.5 Laboratory spectra of muscovite, kaolinite, and alunite resampled to Aster bandpasses. Alunite and kaolinite are typically associated with argillic-altered rocks and muscovite is typically associated with phyllic-altered rocks (Mars and Rowan, 2006).

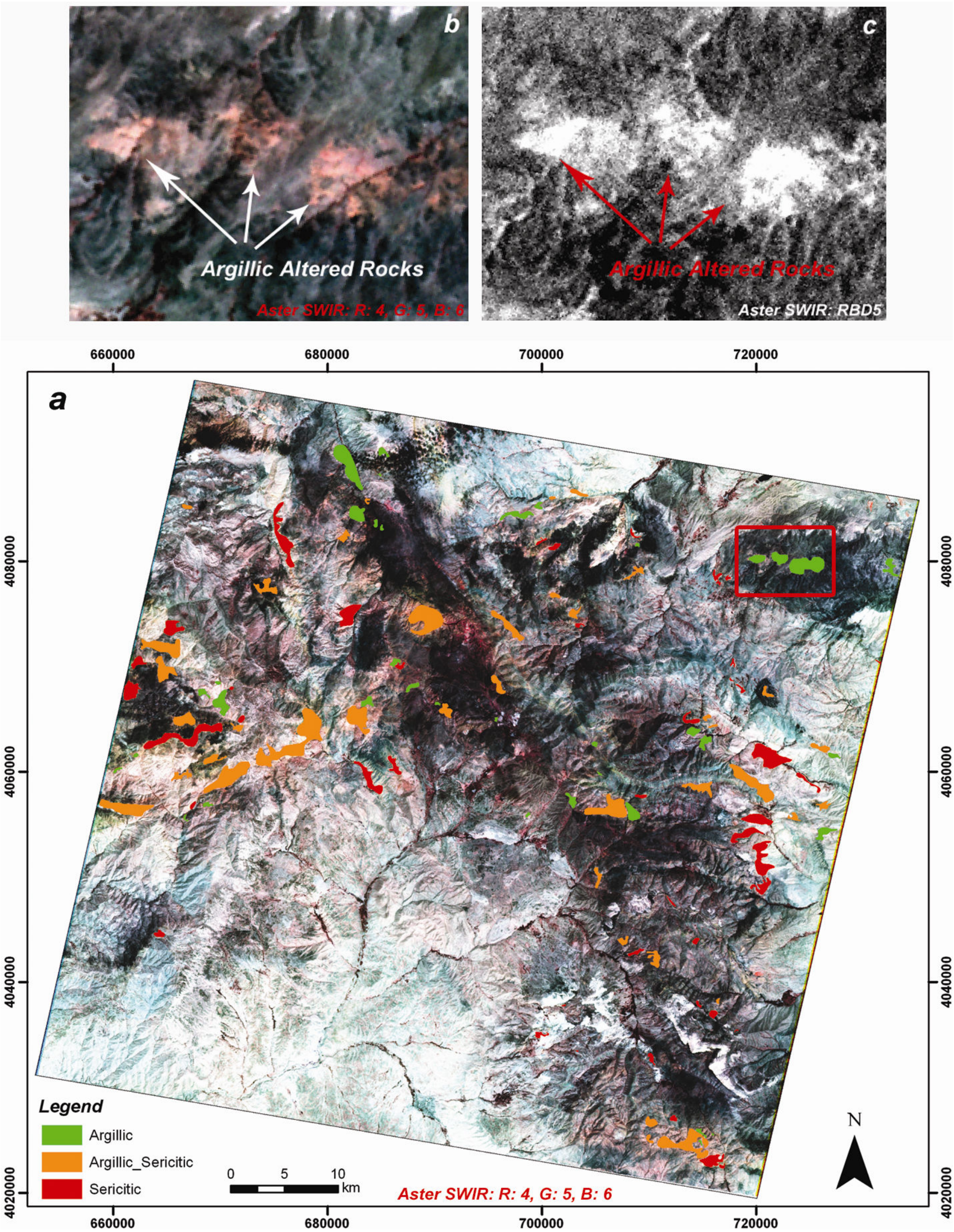

Fig. 4.6 **a** Argillic and sericitic alteration zones in the middle part of the study area (Aster SWIR; R: 4, G: 5, B: 6); **b** Argillic-altered rocks on the Aster SWIR (R: 4, G: 5, B: 6) and **c** Argillic-altered rocks on the Aster SWIR RBD5 [(ASTER band 4 + ASTER band 6)/ ASTER band 5].

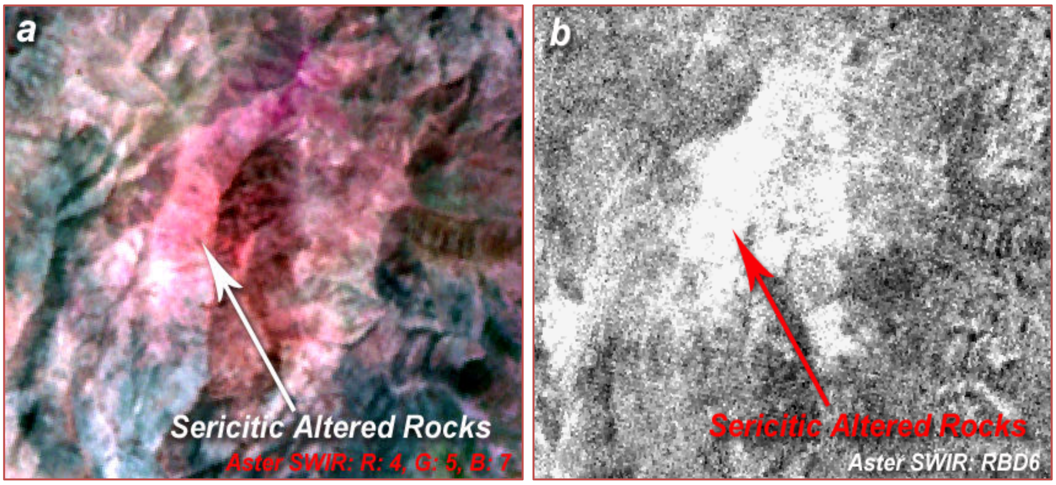

Fig. 4.7 **a** Sericitic-altered rocks on the Aster SWIR (R: 4, G: 5, B: 7) and **b** Sericitic-altered rocks on the Aster SWIR RBD6 [(ASTER band 4 + ASTER band 7)/ ASTER band 6] in the middle part of the study area.

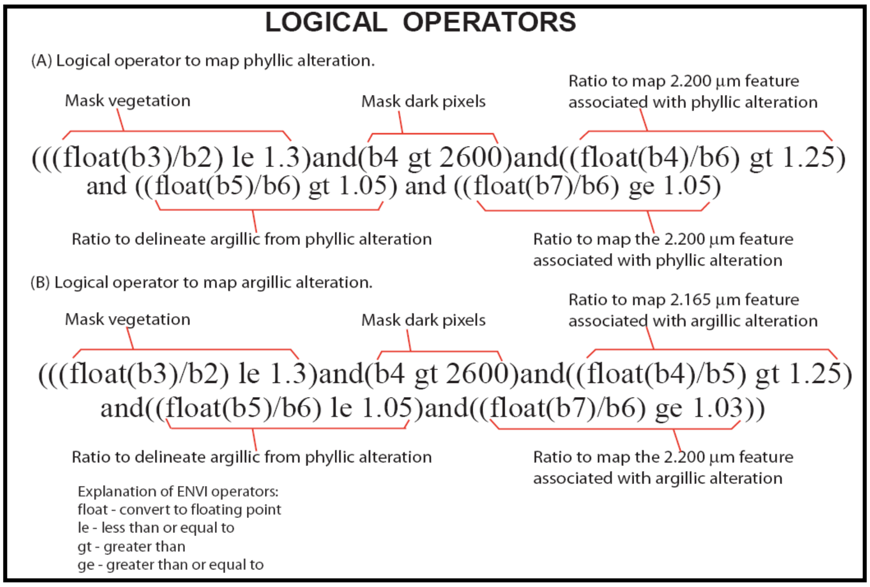

Fig. 4.8 Logical operator algorithms used to map phyllic and argillic-altered rocks (ENVI; after Mars and Rowan, 2006).

Comparison of the resampled library reflectance spectra of selected alteration minerals and the corresponding Aster image spectra in matched-filter processing was applied as other method for extraction of argillic and sericitic alteration zones.

One of the ENVI software techniques to perform partial unmixing–finding the abundances of user defined end-members is matched filtering. All of the end-members in an image don't need to be known. This technique neutralizes the response of the composite unknown background and enhances the response of the known end-member, thus "matching" the known signature. It provides a rapid means detecting specific materials based on matches to library or image end-member spectra and doesn't require knowledge of all end-members within an image scene (Junek, 2004; after ENVI User's Guide, 1999).

Argillic-altered rocks (kaolinite) on the Aster SWIR (R: 4, G: 5, B: 6) and the spectra of the Aster image with a view of this place (north of Aqdarreh gold deposit) are shown in the figure 4.9.

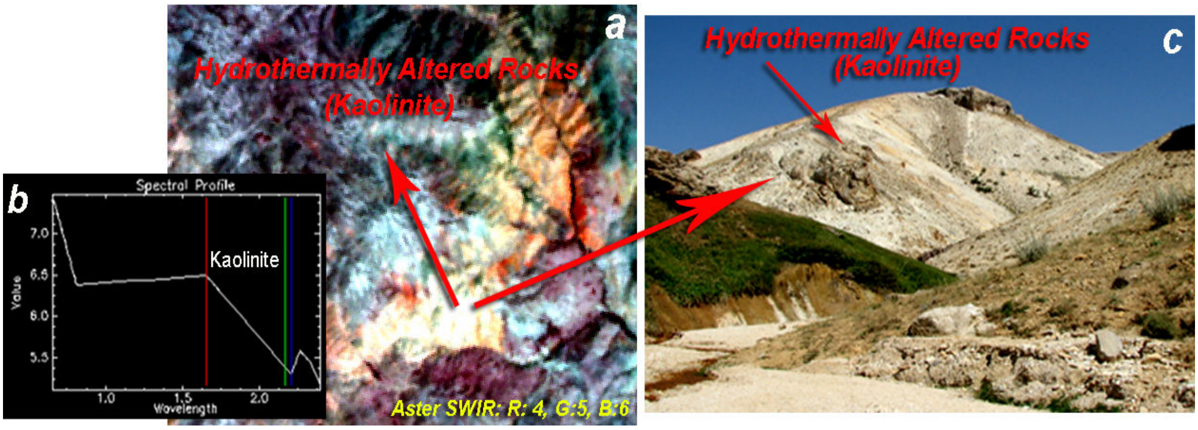

Fig. 4.9 **a** Argillic-altered rocks (kaolinite) on the Aster SWIR (R: 4, G: 5, B: 6); **b** The spectra of the hydrothermally altered rocks (kaolinite) from the Aster image SWIR (R: 4, G: 5, B: 6) and **c** A view of hydrothermally altered rocks in the north of Aqdqrreh gold deposit (argillic-altered rocks; Kaolinite).

The band ratios and common ratios with band combinations can be summarized in the tables 4.1 and 4.2 with the RGB color display correspondents.

Feature	Band or Ratio	Comments	Reference
Iron			
Ferric iron, Fe^{3+}	2/1		Rowan; CSIRO
Ferrous iron, Fe^{2+}	5/3 + 1/2		Rowan
Laterite	4/5		Bierwith
Gossan	4/2		Volesky
Ferrous silicates (biot, chl, amph)	5/4	Fe oxide Cu-Au alteration	CSIRO
Ferric oxides	4/3	Can be ambiguous*	CSIRO
Carbonates / Mafic Minerals			
Carbonate / chlorite / epidote	(7+9)/8		Rowan
Epidote / chlorite / amphibole	(6+9)/(7+8)	Endoskarn	CSIRO
Amphibole / MgOH	(6+9)/8	Can be either MgOH or carbonate*	Hewson
Amphibole	6/8		Bierwith
Dolomite	(6+8)/7		Rowan, USGS
Carbonate	13/14	Exoskarn (cal/dolom)	Bierwith, Nimoyima, CSIRO
Silicates			
Sericite / muscovite / illite / smectite	(5+7)/6	Phyllic alteration	Rowan (USGS); Hewson (CSIRO)
Alunite / kaolinite / pyrophyllite	(4+6)/5		Rowan (USGS)
Phengitic	5/6		Hewson
Muscovite	7/6		Hewson
Kaolinite	7/5	Approximate only*	Hewson
Clay	$(5\times7)/6^2$		Bierwith
Alteration	4/5		Volesky
Host rock	5/6		Volesky
Silica			
Quartz rich rocks	14/12		Rowan
Silica	(11x11)/10/12		Bierwith
Basic degree index (gnt, cpx, epi, chl)	12/13	Exoskarn (gnt, px)	Bierwith, CSIRO
SiO2	13/12	Same as 14/12	Palomera
SiO_2	12/13		Nimoyima
Siliceous rocks	(11x11)/(10x12)		Nimoyima
Silica	11/10		CSIRO
Silica	11/12		CSIRO
Silica	13/10		CSIRO
Other			
Vegetation	3/2		

Tab. 4.1 Summary of the known band ratios of Aster with the RGB color display correspondents (after Kalinowski and Oliver, 2004). CSIRO: Australian Commonwealth Scientific & Research Organization

Features	Red	Green	Blue	Reference
Vegetation and visible bands**	3, 3/2, or NDVI	2	1	
AlOH minerals/advanced argillic alteration***	5/6 (phen)	7/6 (musc)	7/5 (kaol)	Hewson (CSIRO)
Clay, amphibole, laterite	$(5x7)/6^2$ (clay)	6/8 (amph)	4/5 (lat)	Bierwith
Gossan, alteration, host rock	4/2 (goss)	4/5 (alt)	5/6 (host)	Volesky
Gossan, alteration, host rock	6 (goss)	2 (alt)	1 (host)	
Decorellation (envi)	13	12	10	Bierwith
Silica, carbonate, basic degree index	(11x11)/10/12 (silica)	13/14 (carb)	12/13 (basic)	Bierwith
Silica, carbonate	(11x11)/(10x12)	13/14	12/13	Nimoyima
Silica	11/10	11/12	13/10	CSIRO
Discrimination for mapping	4/1	3/1	12/14	Abdelsalam
Discrimination in sulphide rich areas	12	5	3	
Discrimination	4/7	4/1	(2/3) x (4/3)	Sultan
Discrimination	4/7	4/3	2/1	Abrams (USGS)
Silica, Fe^{2+}	14/12	(1/2) + (5/3)	MNF Band 1	Rowan (USGS)
Enhanced structural features	7	4	2	Rowan (USGS)

*Comments by Hewson
**Equivalent to Landsat RGB 432
***Alunite/pyrophyllite, mica, kaolinite/dickite

Tab. 4.2 Summary of the known common band ratios with band combinations of Aster with the RGB color display correspondents (after Kalinowski and Oliver, 2004). CSIRO: Australian Commonwealth Scientific & Research Organization

4.3 Hyperspectral Data

ASD's (Analytical Spectral Devices) field portable spectrometers are widely used for geology and exploration remote sensing applications. Some methods of reflectance spectroscopy have comprehensive applications beyond remote sensing for geologists, especially in mineral exploration, core logging, hydrothermally altered rocks delineation, and lithology mapping (Website of ASD inc.; www.asdi.com). The ASD's TerraSpec© Pro portable spectrometer is optimized for these applications.

A directional light source and fiber optic cable has applied in the TerraSpec© Pro to collect reflected light and transmit the signal to three inbuilt SWIR detectors in the devise case. The TerraSpec© Pro portable spectrometer measures spectra with a range from 350 to 2500 nm and an spectral resolution of 3 nm in the VIR region and 6 nm in the SWIR region at sampling intervals of 1.4 nm for the region 350 – 1000 nm and 2 nm for the region 1000 to 2500 nm. TerraSpec© is the ideal tool for mapping of alteration mineralogy and a wide variety of deposit types from epithermal to porphyries, kimberlites, IOCG (Iron Oxide Copper Gold), carbonate hosted base metals, green schist belts, shear veins, skarns, and disseminated gold systems. Generally, alteration minerals related to an ore deposit have unique and distinct spectral signatures.

The spectral signature of an alteration mineral is determined by the minerals present, their relative abundances, their crystallinity and their compositional variation. Often, the spectra measured identify the mineral phases present and the thermal environment of its formation (Website of ASD inc.; www.asdi.com).

SWIR-spectra of some field samples were measured in the laboratory by using the TerraSpec© Pro portable spectrometer of Analytical Spectral Devices, Inc (ASD) (Fig. 4.10). Spectra of rock samples were taken on different surfaces for three times.

Fig. 4.10 Measuring of the field samples by ASD's TerraSpec© Pro portable spectrometer in the laboratory.

The raw data were statistically averaged for feature determination by the utilization of inbuilt spectral libraries (ASD, JPL, and USGS). Figure 4.11 shows the spectra processing of a field sample.

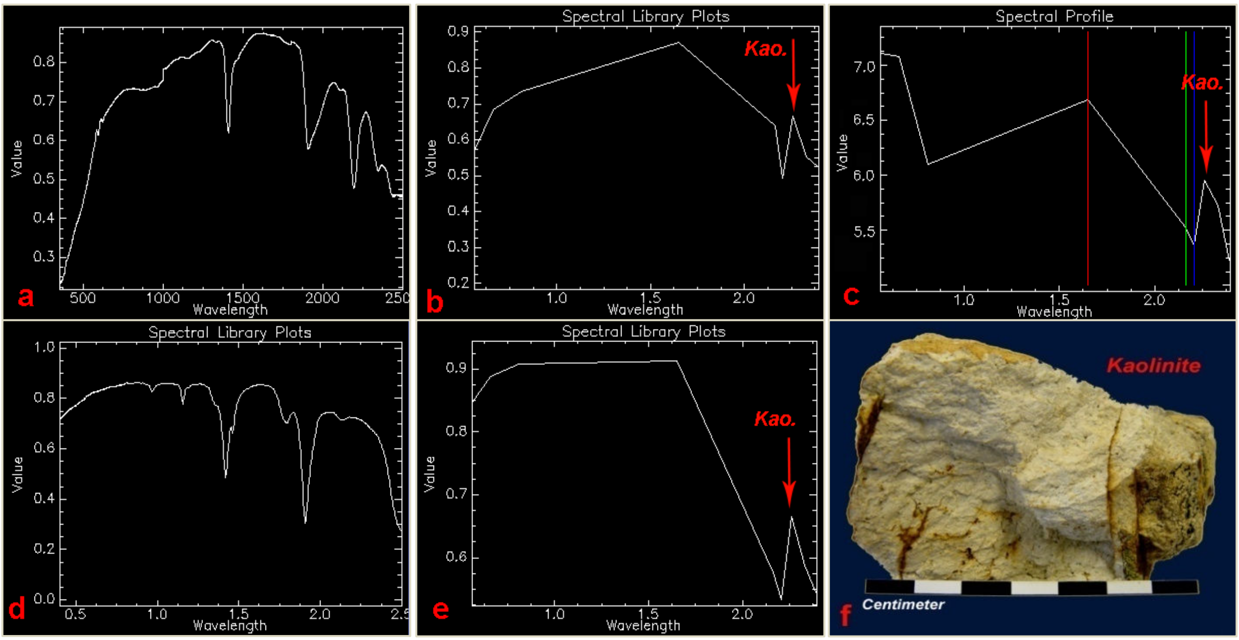

Fig. 4.11 **a** The spectra of a field sample (kaolinite) with TerraSpec© Pro portable spectrometer; **b** Resampled to Aster VNIR and SWIR bandpasses; **c** The spectra of this rock from the Aster image SWIR (R: 4, G: 5, B: 6); **d** The spectra of kaolinite from JPL library; **e** Resampled to Aster VNIR and SWIR bandpasses and **f** The measured field sample (kaolinite).

4.4 Landsat 7 ETM$^+$ Data

The Landsat ETM$^+$ (Enhanced Thematic Mapper Plus) is a sensor carried onboard the Landsat 7 satellite and almost continuously since July 1999 has acquired images of the earth's surface, with a 16-day repeat cycle. It has eight spectral bands (Tab. 4.3). Spatial resolution of bands 1 to 5 and band 7 is 30 meters, resolution for band 6 (thermal infrared) is 60 meters and resolution for band 8 (panchromatic) is 15 meters. The scene size of Landsat 7 ETM$^+$ image is 170 km north-south by 183 km east-west (U.S. Geological Survey; http://edc.usgs.gov).

Landsat 7 ETM$^+$ data was processed for extraction of regional structural features (fault, lineament and circular structure) and alteration zones (clay minerals) by different approaches.

Landsat 7 ETM$^+$	Wavelength (micrometers)	Resolution (meters)
Band 1	0.45-0.52	30
Band 2	0.52-0.60	30
Band 3	0.63-0.69	30
Band 4	0.77-0.90	30
Band 5	1.55-1.75	30
Band 6	10.40-12.50	60
Band 7	2.09-2.35	30
Band 8	0.52-0.90	15

Tab. 4.3 Spectral bands characteristics of Landsat 7 ETM$^+$ data (after U.S. Geological Survey).

4.4.1 Determination of Alteration Zones

Band rationing and RGB color composition were applied for extraction of hydrothermally altered rocks in the study area. For determination of alteration zones, we used the classic 5/7 band ratio (Fig. 4.13a) to identify clay mineral zones. Figure 4.12 shows the 3D Landsat 7 ETM$^+$ image (R: 7, G: 4, B: 2) over the study area based of digital elevation model (DEM).

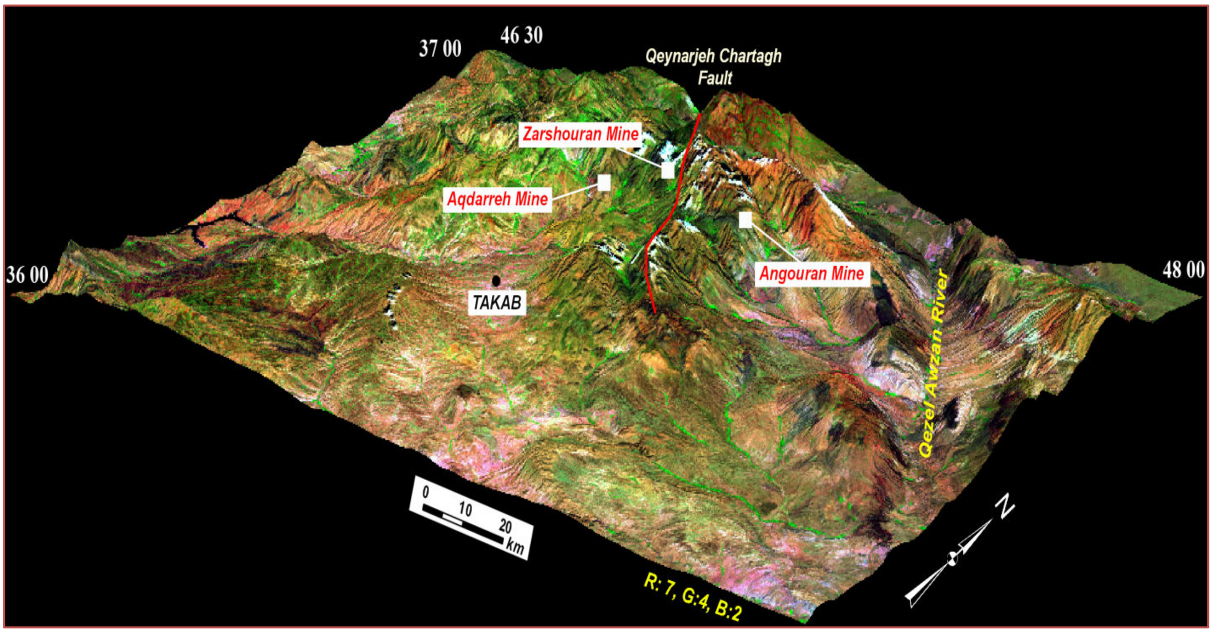

Fig. 4.12 3D Landsat 7 ETM$^+$ image (R: 7, G: 4, B: 2) of the area and the places of main deposits based on DEM.

Figure 4.13b shows the altered rocks (clay minerals) on the false color composite image (R: 5, G: 3, B: 1) of Landsat 7 ETM+ data.

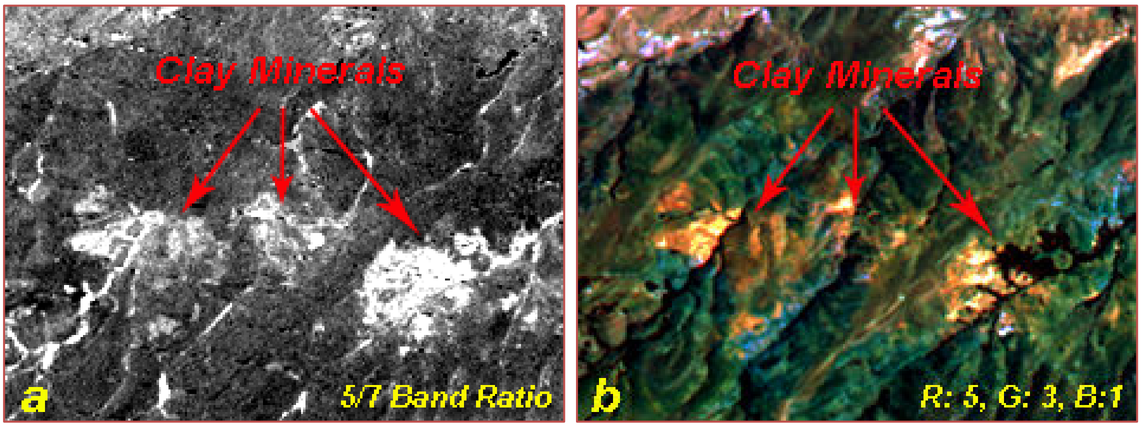

Fig. 4.13 **a** Hydrothermally altered rocks (clay minerals) on the Landsat 7 ETM+ band ratio (5/7) and **b** Hydrothermally altered rocks (clay minerals) on the false color composite image (R: 5, G: 3, B: 1) of Landsat 7 ETM+ in the north part of the study area.

The color composites and color composites with band ratios are summarized in the tables 4.4 and 4.5 with the RGB color display correspondents.

Tab. 4.4 Summary of the known color composites of Landsat 7 ETM+ with the RGB color display correspondents (after Yetkin, 2003).

RGB display of respective ETM bands	***Red correspondent***	***Green correspondent***	***Blue correspondent***	***Reference***
R: 4, G: 7, B: 6	Structural lineament differentiation	Hydrothermal alteration		Rothery, 1987
R: 7, G: 5, B: 4	Hydrothermal alteration and intrusives	Gabbro	Vegetation	Rothery, 1987
R: 7, G: 4, B: 2	Clay minerals are brighter than the others	Vegetation		Chica-Olmo et al., 2002
R: 4, G: 7, B: 5	Vegetation	Clay minerals are brighter	Clay minerals are brighter	Chica-Olmo et al., 2002
R: 7, G: 4, B: 2	Granites, FeO, MnO, displaed as reddish brown areas	Monzogranite is greyish-green	Sedimentary units in bluish-grey	Abdelhamid et al., 1994
R: 4, G: 7, B: 2	Background is pink	FeO is yellow-green		Jingyuan et al., 1991
R: 4, G: 7, B: 3	Background is orange-red	FeO is yellow-green		Jingyuan et al., 1991

Tab. 4.5 Summary of the known band ratio composites of Landsat 7 ETM$^+$ with the RGB color display correspondents (after Yetkin, 2003).

RGB display of respective ETM band ratios	Red correspondent	Green correspondent	Blue correspondent	Extra	Reference
R: 5/7, G: 3/2, B: 4/5	Clay-rich areas	FeO rich areas		Yellow, orange areas both clay and FeO rich	Abrams et al., 1983
R: 7/4, G: 4/3, B: 5/7	Minerals containing iron ions	Vegetated zones	OH/H2O-, SO4- or CO bearing minerals		Kaufmann, 1988
R: 3/4, G: 5, B: 5/7				FeO as apricot yellow and the background as sky-blue	Jingyuan et al., 1991
R: 5/7, G: 5/4, B: 3/1	Clay minerals	Iron minerals	Ferric oxides		Chica-Olmo et al., 2002
R: 3/1, G: 5/7, B: 4/5				Highly altered zones dark-blue to violet-blue	Abdelhamid et al., 1994

4.4.2 Interpretation of Structural Features

The tectonic setting of an area can be an important factor for any type of mineralization and (or) can control the pattern of drainage and rivers of that area. Faults are tectonic structures that can, by forming linear zones of lithological weakness or offsetting some structures or rock units, can control the migration of (metalliferous) hydrothermal solutions related to intrusive bodies and can thus control the precipitation of ore minerals.

Geological structures may be any linear or curve-linear features on satellite images. The association of lithological units and the expression of structural features on the landform are additional important considerations in this interpretation. Lineaments are highly related to lithological boundaries. In many places, lineaments trace fault structures and streams change direction to follow such lineaments (Sadeghi et al., 2008b).

Figure 4.14 shows some types of circular structures related to magmatic intrusions. Kouda and Koide, 1978 discussed ring structures, which occurred in the northern Akita, Japan, and which they extracted from Landsat data and their relationship with vein-type and epithermal ore deposits. Eggers (1979) describes circular features observed on Landsat data over New Zealand, and Saul (1978) has recognized such structures on topographic maps (3D) covering parts of Arizona. Some of these authors also describe the relationships between these features and ore deposits and mineralization (Witschard, 1984).

Some common methods exist for the extraction of structural features from remote sensing data. Structural maps can be produced from remote sensing data by visual interpretation and manual digitizing or by automatic extraction (Palomera, 2004). Many authors (Budkewitsch et al., 1994; Karnieli et al., 1996; Lepage et al., 2000 and Madani, 2001) have automatically extracted lineaments using various methodologies, most of which include edge detection, thresholding, and image classification. Different techniques of image enhancement before visual interpretation of structural features have been widely used by other authors. Some of these authors applied spatial domain filters for linear edge enhancement, such as the Laplacian high frequency spatial filters or, directional filters (e.g., Rokos et al., 2000). Several Landsat 7 ETM$^+$ RGB color composites such as 7/2/1, 7/4/1 and 7/4/2 were also used (e.g. Asadi, 2000 and Rein et al., 2003); others used PC1 from a principal components analysis (e.g., Asadi, 2000).

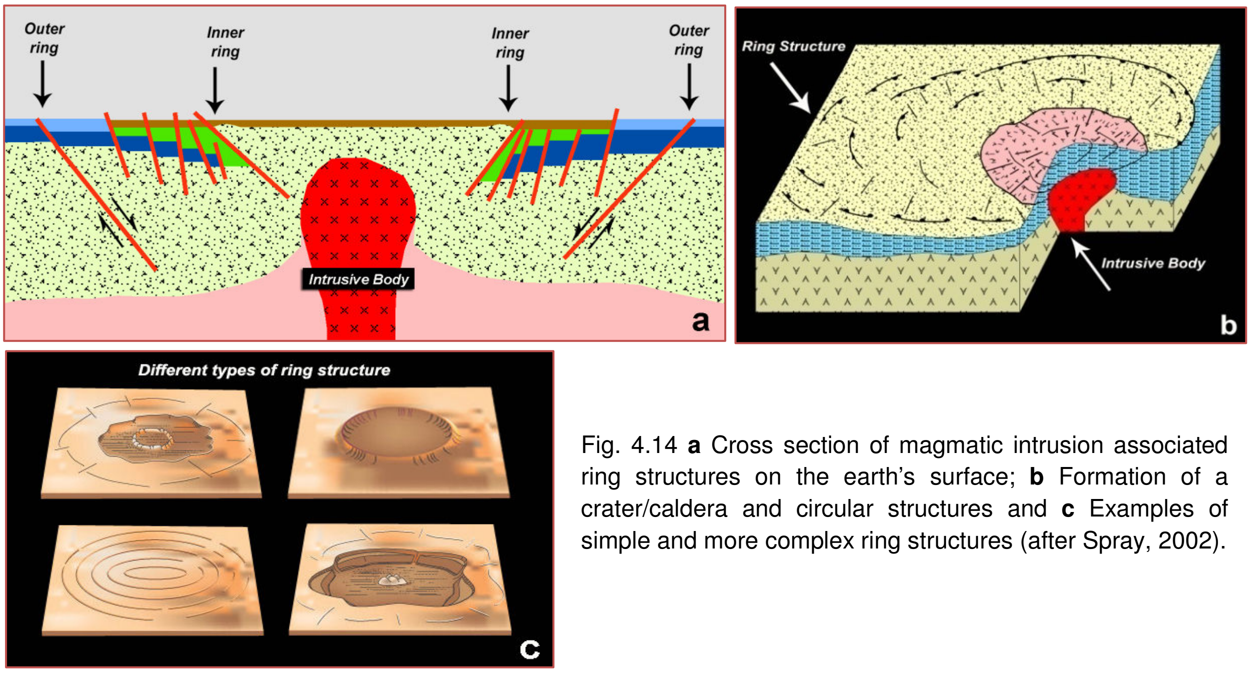

Fig. 4.14 **a** Cross section of magmatic intrusion associated ring structures on the earth's surface; **b** Formation of a crater/caldera and circular structures and **c** Examples of simple and more complex ring structures (after Spray, 2002).

In this study, we used processing techniques to make edge enhancements, using RGB color composite, band-ratio and digital filtering. The structural features were identified using RGB color composition, low pass-filter and edge sharpening detector filter. Landsat 7 ETM⁺ RGB color composites such as 7/4/1, 7/4/2 and 5/3/1 and band-ratio (e.g. 3/1 & 5/7) were useful for enhancement of structural features. Figure 4.15 shows a big circular structure in the study area.

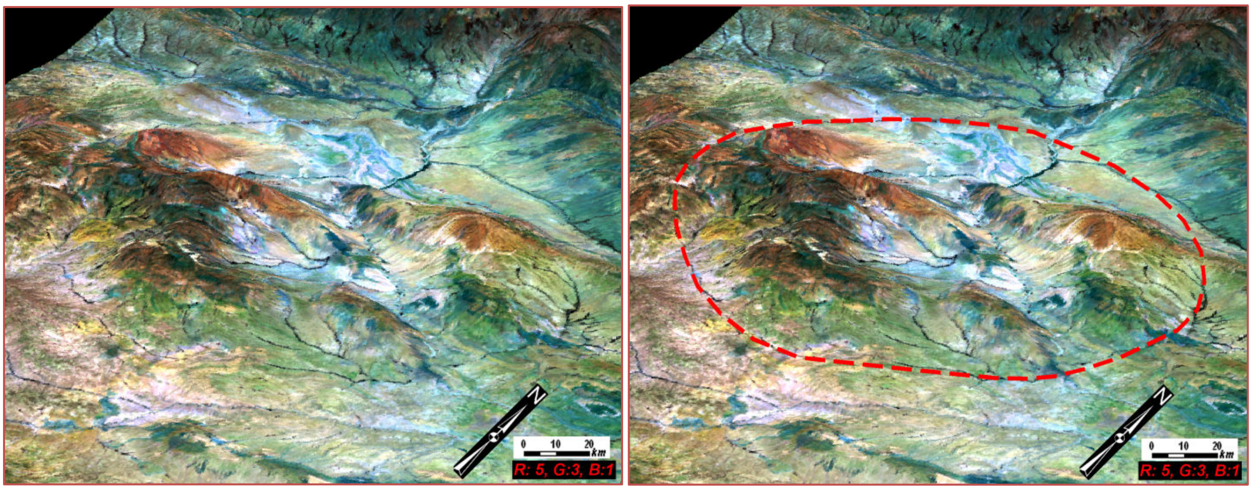

Fig. 4.15 A big circular structure on the false-color composite image (R: 5, G: 3, B: 1) of 3D Landsat 7 ETM$^+$ over the study area and the region N, NE and E of it.

Processing of Landsat 7 ETM$^+$ data and the digital elevation model (DEM) of the study area (Fig 4.16) has revealed the presence of some large-scale circular structures and lineaments (Fig. 4.17).

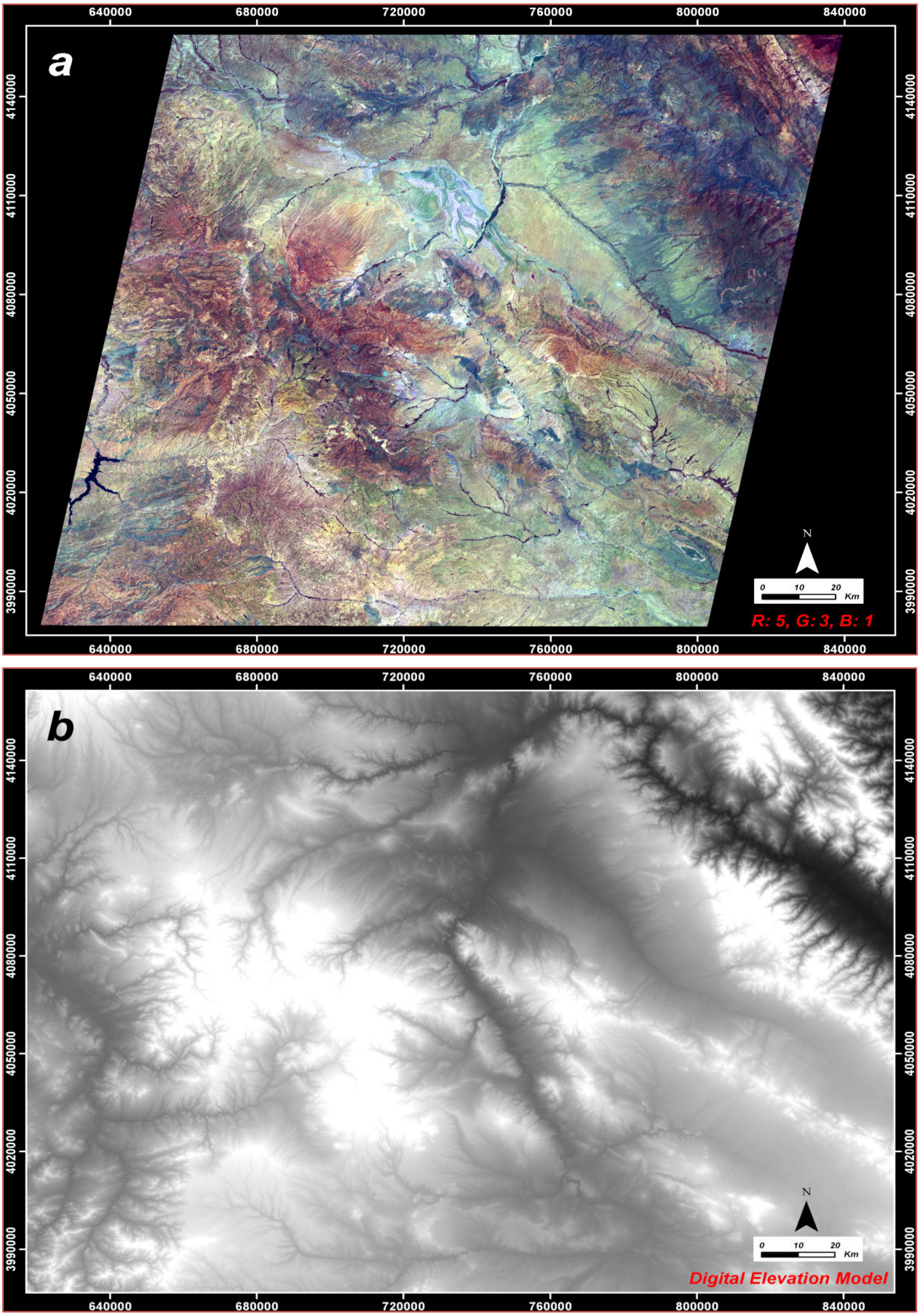

Fig. 4.16 **a** The false-color composite image (R: 5, G: 3, B: 1) of Landsat 7 ETM^{+} and **b** The digital elevation model (DEM) of the study area based on topography data (1:25.000 scale).

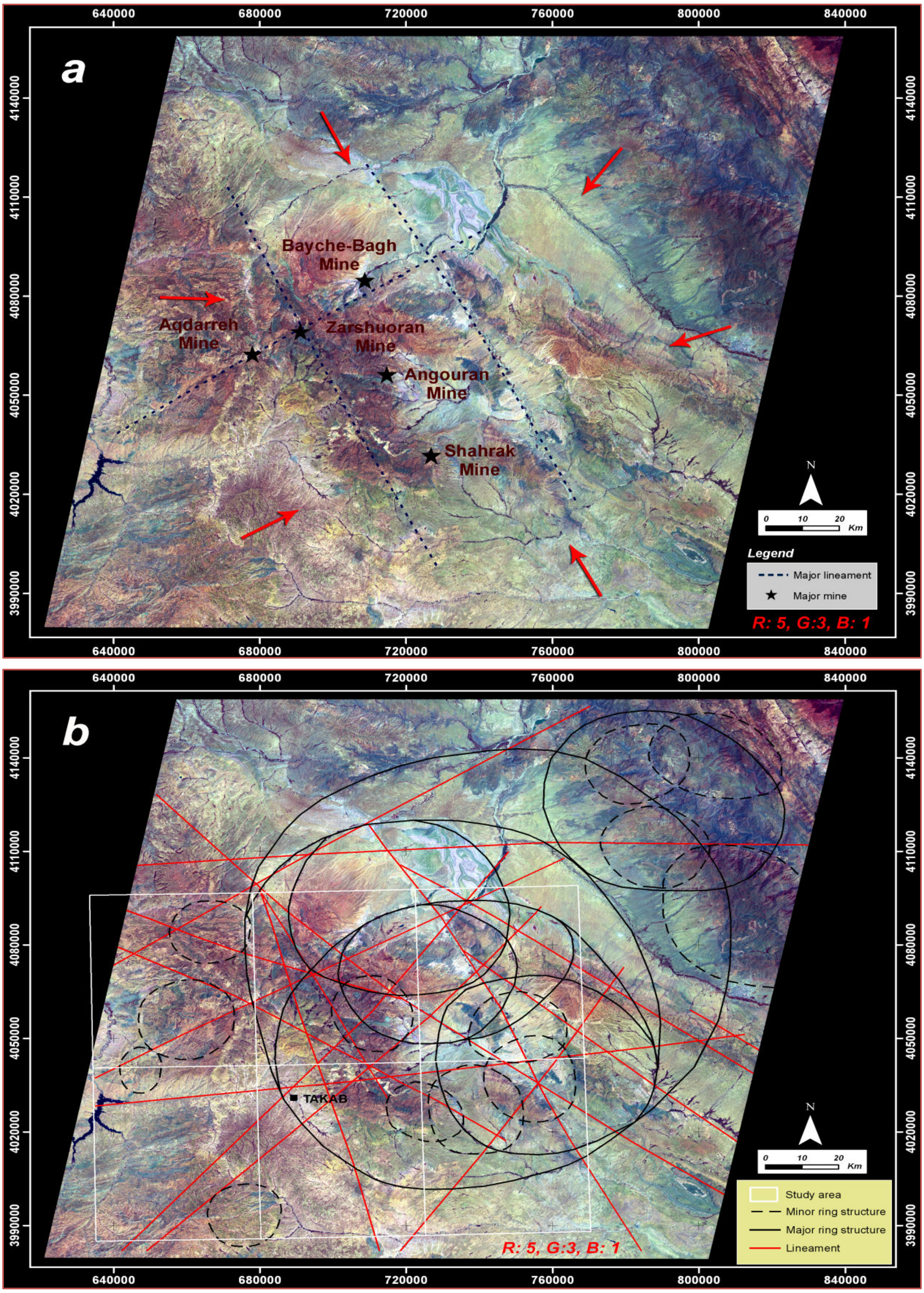

Fig. 4.17 **a** Some major lineaments and a large-scale circular structure on the false-color composite image (R: 5, G: 3, B: 1) of Landsat 7 ETM$^+$ with places of the major mines over the study area (Zarshouran & Aqdarreh gold deposits and Baycheh-Bagh (Cu, Ni, Co, As, Bi) deposit are located on/near one of the major lineaments with NE-SW direction) and **b** The circular structures and lineaments on the Landsat 7 ETM$^+$ image (R: 5, G: 3, B: 1).

These structural features appear to exert extraordinary control on alteration zones (Fig. 4.18), major mines and known ore indications, especially lead-zinc as well as gold, copper and iron occurrences (Fig. 4.19).

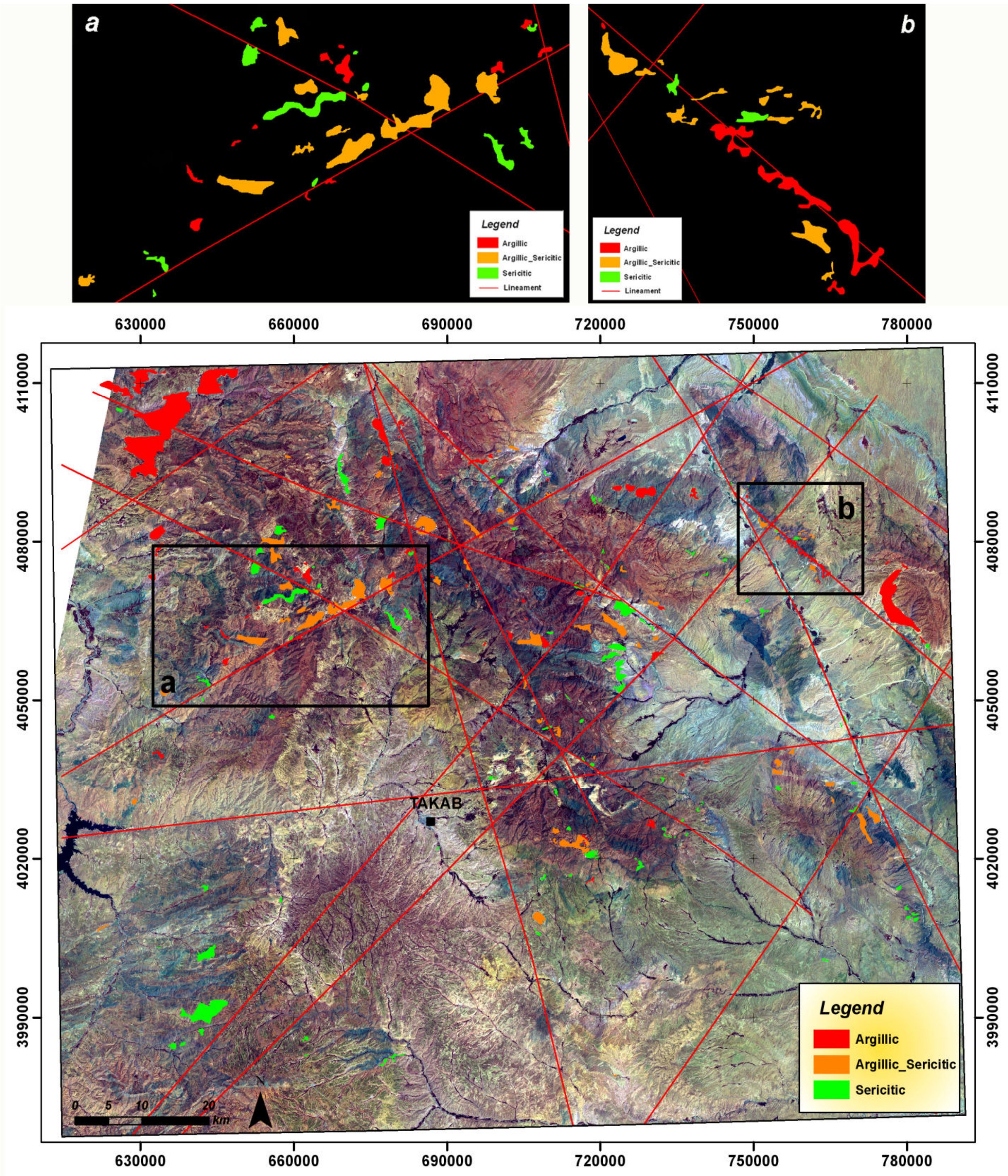

Fig. 4.18 Alteration map of the study area on the false-color composite image (R: 5, G: 3, B: 1) of Landsat 7 ETM$^+$; Areas a and b show an extraordinary coincidence between the hydrothermally altered rocks (argillic and sericitic) and big lineaments.

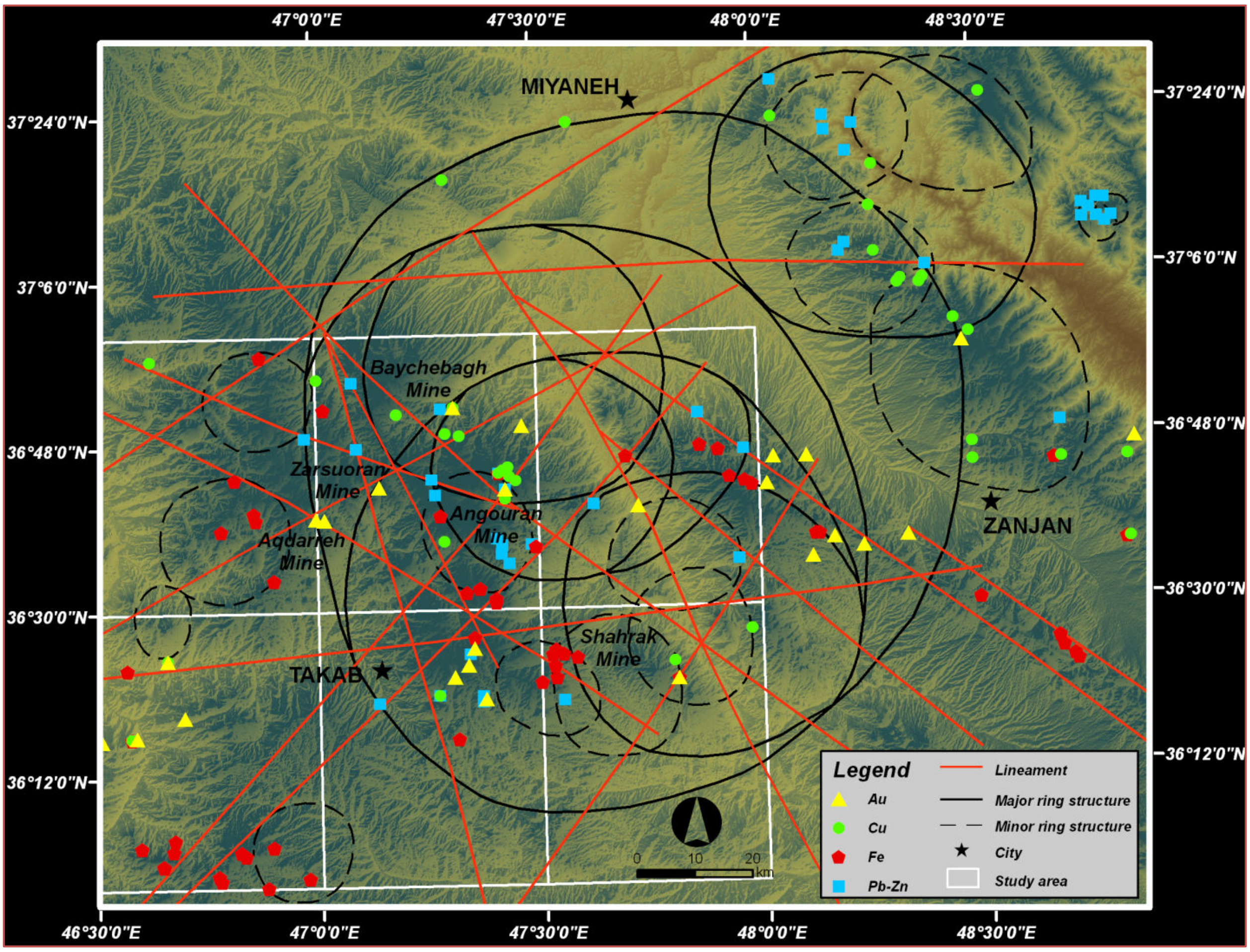

Fig. 4.19 Circular structures and lineaments from Landsat 7 ETM+ data on the DEM of the study area with the places of major mines and Au, Pb-Zn, Cu and Fe occurrences.

4.4.3 Structural Features and Mineralization

From a geological point of view the most favourable places for ore occurrences in the study area are related to tectonic-magmatic activities. Circular structures can be the indication of emplacement of shallow bodies near the earth surface. Some of the identified lineaments seem to be faults, or extension places of the crust. By comparison of geological structures with geophysical data or interpretation results forenamed, they can be identified from lineaments, especially in an area with thick sediment (Chen and Zhou, 2005). Any structures (fault or lineament) crossing the shallow bodies can be control mineralization.

Landsat 7 ETM+ data processed to investigate the spatial relationship between lineaments, structural intersections, circular structures, hydrothermally altered rocks and mineralization (Fig. 4.19). Correlation between, both regional and local-scale structural features is important for the recognition of significant controlling structures in magma emplacement and hydrothermal activity. Lineament trends in the local scale represent bedding or unit traces, fractures or faults. There is a set of strong NW-SE trending lineaments in the study area (Fig. 4.20). Several major lineaments cross some large-scale circular structures. Distribution of mines and ore occurrences has an extraordinary control on mineralization.

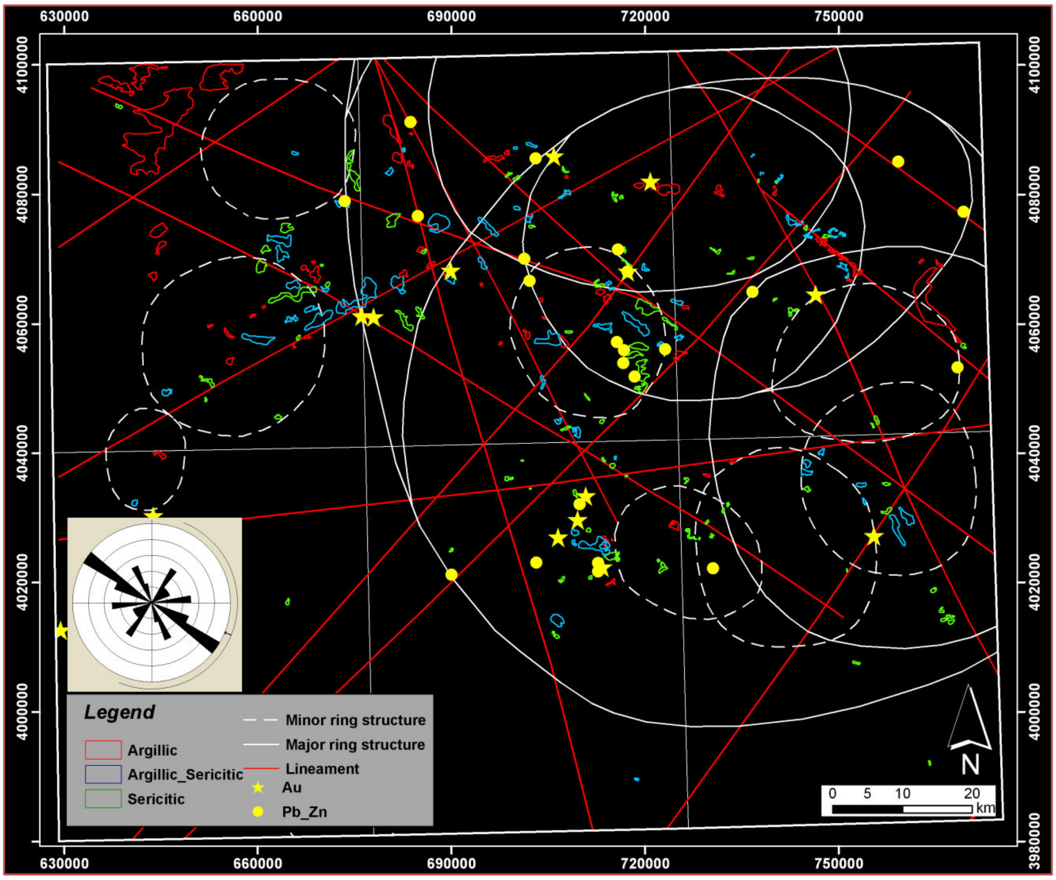

Fig. 4.20 Relationship between lineaments, circular structures, hydrothermally altered rocks and mineralization of Au and Pb-Zn. Rose diagram of the major lineaments from Landsat 7 ETM+ Data shows the main trend in the NW-SE direction.

4.4.4 Conclusions

The processing of remote sensing data can help to recognition of regional structural features and hydrothermally altered rocks and shows the spatial relationships between tectonic and ore deposits and can be defined simply. In the most of mineralization zones, the tectonic phenomena have an important role in the forming of ore deposits in and after mineralization.

The big circular and linear structures described in this study have been concealed through their large size during ground studies and therefore have not been recognized earlier. Only regional satellite data such as Landsat 7 ETM+ has provided an otherwise unobtainable view of large-magnitude structures on the earth's surface.

The integration of remote sensing results and field data and their interpretation in the GIS environment helps to distinguish of favourable structural zones for mineral exploration.

The large-scale circular structures and lineaments identified in the study area are most probably the result of magmatic intrusions. Such intrusive bodies create not only some type of ore deposits and alterations but commonly generate ring fractures and radiating faults and fracture systems. Subsequent hydrothermal stages of mineralization focus mineralizing fluid flow towards areas of optimal, i.e. increased permeability. Such permeable zones are typically provided by the intersection of ring and linear structures (Sadeghi et al., 2008a).

Chapter 5 Spatial Evidence of Mineralization

5.1 Introduction

"Mineral resources are materials that are in such form that economic extraction of a commodity is currently or potentially feasible" (Peters et al., 2007). Mineral potential maps estimate or forecast the presence of probable mineral resources in an exploration area. There is some spatial evidence for any types of ore deposit that can be obtained from spatial geo-exploration datasets in a study area that can be processed for use in GIS modeling.

The main objective of this research is to extract the possible targets of Carbonate Replacement Deposits of Pb-Zn and Au using the integration of geo-exploration datasets interpreted from geological, geochemical, Aster and Landsat 7 ETM^+ data, airborne magnetic and radiometric grid and ground-based data by GIS methods.

In this chapter, the deposits recognition criteria will be mapped as spatial evidential maps of Carbonate Replacement Deposits (CRD) (Mississippi Valley type Pb-Zn and Carlin-type gold deposits). These evidential maps are efficient in data selection and data modeling, in recognition which features to enhance and use as main spatial parameters, and for weighting of the spatial evidence in mineral potential mapping.

5.2 Lithological Evidence

Lithological evidence (host rock) for the Mississippi Valley type (MVT) Pb-Zn and Carlin-type gold occurrences in the study area were extracted, GIS-ready, and merged from the geological maps (six geological maps with 1:100.000 scales; Geological Survey of Iran).

The extensive presence of carbonate formations in the study area can be suitable as a probable host rock for MVT Pb-Zn and Carlin-type gold deposits.

5.2.1 Lithological Evidence for MVT Pb-Zn Occurrences

The main rock types as a probable host rock for MVT Pb-Zn occurrence in the study area include:

Dolomite, Dolomitic limestone, Limestone, Limestone & Marble, Marble & Schist, Shaly limestone, Recrystallized limestone and Sandy or Marly limestone (Fig. 5.1). These rock units were selected from the digital geological map to apply in the GIS modeling with different grades.

5.2.2 Lithological Evidence for Carlin-Type Gold Occurrences

The main rock types as a probable host rock for Carlin-type gold occurrence in the study area include:

Dolomitic, limestone, Dolomite & Shale, Limestone, Recrystallized limestone, Marly or Sandy limestone and Marble (Fig. 5.2).

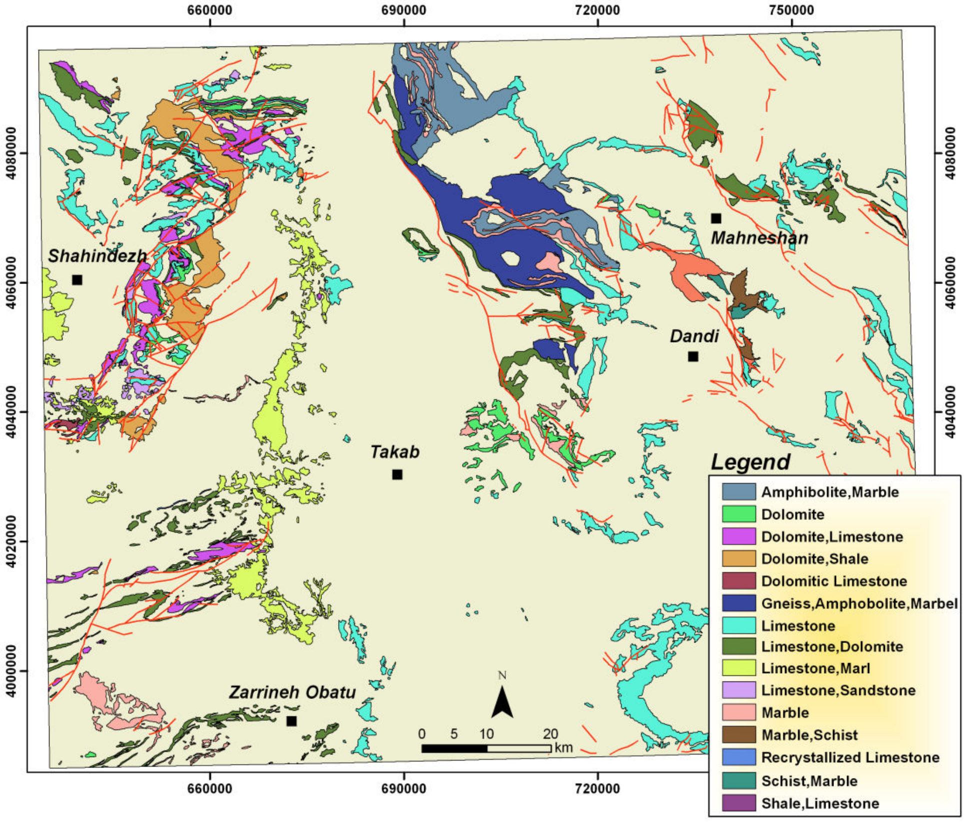

Fig. 5.1 Probable host rocks for MVT Pb-Zn occurrences in the study area (extracted, merged and GIS-ready from six 1:100.000 geological maps, Geological Survey of Iran).

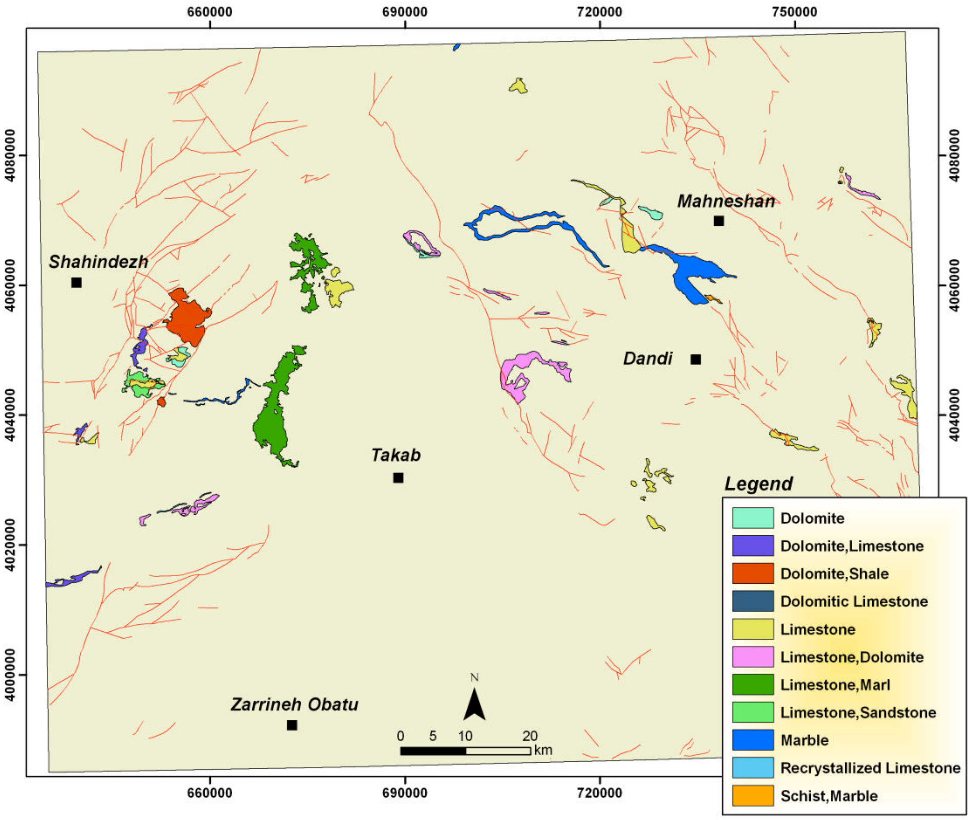

Fig. 5.2 Probable host rocks for Carlin-type gold occurrences in the study area (extracted, merged and GIS-ready from six 1:100.000 geological maps, Geological Survey of Iran).

5.3 Geochemical Evidence

An effective surface geochemical technique would be enhanced exploration of new mineral deposits in an area and allows detection of mineralization through the thick cover (Fabris et al., 2006) and identifies areas with a higher potential for different mineral deposit types.

“A geochemical anomaly is a departure from the geochemical patterns that are normal for a given geochemical environment” (Rose et al., 1979). Geochemical anomalies usually show signatures of subsurface mineralization. The local detected geochemical anomalies of earth surface are invariably the primary geochemical dispersion halo, which may, or may not indicate the presence of a deposit (Clarke and Govett, 1990).

Geochemical evidence for the Mississippi Valley type (MVT) Pb-Zn and Carlin-type gold occurrences in the study area were extracted from the digital geochemical anomaly maps (Geological Survey of Iran). The statistical processing was applied to the geochemical data (stream sediment samples) and the results were integrated with the geological data. After processing of geochemical data some effects unrelated to mineralization are generated that mask anomalies related to mineralization, hence these effects must be evaluated and removed to leave residual geochemical anomalies, which may be due to mineralization (Ahadjie, 2003). The accuracy of the obtained results was assessed by scattergrams, variance analysis, and position plots for the stream sediment geochemical dataset.

5.3.1 Geochemical Evidence for MVT Pb-Zn Occurrences

The geochemical evidence in the study area was validated based on a total of 4501 stream sediment samples in the 15.000 km^2 (Geological Survey of iran).

The high geochemical anomalies of elements related to the MVT deposits were selected as evidence of probable mineralization. Figure 5.3 shows the sample locations and Zn, Pb, Cu, Cd, and As analysis results from the stream sediment samples around the Angouran mine. The highest Zn value reported in the study area is 3061 ppm in a sample in the Takab sheet (1:100.000), near the Ay Qalehsi Pb-Zn deposit. The highest values for Pb, Cu, Cd, and As respectively are 2200, 2208, 6124, and 3263 ppm. Some of the geochemical anomalies appear to be spatially related to the structural features (lineament and circular structure) (Fig 5.4). The main structural features control the distribution of geochemical anomalies, as a result of elements mobilization and transport by hydrothermal fluids, groundwater or meteoric waters along the cross-structures.

Figure 5.5 shows the drainage 3D map of the study area and the spatial relationship between big lineament and some geochemical anomalies of stream sediment samples.

Lead and zinc anomalies are the primary geochemical evidence for MVT Pb-Zn deposits. The stream sediments of the regions surrounding the deposits may contain anomalous concentrations of Zinc (Zn), Lead (Pb), Copper (Cu), Arsenic (As), Silver (Ag), Molybdenum (Mo), Cobalt (Co), Nickel (Ni), Cadmium (Cd), Boron (B), Antimony (Sb), and Fluorine (F). In the study area we used the geochemical anomalies data (stream sediment samples) of Pb, Zn, Cu, Mo, Ag, Co, Ni, Cd, As, B, and Sb (Fig. 5.6) as geochemical evidence of MVT Pb-Zn occurrences. These geochemical anomaly data will be used to validate the results of the predictive mineral potential mapping.

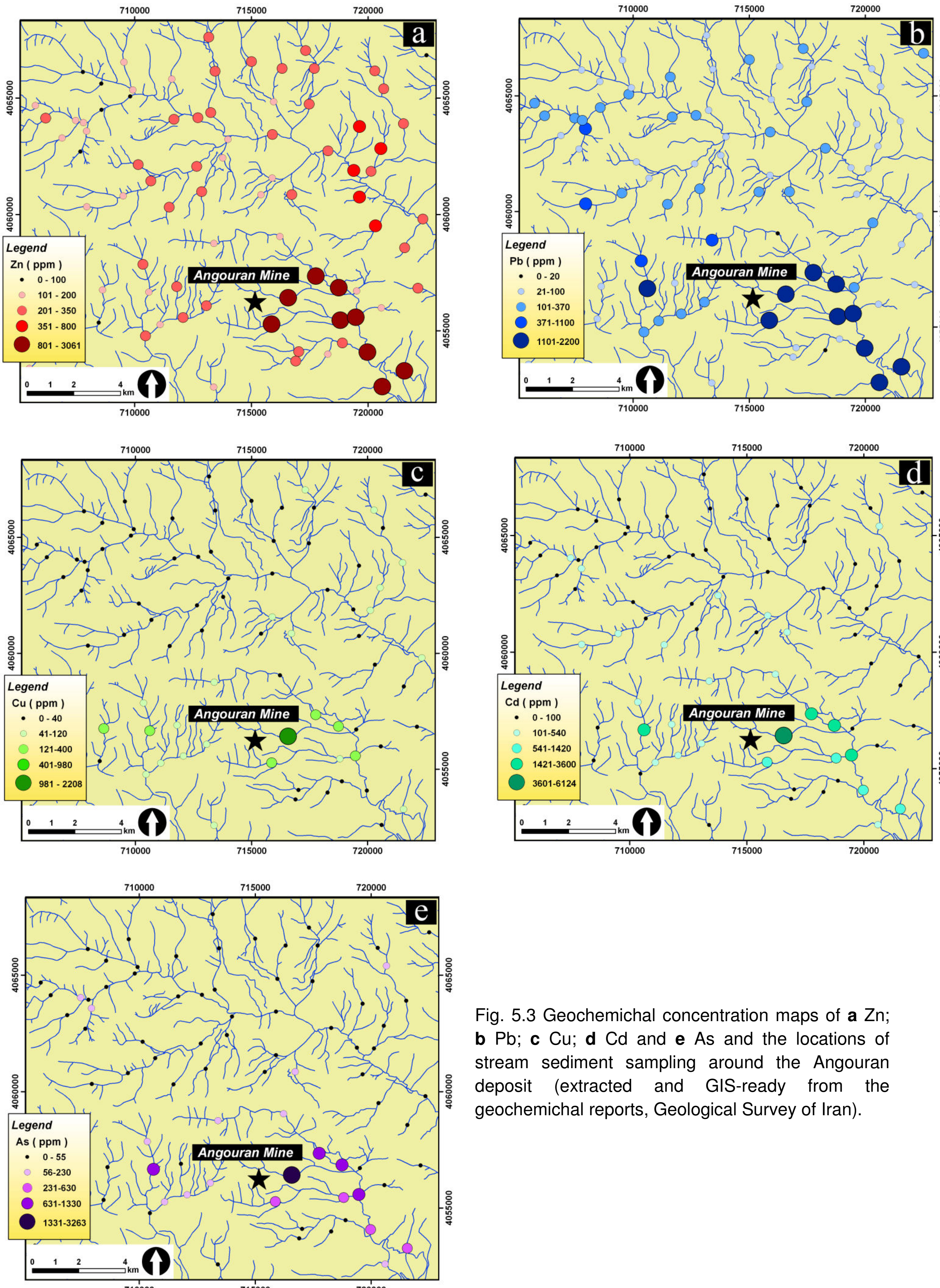

Fig. 5.3 Geochemichal concentration maps of **a** Zn; **b** Pb; **c** Cu; **d** Cd and **e** As and the locations of stream sediment sampling around the Angouran deposit (extracted and GIS-ready from the geochemical reports, Geological Survey of Iran).

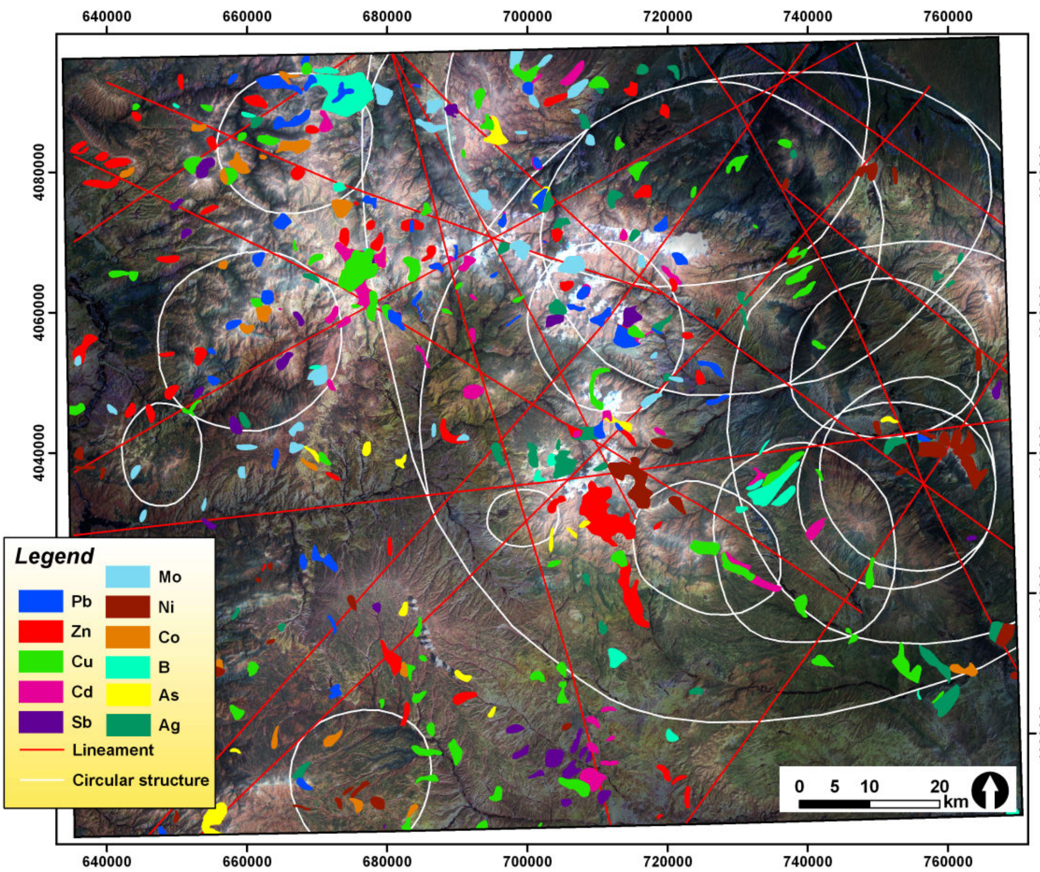

Fig. 5.4 Circular structures and lineaments from Landsat 7 ETM+ data. These structural features appear to exert control on geochemical anomaly of some group of elements.

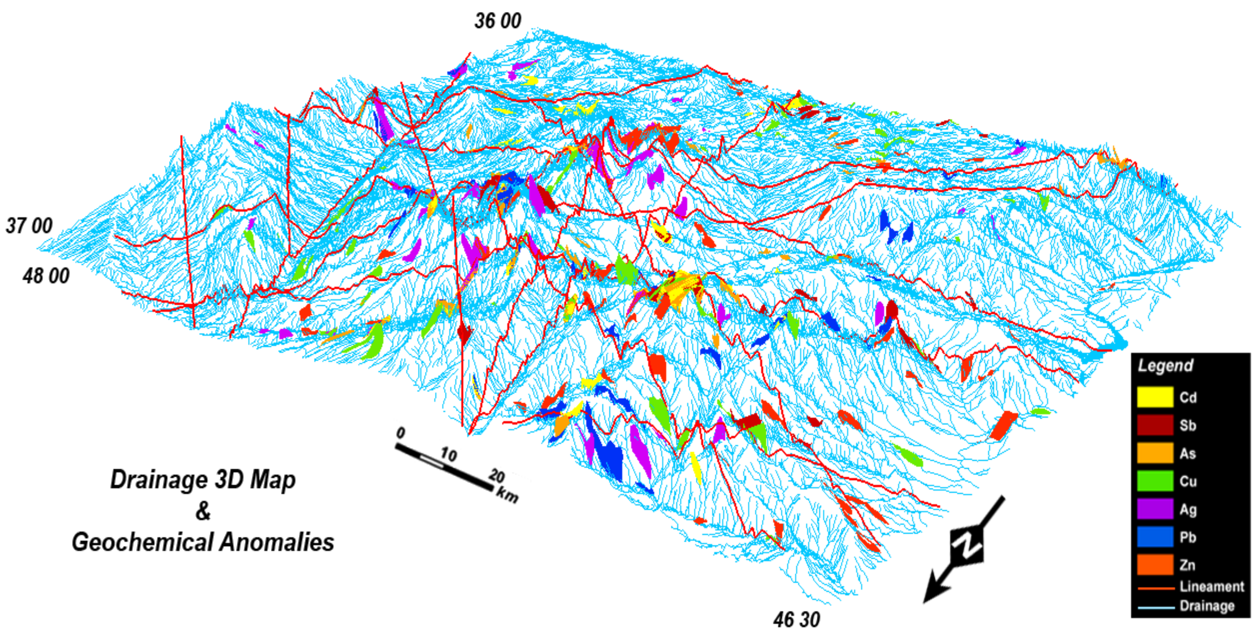

Fig 5.5 3D map of drainage (based on DEM) and the spatial relationship between big lineaments and some geochemical anomalies of stream sediment samples in the study area.

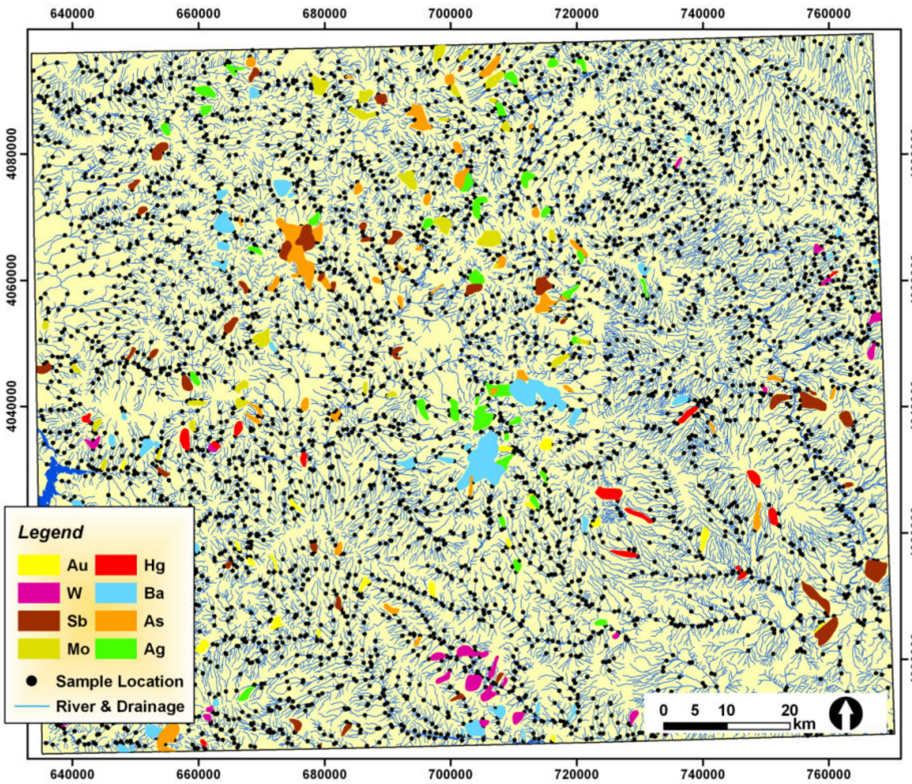

Fig. 5.6 Distribution map of geochemical anomalies from stream sediment samples as geochemical evidence of MVT Pb-Zn occurrences (The block spots are locations of sampling).

5.3.2 Geochemical Evidence for Carlin-Type Gold Occurrences

Generally, most deposits have a geochemical aspect that appears in the form of a geochemical anomaly and for Carlin-type gold deposits, gold anomaly is the primary geochemical evidence. The stream sediments of the regions surrounding the deposits may contain anomalous concentrations of Gold (Au), Arsenic (As), Silver (Ag), Mercury (Hg), Antimony (Sb), Molybdenum (Mo), Tungsten (W), Thallium (Tl), Fluorine (F), Barium (Ba). In the study area we used the geochemical anomalies data (stream sediment samples) of Au, Ag, As, Hg, W, Sb, Ba, Mo (Fig. 5.7) as geochemical evidence of Carlin-type gold occurrences. In some localities, there are several stream sediment geochemical anomalies in the same place with much covering and somewhen with distinct zoning and it can show a geochemical assemblage related to a probable mineral occurrence.

5.4 Structural Evidence

Structural data play a critical role in mineral exploration for many types of deposits. A structural feature can be a fault or a lineament. “A lineament is a mappable, simple or composite linear feature of a surface, whose parts are aligned in a rectilinear or slightly curvilinear relationship which differs distinctly from the patterns of adjacent features and presumably reflects a subsurface phenomenon” (O’Leary et al., 1976). Lineaments are believed to be the expressions of ancient, deep-crustal or trans-lithospheric structures, which periodically have been reactivated as planes of weakness during subsequent tectonic events. High-permeability channels for ascent of deeply derived mineralization fluids may provide by these planes of weakness, and in particular their intersections (Richards, 2000).

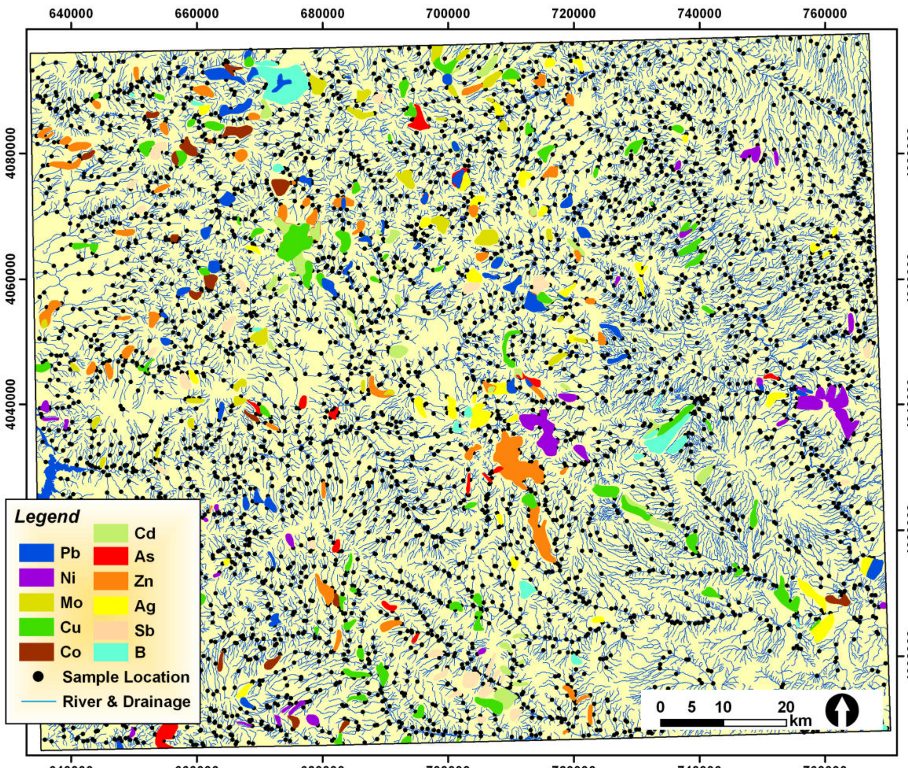

Fig. 5.7 Distribution map of geochemical anomalies from stream sediment samples as geochemical evidence of Carlin-type gold occurrences. The block spots are locations of sampling.

Structural features, particularity, faults must be refined on the basis of their time relations to the mineralization of interest. Generally, the structures that are generated after mineralization stage must be removed from the structural dataset but it is usually difficult in early exploration stages, however, it is possible when the modeling is made for an explored district. For analysis of structural data, it is useful to divide the structural features into two classes: regional and local. Spatial relations between deposits are indicated by regional structures, while the local structures control the spatial characteristics of individual deposits (Pan and Harris, 2000). The structural evidence as a spatial dataset can be obtained from geological, geophysical or remote sensing data.

5.4.1 Geological Structures

The geological structures (faults) extracted from the digital geological map (1:100.000 scale). Fig. 5.8 shows the digital fault map and three rose diagrams, which provides a general view of the faults orientation. The rose diagram of major faults shows two main trends at NW-SE and NE-SW directions. There are also a small number of WE and NS trending faults. The NW-SE and NE-SW trending faults were extracted as two main directions for further use in the analysis of modeling for mineral potential mapping of MVT Pb-Zn and Carlin-type gold occurrences. The rose diagram of minor faults shows a main trend at NE-SW direction and upshot the rose diagram of thrust faults shows a main trend at NW-SE direction.

5.4.2 Geophysical Structures

Structural features (lineament and circular structure) could also be obtained from aeromagnetic data. For identifying presence of linear features such as faults, lineaments

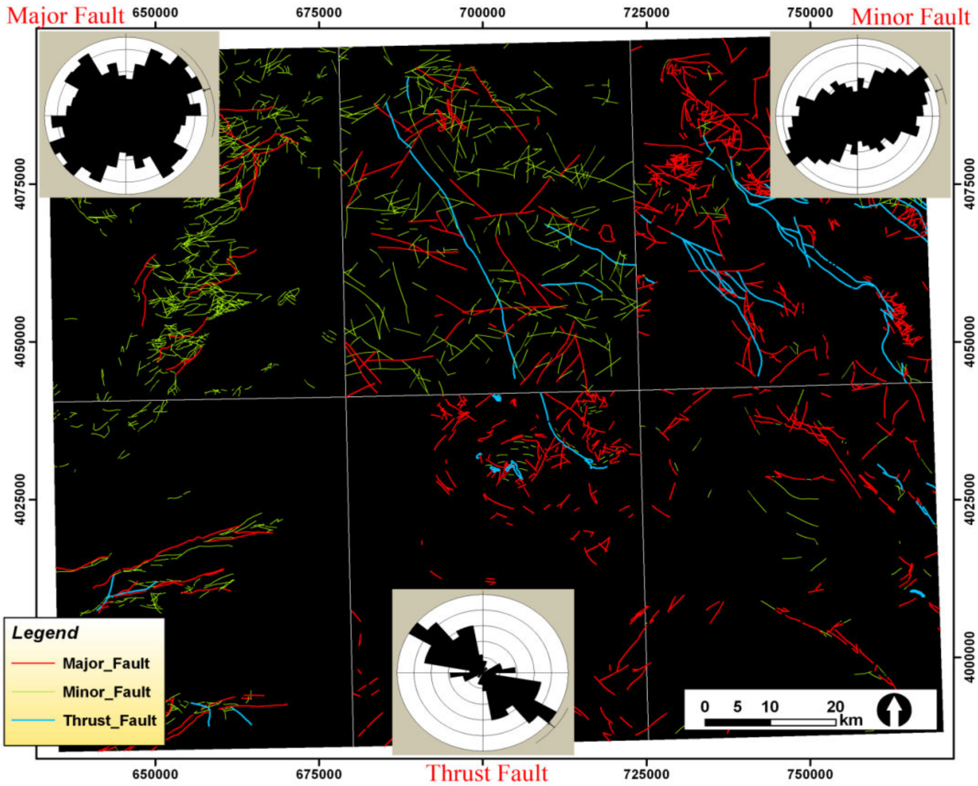

Fig. 5.8 Structural features (faults) from geological maps and corresponding rose diagrams (extracted and GIS-ready from 1:100.000 geological maps, Geological Survey of Iran).

and circular structures from aeromagnetic data, the first vertical derivative was applied (Carballo, 1998) (Fig. 5.9). First vertical derivates are essentially a measure of the rate of change of the field with the height (Alvarez, 2000). "The calculation of the first vertical derivative of the aeromagnetic field is physically equivalent to measuring the magnetic field simultaneously at two points vertically above each other (magnetic gradiometer), subtracting the data and dividing the result by the spatial separation of the measuring point" (Rojas, 2003).

Circular structures usually reflect the traces of intrusive shallow bodies on the earth surface. These extracted structural features (lineaments and circular structures) appear to exert extraordinary control on occurrences of Pb-Zn, Au, Cu and Fe in the study area.

5.4.3 Remote Sensing Structures

Analysis of remote sensing structures can delineate the regional structural elements at emplacement of shallow intrusive bodies. In this area, structural features (lineament and circular structure) were considered as conduits and trap zones for mineralization fluids. To detect structures from remote sensing data, some procedures were carried out that explained in chapter 4. For example, several suitable color composites and band-ratios were generated from which lineaments were interpreted visually. Also digital filtering (described in chapter 4) was applied to all bands to enhance detection of lineaments. Landsat 7 ETM$^+$ data of the study area with a resolution of 30m was used to detect lineaments and circular structures. The rose diagram of remote sensing lineaments (Landsat 7 ETM$^+$ data) shows a predominant trend at NW-SE direction and some secondary trends at NE-SW and W-E directions (Fig. 5.10). This structural evidence (geological, geophysical and remote sensing) are used in spatial data integration for predictive modeling of MVT Pb-Zn and Carlin-type gold occurrences.

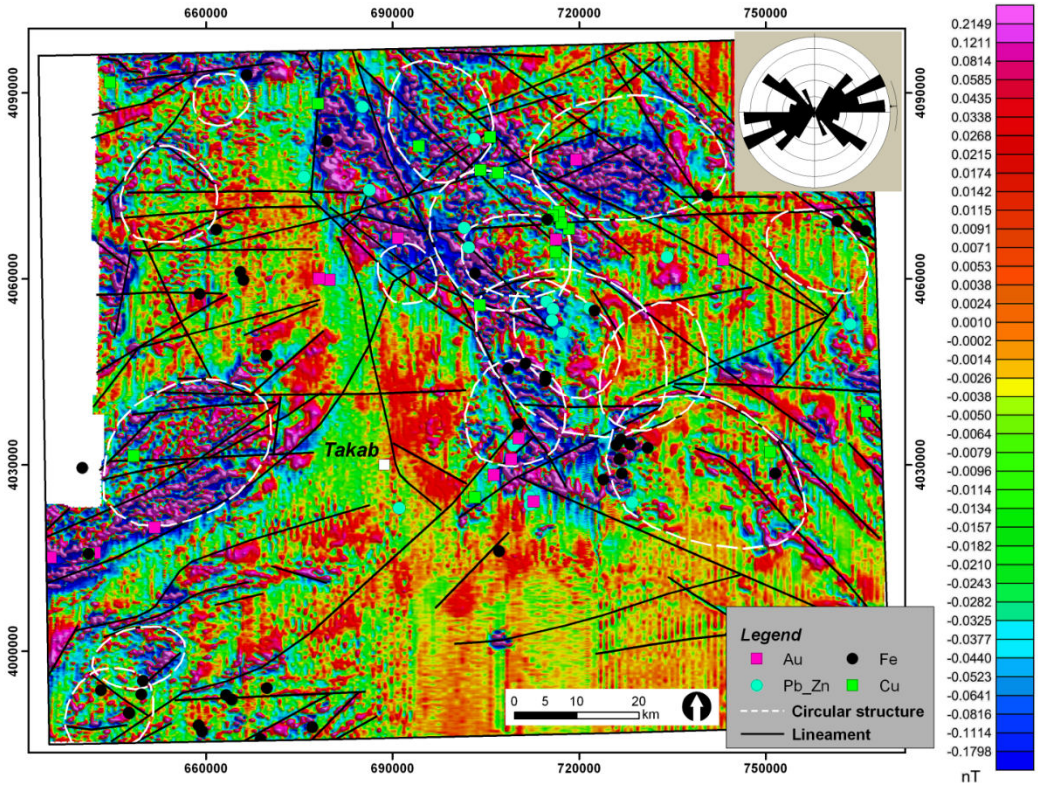

Fig. 5.9 Structural features from first vertical derivative of geophysical data (described in chapter 3) and corresponding rose diagram. The NE-SW, W-E and NW-SE directions are respectively the main trends of the geophysical lineaments. These structural features appear to exert control on occurrences of Pb-Zn, Au, Cu and Fe in the study area (extracted and GIS-ready from geophysical data, Geological Survey of Iran, unpublished).

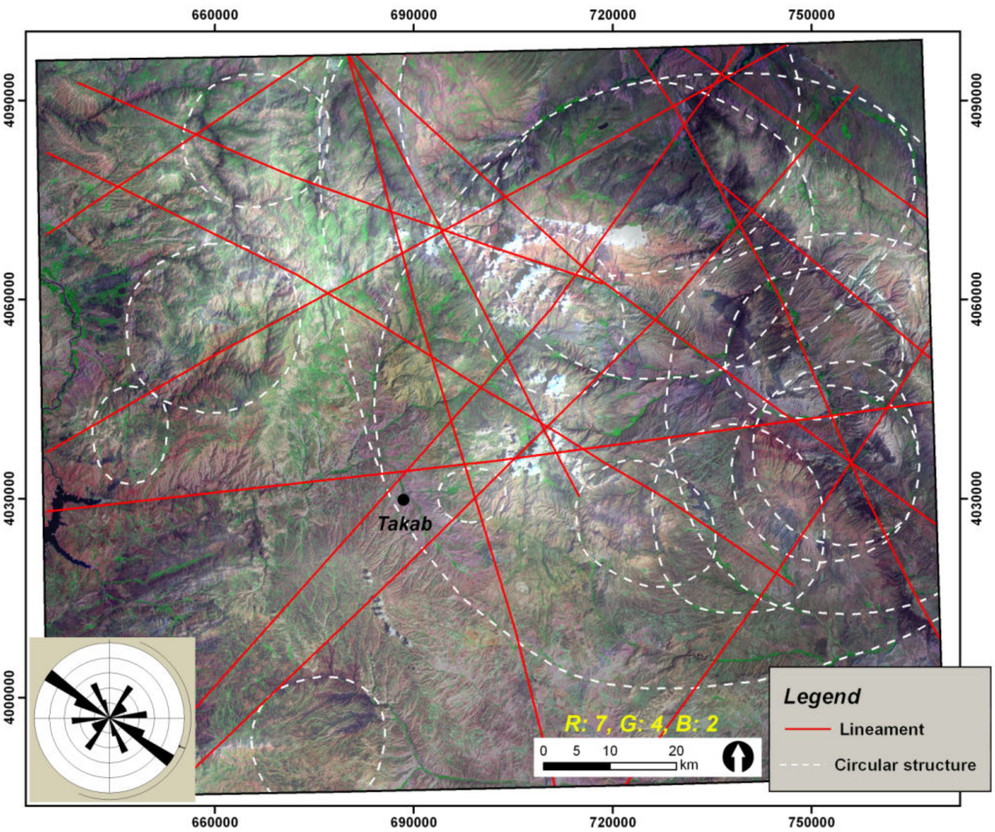

Fig. 5.10 Structural features from remote sensing data (Landsat 7 ETM+) and corresponding rose diagram. The rose diagram shows a predominant direction at NW-SE and a secondary one at NE-SW and W-E trends.

5.5 Heat/Metal Source Evidence

In this study, indications of shallow intrusive bodies were interpreted from the aeromagnetic data and were considered as spatial heat source evidence for MVT Pb-Zn occurrences and Integration of geophysical results and geological data were applied as heat/metal source evidence of Carlin-type gold occurrences. Figure 5.11 shows the total magnetic intensity 3D map of the study area and the places of main deposits.

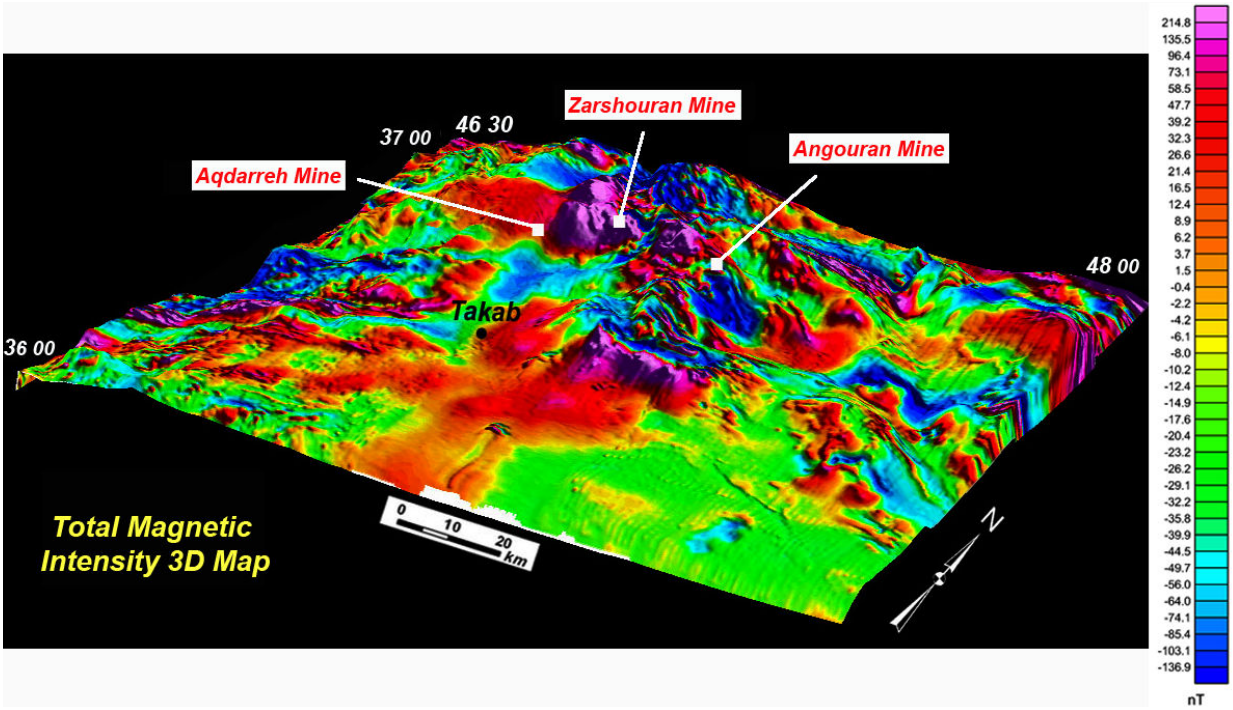

Fig. 5.11 Total magnetic intensity 3D map of the study area and the places of main deposits (extracted from geophysical data, Geological Survey of Iran, unpublished).

5.5.1 Heat Source Evidence for MVT Pb-Zn Occurrences

One of the recognition criteria for MVT Pb-Zn occurrences is the magmatic activity as heat sources, such as buried shallow intrusive rocks. They are generally not exposed on the earth surface, thus the geophysical data processing can help to delineate such subsurface bodies. This presumption is based on a spatial association of geophysical shallow bodies (aeromagnetic data) with some known Pb-Zn occurrences in the study area. First vertical derivative of the aeromagnetic field enhance near-surface magnetic sources such as shallow-level intrusive bodies.

Figure 5.12 shows the extracted shallow intrusive bodies on the first vertical derivative of the aeromagnetic map in the study area. This data layer is used in the GIS modeling for predictive mineral potential mapping.

5.5.2 Heat/Metal Source Evidence for Carlin-Type Gold Occurrences

“Historically, genetic hypotheses for Carlin-type deposits comprise three general groups, advocating magmatic, metamorphic, or circulated meteoric waters for their generative fluids” (Emsbo et al., 2006).

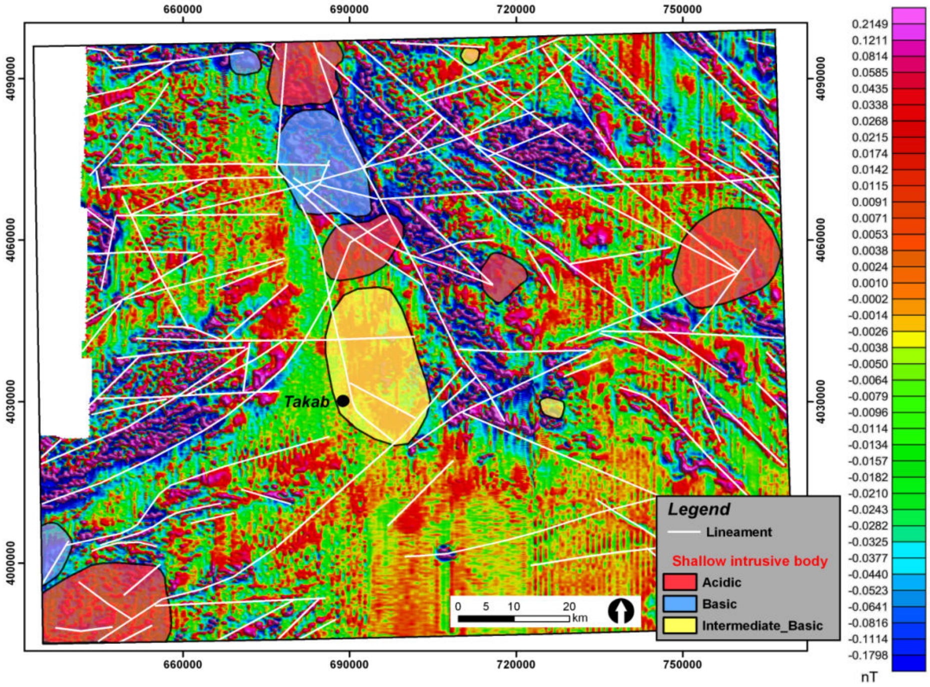

Fig. 5.12 Shallow intrusive bodies from the first vertical derivative of the aeromagnetic data (extracted and GIS-ready from geophysical data, Geological Survey of Iran, unpublished).

In magmatic models hydrothermal fluids, ore minerals, and heat sources are related to the magmas intrusion and thermal energy of magmas cause the movement of hydrothermal fluids and deposit of gold (Ressel et al., 2000 and Kesler et al., 2005). Magma activity in the sediment-hosted deposits (Carlin-type gold deposits) in Nevada is interpreted to have been the heat source for the hydrothermal systems, and may have been the source of the gold-bearing fluids in the sediment-hosted deposits (Sillitoe and Bonham, 1990). Igneous rocks at range of granodiorite to rhyodacite in forms of stock, dyke and sill almost have a spatial association with Carlin-type gold deposits (Hassanipak and Shojaat, 2000). The probable heat/metal sources for Carlin-type gold occurrences were extracted from processing of geological and geophysical datasets. The geological maps (100.000 scale) were used to extract the felsic and felsic-intermediate magmatic rocks at juxtaposition of selected Carlin-type gold host rocks (Fig. 5.13) and combined with the aeromagnetic data (felsic shallow intrusive bodies) (Fig. 5.12) to generate heat/metal source evidence for predictive mineral potential mapping.

5.6 Hydrothermal Activity Evidence

Hydrothermal fluids are one of the important factors in transport of ore minerals and forming of more deposits. They play an important role to alter the rocks surrounding ore deposits. Thus, recognition of these hydrothermally altered rocks and different types of alteration minerals is necessary to understand the mineralization systems and mineral exploration. Typically altered rocks associated with Carlin-type gold deposits are decalcification and silicification (jasperoid) of carbonate rocks, and may be enveloped by a halo of argillic and sericitic alteration zones (Robert et al., 1997). Argillic alteration rocks are formed typically surrounding the Carlin-type gold deposits as a residual product of carbonate dissolution and acid attack of detrital silicate minerals (Teal and Jackson, 2002).

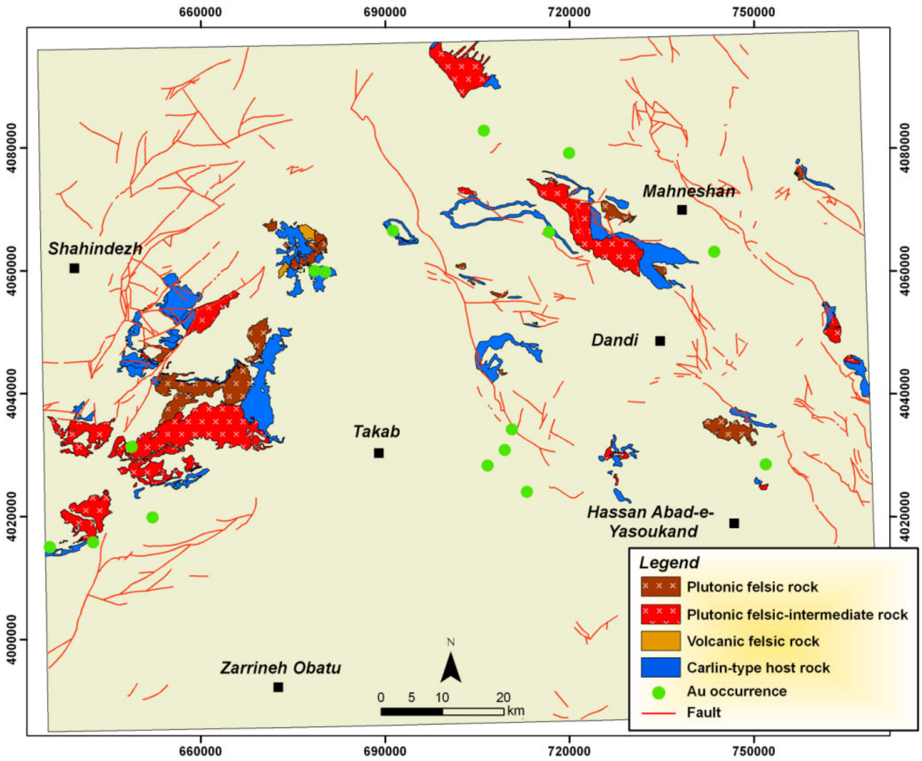

Fig. 5.13 Probable heat/metal sources for Carlin-type gold and their proximity to the selected Carlin-type gold host rocks in the study area and the places of known gold occurrences (after 1:100.000 geological maps, Geological Survey of Iran) (extracted and GIS-ready from 1:100.000 geological maps, Geological Survey of Iran).

In Carlin-type deposits, there are several possibilities for generation of sericite: in sedimentary host rocks as detrital grains; in igneous rocks as deuteric or magmatic minerals; and hydrothermal (related or not related to Au) sericite. Also, pre-ore sericite has the potential for being reset to reflect hydrothermal activity, if the Au-related hydrothermal event was of sufficient temperature and duration (Arehart et al., 2003). Figure 5.14 shows the generalized paragenetic sequence for Carlin-type gold deposits.

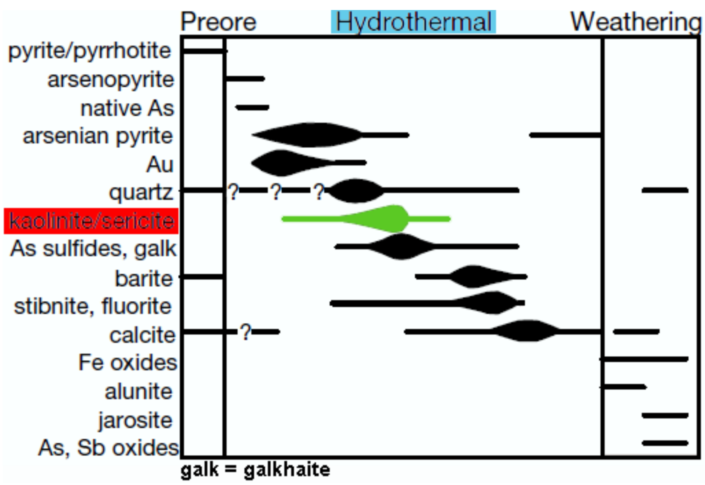

Fig. 5.14 Generalized paragenetic sequence for Carlin-type gold deposits (Arehart et al., 2003; modified from Arehart, 1996).

The hydrothermally altered rocks (argillic and sericitic) adjacent to the probable Carlin-Type host rocks that have been mapped using Aster and Landsat 7 ETM^{+} data (see chapter 4) were selected as a spatial evidence for GIS modeling of predictive mineral potential mapping of Carlin-type gold occurrences in the study area (Fig 5.15).

Airborne gamma-ray spectrometry (K, eU & eTh) is one of the geophysical surveys that can be useful in exploration of several deposit types particularly epithermal deposits. The abundance of Potassium (K), Thorium (eTh) and Uranium (eU) in rocks and altered and weathered materials can be measure via airborne gamma-ray spectrometry method by detecting emitted gamma-rays due to the natural radioelement decay of these elements. When ^{40}K decays to Argon, content of Potassium can be measured directly from emitted gamma-rays but Uranium and Thorium cannot be measured directly. For calculating the concentration of Th and U, distinct emission peaks associated with ^{208}Tl and ^{214}Bi are used. Therefore, U and Th are expressed in equivalent ppm (eU and eTh) (Wilford, 2002).

These data is used to investigate the geophysical expression of the hydrothermally altered rocks (Hariss et al., 2005). Factors eTh and eTh/K are very useful in identifying of rock weathering (Galbraith and Saunders, 1983; Portnov, 1987 and Braun et al., 1993) and content of clay minerals (Portnov, 1987) and Factors K, eU/K and eTh/K are sensitive to hydrothermally altered rocks (Portnov, 1987).

Generally, concentration of K decreases with increasing weathering because K is highly soluble under most weathering environments and is rapidly leached from weathered and altered rocks but U and Th are associated with resistant minerals and can find in such environments (Wilford, 2002).

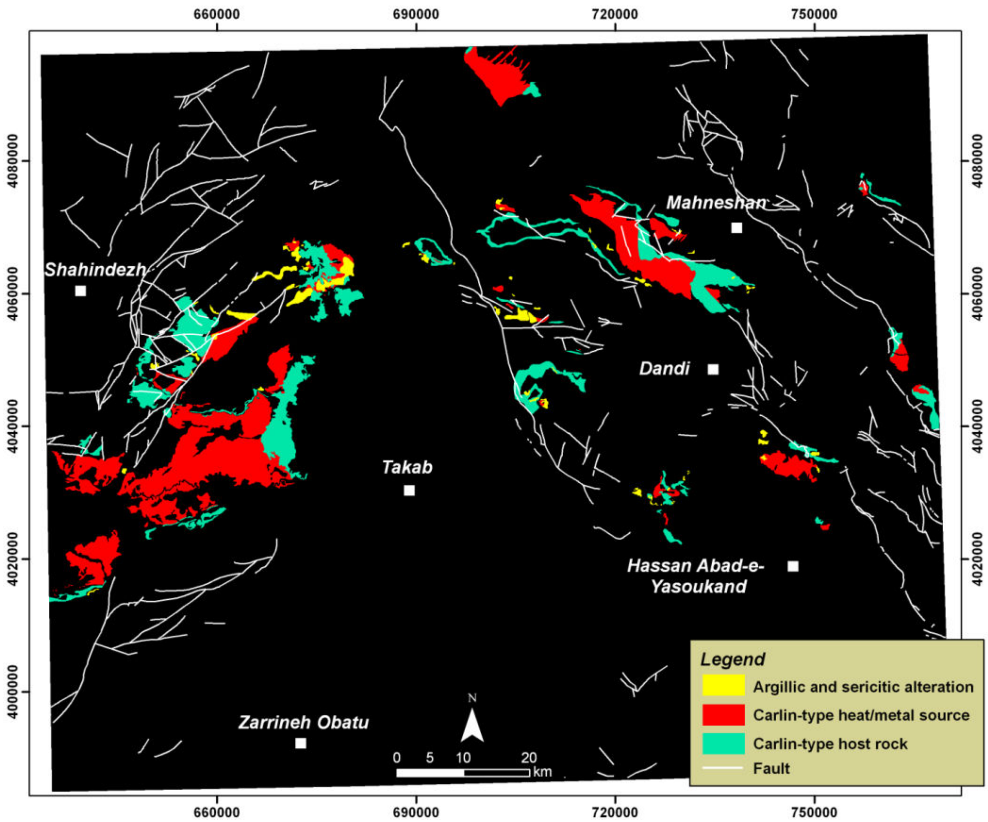

Fig. 5.15 Hydrothermally altered rocks (argillic and sericitic) at proximity of probable heat/metal sources and host rocks of Carlin-type gold occurrences in the study area (extracted and GIS-ready from 1:100.000 geological maps, Geological Survey of Iran).

Except Aster and Landsat 7 ETM^{+} data, the airborne radiometric data (K, eU and eTh) also was processed to extract the hydrothermally altered rocks for integration with remote sensing data but it isn't used in the predictive mineral potential mapping of Carlin-type gold occurrences as a realty data layer because the remote sensing data give us more effective information about hydrothermally altered rocks than airborne radiometric data.

Figure 5.16 shows the K, eU and eTh grid maps of the airborne radiometric data and the ternary (K, eU, eTh) grid map over the study area and figure 5.17 shows the Moghanlu anatectic granite (in the western part of the study area; Mahneshan 1:100.000 geological sheet) and surrounding argillic alteration zone on the geological map, Aster and Landsat 7 ETM^{+} data, K and eTh airborn radiometric maps and ternary (K, eU, eTh) grid map of geophysical data. The hydrothermally altered rocks (argillic alteration) show low K due to leaching and high eTh on the corresponding maps.

The hydrothermally altered rocks have not reported around the Mississippi Valley type Pb-Zn deposits, hence, in this research the alteration data layer will use only for modeling of Carlin-type gold occurrences.

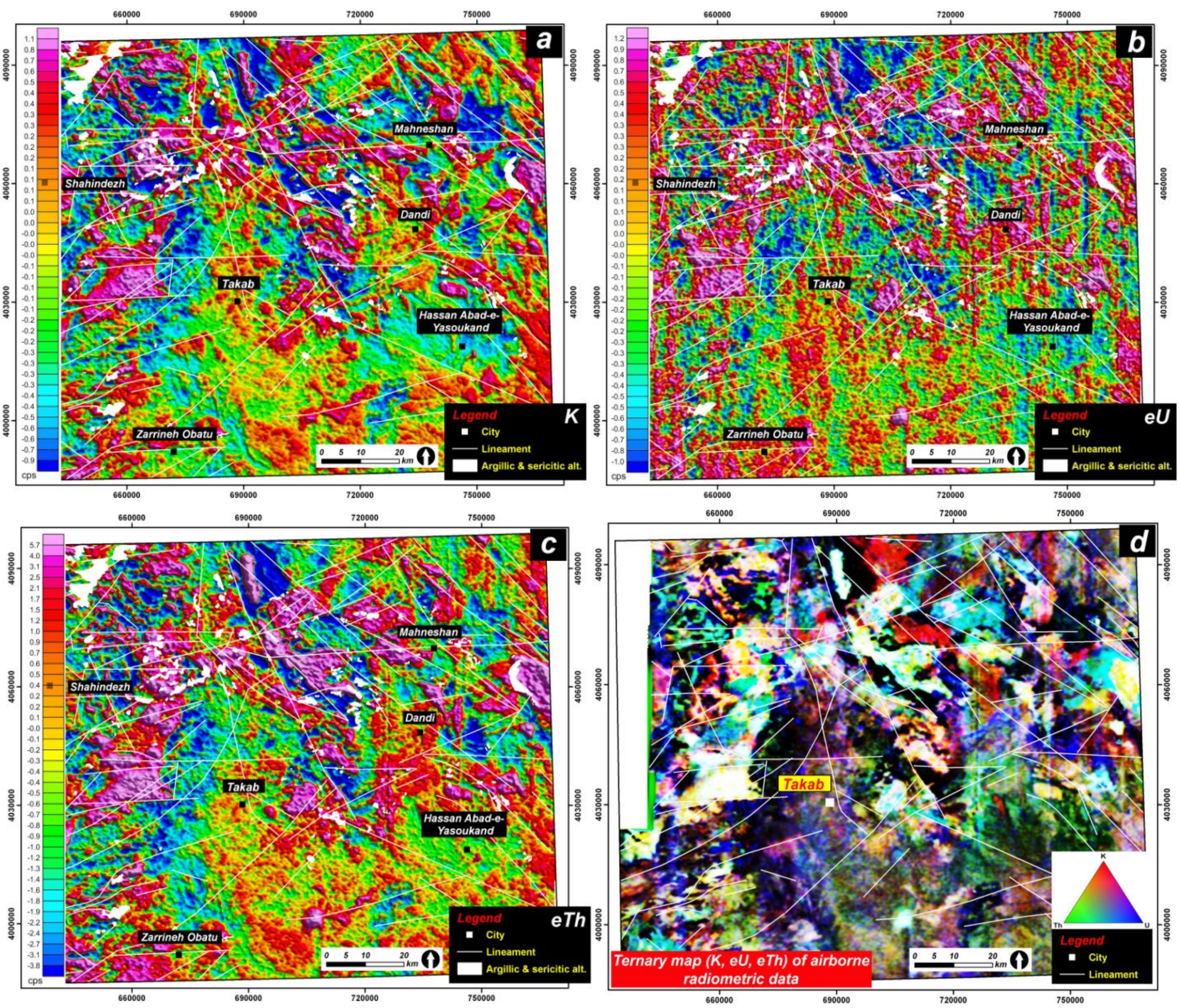

Fig. 5.16 presentations of gridded gamma ray spectrometry data: **a** Potassium (K) grid; **b** Uranium (eU) grid; **c** Thorium (eTh) grid with the hydrothermally altered rocks and geophysical lineaments and **d** Ternarry (K, eU, eTh) grid map of airnborne radiometric data over the study area (extracted and GIS-ready from geophysical data, Geological Survey of Iran, unpublished).

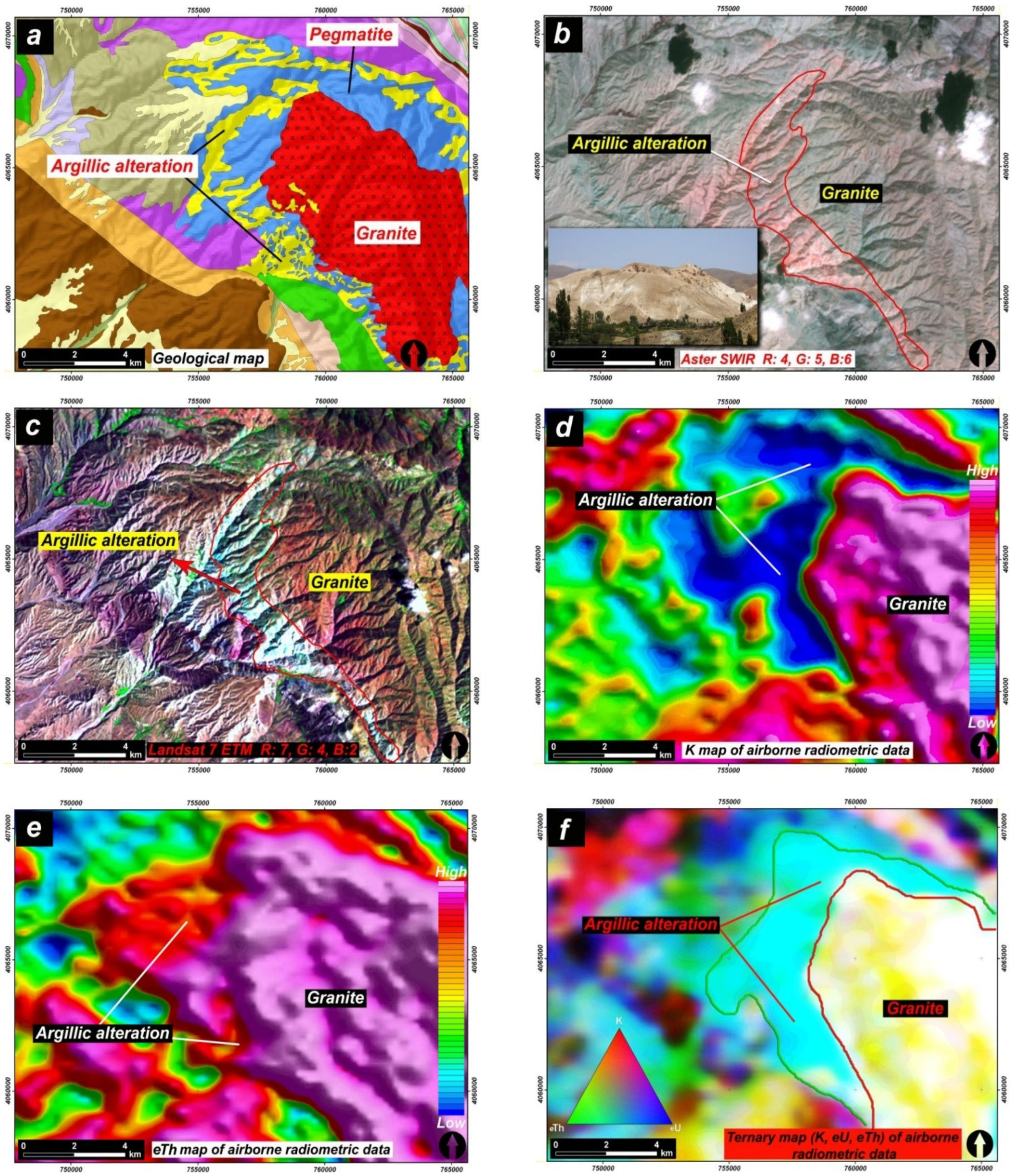

Fig. 5.17 Moghanlu anatectic granite (in the western part of the study area; Mahneshan 1:100.000 geological sheet) and surrounding argillic alteration zone on the **a** Geological map; **b** Aster SWIR (R: 4, G: 5, B: 6); **c** Landsat 7 ETM^{+} (R: 7, G: 4, B: 2); **d** Potassium (K) grid; **e** Thorium (eTh) grid and **f** Ternarry (K, eU, eTh) grid map of airborne radiometric data. The abundance of potassium (K) in low in the argillic alteration zone due to leaching (d) but the abundance of Thorium is high (e) because Th is associated with resistant minerals.

Chapter 6 Spatial Analysis and GIS Modeling for Mineral Potential Mapping

6.1 Introduction

Previously, in a mineral exploration project, each data layer separately processed, interpreted and applied by geologists but recently, they usually use geographic information systems (GIS) for inputting, classification, processing, and modeling of geo-exploration datasets.

Geographic information systems are computer-based technologies designed for the efficient inputting and storage of different types of spatial data and have capabilities for the effective visualization, analysis, integration and modeling of geo-exploration datasets and can be streamline the exploration process (Knox-Robinson, 2000). GIS techniques and dependent database are useful tools in data management and applicable in local and regional exploration analysis for predictive mineral potential mapping. This technology has ability to apply three-dimensional (3D) visualization methods for perspective presentation and analysis of spatial datasets to enhance the quality of exploration decisions.

6.2 Geographic Information Systems (GIS)

GIS is "a system for capturing, storing, checking, manipulating, analyzing and displaying data which are spatially referenced to the Earth" (DoE, 1987).

One of the important applications of a GIS in geosciences is the ability of processing and integration of multiple geo-exploration datasets such as lithological, structural, geophysical, geochemical and remote sensing data to delineate predictive mineral potential maps (e.g. Chung and Agterberg, 1980; Bonham-Carter et al., 1988; Harris, 1989; Moon et al., 1991; Bonham-Carter, 1994; Rencz et al., 1994; Wright and Bonham-Carter, 1996; Raines, 1999 and Harris et al., 2000 & 2008). Mineral potential mapping is one of the important types of geo-exploration mapping and usually utilized several different methods such as lithological data classification (e.g. Longhi et al., 2001), geological mapping (e.g. Cox et al., 2007), extraction of hydrothermally altered rocks (e.g. Podwysocki et al., 1983 and Herrmann et al., 2001), mapping of structural features (e.g. Liu et al., 2000), delineation of alteration zones (e.g. Tangestani and Moore, 2002), processing of hyperspectral data (e.g. Neville et al., 2003), geochemical data processing (e.g. Ahadjie, 2003), geophysical data analysis (e.g. Neawsuparp et al., 2005) and the spatial data integration by GIS methods (e.g. Akhavi et al., 2001 and Harris et al., 2008). For use of spatial geo-exploration datasets in a GIS environment, it is necessary to know some important rules about geology and mineral exploration. Locating mineral resources relies primarily on the knowledge and understanding of the general and detailed geology of an area. Therefore, the following basic geo-exploration information regarding mineral deposits is relevant (Rajesh, 2004):

- Generally each type of mineral deposits occurs in a specific rock unit (e.g. MVT Pb-Zn deposits usually occur in the carbonate rocks).

- Local or regional structural features usually play an important role in forming of several mineral deposit types.

- More of Mineral deposits usually show an alteration zone on the Earth's surface.

- Certain mineral deposits can typically show a particular geochemical or geophysical characteristic.

- Certain mineral deposits usually occur near the contact between favourable rock types (e.g. porphyry copper deposits have a direct spatial association with the contact of granitic to intermediate intrusive rocks; Guilbert and Park, 1996).

Based on the region properties and metallogenetic model in the study area, we performed GIS modeling (Fig. 6.1) for prediction of carbonate replacement deposits (CRD) such as Mississippi-Valley type Zn-Pb and Carlin type gold mineralization.

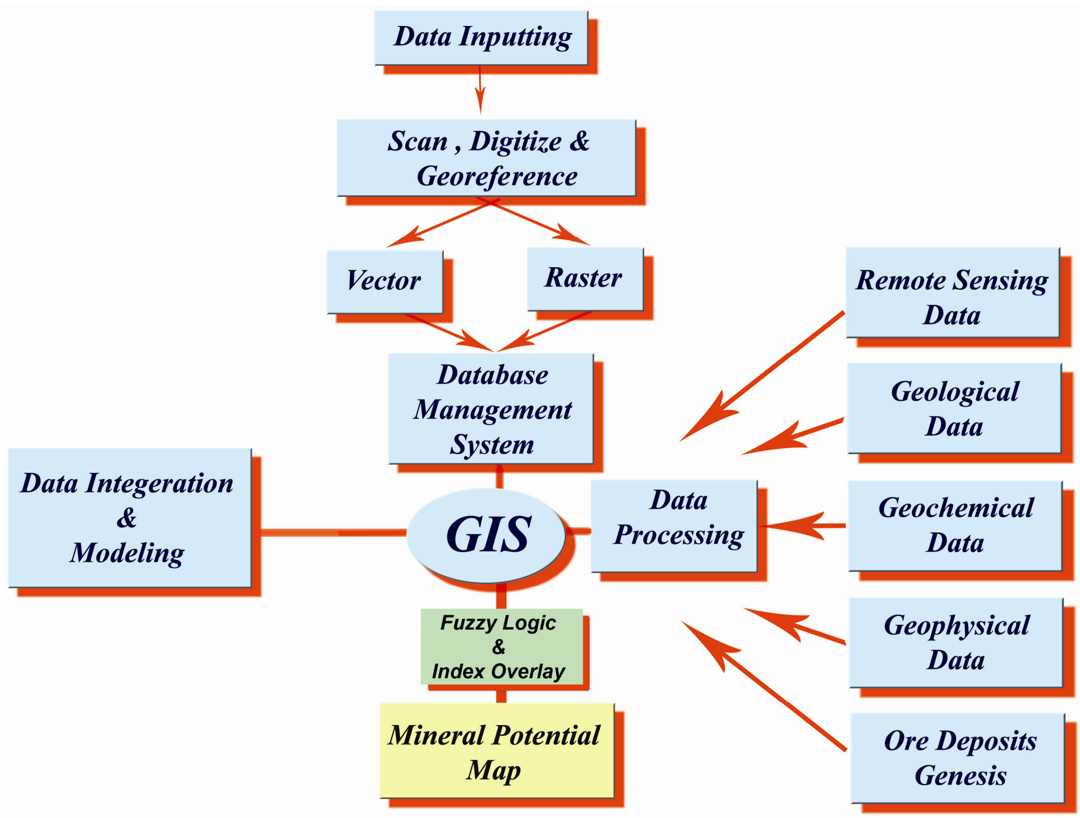

Fig. 6.1 Flowchart of the methodology for predictive mineral potential mapping based on GIS modeling in the study area (modified after Pan & Harris, 2000).

6.3 Mineral Potential Mapping Methods

There are several GIS-based modeling methods for mineral potential mapping that have been developed over the past 20 years. These methods can be divided into two main categories: data-driven and knowledge-driven techniques (Harris et al., 2008; See e.g. Bonham-Carter, 1994 and Wright et al., 1996 for more information).

Knowledge-driven methods are based on a weighting system that for every spatial evidence layer in each mineral deposit model is usually assigned a relative weight ranging from 1 to 10 (reflecting importance) but Data-driven techniques use the location of known mineral deposits with respect to individual evidence layers to infer the weights for each evidence map (Harris et al., 2008; after Bonham-Carter, 1994).

Fuzzy logic and index overlay are two types of Knowledge-driven methods. The extracted spatial evidence from geo-exploration datasets (chapter 5) in the study area were processed in a GIS using two GIS-based knowledge-driven methods (fuzzy logic and index overlay) for generation of predictive mineral potential maps of MVT Pb-Zn and Carlin-type gold occurrences.

6.3.1 Fuzzy Logic

The idea of fuzzy logic was first invented by Zadeh, 1965 in field of electronic engineering based on "degrees of truth" instead of the usual "true or false". In this method the spatial objects on a map are considered as members of a set. In classical set theory, an object is a member of a set if it has a membership value of 1 and isn't a member if it has a membership value of 0 but in fuzzy set theory, the value of each membership can be defined between 0 and 1, reflecting the degree of membership certainty (Tangestani and Moore, 2003).

Fuzzy logic as one of the knowledge-driven methods uses the recognition criteria of the mineralization for mineral potential mapping. These factors are usually selected based on a statistical evaluation of geological characteristics of known mineral deposits by using empirical methods or by an appropriate genetic mineral deposit model. The extracted recognition criteria evidence is processed to generate multiclass evidential maps for modeling. The definition of fuzzy membership values of multiclass evidential maps and the selection of appropriate inference network and fuzzy set operators for combining the evidential maps are the most significant procedures in fuzzy modeling (Poweral et al., 2003).

In the framework of the fuzzy logic method, each multiclass evidential map (fuzzy membership) is weighted based on their significance (between 0 and 1). The fuzzy membership values must reflect the relative importance of each map, as well as the relative importance of each class of a single map. The evidential maps integrated by one or a combination of some fuzzy operators.

Five operators that were found to be useful for combining exploration datasets are the fuzzy AND, fuzzy OR, fuzzy algebraic product, fuzzy algebraic sum, and fuzzy gamma operator. These operators are briefly reviewed here (Bonham-Carter, 1994).

The fuzzy AND operation is equivalent to a Boolean AND operation on a classical set and is defined as equation 6.1.

$$\mu_{Combination} = \mathrm{MIN}\,(\mu_A, \mu_B, \mu_C, \ldots) \qquad (6.1)$$

Where µA, µB,… are the fuzzy membership values for maps A, B, … at a particular location. This operation is appropriate where two or more pieces of evidence for a hypothesis must be present together, for the hypothesis to be accepted.

The fuzzy OR is like the Boolean OR operation. This operator is defined as equation 6.2.

$$\mu_{Combination} = \text{MAX}\,(\mu_A, \mu_B, \mu_C, \ldots) \quad (6.2)$$

This operator, where favourable evidences for the occurrence of mineralization are rare and the presence of any evidence may be sufficient to suggest favourability.

The fuzzy algebraic product is defined as equation 6.3.

$$\mu_{Combination} = \prod_{i=1}^{n} \mu_i \quad (6.3)$$

Where µi is the fuzzy membership values for the i-th (i = 1, 2…, n) maps that are to be combined. The combined fuzzy membership values tend to be very small with this operator, due to the effect of multiplying several numbers less than 1.

The combination fuzzy membership value is always smaller than, or equal to, the smallest contributing fuzzy membership value and is thus "decreasive".

The fuzzy algebraic sum operator is complementary to the fuzzy algebraic product, and is defined as equation 6.4.

$$\mu_{Combination} = 1 - [\prod_{i=1}^{n} (1-\mu_i)] \quad (6.4)$$

The result of this operation is always larger than, or equal to, the largest contributing fuzzy membership value. The effect is thus "increasive".

Two or more pieces of evidence that both favor a hypothesis reinforce one another and the combined evidence is more supportive than either piece of evidence taken individually.

The fuzzy gamma (γ) operation is defined in term of the fuzzy algebraic product and the fuzzy algebraic sum by equation 6.5.

$$\mu_{Combination} = [1 - (\prod_{i=1}^{n} (1-\mu_i)]^{\gamma} * (\prod_{i=1}^{n} \mu_i)^{1-\gamma} \quad (6.5)$$

Where γ is a parameter chosen in the range (0, 1) (Zimmermann and Zysno, 1980).

When γ is 1, the combination is the same as the fuzzy algebraic sum and when γ is 0, the combination equals the fuzzy algebraic product (Fig 6.2).

The proper selection of γ content produce output values that ensure a flexible compromise between the "increasive" tendencies of the fuzzy algebraic sum and the "decreasive" effects of the fuzzy algebraic product (Bonham-Carter, 1994) and can be help us to evaluate the mineral deposit models.

Generally an Inference network is applied to define the sequence of fuzzy operations for combining input evidential maps.

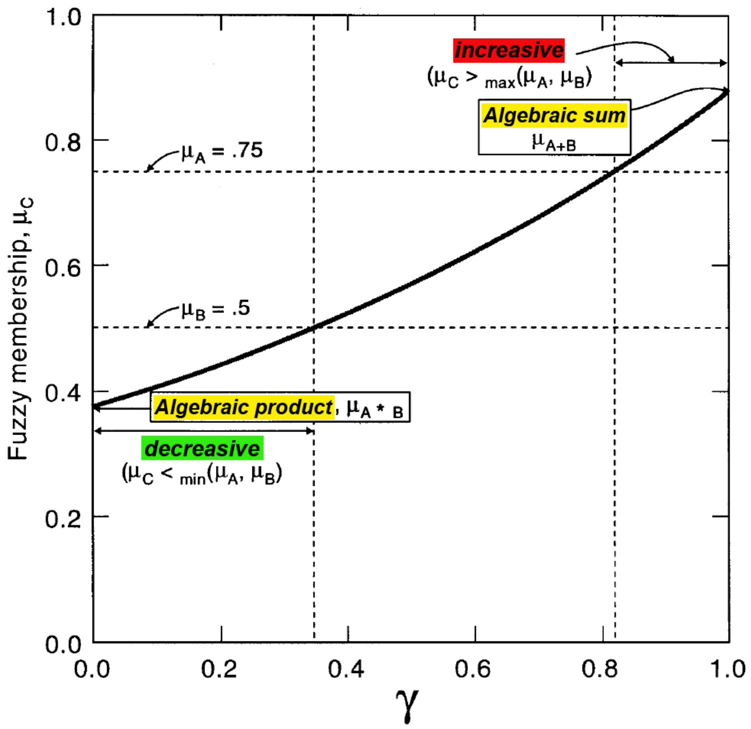

Fig. 6.2 This graph shows the effect of variations in γ (between 0 and 1) for the case of combining (μC) two fuzzy membership values, $\mu A=0.75$ and $\mu B=0.5$. When, $\gamma=0$, the combination equals the fuzzy algebraic product and when, $\gamma=1$, the combination equals the fuzzy algebraic sum (after Bonham-Carter, 1994).

6.3.2 Index Overlay

The Index Overlay method is one of the knowledge-driven methods. In this method, for every class of each map is assigned a distinct score. It makes a flexible weighting system and the table of scores and the map weights can be adjusted to reflect the judgment of an expert in the domain of the application under consideration. The greatest disadvantage of this method probably lies in its linear additive nature (Karimi et al., 2004). A weighted average score for any location (polygon or pixel) is defined by equation 6.6.

$$S = \frac{\sum_{i}^{n} SijWi}{\sum_{i}^{n} Wi} \qquad (6.6)$$

Where S is the weighted score for each feature, Wi is the weight of the i-th input map, Sij is the score for the j-th class of the i-th map and j is related to the class weighted and scored in all the maps (Bonham-Carter, 1994). With the index overlay method, prospectivity is represented by ordinal-scale numbers (Rock, 1988), such that a location with a value of 2 is more prospective than a location with a value of 1, but not twice as prospective. The resultant prospectivity map is constructed by the summation, at each location, of all of the input datasets. In the prospectivity map based on this method, the higher the resultant number, the more prospective the location (Knox-Robinson, 2000).

6.4 Spatial Analysis and Data Integration

Before the evidential maps (chapter 5) can be applied by a GIS method for modeling, they require a number of spatial analyses. There are several analytical techniques in GIS for spatial analysis and integration of datasets. GIS provides some useful tools for spatial analysis of distinct objects in a data layer such as buffering, density, classification, dissolving and interpolation, also for spatial analysis and integration of selected features from different data layers such as combining, overlaying and joining of attribute tables.

Mineral potential mapping using GIS-based spatial analysis and data integration was performed for MVT Pb-Zn and Carlin-type gold occurrences by fuzzy logic and index overlay methods in the study area using ArcGIS 9.2 (ESRI) software and Spatial Data Modeller extension (ArcSDM).

6.5 Mineral Potential Mapping by Fuzzy Logic Method

Extracted information layers of geo-exploration datasets were buffered and weighted based on ore deposit models (MVT Pb-Zn and Carlin-type gold). Vectorized forms of input maps were converted to a raster format with a grid size of 50*50m and reclassified for production of evidential maps and using in the fuzzy logic method. A membership function was assigned to each map so that each class on the map had a value between 0 and 1. For each model, a fuzzy inference network was designed for spatial integration of evidential grid maps and generation of mineral potential maps by fuzzy operators.

Generally there are three main steps in fuzzy modeling:

(1) Spatial database generation (inputting of selected geo-exploration datasets and attribute tables in a GIS).

(2) Data processing and spatial analysis (spatial analysis of extracted features based on data model and definition of fuzzy memberships in evidential maps).

(3) Spatial integration of evidential grid maps by fuzzy operators (fuzzy AND, fuzzy OR, fuzzy algebraic product, fuzzy algebraic sum, and fuzzy gamma) for mineral potential mapping.

Table 6.1 and 6.2 show the main steps of predictive mineral potential mapping of MVT Pb-Zn and Carlin-type gold occurrences in the study area.

6.5.1 Evidence Maps

Based on selected ore deposits models, the favourable host rocks and probable heat/metal sources in proximity to the selected host rocks were extracted from the geological and geophysical data layers and weighted for generation of lithological and heat/metal source evidential maps.

Extracted structural information from the various sources (geological, geophysical and remote sensing data) was buffered and weighted based on their importance and main trends as structural evidence maps. Favourable stream sediment anomalies for each model were weighted to generate the geochemical evidence maps and hydrothermally altered rocks adjacent to the host rocks were selected, buffered and weighted as hydrothermal activity evidence maps. Four evidential maps including favourable host rocks, structural features, stream sediment geochemical anomalies, and the locations of shallow intrusive bodies adjacent to the selected host rocks as probable heat sources were used to produce a MVT Pb-Zn mineral potential map.

For generation of a Carlin-type gold mineral potential map, five evidential maps including favourable host rocks proximity to the younger felsic and felsic-intermediate intrusive bodies, structural features, stream sediment geochemical anomalies, and the locations of felsic and felsic-intermediate intrusions related to the selected host rocks as probable heat/metal sources, as well as hydrothermally altered rocks adjacent to the selected host rocks and heat/metal sources were used.

The main trends of structural features (faults and lineaments) in the various sources were obtained from the corresponding rose diagrams. These trends were selected and buffered into several zones with different widths and for each zone a distinct value based on proximity to the favourable host rocks was assigned. The evidential data layers and their processing details, map classes and fuzzy memberships are summarized in table 6.3 for MVT Pb-Zn and table 6.4 for Carlin-type gold deposit.

In these modeling, a fuzzy membership of 0.01 was used instead of nodata values, the smallest possible, which does not affect the prospectivity results but still allows these areas to be included in the analysis area (after D'ercole et al., 2000).

Tab. 6.1. Main steps of GIS modeling using fuzzy logic method for predictive mineral potential mapping of MVT Pb-Zn occurrences in the study area.

<table>
<tr><th colspan="2" rowspan="2">Main Steps</th><th colspan="4">Geo-exploration Datasets</th></tr>
<tr><th>Geological data</th><th>Geochemical data</th><th>Geophysical data</th><th>Remote Sensing data</th></tr>
<tr><td rowspan="2">Spatial Database Generation</td><td>Data gathering and pre-processing</td><td colspan="4">gathering of geo-exploration datasets based on MVT Pb-Zn deposit model and scan, georeference, coordinate system and ...</td></tr>
<tr><td>Spatial data inputting</td><td>digitize, attribute tables, data merge and …</td><td>digitize, attribute tables, data interpolate and …</td><td>digitize, attribute tables, filtering, data derivation and …</td><td>data correction (radiometric and geometric), mosaic and ...</td></tr>
<tr><td rowspan="4">Data Processing and Spatial Analysis</td><td rowspan="2">Extraction and analysis of MVT Pb-Zn deposits spatial features</td><td>favourable host rocks and main trend of structural features</td><td>favourable stream sediment anomalies</td><td>probable heat sources and main trend of structural features</td><td>main trend of regional structural features</td></tr>
<tr><td colspan="4">multiclass vector data layers are buffered, weighted (between 0 and 10), converted to grid and reclassified for generation of evidence maps</td></tr>
<tr><td>Evidential data layers generation</td><td>lithological and geological structural evidence maps</td><td>geochemical evidence map</td><td>heat source and geophysical structural evidence maps</td><td>remote sensing structural evidence map</td></tr>
<tr><td>Definition of fuzzy memberships</td><td colspan="4">multiclass evidential grid maps (fuzzy membership) are weighted based on their significance between 0 and 1</td></tr>
<tr><td rowspan="2">Generation of Mineral Prospectivity Maps by GIS Modeling</td><td>Integration of evidential maps</td><td colspan="4">integration of evidential grid maps based on inference network by fuzzy operators (fuzzy AND, fuzzy OR, fuzzy algebraic product, and fuzzy algebraic sum)</td></tr>
<tr><td>Predictive mineral potential map of MVT Pb-Zn</td><td colspan="4">using fuzzy gamma operator for integration of final evidential maps and generation of mineral potential map of MVT Pb-Zn occurrences</td></tr>
</table>

6.5.2 Integration of Evidence Maps

After each evidence map has been weighted by assigning membership functions, the input maps were combined using the fuzzy operators based on designed inference networks for each model. These maps were then combined using the fuzzy gamma operator to produce the final prospectivity mineral potential maps. The Inference networks show the integration steps of evidence maps. Selected geological (Fig 6.4), geophysical (Fig 6.5) and remote sensing (Fig 6.6) structures were buffered, weighted and integrated by fuzzy OR operator as favourable structural features map (Fig. 6.7), also geochemical stream sediment anomalies were weighted and integrated by fuzzy OR operator (favourable stream sediment anomalies map; Fig 6.8c). In the end step all favorable evidence layers (Fig. 6.8) were integrated by fuzzy gamma operator (γ =0.95).

Figure 6.3 shows the inference network for producing fuzzy predictive map of MVT Pb-Zn potential and figure 6.10 shows the places of Pb-Zn mineralization on the predictive mineral potential map of MVT Pb-Zn occurrences in the study area.

Tab. 6.1. Main steps of GIS modeling using fuzzy logic method for predictive mineral potential mapping of Carlin-type gold occurrences in the study area.

Main Steps		***Geo-exploration Datasets***			
		Geological data	***Geochemical data***	***Geophysical data***	***Remote Sensing data***
Spatial Database Generation	*Data gathering and pre-processing*	gathering of geo-exploration datasets based on Carlin-type gold deposit model and scan, georeference, coordinate system and ...			
	Spatial data inputting	digitize, attribute tables, data merge and …	digitize, attribute tables, data interpolate and …	digitize, attribute tables, filtering, data derivation and …	data correction (radiometric and geometric), mosaic and ...
Data Processing and Spatial Analysis	*Extraction and analysis of Carlin-type gold deposits spatial features*	favourable host rocks, probable heat/metal sources and main trend of structural features	favourable stream sediment anomalies	probable heat/metal sources and main trend of structural features	hydrothermally altered rocks and main trend of regional structural features
		multiclass vector data layers are buffered, weighted (between 0 and 10), converted to grid and reclassified for generation of evidence maps			
	Evidential data layers generation	lithological, heat/metal source and geological structural evidence maps	geochemical evidence map	heat/metal source and geophysical structural evidence maps	hydrothermal activity and remote sensing structural evidence map
	Definition of fuzzy memberships	multiclass evidential grid maps (fuzzy membership) are weighted based on their significance between 0 and 1			
Generation of Mineral Prospectivity Maps by GIS Modeling	*Integration of evidential maps*	integration of evidential grid maps based on inference network by fuzzy operators (fuzzy AND, fuzzy OR, fuzzy algebraic product, and fuzzy algebraic sum)			
	Predictive mineral potential map of Carlin-type gold	using fuzzy gamma operator for integration of final evidential maps and generation of mineral potential map of Carlin-type gold occurrences			

Tab. 6.3. Fuzzy membership values for evidential maps of MVT Pb-Zn model.

Factor	*Map class*	*Fuzzy Membership*
Geological Data		
-Evidential Map of Lithology (as favourable host rocks):		
Dolomitic limestone	1	0.99
Dolomite	2	0.90
Limestone	3	0.85
Limestone and Marble	4	0.80
Marble and Schist	5	0.75
Shaly limestone	6	0.65
Recrystallized limestone	7	0.55
Sandy or Marly limestone	8	0.45
-Evidential Map of Buffered Distances from Geological Structures:		
Proximity to thrust faults, NW-SE trend, 0-1000 m	1	0.9
Proximity to thrust faults, NW-SE trend, 1000-2000 m	2	0.7
Proximity to thrust faults, NW-SE trend, 2000-3000 m	3	0.5
Proximity to major faults, NW-SE and NE-SW trends, 0-500 m	1	0.9
Proximity to major faults, NW-SE and NE-SW trends, 500-1000 m	2	0.7
Proximity to major faults, NW-SE and NE-SW trends, 1000-1500 m	3	0.5
Proximity to major faults, N-S and W-E trends, 0-500 m	1	0.7
Proximity to major faults, N-S and W-E trends, 500-1000 m	2	0.5
Proximity to major faults, N-S and W-E trends, 1000-1500 m	3	0.3
Proximity to minor faults, 0-500 m	1	0.5
Geochemical Data		
-Evidential Map of Stream Sediment Anomalies:		
Stream sediment anomalies of Zn and Pb	1	1.0
Stream sediment anomalies of As and Cu	2	0.8
Stream sediment anomalies of Ag, Cd, Mo, Ni and Co	3	0.5
Stream sediment anomalies of B	4	0.3
Stream sediment anomalies of Sb	5	0.2
Geophysical Data		
-Evidential Map of Intrusive Shallow Bodies (as probable heat sources)	1	0.5
-Evidential Map of Buffered Distances from Geophysical Structures:		
Proximity to lineaments, 0-1000 m	1	0.9
Proximity to lineaments, 1000-2000 m	2	0.7
Proximity to lineaments, 2000-3000 m	3	0.5
Proximity to circular structures, 0-1000 m	1	0.7
Proximity to circular structures, 1000-2000 m	2	0.5
Proximity to circular structures, 2000-3000 m	3	0.3
Remote Sensing Data		
-Evidential Map of Buffered Distances from Remote Sensing Structures:		
Proximity to lineaments, NW-SE trend, 0-500 m	1	0.9
Proximity to lineaments, NW-SE trend, 500-1000 m	2	0.7
Proximity to lineaments, NW-SE trend, 1000-1500 m	3	0.5
Proximity to lineaments, NE-SW trend, 0-500 m	1	0.7
Proximity to lineaments, NE-SW trend, 500-1000 m	2	0.5
Proximity to lineaments, NE-SW trend, 1000-1500 m	3	0.3
Proximity to circular structures, 0-1000 m	1	0.7
Proximity to circular structures, 1000-2000 m	2	0.5
Proximity to circular structures, 2000-3000 m	3	0.3

Tab. 6.4. Fuzzy membership values for evidential maps of Carlin-type gold model.

Factor	***Map class***	***Fuzzy membership***
Geological Data		
-Evidential Map of Lithology (as favourable host rocks):		
Dolomitic Limestone	1	0.99
Dolomite and Limestone	2	0.90
Dolomite, Shale	3	0.85
Limestone	4	0.80
Crystalline Limestone, Marly or Sandy limestone	5	0.70
Marble	6	0.60
-Evidential Map of Buffered Distances from Felsic Intrusive Bodies Adjacent to the Older Favourable Host Rocks (as probable heat/metal sources):		
Proximity to Intrusive Body, 0-250 m	1	0.90
Proximity to Intrusive Body, 250-500 m	2	0.80
Proximity to Intrusive Body, 500-750 m	3	0.70
Proximity to Intrusive Body, 7500-1000 m	4	0.60
-Evidential Map of Buffered Distances from Geological Structures:		
Proximity to thrust faults, NW-SE trend, 0-1000 m	1	0.9
Proximity to thrust faults, NW-SE trend, 1000-2000 m	2	0.7
Proximity to thrust faults, NW-SE trend, 2000-3000 m	3	0.5
Proximity to major faults, NW-SE and NE-SW trends, 0-500 m	1	0.9
Proximity to major faults, NW-SE and NE-SW trends, 500-1000 m	2	0.7
Proximity to major faults, NW-SE and NE-SW trends, 1000-1500 m	3	0.5
Proximity to major faults, N-S and W-E trends, 0-500 m	1	0.7
Proximity to major faults, N-S and W-E trends, 500-1000 m	2	0.5
Proximity to major faults, N-S and W-E trends, 1000-1500 m	3	0.3
Proximity to minor faults, 0-500 m	1	0.5
Geochemical Data		
-Evidential Map of Stream Sediment Anomalies:		
Stream Sediment Anomaly of Au	1	1.0
Stream Sediment Anomaly of Ag	2	0.90
Stream Sediment Anomaly of As, Hg, Sb and W	3	0.80
Stream Sediment Anomaly of Ba	4	0.50
Stream Sediment Anomaly of Mo	5	0.40
Geophysical Data		
-Evidential Map of Felsic Intrusive Shallow Bodies Adjacent to the Selected Host Rocks (as probable heat/metal sources)	1	0.50
-Evidential Map of Buffered Distances from Geophysical Structures:		
Proximity to Lineament, 0-500 m	1	0.80
Proximity to Lineament, 500-1000 m	2	0.70
Proximity to Lineament, 1000-1500 m	3	0.60
Proximity to Ring Structure, 0-500 m	1	0.70
Proximity to Ring Structure, 500-1000 m	2	0.60
Proximity to Ring Structure, 1000-1500 m	3	0.50
Remote Sensing Data		
-Evidential Map of Buffered Distances from Remote Sensing Structures:		
Proximity to lineaments, NW-SE trend, 0-500 m	1	0.9
Proximity to lineaments, NW-SE trend, 500-1000 m	2	0.7
Proximity to lineaments, NW-SE trend, 1000-1500 m	3	0.5
Proximity to lineaments, NE-SW trend, 0-500 m	1	0.7
Proximity to lineaments, NE-SW trend, 500-1000 m	2	0.5
Proximity to lineaments, NE-SW trend, 1000-1500 m	3	0.3
Proximity to circular structures, 0-1000 m	1	0.7
Proximity to circular structures, 1000-2000 m	2	0.5

Proximity to circular structures, 2000-3000 m	3	0.3
-Evidential Map of Buffered Distances from Hydrothermally Altered Rocks Adjacent to the Selected Host Rocks and Heat/Metal Sources:		
Proximity to Argillic Alteration, 0-250 m	1	0.80
Proximity to Argillic Alteration, 250-500 m	2	0.70
Proximity to Argillic Alteration, 500-750 m	3	0.60
Proximity to Argillic Alteration, 750-1000 m	4	0.50
Proximity to Sericitic Alteration, 0-250 m	1	0.60
Proximity to Sericitic Alteration, 250-500 m	2	0.50
Proximity to Argillic-Sericitic Alteration, 0-250 m	1	0.70
Proximity to Argillic-Sericitic Alteration, 250-500 m	2	0.60

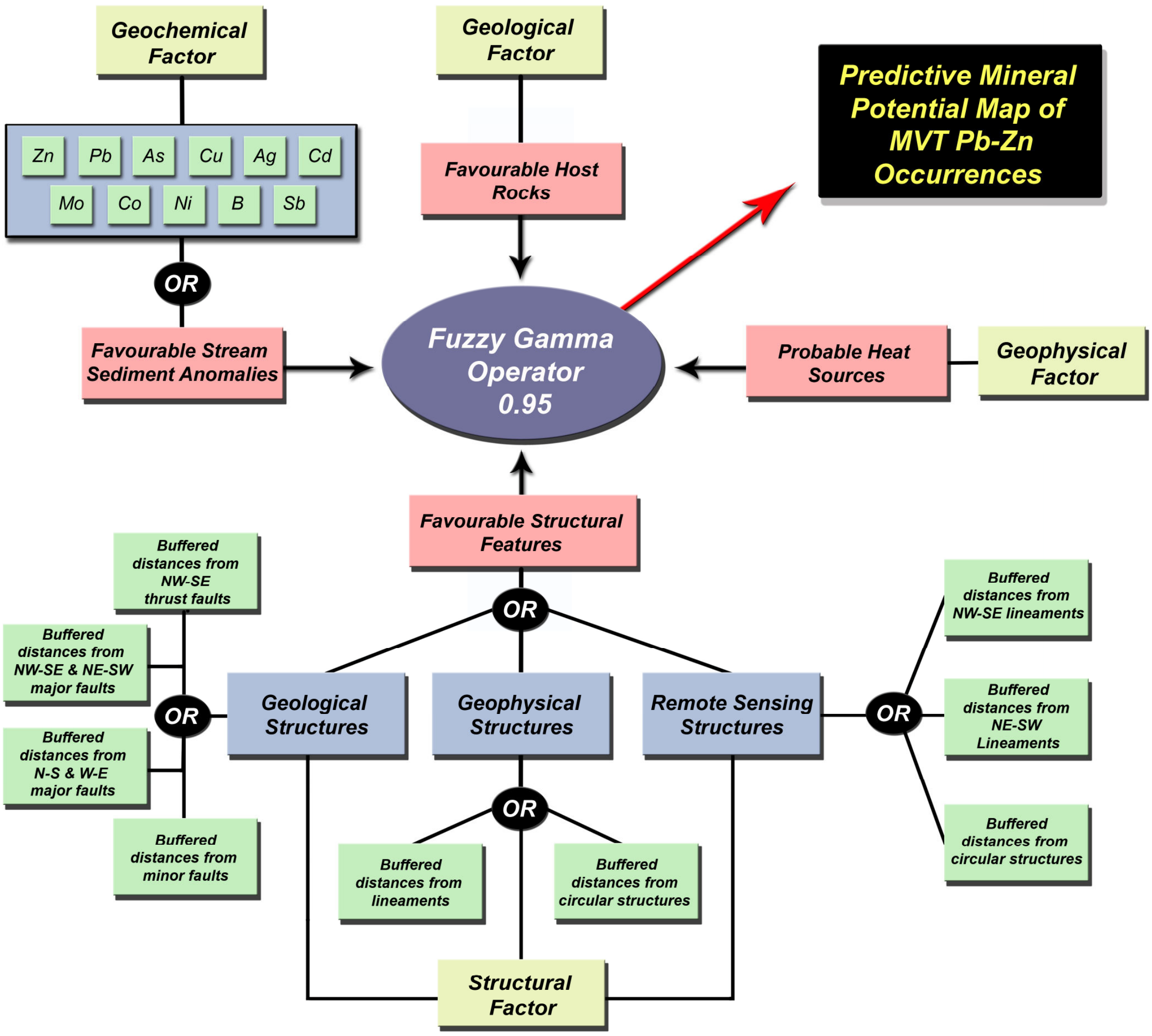

Fig.6.3 Inference network for producing fuzzy predictive map of MVT Pb-Zn potential in the study area.

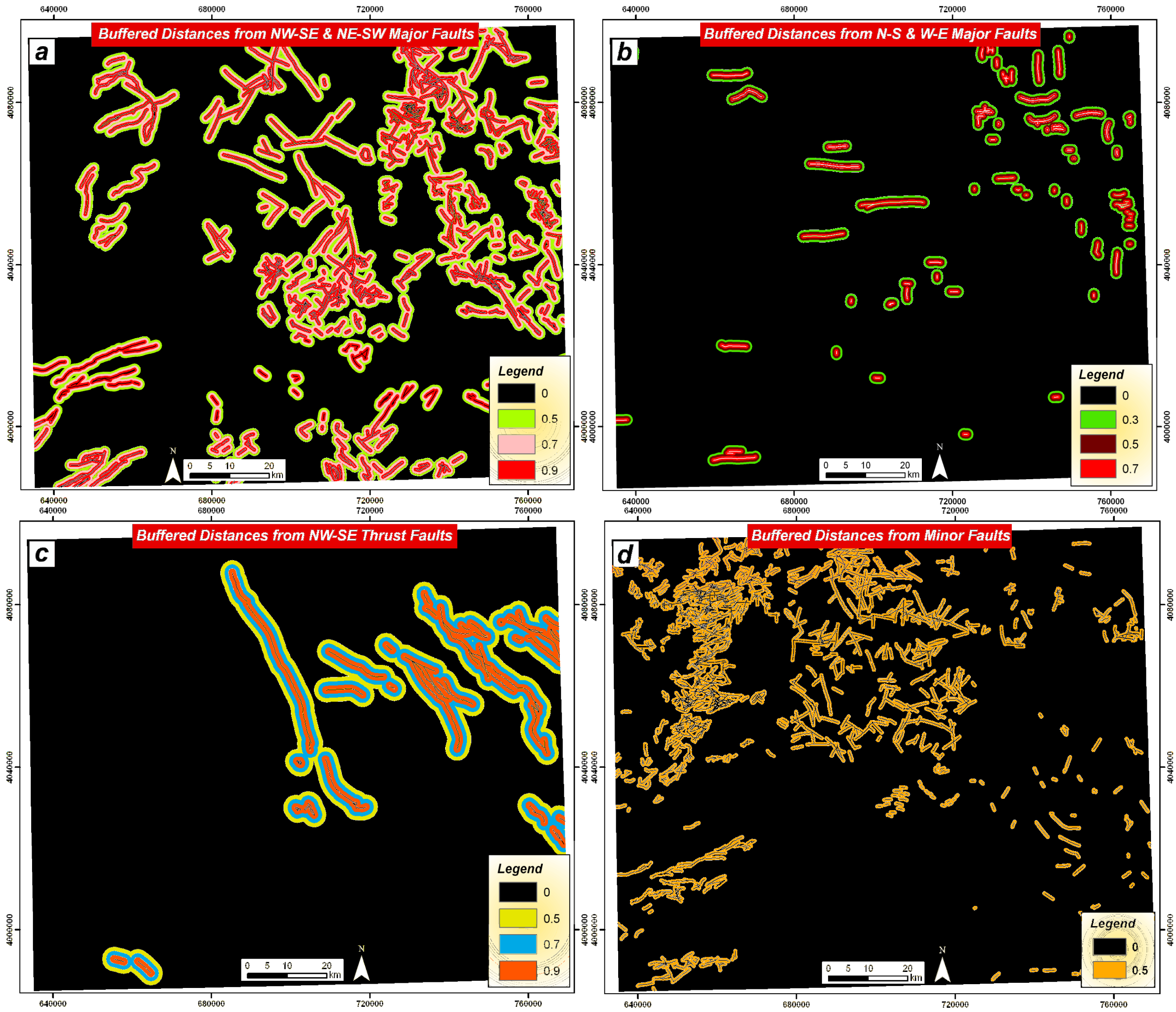

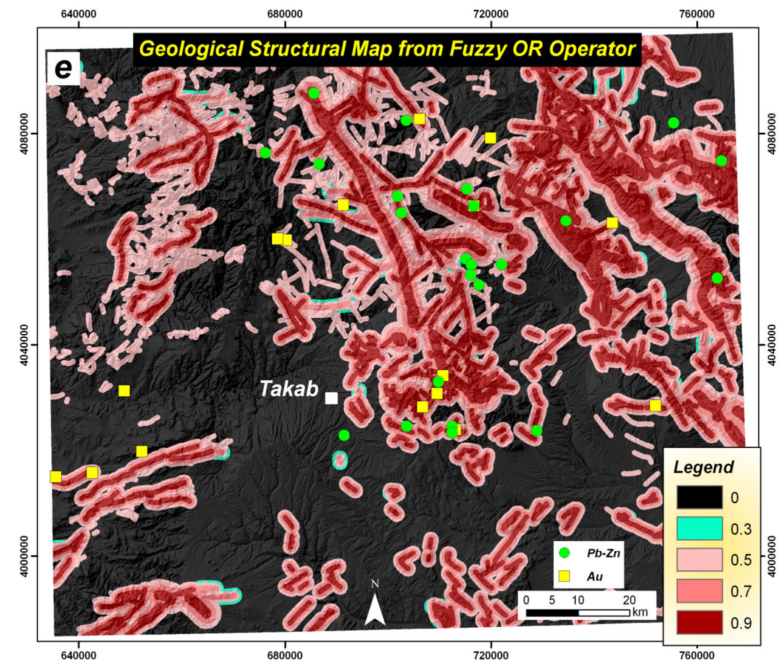

Fig. 6.4 **a** Buffered distances from NW-SE and NE-SW major faults; **b** Buffered distances from N-S and W-E major faults; **c** Buffered distances from NW-SE thrust faults; **d** Buffered distances from minor faults and **e** Geological structural map from fuzzy OR operator and the places of lead-zinc (Pb-Zn) and gold (Au) occurrences.

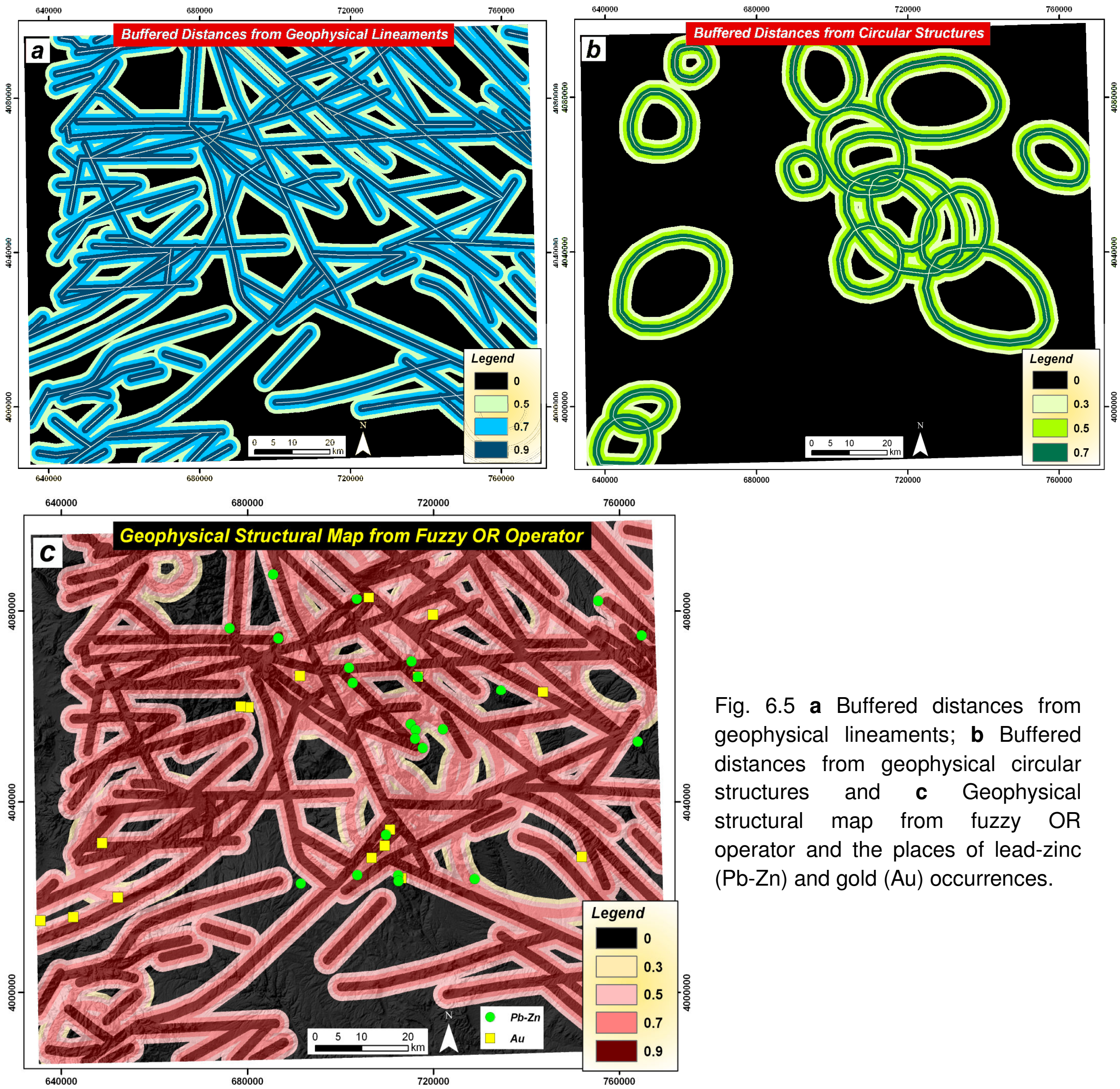

Fig. 6.5 **a** Buffered distances from geophysical lineaments; **b** Buffered distances from geophysical circular structures and **c** Geophysical structural map from fuzzy OR operator and the places of lead-zinc (Pb-Zn) and gold (Au) occurrences.

The predictive mineral potential maps were classified based on plotting the predictive classification value versus cumulative percent area curves (after Porwal et al., 2004). Inflection point of each curve shows the boundary of high and low favorability areas of mineral potential maps in corresponding deposit models.

The inflection point value for fuzzy mineral potential map of MVT Pb-Zn occurrences is 0.61 (Fig. 6.9) and for Carlin-type gold occurrences is 0.51 (Fig. 6.13). The values of high favourability area in MVT Pb-Zn potential map are between 0.61 and 0.96 that were classified in seven priorities and values less than 0.61 are low favorability area (Fig. 6.10). The values of high favourability area for Carlin-type gold potential map are between 0.51 and 0.95 and less than 0.51 are low favourability area (Fig. 6.14) also high favourability values of Carlin-type gold potential map were classified in seven priorities.

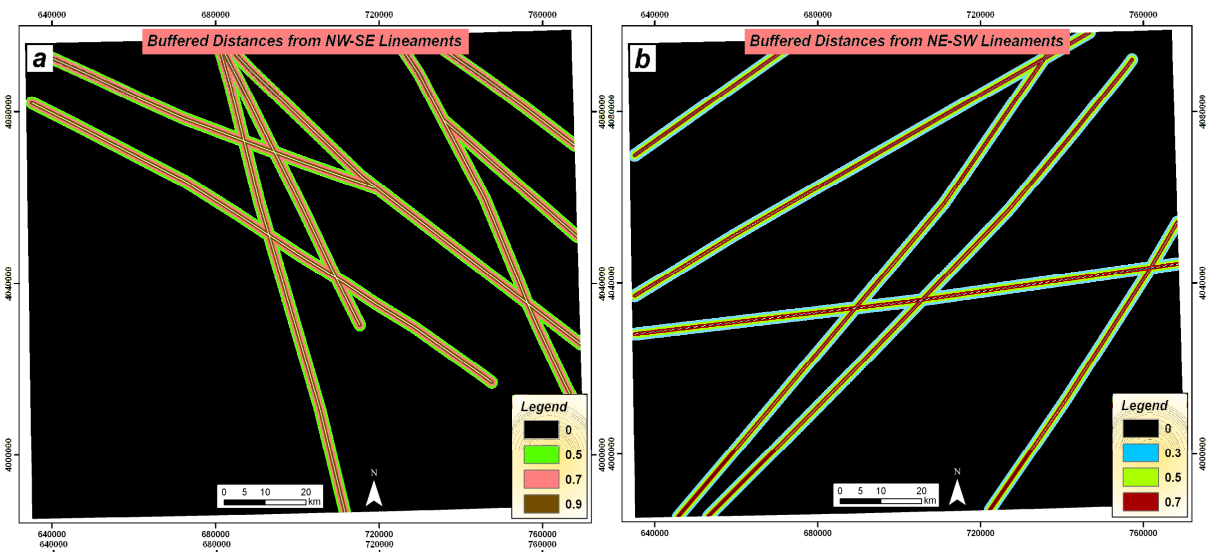

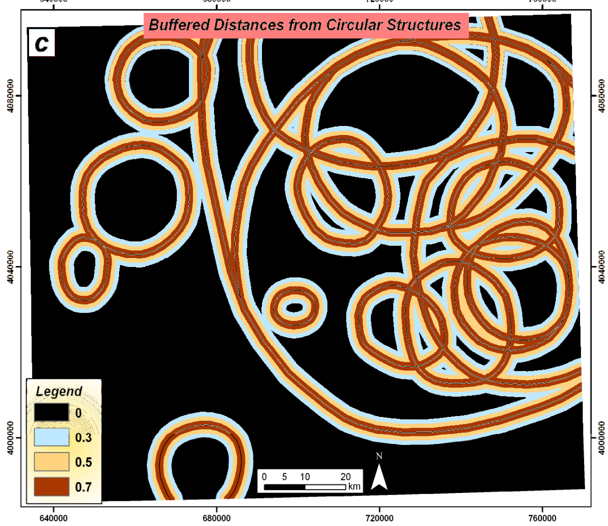

Fig. 6.6 **a** Buffered distances from NW-SE remote sensing lineaments; **b** Buffered distances from remote sensing NE-SW lineaments; **c** Buffered distances from remote sensing circular structures and **d** Remote sensing structural map from fuzzy OR operator and the places of lead-zinc (Pb-Zn) and gold (Au) occurrences.

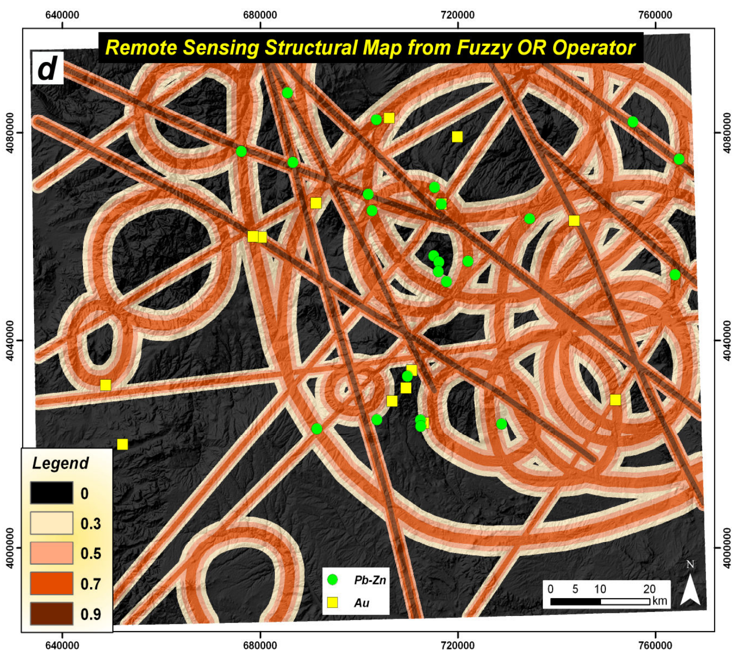

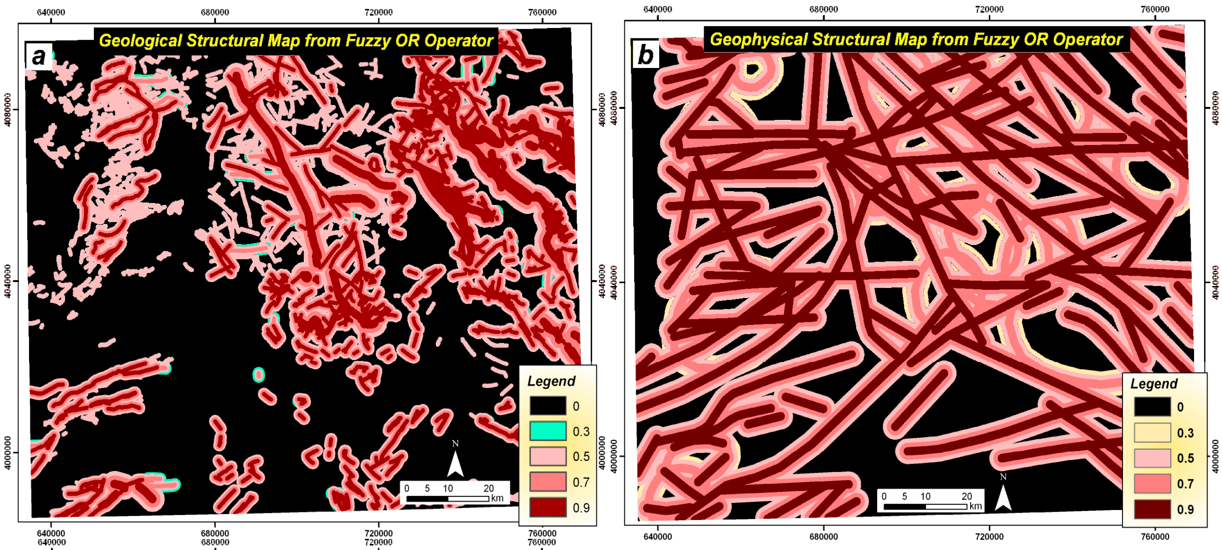

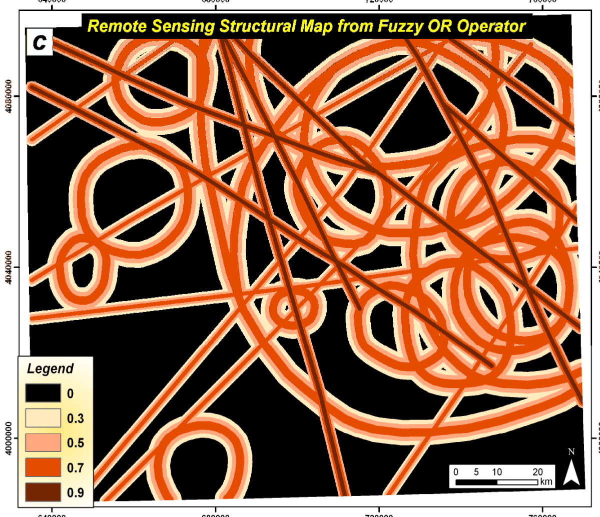

Fig. 6.7 **a** Geological structural map from fuzzy OR operator; **b** Geophysical structural map from fuzzy OR operator; **c** Remote sensing structural map from fuzzy OR operator and **d** Favourable structural features map from fuzzy OR operator (integration of geological, geophysical and remote sensing structures).

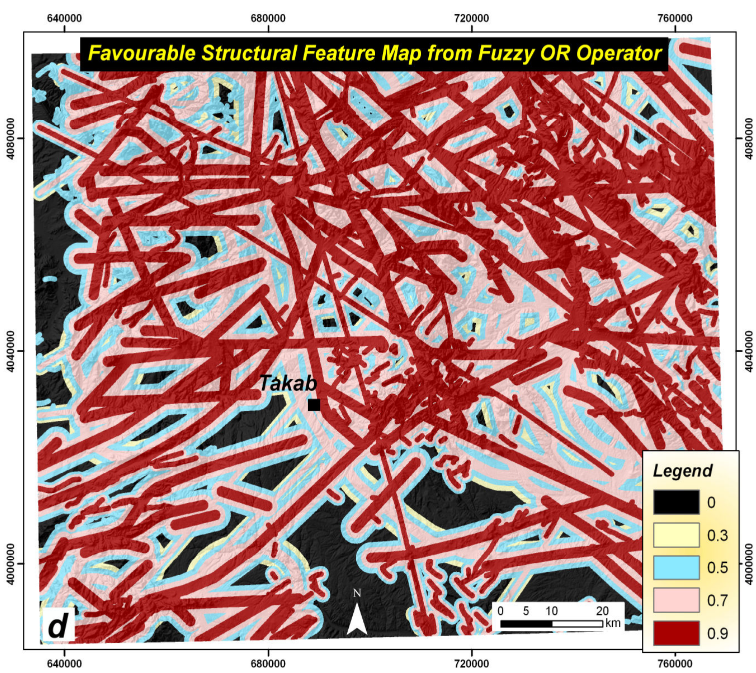

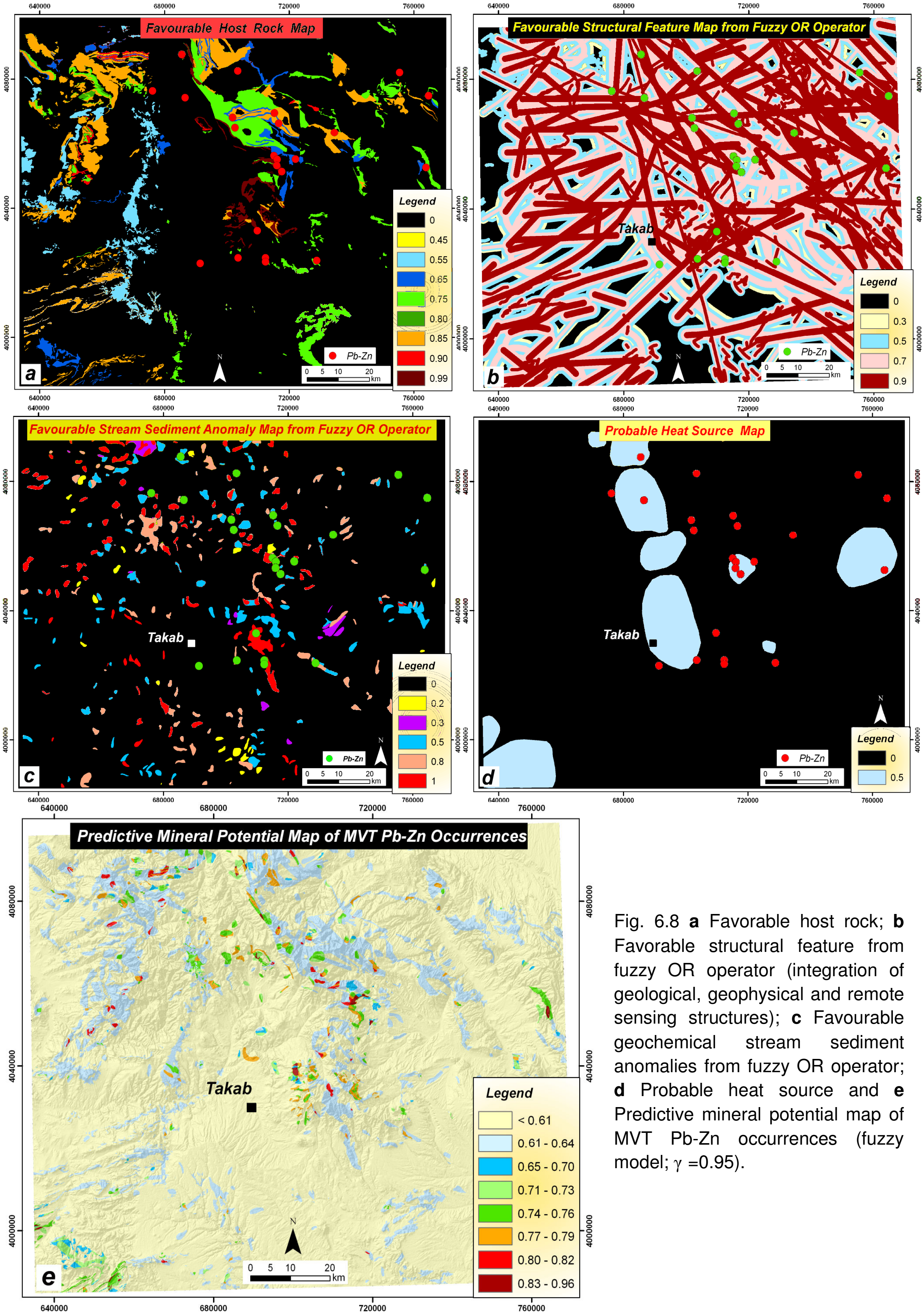

Fig. 6.8 **a** Favorable host rock; **b** Favorable structural feature from fuzzy OR operator (integration of geological, geophysical and remote sensing structures); **c** Favourable geochemical stream sediment anomalies from fuzzy OR operator; **d** Probable heat source and **e** Predictive mineral potential map of MVT Pb-Zn occurrences (fuzzy model; γ =0.95).

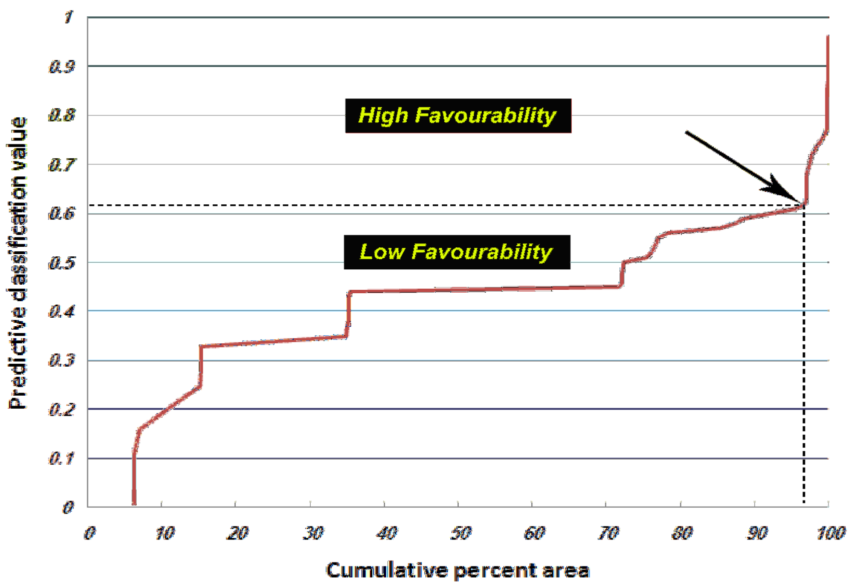

Fig. 6.9 Variation of predictive classification values with cumulative percent area for MVT Pb-Zn occurrences. Inflection point (marked by arrow) corresponds to threshold value used for generating binary favourability map.

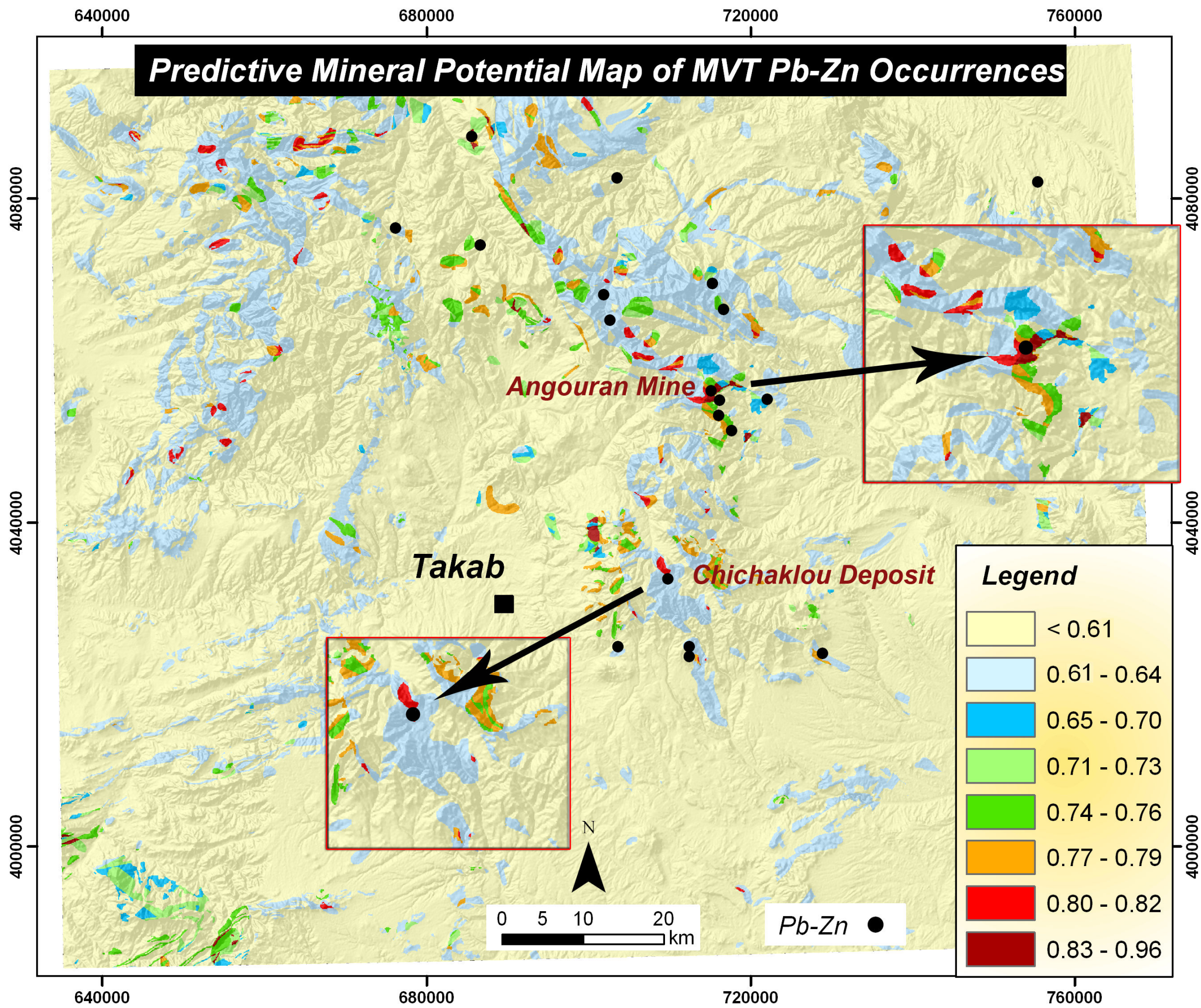

Fig. 6.10 Predictive mineral potential map of MVT Pb-Zn occurrences (fuzzy model; γ =0.95) and the places of lead-zinc (Pb-Zn) occurrences.

Any good integration for each model should be able to predict the area covering the known mineralization as regions with high score or else the validity of model results is questionable (Daneshfar et al., 2006). The predictive mineral potential map of MVT Pb-Zn in the study area highlights the places of known MVT deposits as well as new areas. This GIS study shows that the predictive mineral potential map of MVT Pb-Zn provides the best evidence for predicting the known deposits in the Takab district. Angouran mine and Chichaklou Pb-Zn deposit are two major of carbonate hosted Pb-Zn mineralization in the study area that locate in the high priority of the predictive mineral potential map (Fig 6.10). This prospectivity map shows the potential for exploration of unknown MVT Pb-Zn deposits in this area.

Figure 6.11 shows the inference network for producing fuzzy predictive map of Carlin-type gold potential based on integration of five favourable evidential maps. Figure 6.12 shows the evidential maps (a-e) and predictive mineral potential map of Carlin-type gold occurrences (f) in the Takab area and figure 6.14 shows the places of gold mineralization on the mineral potential map of Carlin-type gold occurrences. Zarshouran and Aqdarreh gold mines are two major of carbonate hosted Au mineralization in the Takab district that locate in the high priority of the predictive mineral potential map of Carlin-type gold occurrences (Fig 6.14).

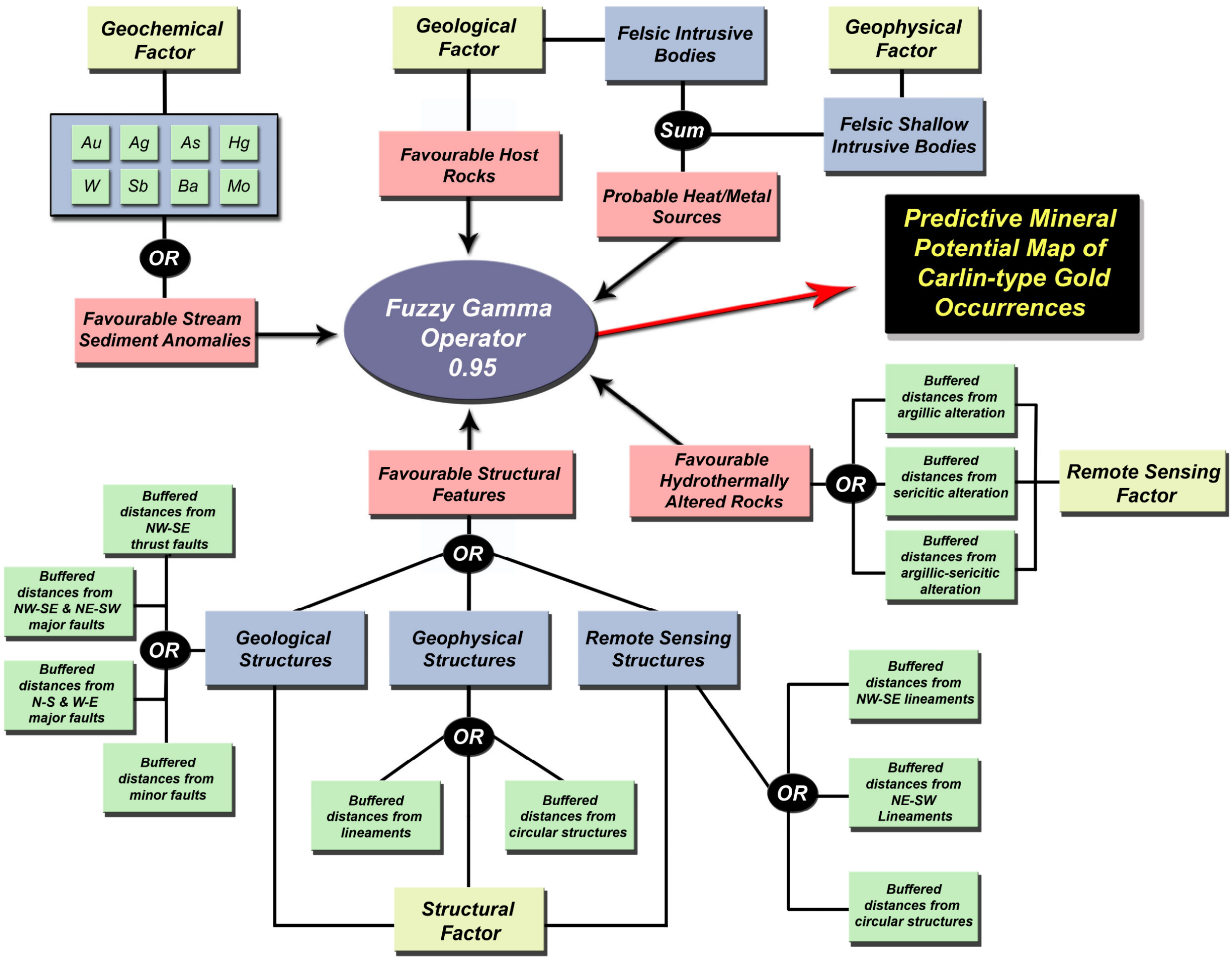

Fig. 6.11 Inference network for producing fuzzy predictive map of Carlin-type gold potential in the study area.

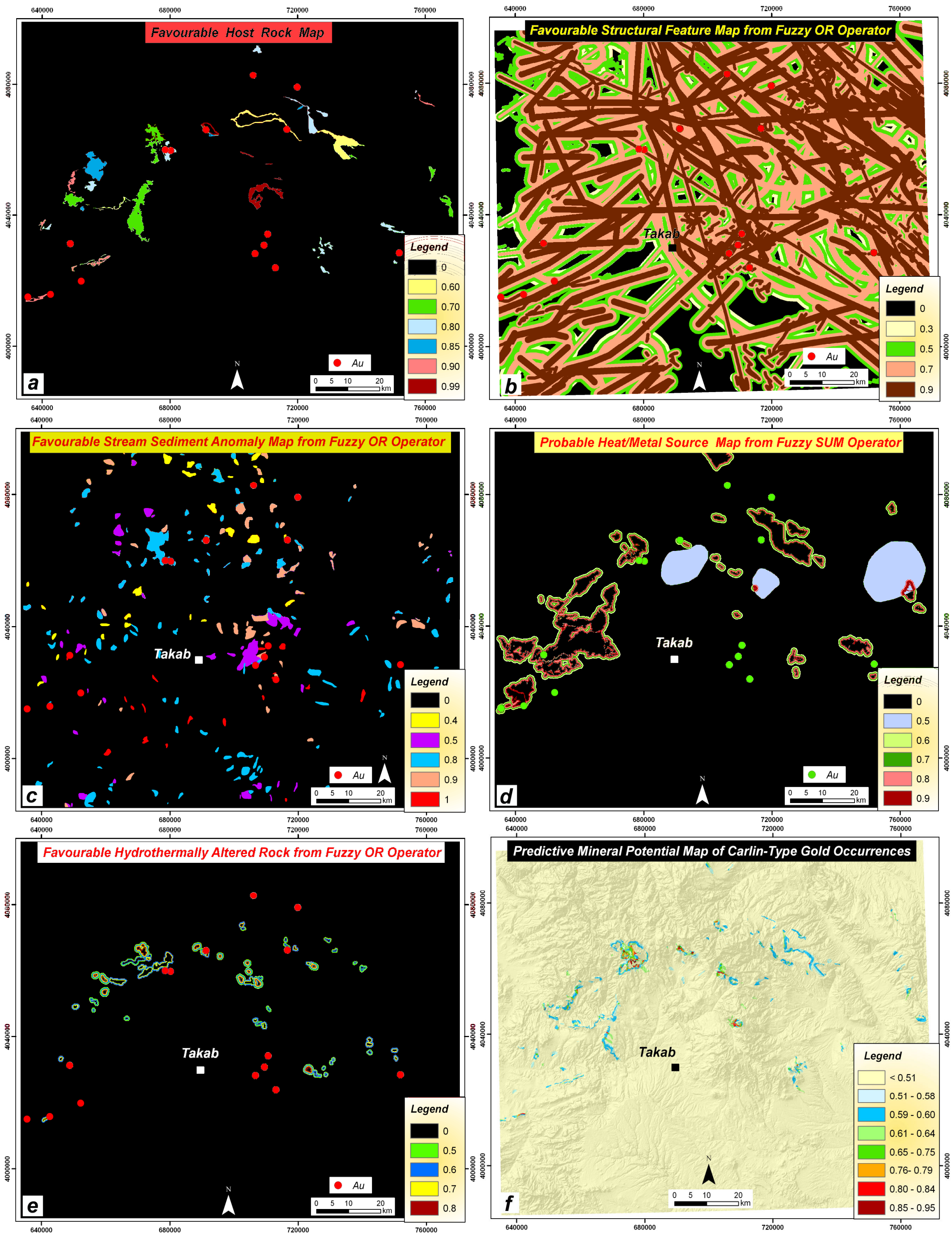

Fig. 6.12 **a** Favorable host rock; **b** Favorable structural feature from fuzzy OR operator (integration of geological, geophysical and remote sensing structures); **c** Favourable geochemical stream sediment anomalies from fuzzy OR operator; **d** Probable heat/metal source from fuzzy OR operator; **e** Favourable hydrothermally altered rock from fuzzy OR operator and **f** Predictive mineral potential map of Carlin-type gold occurrences (fuzzy model; γ =0.95).

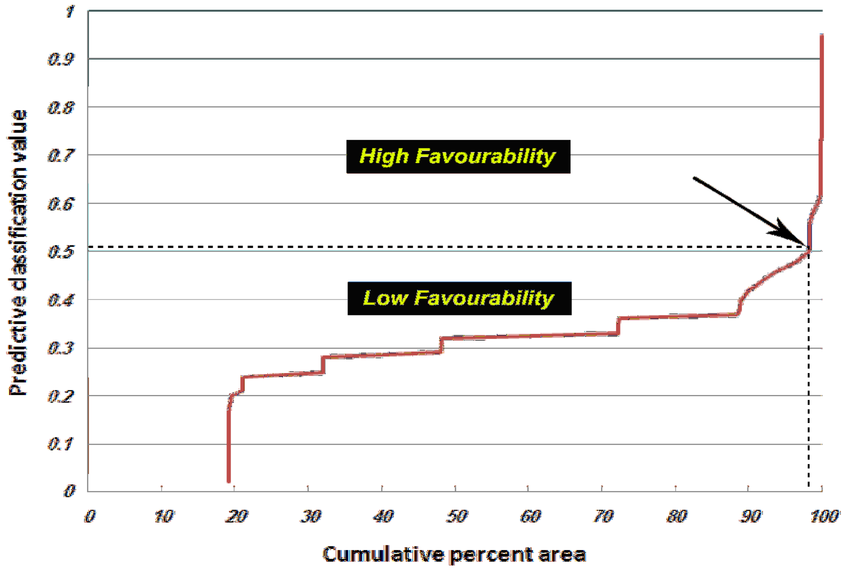

Fig. 6.13 Variation of predictive classification values with cumulative percent area for Carlin-type gold occurrences. Inflection point (marked by arrow) corresponds to threshold value used for generating binary favourability map.

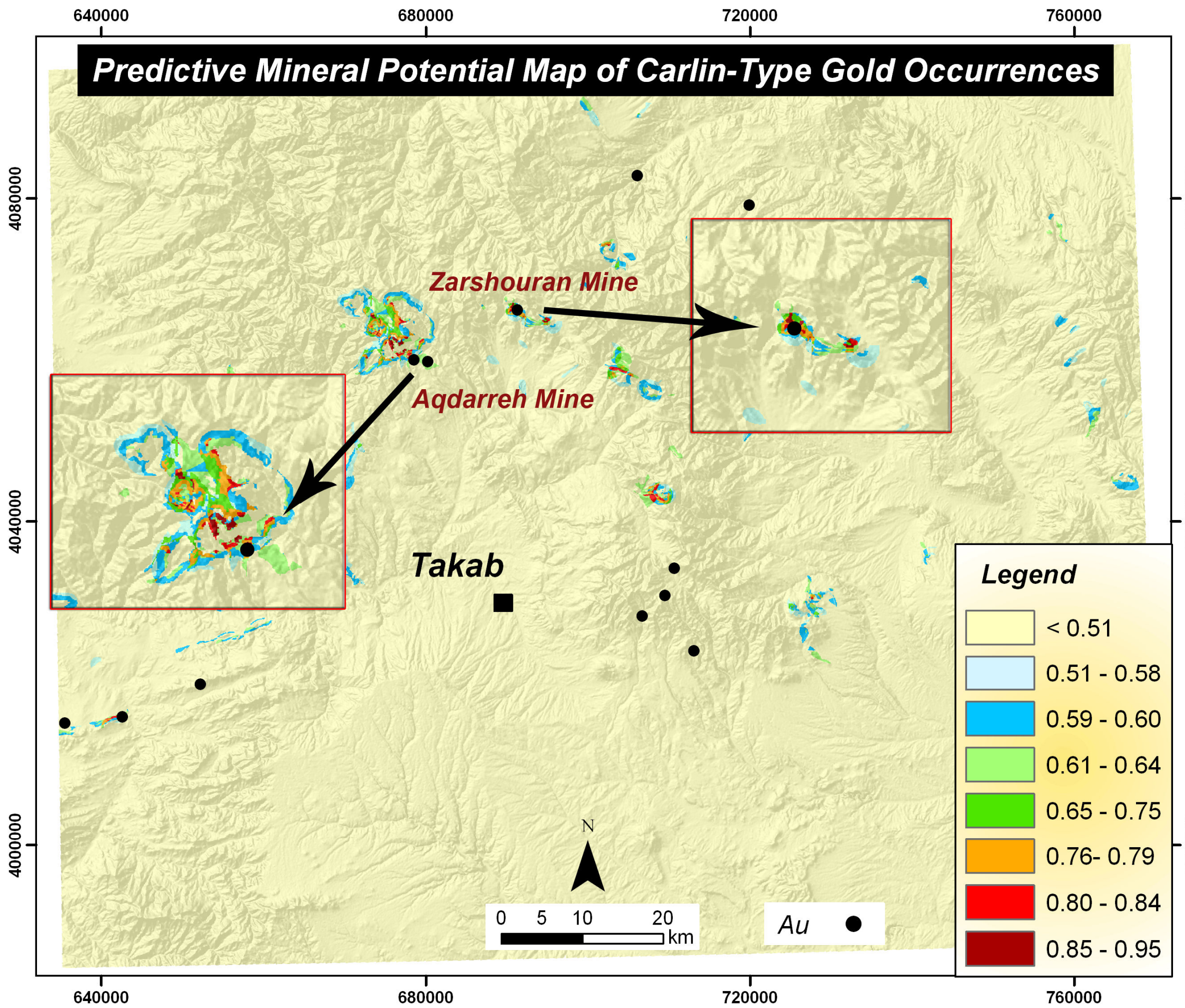

Fig. 6.14 Predictive mineral potential map of Carlin-type gold occurrences (fuzzy model; γ =0.95) and the places of gold (Au) occurrences.

6.6 Mineral Potential Mapping by Index Overlay Method

In the index overlay method, each data layer to be used as evidence map is assigned a different score (weight), as well as the map themselves are receiving different weight (Bonham-carter, 1994) depending on the exploration models. The weight can be calculated statistically depending on the number of input mineral occurrences and its relationship with a particular element or object on a map. Otherwise, weight can be calculated on the basis of relative importance of elements/objects on the input and evidential maps by mineral deposit experts (as expected in knowledge driven approach) (Mukhopadhyay et al., 2002).

For the study area, we applied the same data layers (evidence maps) of the fuzzy logic modeling of MVT Pb-Zn and Carlin-type gold occurrences but classified the scores between 1 and 10 and integrated based on equation 6.6. The predictive mineral potential maps of MVT Pb-Zn and Carlin-type gold occurrences are shown in figures 6.15 and 6.16.

6.7 Conclusions

Knowledge-driven fuzzy logic is an appropriate methodology for dealing with regional-scale databases and is a flexible method for geologist to use different integrations with several evidential layers and generate predictive mineral potential maps based on deposits models. The design of the fuzzy inference network to combine the evidence layers for mapping mineral potential must be based upon the knowledge of the genesis or mode of formation of known mineralization in study area. The inference networks of predictive mineral potential maps reflect the main process used by exploration and GIS experts.

The data layers were combined with the gamma operator using γ =0.95 to produce the final prospectivity map and indicated areas of known MVT Pb-Zn and Carlin-type gold mineralization as well as new targets in the study area. The fuzzy mineral potential maps of MVT Pb-Zn and Carlin-type gold occurrences show that the high favorability zones respectively occupy 8.12% and 1.87% of the study area also 91.88% of MVT Pb-Zn potential map and 98.13% of Carlin-type gold potential map lie in the low favorability zones.

Fuzzy logic and index overlay method comparison indicates some differences in the patterns but almost all of the most important deposits in the district are predicted satisfactorily (Carbonate hosted Pb-Zn: Angouran and Chichaklou deposits and Carbonate hosted gold: Zarshouran and Aqdarreh deposits).

High probability areas in both models show differences in absolute values, according to the method, but generally predict the same regions. Additionally, there are several priorities for two types of mineralization in the predictive mineral potential maps that can be considered in new explorations.

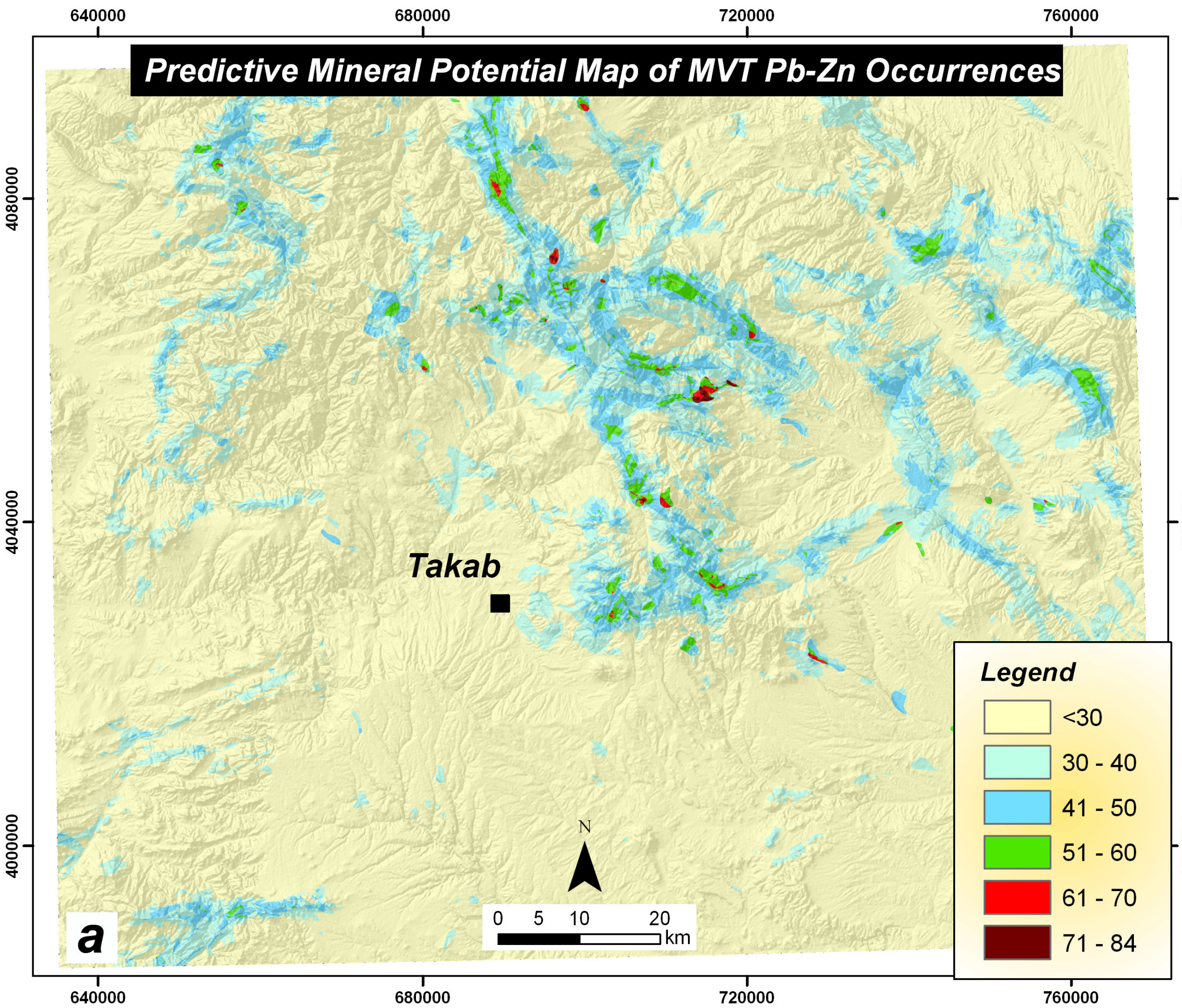

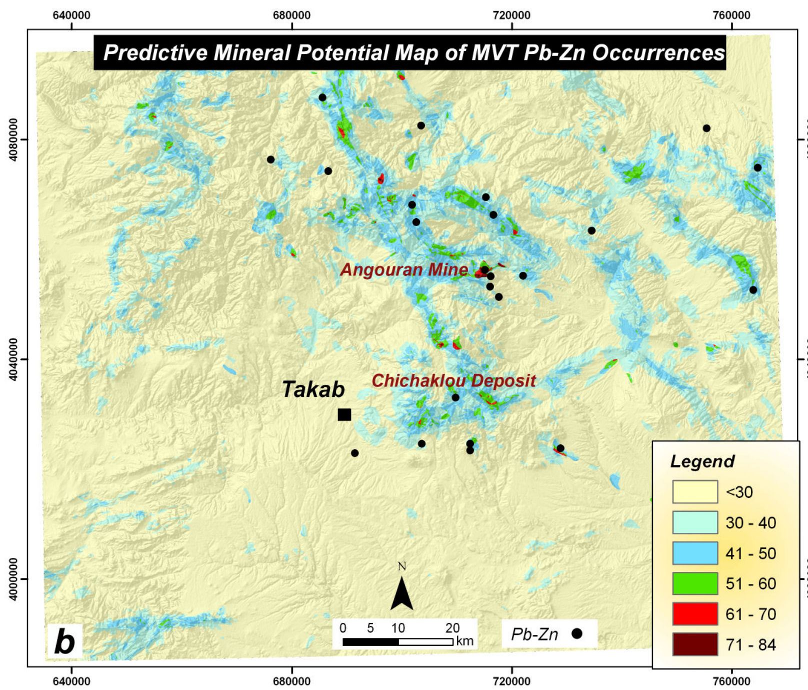

Fig. 6.15 **a** Predictive mineral potential map of MVT Pb-Zn occurrences (index overlay model) and **b** the places of lead-zinc (Pb-Zn) occurrences on the predictive mineral potential map.

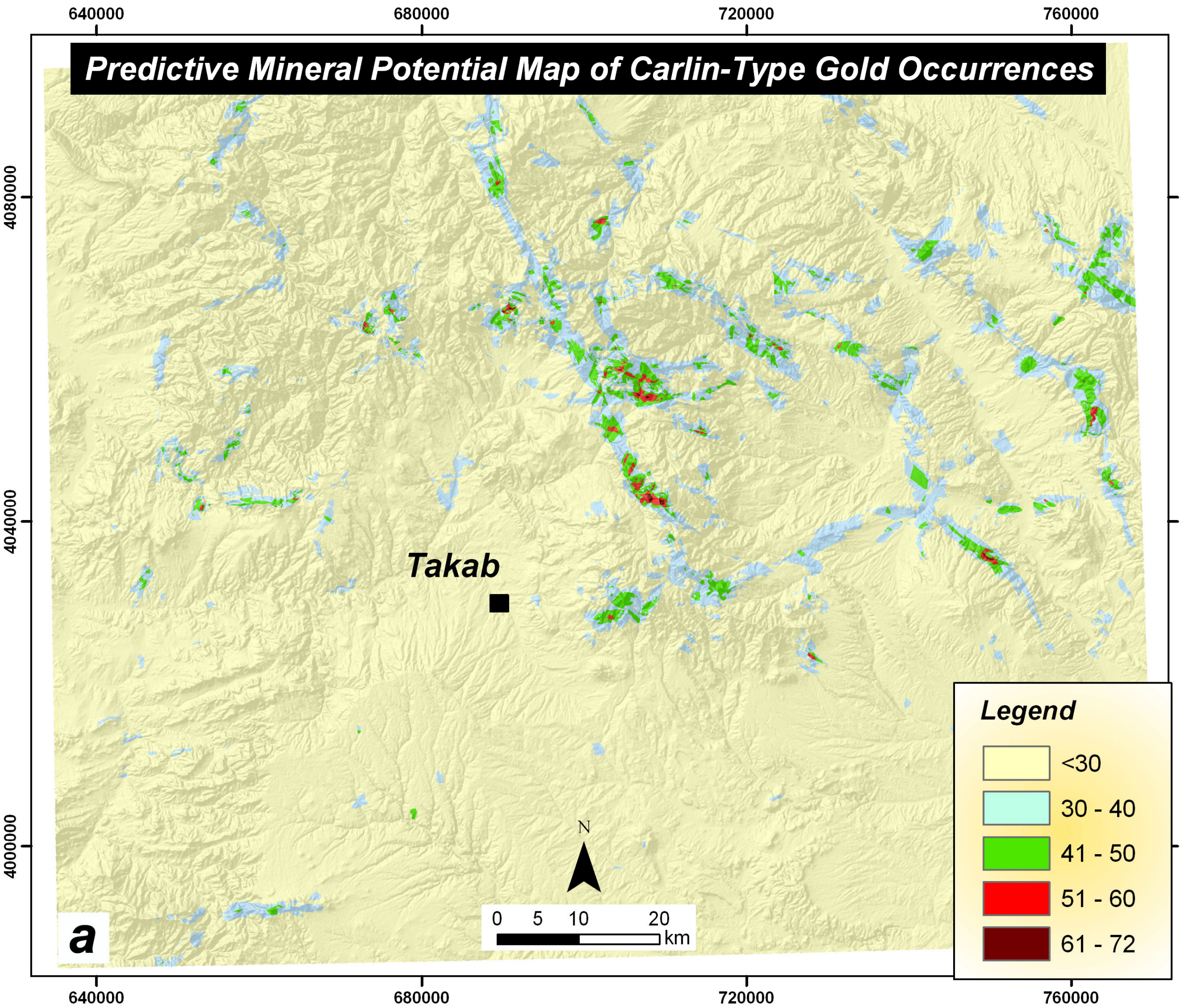

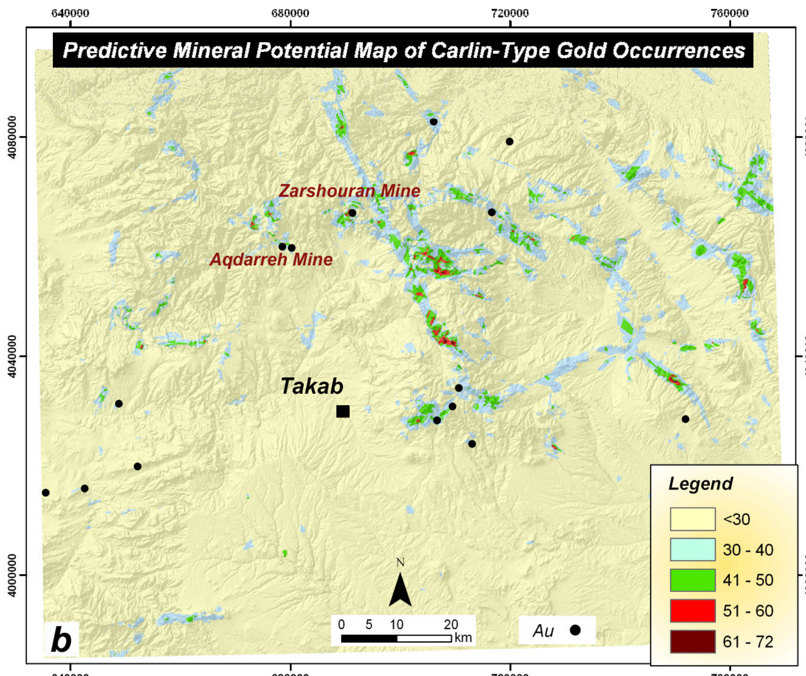

Fig. 6.16 **a** Predictive mineral potential map of Carlin-type gold occurrences (index overlay model) and **b** the places of gold (Au) occurrences on the predictive mineral potential map.

Chapter 7 Fieldwork and Characteristics of Prospecting Areas

7.1 Introduction

A mineral occurrence database was compiled from various available sources. Principally these data were extracted from the National Geosciences Database of Iran (NGDIR; Geological Survey of Iran) as well as the 1:250.000 and 1:100.000 scale geology maps covering the study area. Additionally mineral occurrences were also digitized from the reports, student researches (thesis) and articles that published by the GSI, universities and … about this region. Fieldwork in the study area was carried out in several steps. In order to optimize the GIS modeling results, some field trips were initiated to investigate the primary data layers.

There were two primary objectives of the field program. One was to collect information on the economic mineral potential in the study area. The other was to check identified remote sensing alteration zones, geochemical anomalies and rock units related to our selected models to gather new data. The latter information was used to optimize mineral potential mapping.

7.2 Exploration Targets in the Study Area

More of 22 target areas that were identified in the predictive mineral potential maps (Fuzzy logic method; Chapter 6) for MVT Pb-Zn (12 target areas; Fig. 7.1 & 7.2) and Carlin-type gold (10 target areas; Fig. 7.3 &7.4) mineralization have been field-checked in a combination of geology rock units, geochemical anomalies, remote sensing and geophysical results in GIS modeling. Systematic follow up of these targets generally consisted of a number of prospecting traverses across some of the high and medium grade areas of favourable areas with rock and soil samples taken where appropriate.

A total of 144 rock and soil samples were collected for chemical analysis, petrography and mineralography studying (Fig. 7.5; analysis results attached in appendices).

Some of these samples had been taken in an exploration project of Angouran type Zn-Pb mineralization in 4000 km^2 around of Angouran Mine (Fonoudi and Sadeghi, 2001). Figure of some of sampling places attached in appendices.

7.2.1 Mississippi Valley Type Pb-Zn Target Areas

There were several possibilities for combination of fuzzy operations to integrate the fuzzy evidential maps and produce a mineral potential map of MVT Pb-Zn mineralization. Various inference networks were applied to derive the best final predictive map. The predictive mineral potential map resulting from the inference network shown in figure 6.3 was selected as a favourable predictive map for field checking of MVT Pb-Zn target areas. Figure 7.1 and 7.2 show 12 target areas of MVT Pb-Zn potential on the fuzzy mineral potential map Landsat 7 ETM^+ image.

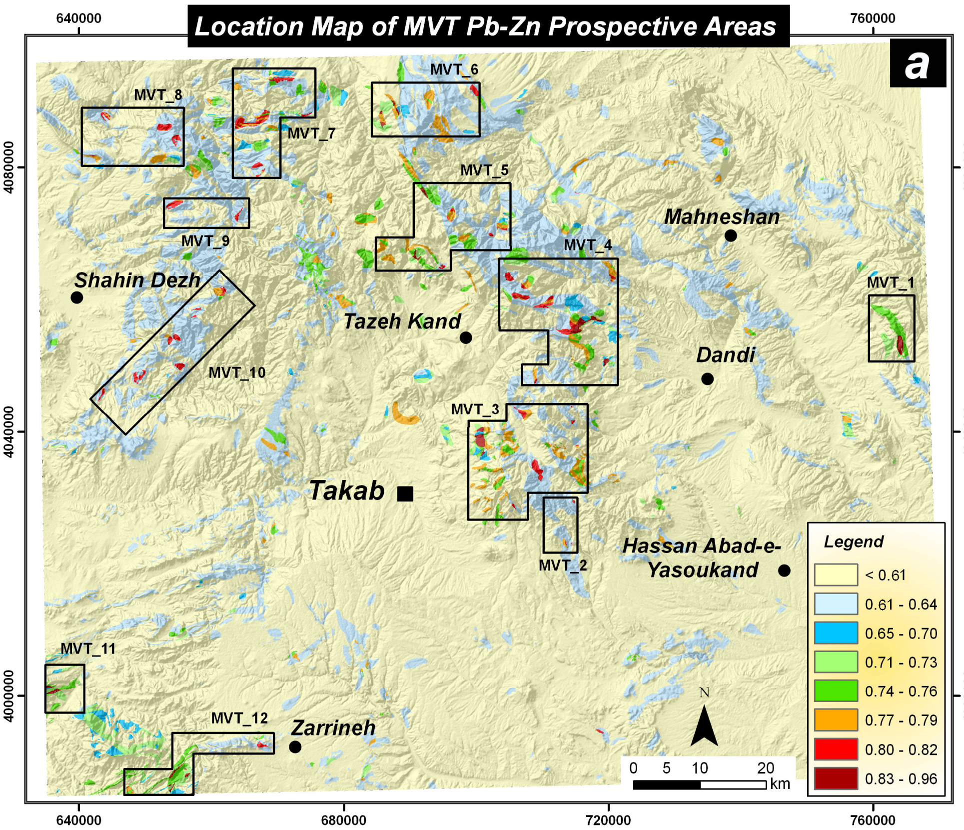

Fig. 7.1 Location map of MVT Pb-Zn prospective areas on the mineral potential map (Fuzzy logic method).

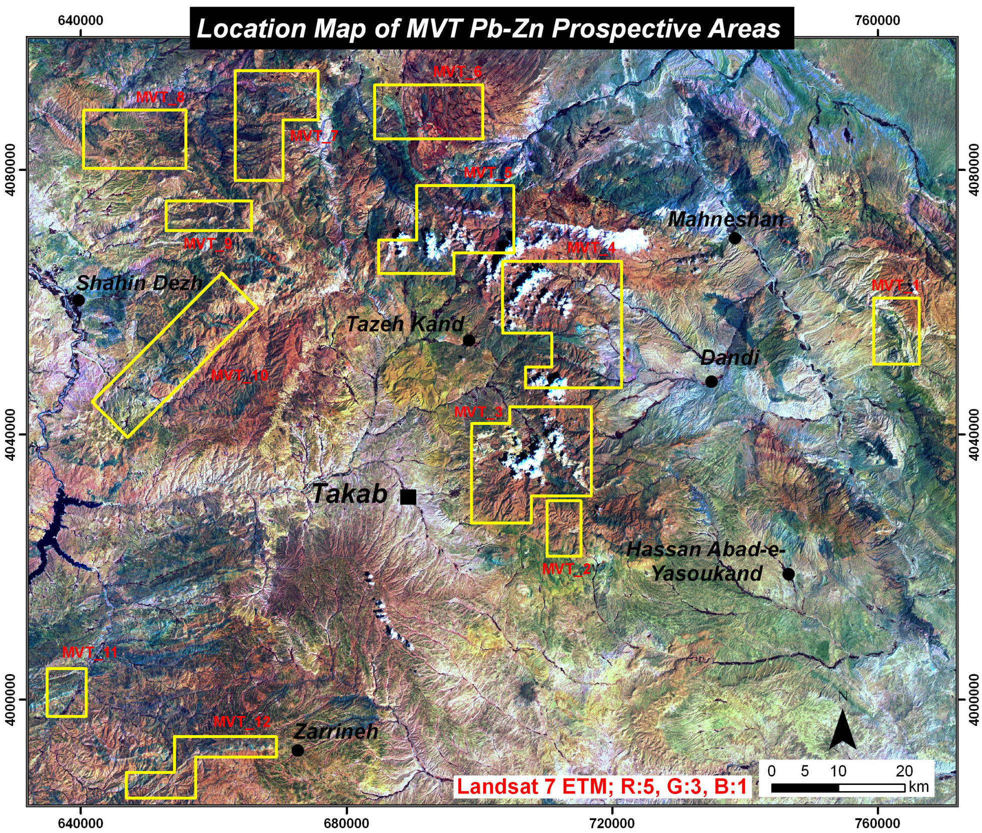

Fig. 7.2 Location map of MVT Pb-Zn prospective areas on the Landsat 7 ETM^{+} Image (R:5, G:3, B:1).

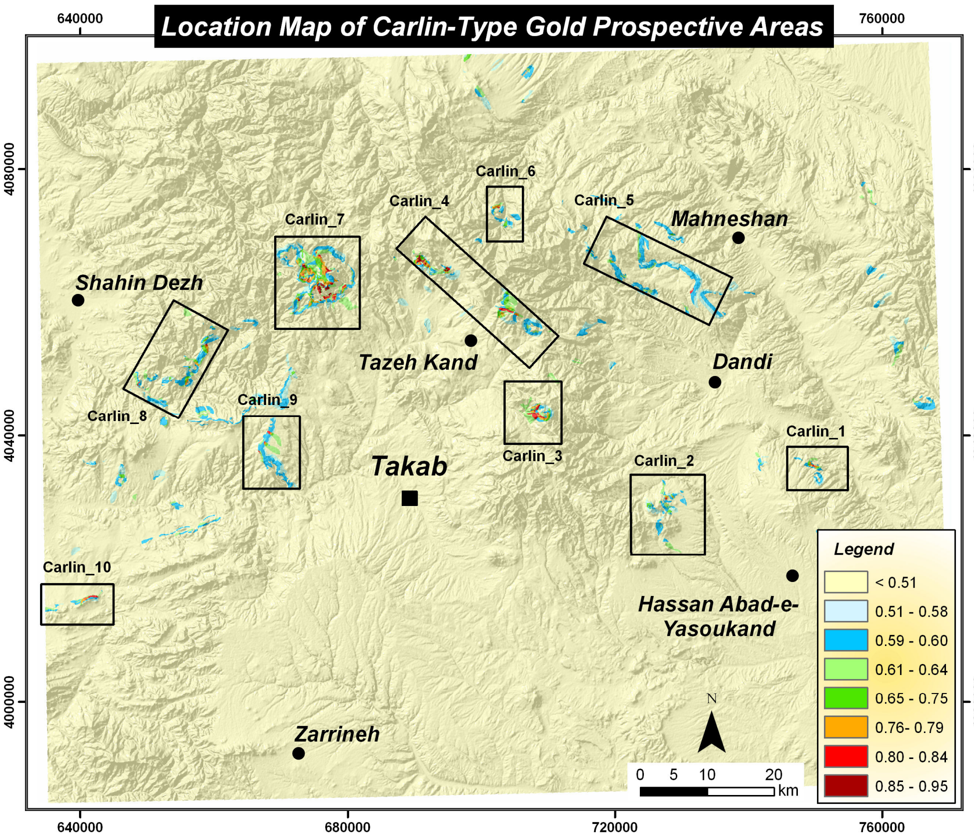

Fig. 7.3 Location map of Carlin-type gold prospective areas on the mineral potential map (Fuzzy logic method).

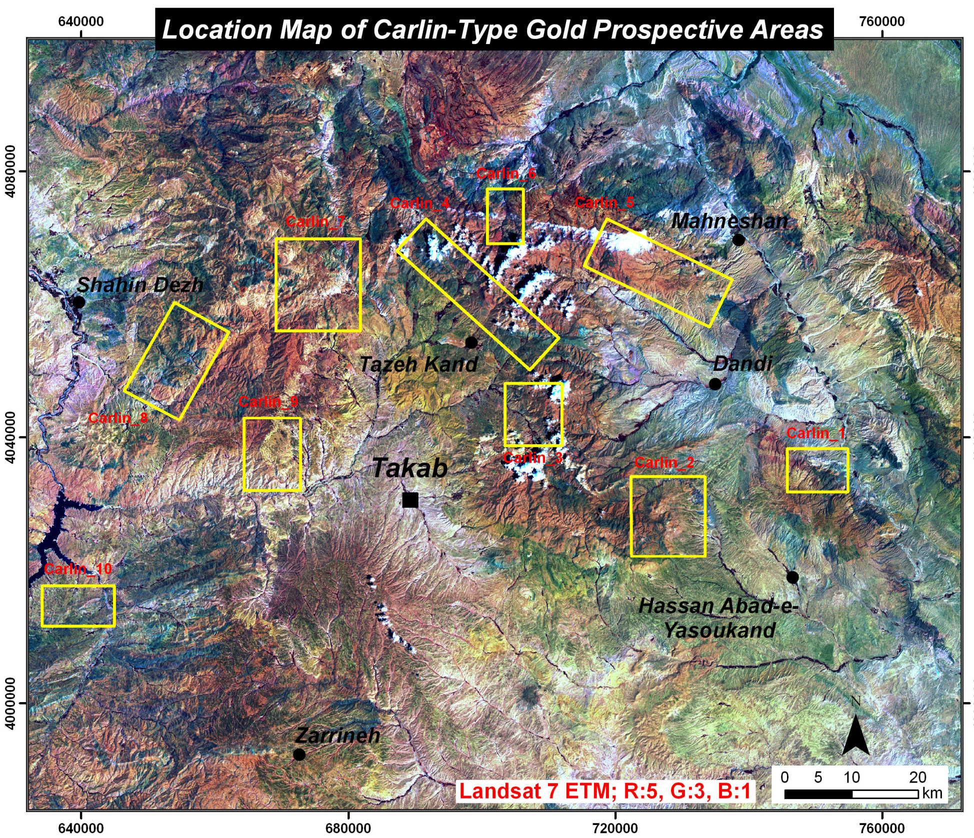

Fig. 7.4 Location map of Carlin-type gold prospective areas on the Landsat 7 ETM+ Image (R:5, G:3, B:1).

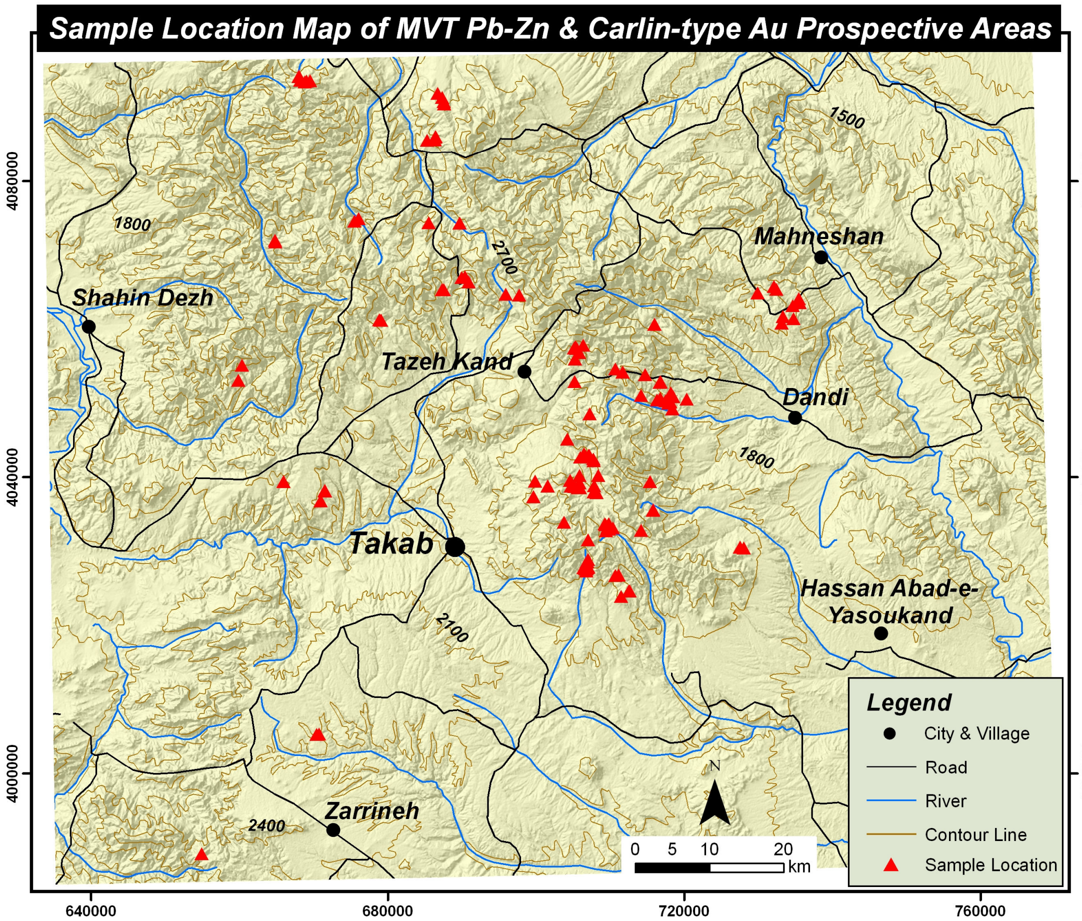

Fig. 7.5 Sample location map of MVT Pb-Zn and Carlin-type gold prospective areas (144 rock and soil samples).

The geo-exploration characteristics of MVT Pb-Zn target areas, chemical analysis results of samples and description of sampling places are as follows:

1- Area 1 (MVT Pb-Zn)

General Description: This target area is located in the eastern portion of the study area (Fig. 7.6a) covered by the 1:100.000 geological map of Mahneshan. Access to this area is by road from Dandi through Ebrahimabad, Kahrizbeyk, Incheh and Moghanlou.

Geology: The predominant geological rock units in this area include granite, granodiorite, limestone (locally dolomite), marl, conglomerate and tuff (Fig 7.6b; extracted and GIS-ready from 1:100.000 geological map of Mahneshan).

Structure: The major geological structural trend in this target area is NW-SE and the trend of minor faults is NE-SW (Fig. 7.6b).

Alteration and Mineralization: Argillic altered rocks (mostly kaolinite) is very intense around a granitic intrusive body (Moghanlou granite) in the northern to eastern parts of this target area and there is also some sericitic alteration in the same place (Fig. 7.6c).

There is a Pb-Zn anomaly (Haji Bacheh; Fig.7.6) in this target area that has been occurred as a high priority of the fuzzy mineral potential map (Fig 7.6d). In the northern part, the abandoned Moghanlou antimony mine, a hydrothermal vein, is located in the argillic alteration zone of the Moghanlou granite (Fig. 7.6).

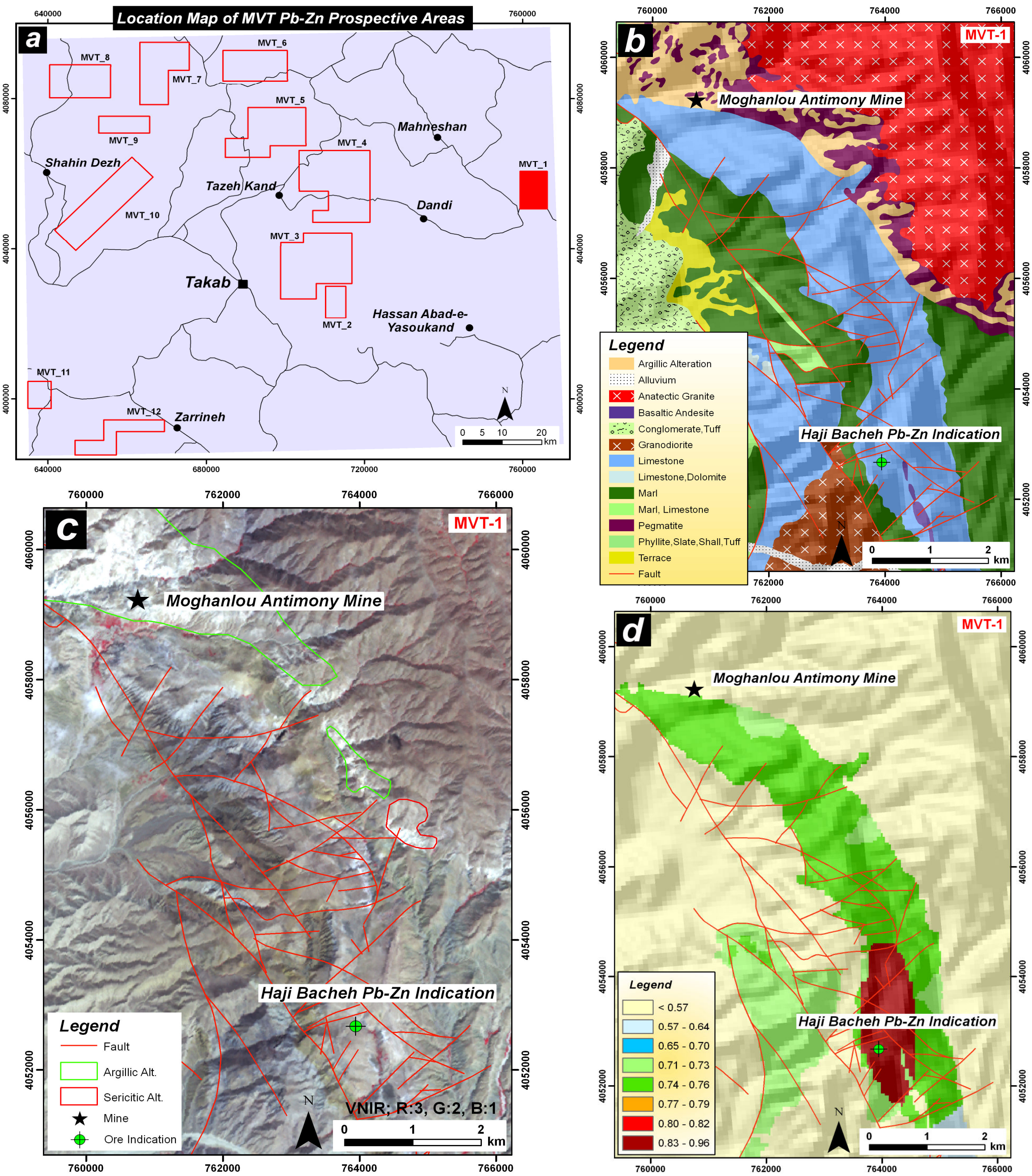

Fig. 7.6 **a** Location map of target area 1 (MVT Pb-Zn) in the study area; **b** Geological map of this area (extracted and GIS-ready from 1:100.000 geological map of Mahneshan); **c** Aster image (VNIR; R:3, G:2, B:1) and hydrothermally altered rocks (argillic and sericitic alteration) and **d** Fuzzy mineral potential map and places of mineralization (the Haji Bacheh Pb-Zn anomaly is located in the high priority category of this map).

2- Area 2 (MVT Pb-Zn)

General Description: This target area is located in the central to southern part of the study area (Fig. 7.8a) covered by the 1:100.000 geological map of Takab. Access to this area is by road from Takab through Sabil, Arabshah and Ay-Qaleh-Si.

Geology: The predominant geological rock units in this area include sandstone, marl, limestone, granite and volcanic rocks such as dacite, andesite, basalt and tuff (Fig 7.8b; extracted and GIS-ready from 1:100.000 geological map of Takab). Figure 7.7 shows the geological sketch map of the Ay-Qaleh-Si sampling area.

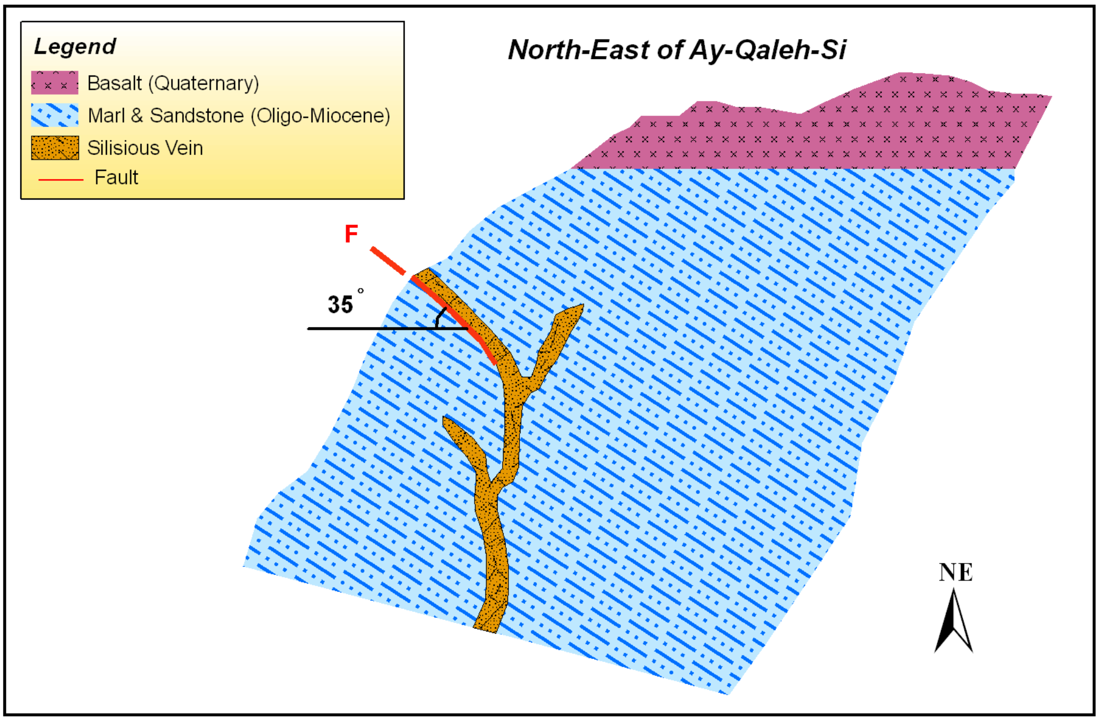

Fig. 7.7 Geological sketch map of the Ay-Qaleh-Si sampling place. "n.b. schematic sketch map, not to scale".

Structure: The major geological structural trend in this target area is NE-SW (Fig. 7.8b).

Alteration and Mineralization: Argillic (mostly kaolinite) and sericitic altered rocks are seen from west toward east of this target area and also there are some hydrothermally altered rocks in the north and south of it (Fig. 7.8c).

There is a Pb-Zn anomaly (Morshedan; Fig.7.8) in the southern part of this target area and the abandoned Ay-Qaleh-Si Pb-Zn mine is located in the central part (Fig. 7.8).

Samples Description: 7 samples (Ta_1-7; Fig. 7.8) were taken from this target area. Three of them selected for XRD analysis (Ta_4, Ta_6 and Ta_7). Maximum values of lead and zinc belong to the sample Ta_5 (Pb = 3400 ppm and Zn = 4500 ppm) also the zinc value of sample Ta_1 is 1558 ppm (analysis results and coordinate of sampling places attached in appendices).

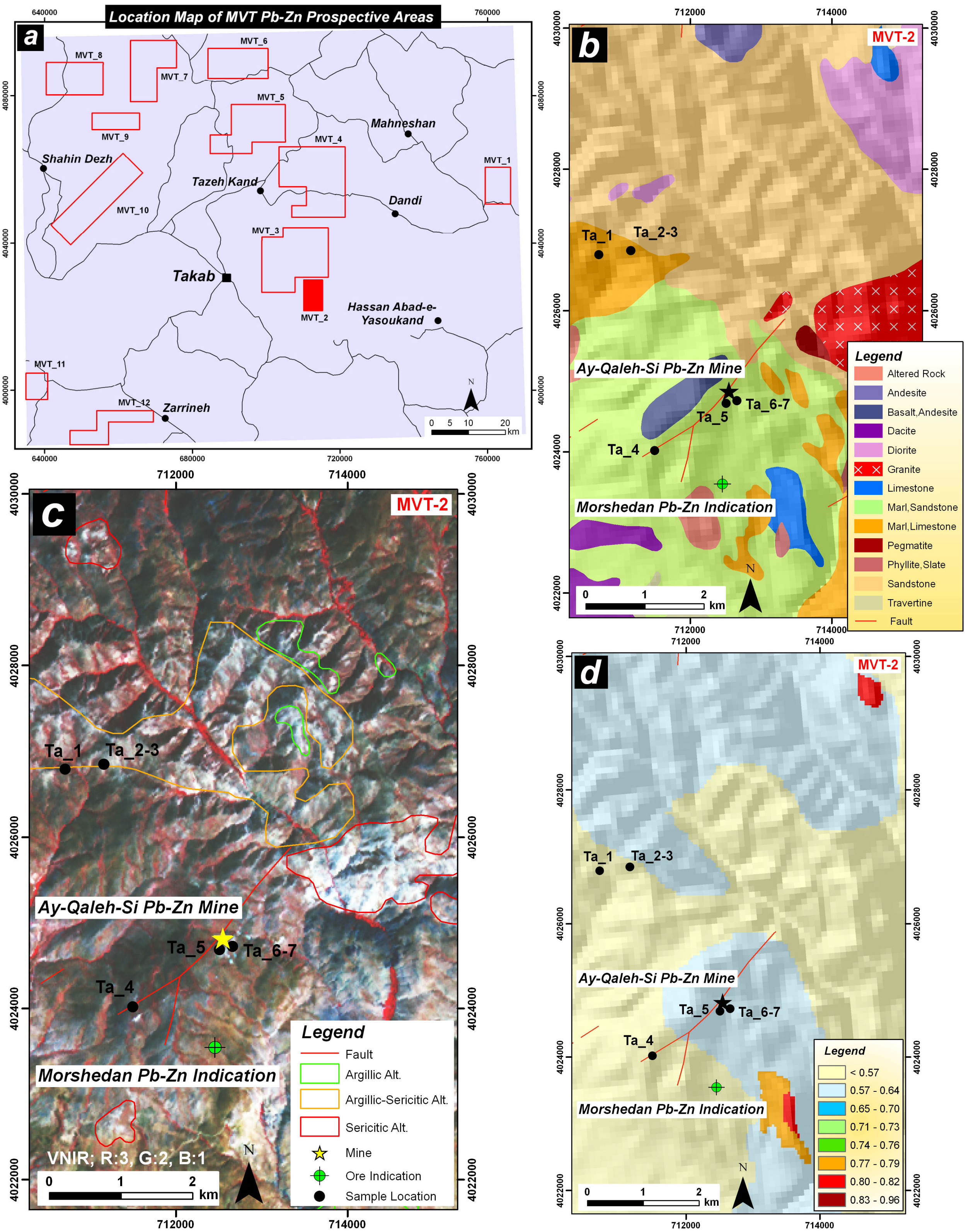

Fig. 7.8 **a** Location map of target area 2 (MVT Pb-Zn) in the study area; **b** Geological map of this area (extracted and GIS-ready from 1:100.000 geological map of Takab); **c** Aster image (VNIR; R:3, G:2, B:1) and hydrothermally altered rocks (argillic and sericitic alteration) and **d** Fuzzy mineral potential map and places of Pb-Zn mineralization.

3- Area 3 (MVT Pb-Zn)

General Description: This target area is located in the central portion of the study area (Fig. 7.10a) covered by the 1:100.000 geological maps of Takab and Takht-e-Soleyman. Access to this area is by road from 1- Takab through Badrlou, Chahar Tagh and Chichaklou (toward south) or Ghoushkhaneh (toward north) 2- Takab through Sabil and Arabshah.

Geology: The predominant geological rock units in this target area include micaschist and quartzite, dolomite, marble, sandstone and travertine (Fig 7.10b; extracted and GIS-ready from 1:100.000 geological maps of Takab and Takht-e-Soleyman). Figure 7.9 shows the geological sketch map of the Arabshah, Badrlou, Chichaklou and Ghouzijagh sampling areas.

Structure: The major geological structural trend in this area is NW-SE and the trends of minor faults are NE-SW and W-E (Fig. 7.10b).

Alteration and Mineralization: Argillic and sericitic altered rocks are seen in the northern, western and eastern portion (Fig. 7.10c) and the Chichaklou Pb-Zn deposit is located in the southern part of this area as a high priority of the fuzzy mineral potential map (Fig. 7.10d).

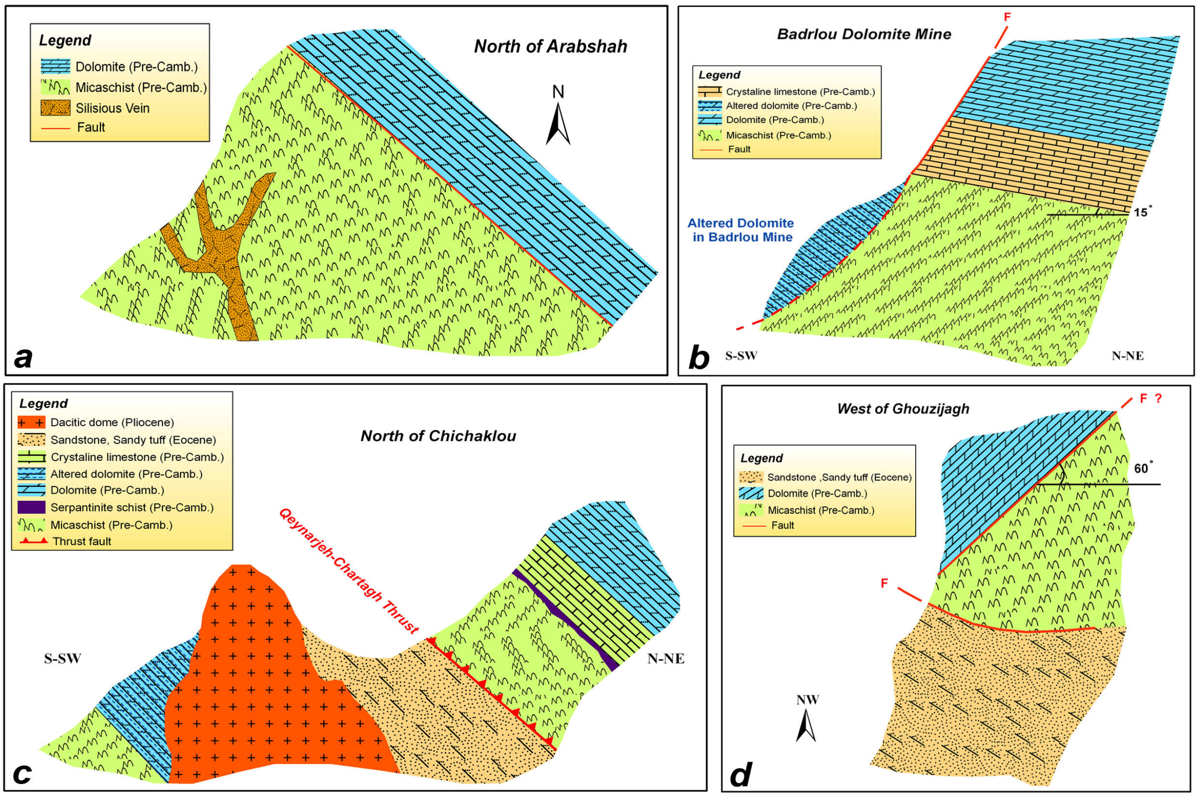

Fig. 7.9 Geological sketch map of the **a** Arabshah; **b** Badrlou; **c** Chichaklou and **d** Ghouzijagh sampling areas. "n.b. schematic sketch map, not to scale".

Samples Description: 58 samples (Ta_8-65; Fig. 7.10) were taken from this target area. Maximum values of lead belong to the sample Ta_33 (Pb = 54300 ppm) and for zinc is 124900 ppm (sample Ta_29) also the zinc value of samples Ta_31-30-35-32-33-25 and 53 respectively are 58200, 43200, 26800, 26400, 12450, 7900 and 5000 ppm. The value of lead for samples Ta_32-21-30 and 60 are 13000, 9600, 6100 and 5500 ppm (see appendices).

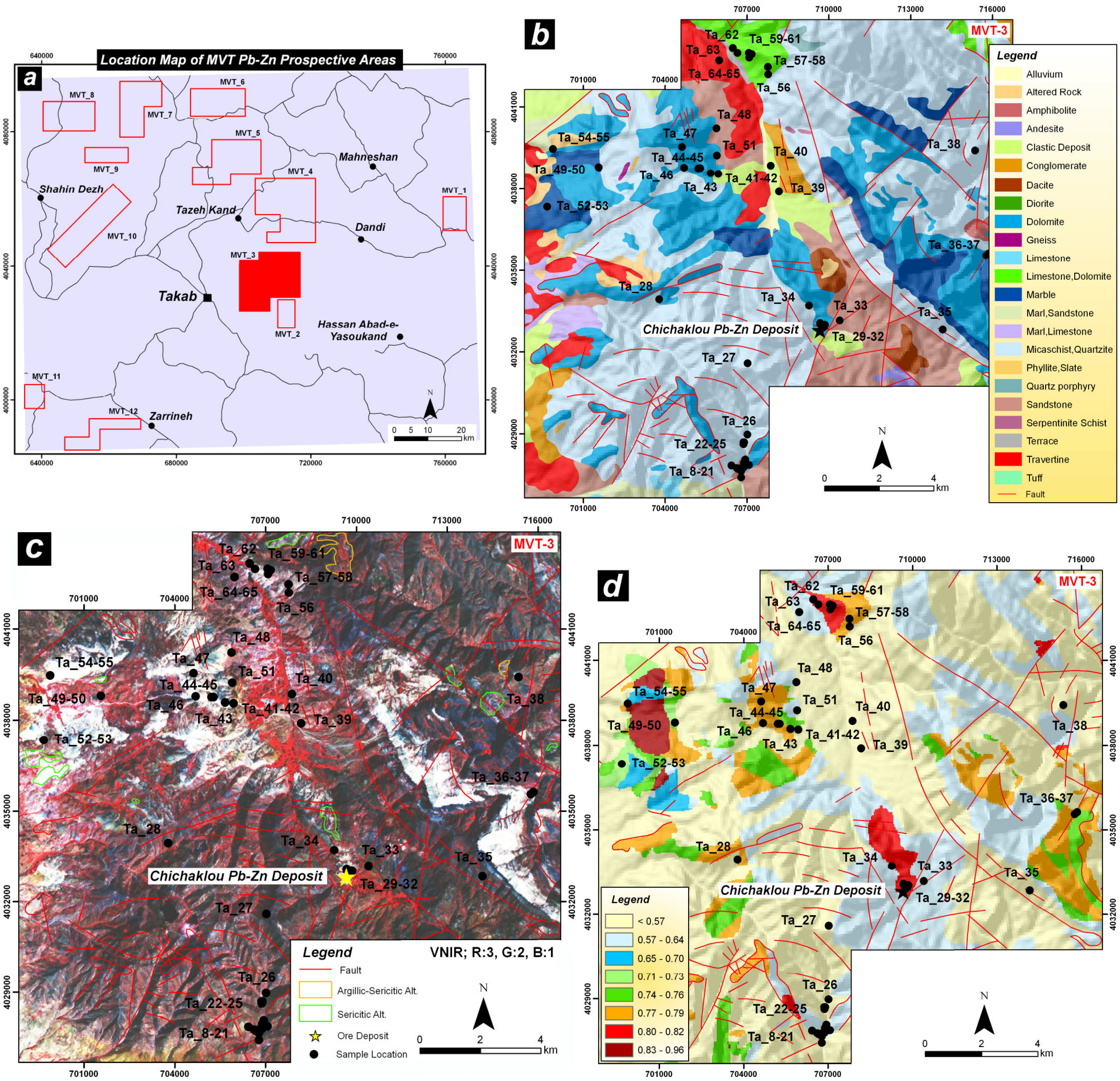

Fig. 7.10 **a** Location map of target area 3 (MVT Pb-Zn) in the study area; **b** Geological map of this area (extracted and GIS-ready from 1:100.000 geological maps of Takab and Takht-e-Soleyman); **c** Aster image (VNIR; R:3, G:2, B:1) and hydrothermally altered rocks (argillic and sericitic alteration) and **d** Fuzzy mineral potential map and place of Pb-Zn mineralization (the Chichaklou Pb-Zn deposit is located in the high priority category of this map).

4- Area 4 (MVT Pb-Zn)

General Description: This target area is located in the central portion of the study area (Fig. 7.12a) covered by the 1:100.000 geological map of Takht-e-Soleyman. Access to this area is by road from Takab through Shirmard, Nosratabad and Angouran mine.

Geology: The predominant rock units in this target area include limestone, dolomite, marble, micaschist and quartzite, tuff, marl, sandstone and volcanic rocks (Fig 7.12b; extracted and GIS-ready from 1:100.000 geological map of Takht-e-Soleyman). Figure

7.11 shows the geological sketch map of the Amirabad, Golablou, Yasti Qaleh, Angouran, Aghbolagh and Ghoushkhaneh sampling areas.

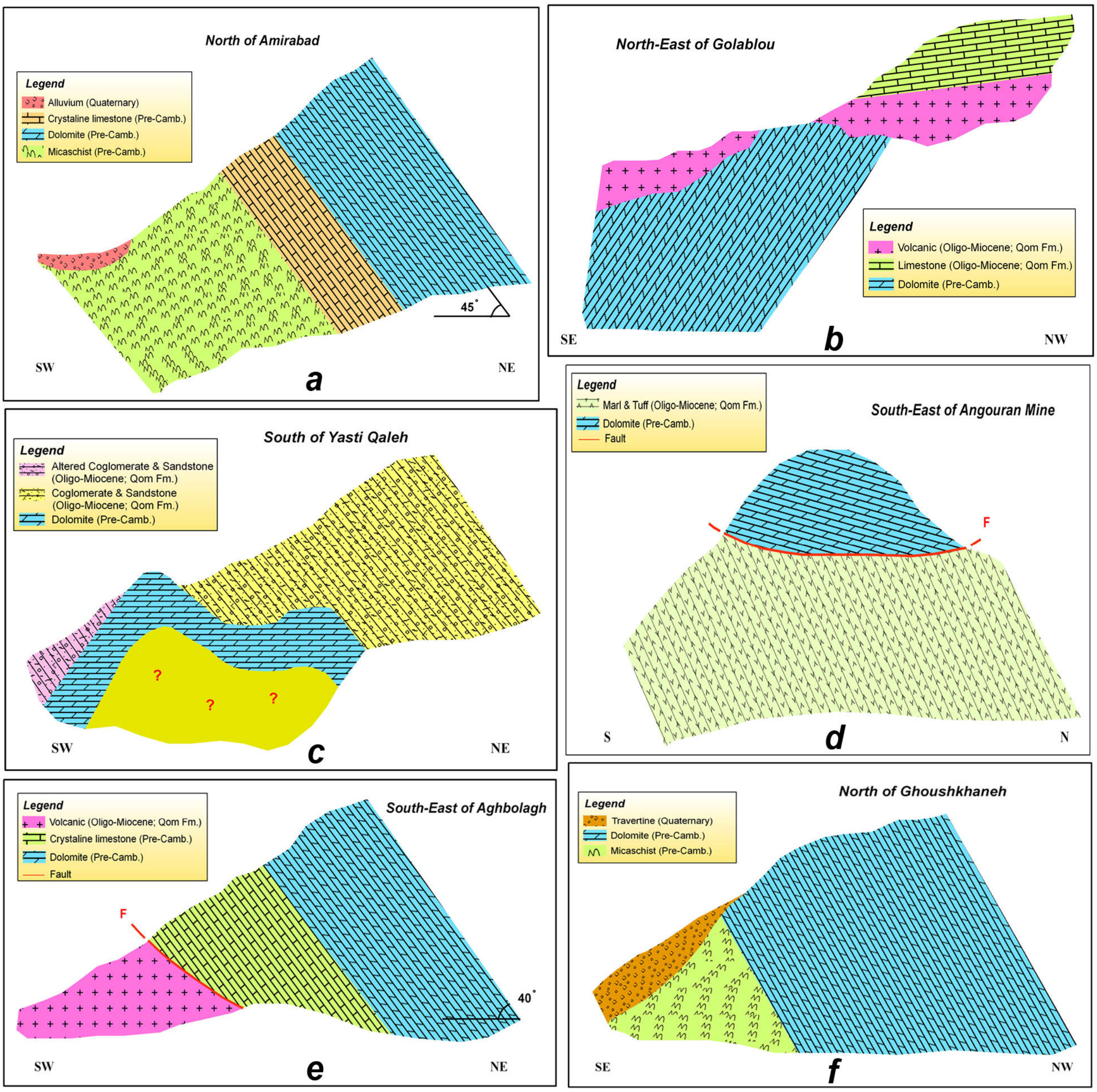

Fig. 7.11 Geological sketch map of the **a** Amirabad; **b** Golablou; **c** Yasti Qaleh; **d** Angouran; **e** Aghbolagh and **f** Ghoushkhaneh sampling areas. "n.b. schematic sketch map, not to scale".

Structure: The major geological structural trend in this area is NW-SE but the trends of minor faults are NE-SW and W-E (Fig. 7.12b).

Alteration and Mineralization: Argillic and sericitic altered rocks are exposed in parts of this area (Fig. 7.12c). The Angouran Pb-Zn and Ghuzlou Au-Pb mines and also the Golablou and Esfaran Pb-Zn anomalies (Fig.7.12) are located in this target area. The Angouran Pb-Zn deposit is located in the high priority category of the fuzzy mineral potential map (Fig. 7.12d).

Samples Description: 24 samples (Ta_66-89; Fig. 7.12) were taken from this target area. Maximum values of lead belong to the sample Ta_73 (Pb = 3400 ppm) and for zinc (sample Ta_88) is 6700 ppm (analysis results and coordinate of sampling places attached in appendices).

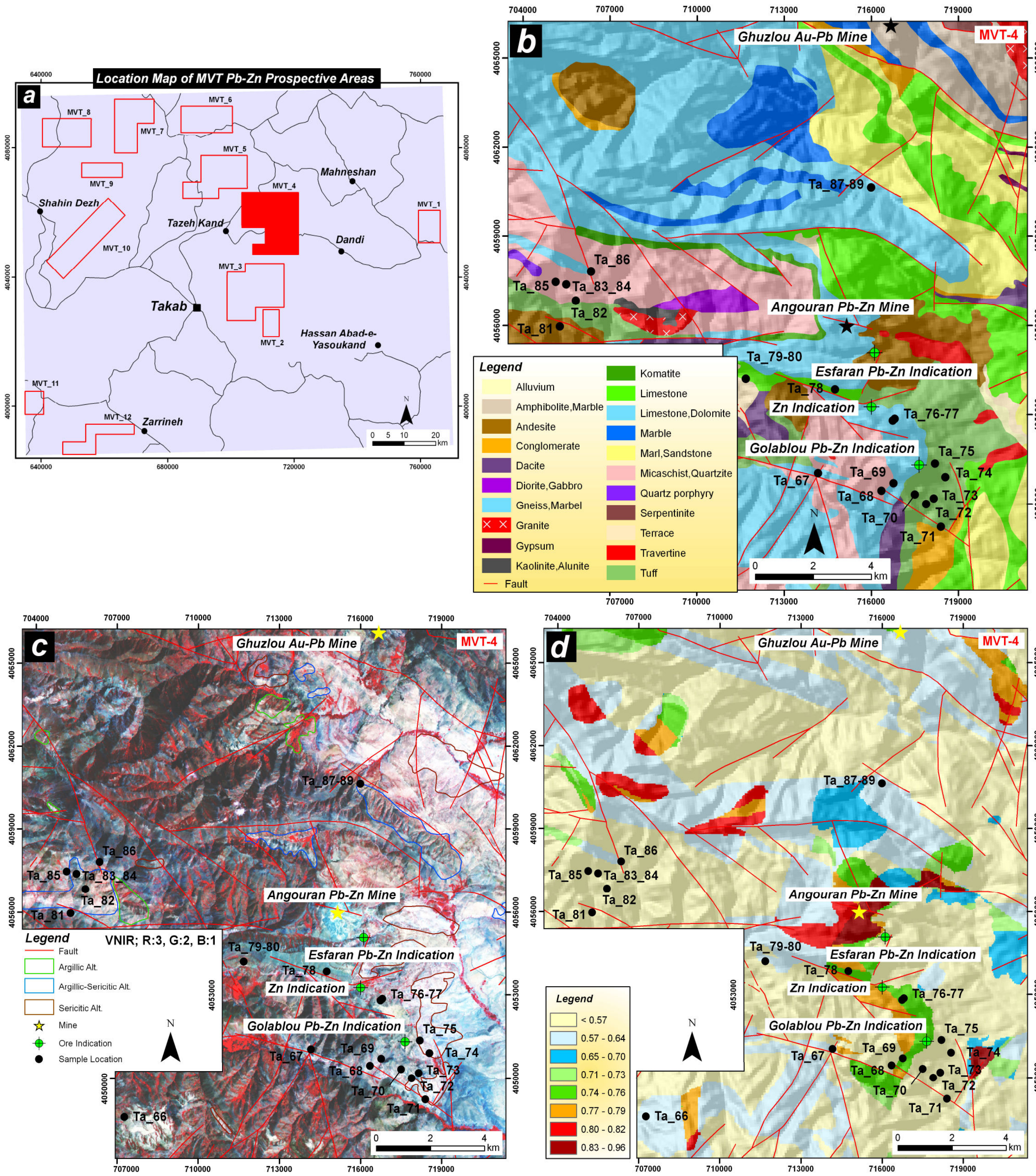

Fig. 7.12 **a** Location map of target area 4 (MVT Pb-Zn) in the study area; **b** Geological map of this area (extracted and GIS-ready from 1:100.000 geological map of Takht-e-Soleyman); **c** Aster image (VNIR; R:3, G:2, B:1) and hydrothermally altered rocks (argillic and sericitic alteration) and **d** Fuzzy mineral potential map and places of Pb-Zn mineralization (the Angouran Pb-Zn deposit is located in the high priority category of this map).

5- Area 5 (MVT Pb-Zn)

General Description: This target area is located in the northern portion of the study area (Fig. 7.14a) covered by the 1:100.000 geological map of Takht-e-Soleyman. Access to this area is by road from Takab through Shirmard, Zarshouran, Ghinarjeh and Alam Kandi.

Geology: The predominant rock units include an alternation of gneiss, marble and amphibolite, porphyritic andesitic lava, tuff, dolomite, limestone, marble, marl and sandstone (Fig 7.14b; extracted and GIS-ready from 1:100.000 geological map of Takht-e-Soleyman). Figure 7.13 shows the geological sketch map of the Zarshouran and Ghinarjeh sampling areas.

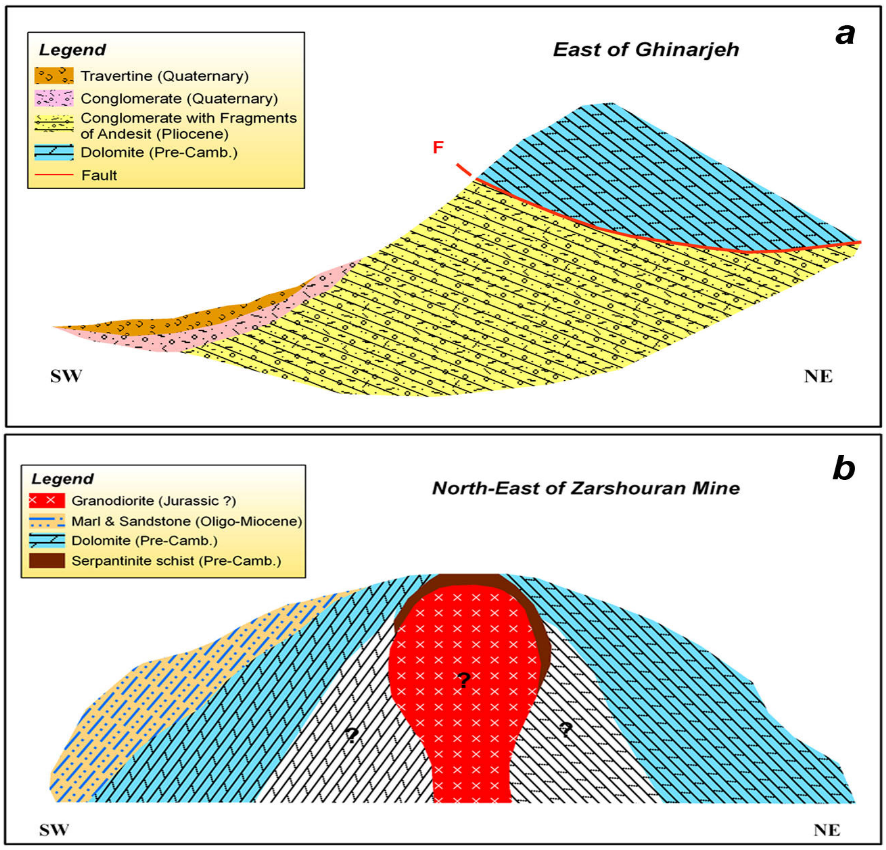

Fig. 7.13 Geological sketch map of the **a** Ghinarjeh and **b** Zarshouran sampling areas. "n.b. schematic sketch map, not to scale".

Structure: The major geological structural trend in this area is NW-SE but the trends of minor faults are NE-SW, N-S and W-E (Fig. 7.14b).

Alteration and Mineralization: Argillic and sericitic altered rocks are exposed in the northeastern, central and southwestern parts of this area (Fig. 7.14c). The Alam Kandi Pb-Zn mine (Fig.7.14) is located in this target area.

Samples Description: 7 samples (Ta_90-96; Fig. 7.14) were taken from this target area. Maximum values of lead belong to the samples Ta_95 and Ta_96 (Pb = 2700 ppm) and for zinc (sample Ta_96) is 6000 ppm (analysis results and coordinate of sampling places attached in appendices).

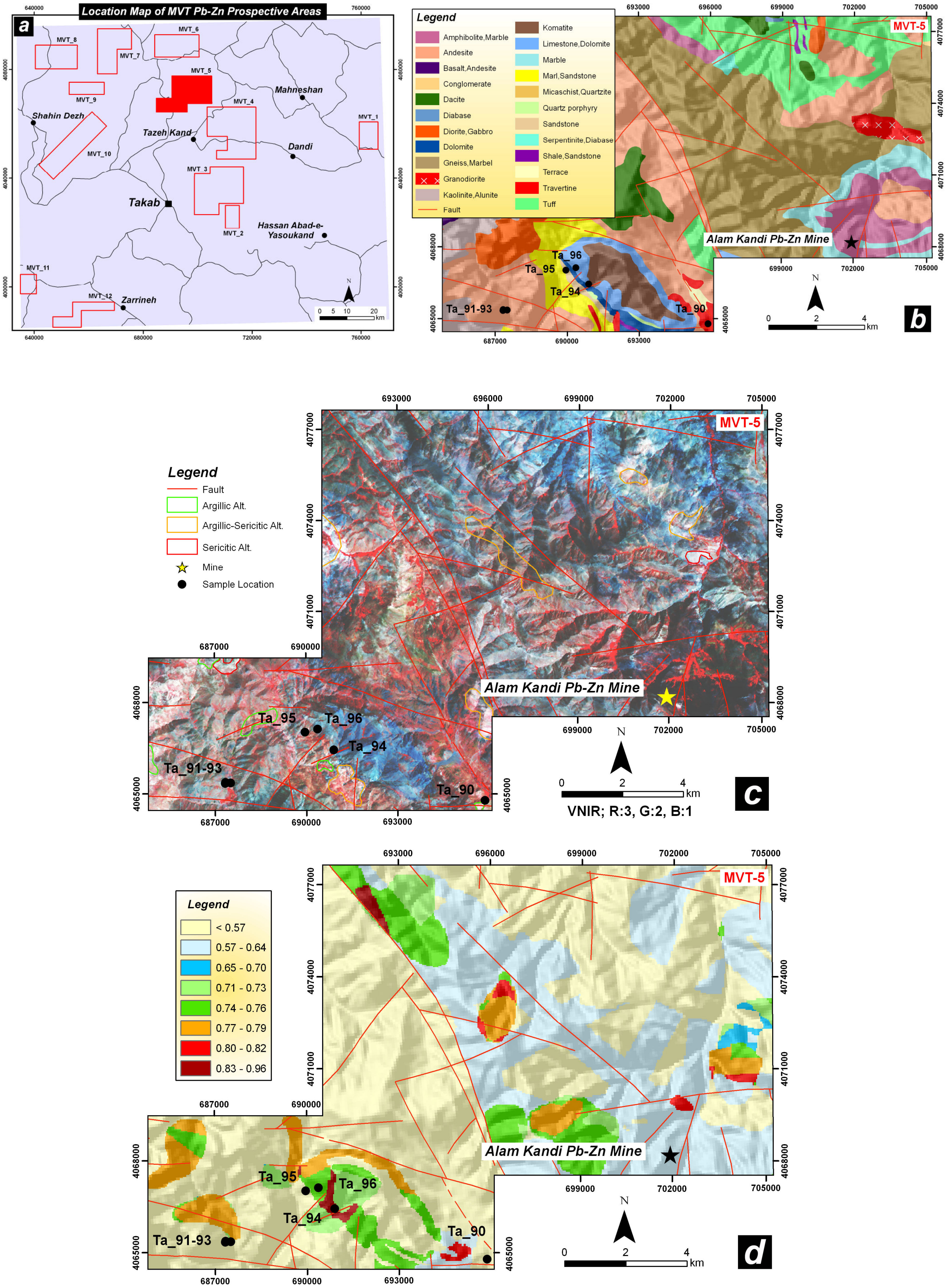

Fig. 7.14 **a** Location map of target area 5 (MVT Pb-Zn) in the study area; **b** Geological map of this area (extracted and GIS-ready from 1:100.000 geological map of Takht-e-Soleyman); **c** Aster image (VNIR; R:3, G:2, B:1) and hydrothermally altered rocks (argillic and sericitic alteration) and **d** Fuzzy mineral potential map and place of Pb-Zn mineralizatio

6- Area 6 (MVT Pb-Zn)

General Description: This target area is located in the northern portion of the study area (Fig. 7.16a) covered by the 1:100.000 geological map of Takht-e-Soleyman. Access to this area is by road from Takab through Shirmard, Zarshouran, Arpachai, Chogati and Tazeh Kand.

Geology: The predominant rock units include amphibolites, gneiss, marble, limestone, dolomite, travertine, granodiorite, micaschist and serpentinite (Fig 7.16b; extracted and GIS-ready from 1:100.000 geological map of Takht-e-Soleyman). Figure 7.15 shows the geological sketch map of the west of Tazeh Kand, north of Tazeh Kand and Ghareh Saghar sampling area.

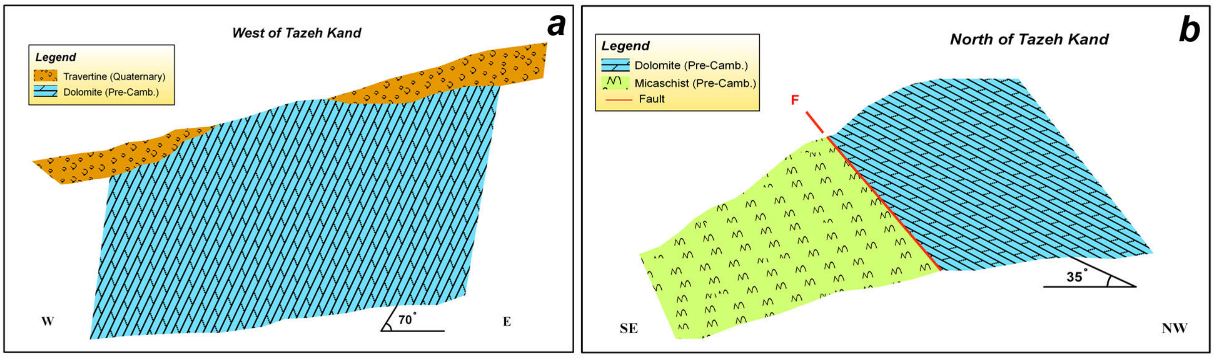

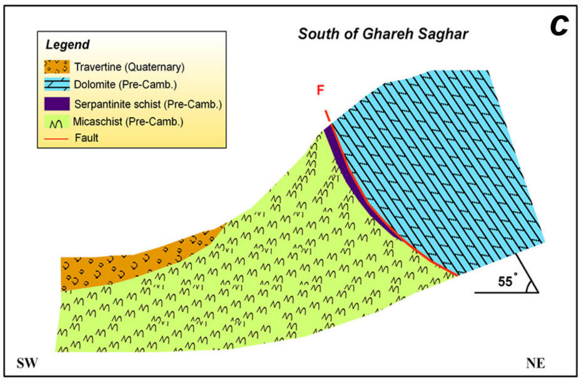

Fig. 7.15 Geological sketch map of the **a** Tazeh Kand; **b** North of Tazeh Kand and **c** Ghareh Saghar sampling areas. "n.b. schematic sketch map, not to scale".

Structure: The major geological structural trends in this area are N-S and NW-SE and the minor fault trend is NE-SW (Fig. 7.16b).

Alteration and Mineralization: Argillic altered rocks are seen in the western portion of this target area (Fig. 7.16c) and the abandoned Jabalkou Pb-Zn mine (Fig. 7.16) is located in the western part, in the medium to high priority category of the fuzzy mineral potential map (Fig. 7.16d).

Samples Description: 9 samples (Ta_97-105; Fig. 7.16) were taken from this target area. Maximum values of lead and zinc belong to the sample Ta_105 (Pb = 2800 ppm and Zn= 5400 ppm) (analysis results and coordinate of sampling places attached in appendices).

7- Area 7 (MVT Pb-Zn)

General Description: This target area is located in the north-west of the study area (Fig. 7.17a) covered by the 1:100.000 geological map of Shahindezh. Access to this area is by road from Qareh Aghaj through Barijough, Shaaban, Ali Beyglou Bala, Badamou and Mohammad Qoli Gheshlaghi.

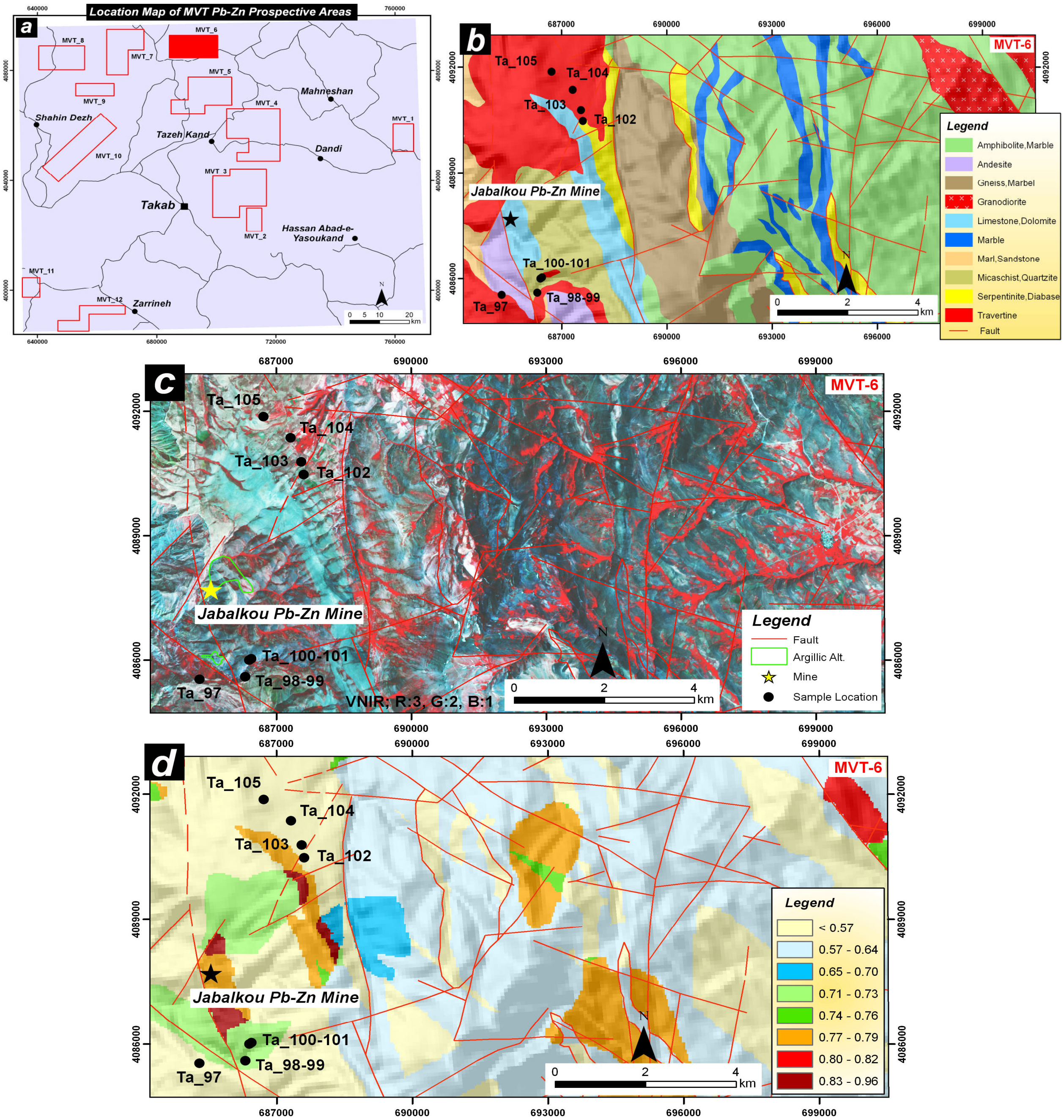

Fig. 7.16 **a** Location map of target area 6 (MVT Pb-Zn) in the study area; **b** Geological map of this area (extracted and GIS-ready from 1:100.000 geological map of Takht-e-Soleyman); **c** Aster image (VNIR; R:3, G:2, B:1) and hydrothermally altered rocks (argillic alteration) and **d** Fuzzy mineral potential map and place of Pb-Zn mineralization.

Geology: The predominant rock units include shale and slate, dolomite, limestone, sandstone, andesite and conglomerate (Fig 7.17b; extracted and GIS-ready from 1:100.000 geological map of Shahindezh).

Structure: The major geological structural trend in this area is NE-SW and the minor fault trend is NW-SE (Fig. 7.17b).

Alteration: The limited argillic-sericitic altered rocks are seen in the southern part of this target area (Fig. 7.17c).

Samples Description: 7 samples (Ta_106-112; Fig. 7.17) were taken from this target area. Maximum values of lead belong to the sample Ta_108 (Pb = 5921 ppm) and for zinc (sample Ta_112) is 6257 ppm (analysis results and coordinate of sampling places attached in appendices).

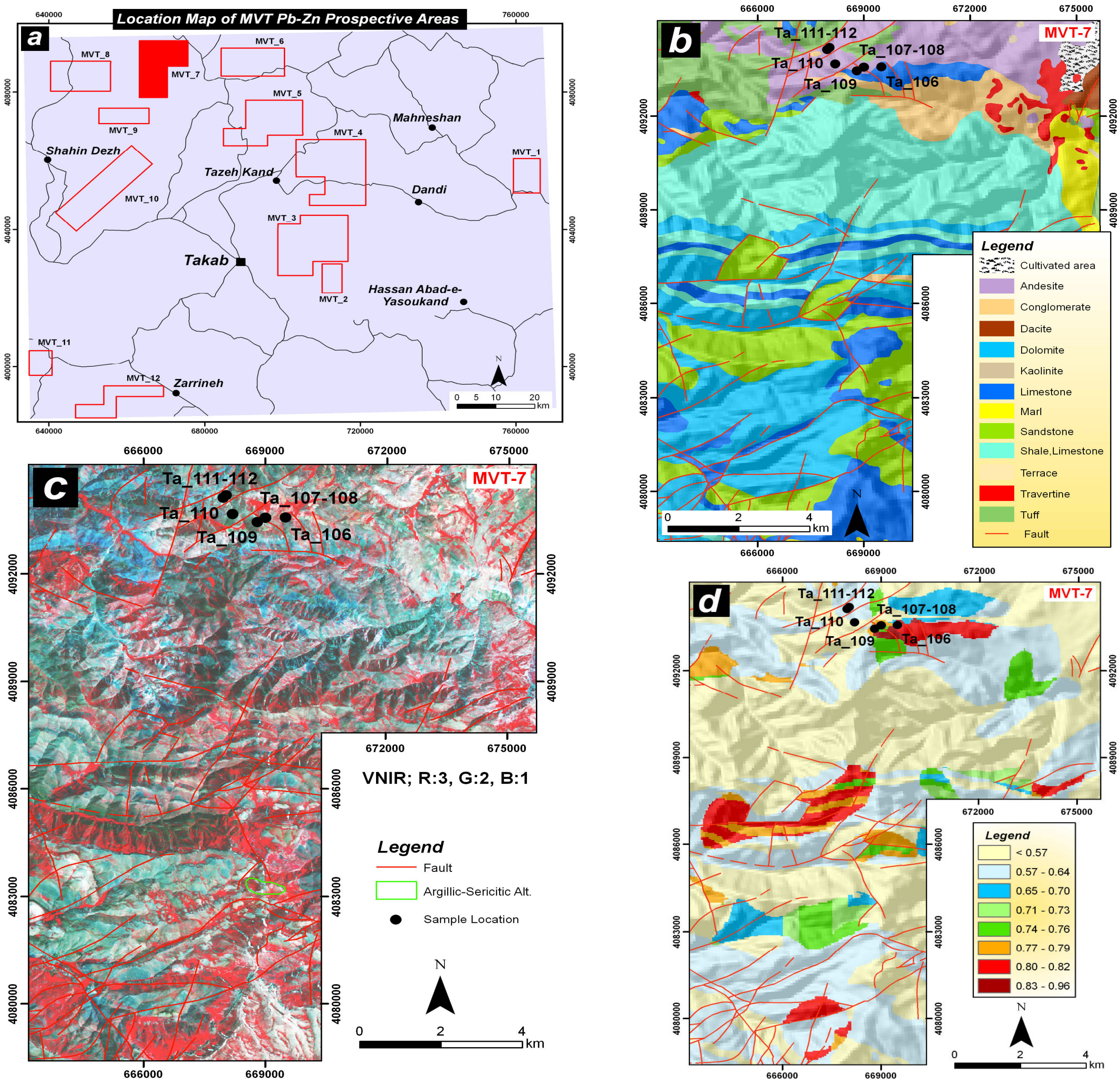

Fig. 7.17 **a** Location map of target area 7 (MVT Pb-Zn) in the study area; **b** Geological map of this area (extracted and GIS-ready from 1:100.000 geological map of Shahindezh); **c** Aster image (VNIR; R:3, G:2, B:1) and hydrothermally altered rocks (argillic-sericitic alteration) and **d** Fuzzy mineral potential map.

8- Area 8 (MVT Pb-Zn)

General Description: This target area is located in the north-west of the study area (Fig. 7.18a) covered by the 1:100.000 geological map of Shahindezh. Access to this area is by road from Miandoab (to Shahindezh) through Hoseinabad, Sehvari, Qareh Adnan and

Gheynarjeh.

Geology: The predominant rock units include limestone, dolomite, tuff, sandstone, conglomerate, travertine and andesite (Fig 7.18b; extracted and GIS-ready from 1:100.000 geological map of Shahindezh).

Structure: The major geological structural trend in this area is NE-SW but the minor fault trend is NW-SE (Fig. 7.18b).

Alteration: Argillic altered rocks are exposed in the most part of this target area (Fig. 7.18c).

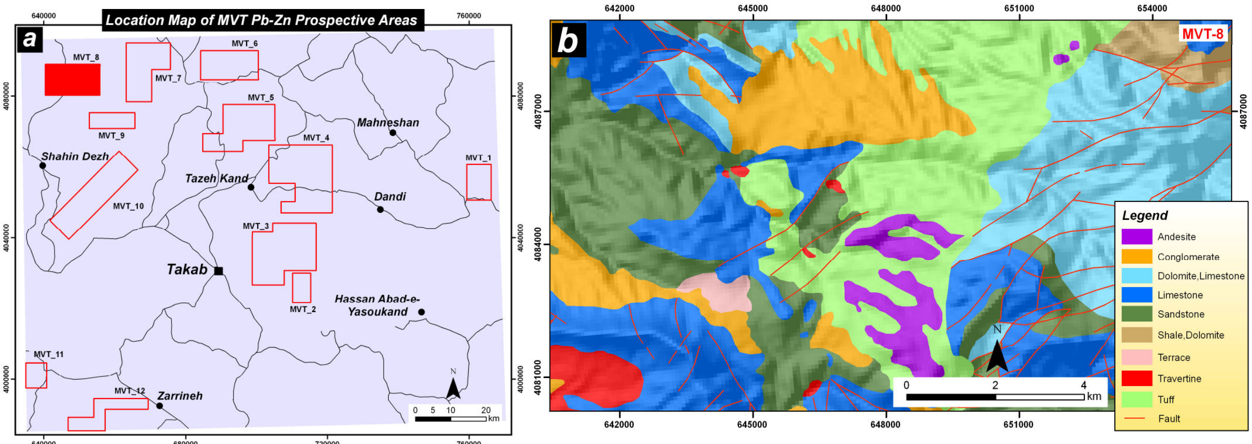

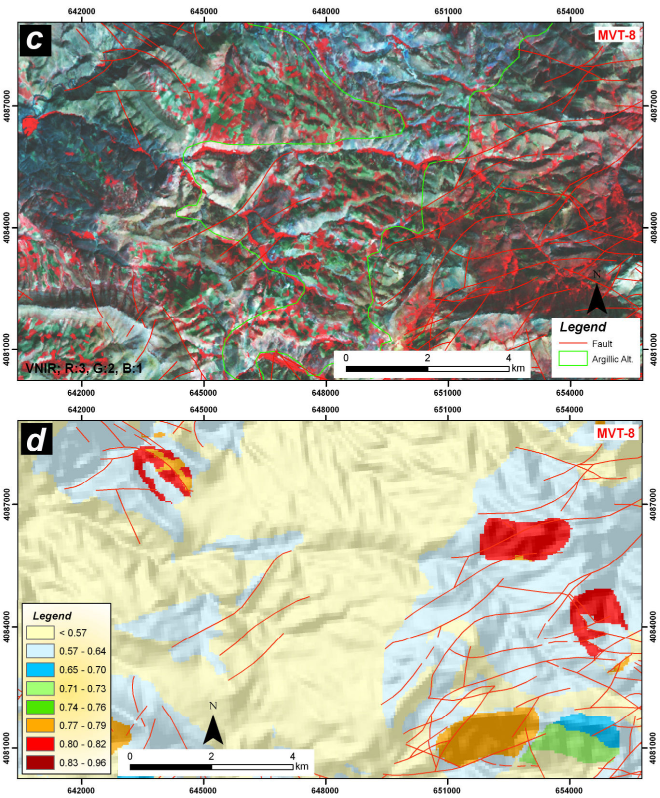

Fig. 7.18 **a** Location map of target area 8 (MVT Pb-Zn) in the study area; **b** Geological map of this area (extracted and GIS-ready from 1:100.000 geological map of Shahindezh); **c** Aster image (VNIR; R:3, G:2, B:1) and hydrothermally altered rocks (argillic alteration) and **d** Fuzzy mineral potential map.

9- Area 9 (MVT Pb-Zn)

General Description: This target area is located in the north-west of the study area (Fig. 7.19a) covered by the 1:100.000 geological map of Shahindezh. Access to this area is by road from Shahindezh through Mahmud Gigh, Qareh Qayeh, Chapow (in the west) and Zeynali (in the south).

Geology: The predominant geological rock units in this area include limestone, dolomite, sandstone, shale, conglomerate and granite (Fig 7.19b; extracted and GIS-ready from 1:100.000 geological map of Shahindezh).

Structure: The major geological structural trend in this target area is NE-SW (Fig. 7.19b).

Alteration: The limited argillic-sericitic altered rocks are exposed in the south-east of this target area *(Fig. 7.19c).*

Samples Description: 2 samples (Ta_113-114; Fig. 7.19) were taken from this target area. Maximum values of lead belong to the sample Ta_113 (Pb = 122 ppm) and for zinc (sample Ta_114) is 140 ppm (analysis results and coordinate of sampling places attached in appendices).

10- Area 10 (MVT Pb-Zn)

General Description: This target area is located in the western portion of the study area (Fig. 7.20a) covered by the 1:100.000 geological map of Shahindezh. Access to this area is by road from 1- Takab (to Shahindezh) through Sanjud, Zeyd Kandi and Pichaghchi 2- Shahindezh (to Takab) through Aghajeri and Ghozlou.

Geology: The predominant geological rock units in this area include limestone, dolomite, sandstone, rhyoloite, granite, tuff, schist and gneiss (Fig 7.20b; extracted and GIS-ready from 1:100.000 geological map of Shahindezh).

Structure: The major geological structural trend in this target area is NE-SW (Fig. 7.20b).

Alteration: Argillic and sericitic altered rocks are seen in different parts of this area (Fig. 7.20c).

Samples Description: 3 samples (Ta_115-117; Fig. 7.20) were taken from this target area. Maximum values of lead belong to the sample Ta_115 (Pb = 11 ppm) and for zinc (sample Ta_116) is 16 ppm (analysis results and coordinate of sampling places attached in appendices).

11- Area 11 (MVT Pb-Zn)

General Description: This target area is located in the south-east of the study area (Fig. 7.21a) covered by the 1:100.000 geological map of Irankhah. Access to this area is by road from Irankhah through Chapan-e-Bala, Khaneh Miran and Sheikh Ali.

Geology: The predominant geological rock units in this area include sandstone, limestone, dolomite, marble, shale and andesite (Fig 7.21b; extracted and GIS-ready from 1:100.000

geological map of Irankhah).

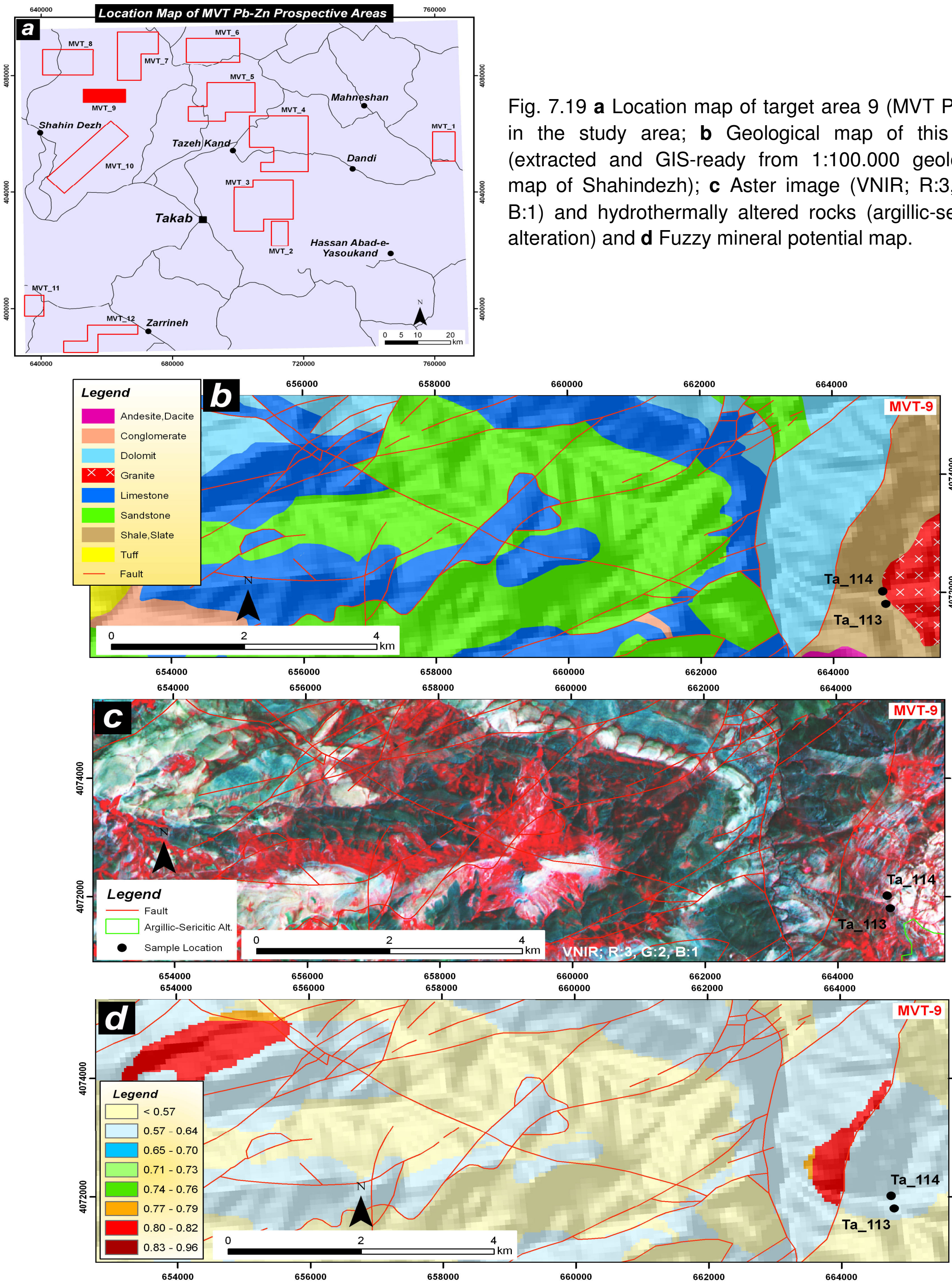

Fig. 7.19 **a** Location map of target area 9 (MVT Pb-Zn) in the study area; **b** Geological map of this area (extracted and GIS-ready from 1:100.000 geological map of Shahindezh); **c** Aster image (VNIR; R:3, G:2, B:1) and hydrothermally altered rocks (argillic-sericitic alteration) and **d** Fuzzy mineral potential map.

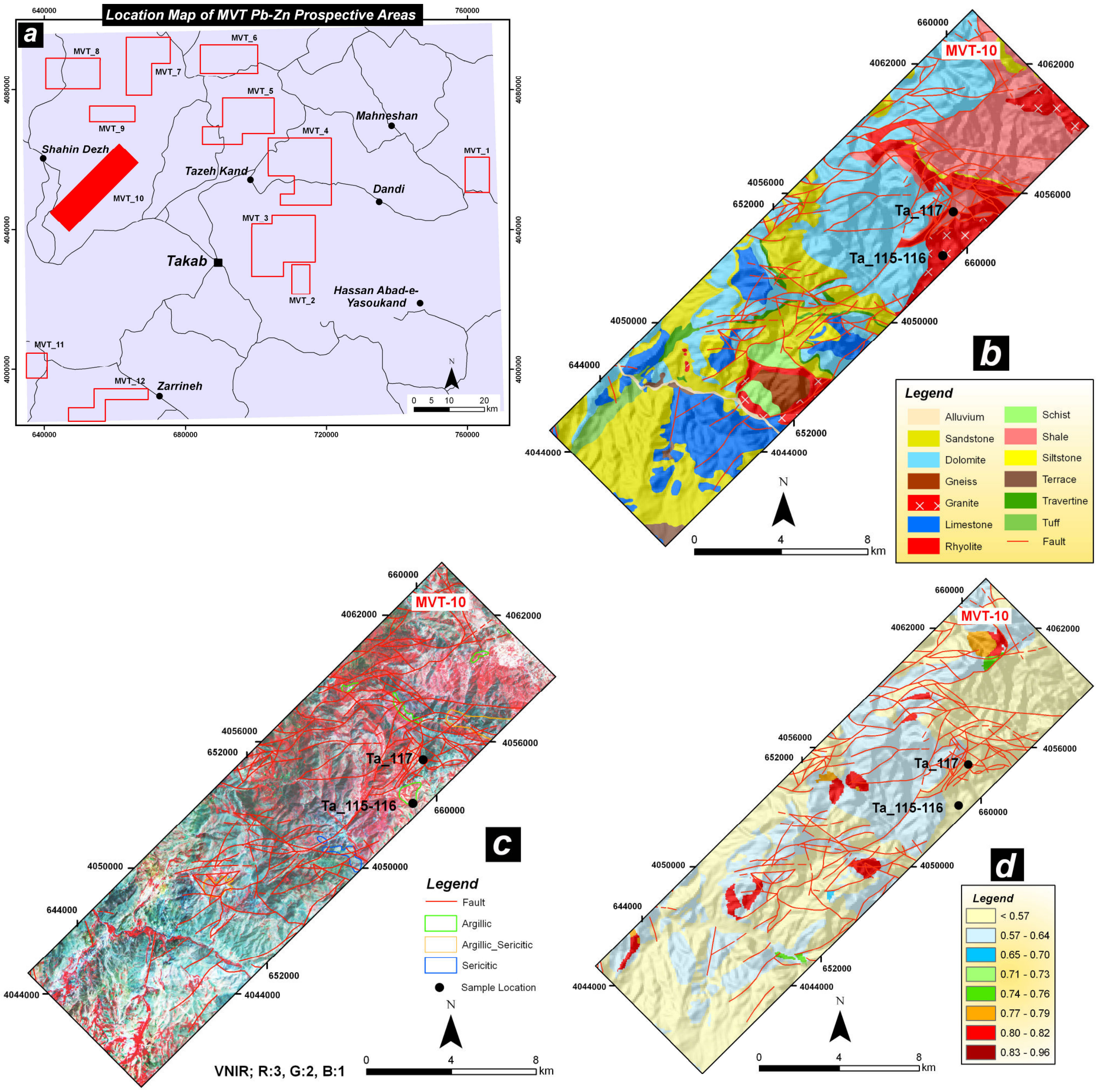

Fig. 7.20 **a** Location map of target area 10 (MVT Pb-Zn) in the study area; **b** Geological map of this area (extracted and GIS-ready from 1:100.000 geological map of Shahindezh); **c** Aster image (VNIR; R:3, G:2, B:1) and hydrothermally altered rocks (argillic and sericitic alteration) and **d** Fuzzy mineral potential map.

Structure: The major geological structural trend in this target area is NE-SW (Fig. 7.21b).

12- Area 12 (MVT Pb-Zn)

General Description: This target area is located in the south-east of the study area (Fig. 7.22a) covered by the 1:100.000 geological map of Irankhah. Access to this area is by road from Irankhah through Qaleh Jogheh, Teyman Qaleh, Bashmagh and Jafar Khani.

Geology: The predominant geological rock units in this area include amphibolites and gneiss, limestone and dolomite, andesite, sandstone and conglomerate (Fig 7.22b;

extracted and GIS-ready from 1:100.000 geological map of Shahindezh).

Structure: The major geological structural trend in this target area is NE-SW (Fig. 7.22b).

Samples Description: 1 sample (Ta_118; Fig. 7.22) were taken from this target area. The values of lead and zinc respectively are 7 ppm and 114 ppm (analysis results and coordinate of sampling places attached in appendices).

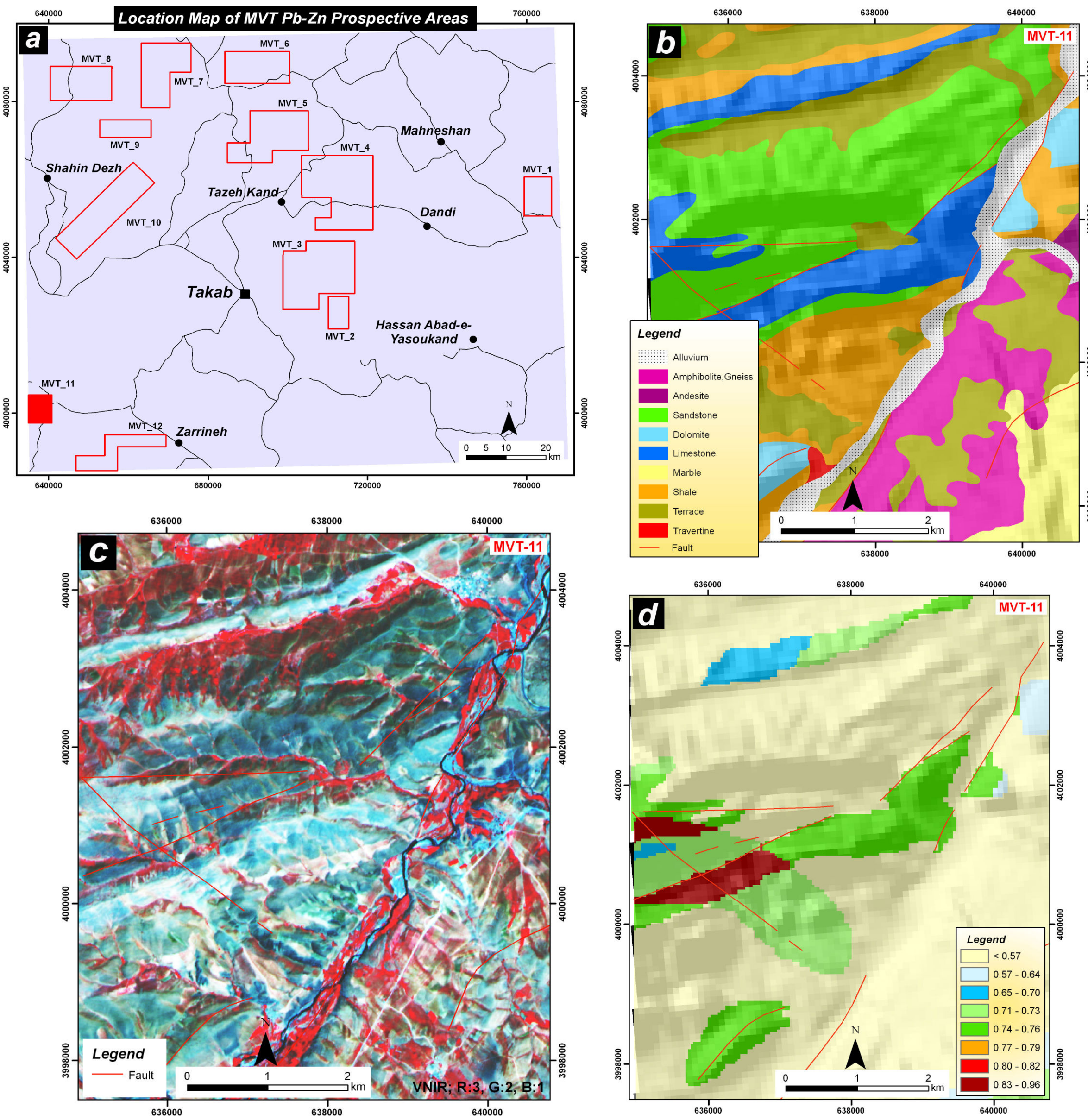

Fig. 7.21 **a** Location map of target area 11 (MVT Pb-Zn) in the study area; **b** Geological map of this area (extracted and GIS-ready from 1:100.000 geological map of Irankhah); **c** Aster image (VNIR; R:3, G:2, B:1) and **d** Fuzzy mineral potential map.

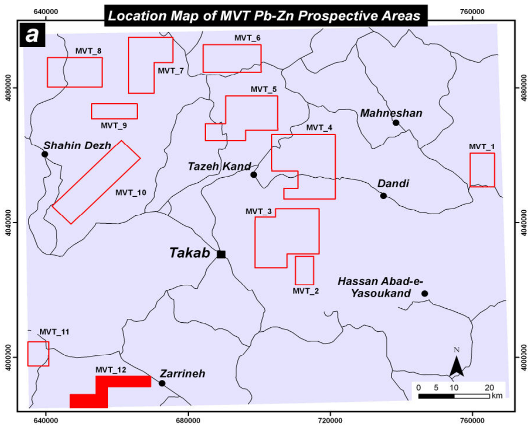

Fig. 7.22 **a** Location map of target area 12 (MVT Pb-Zn) in the study area; **b** Geological map of this area (extracted and GIS-ready from 1:100.000 geological map of Irankhah); **c** Ladsat 7 ETM+ (R:7, G:4, B:2) and **d** Fuzzy mineral potential map.

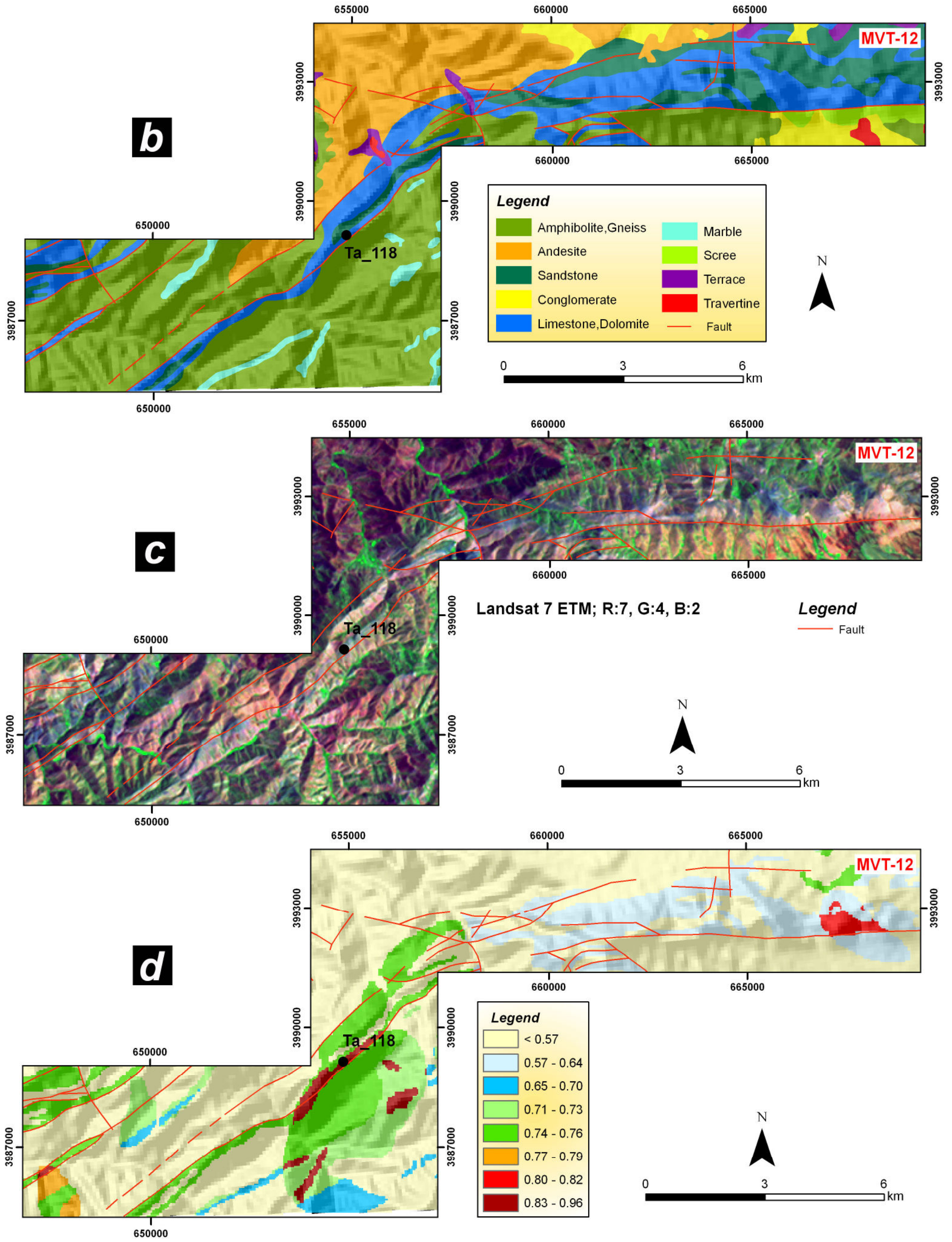

7.2.2 Carlin-Type Gold Target Areas

There were several possibilities for combination of fuzzy operations to integrate the fuzzy evidential maps and produce a mineral potential map of Carlin-type gold mineralization. Various inference networks were applied to derive the best final predictive map.

The predictive mineral potential map resulting from the inference network shown in figure 6.11 was selected as a favourable predictive map for field checking of Carlin-type gold target areas. Figure 7.3 and 7.4 show 10 target areas of Carlin-type gold potential on the fuzzy mineral potential map and Landsat 7 ETM$^+$ image.

The geo-exploration characteristics of Carlin-type gold target areas, chemical analysis results of samples and description of sampling places are as follows:

1- Area 1 (Carlin-type Au)

General Description: This target area is located in the eastern portion of the study area (Fig. 7.23a) covered by the 1:100.000 geological map of Yasoukand. Access to this area is by road from Dandi through Ebrahimabad, Qaleh Jough-e-Siah Mansour, Vizmak, Gaf Gol and Chahar Tagh.

Geology: The predominant geological rock units in this area include limestone, marl, schist, dacite, andesite and granite (Fig 7.23b; extracted and GIS-ready from 1:100.000 geological map of Yasoukand).

Structure: The major geological structural trend in this target area is NW-SE but the trend of minor faults is NE-SW (Fig. 7.23b).

Alteration: Argillic and sericitic altered rocks are seen in the central, eastern and southern parts of this target area (Fig. 7.23c).

2- Area 2 (Carlin-type Au)

General Description: This target area is located in the eastern portion of the study area (Fig. 7.24a) covered by the 1:100.000 geological maps of Yasoukand and Takab. Access to this area is by road from Hassan Abad-e-Yasoukand through Sheykh Besharat, Sarab and Agh Kand.

Geology: The predominant geological rock units in this area include limestone, sandstone, conglomerate, travertine, andesite, diorite, granite and rhyolite (Fig 7.24b; extracted and GIS-ready from 1:100.000 geological maps of Yasoukand and Takab).

Structure: The major geological structural trends in this target area are NW-SE and NE-SW (Fig. 7.24b).

Alteration: Argillic and sericitic altered rocks are exposed in different parts of this area (Fig. 7.24c).

Samples Description: 2 samples (Ta_119-120; Fig. 7.24) were taken from this target area. Values of gold respectively are 130 ppb and 25 ppb (analysis results and coordinate of sampling places attached in appendices).

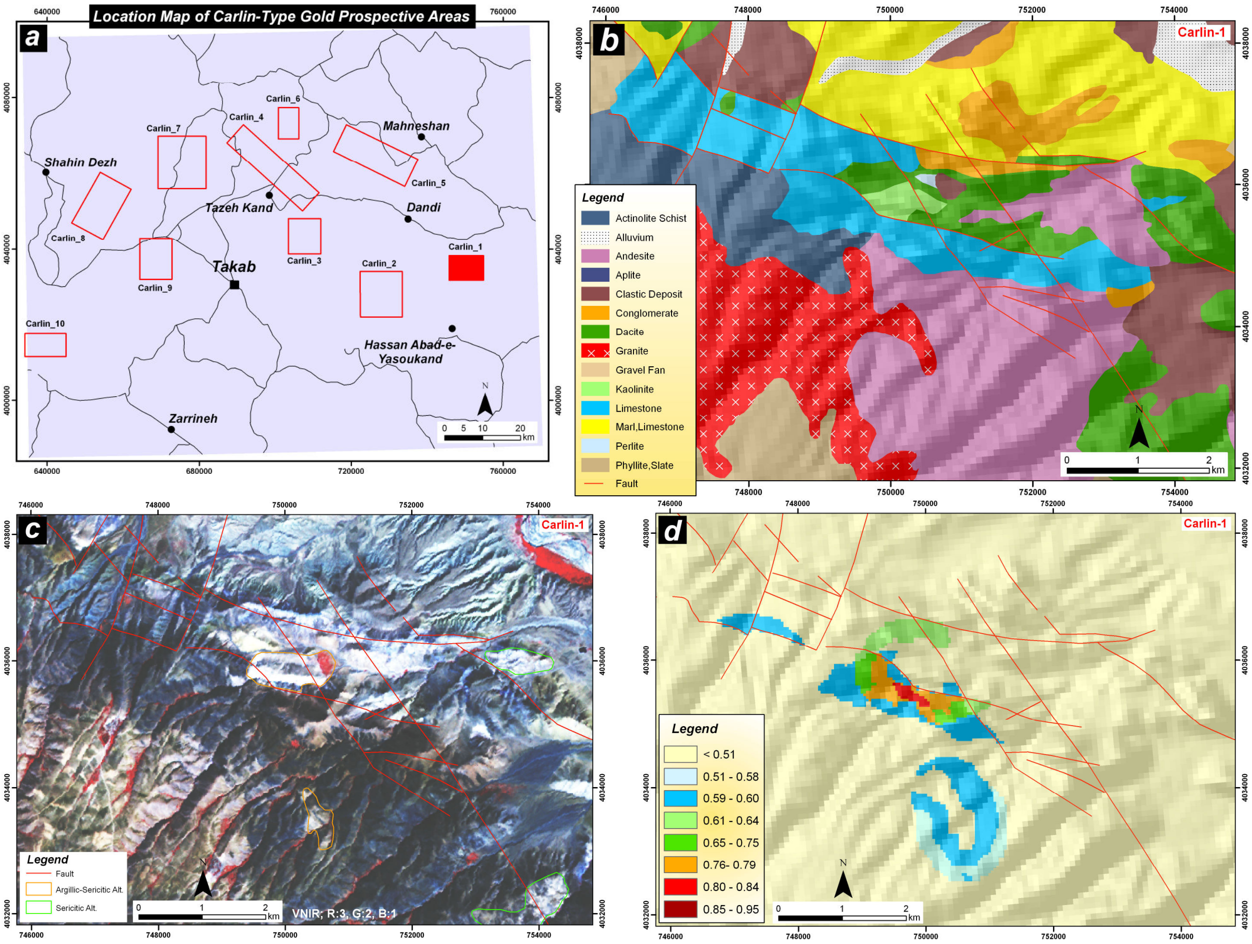

Fig. 7.23 **a** Location map of target area 1 (Carlin-type Au) in the study area; **b** Geological map of this area (extracted and GIS-ready from 1:100.000 geological map of Yasoukand); **c** Aster image (VNIR; R:3, G:2, B:1) and hydrothermally altered rocks (argillic and sericitic alteration) and **d** Fuzzy mineral potential map.

3- Area 3 (Carlin-type Au)

General Description: This target area is located in the central portion of the study area (Fig. 7.25a) covered by the 1:100.000 geological maps of Takab and Takht-e-Soleyman. Access to this area is by road from Takab through Badrlou, Chahar Tagh and Ghoushkhaneh.

Geology: The predominant geological rock units in this area include dolomite, limestone, travertine, micaschist, sandstone, conglomerate and quartz porphyry (Fig 7.25b; extracted and GIS-ready from 1:100.000 geological maps of Takab and Takht-e-Soleyman).

Structure: The major geological structural trends are NW-SE and NE-SW (Fig. 7.25b).

Alteration: Argillic and sericitic altered rocks are exposed in central part of this area (Fig. 7.25c).

Samples Description: 18 samples (Ta_40, Ta_44-48, Ta_51, Ta_56-59, Ta_60-65 and Ta_121; Fig. 7.25) were taken from this target area. A part of this target area is shared with area 3 of MVT Pb-Zn. Maximum value of gold belongs to the sample Ta_60 (120 ppb) (analysis results and coordinate of sampling places attached in appendices).

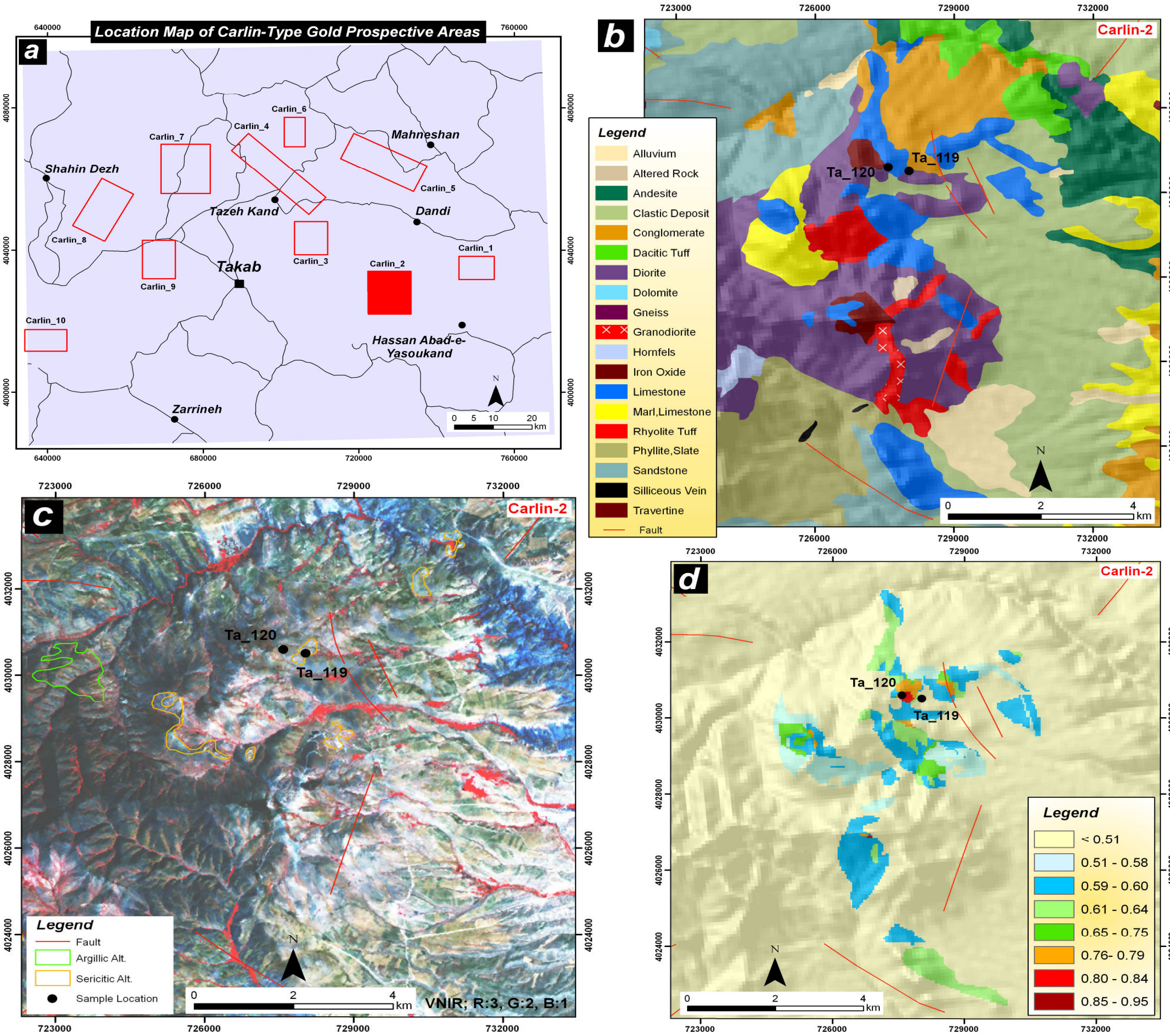

Fig. 7.24 **a** Location map of target area 2 (Carlin-type Au) in the study area; **b** Geological map of this area (extracted and GIS-ready from 1:100.000 geological maps of Yasoukand and Takab); **c** Aster image (VNIR; R:3, G:2, B:1) and hydrothermally altered rocks (argillic and sericitic alteration) and **d** Fuzzy mineral potential map.

4- Area 4 (Carlin-type Au)

General Description: This target area is located in the central to northern part of the study area (Fig. 7.26a) covered by the 1:100.000 geological map of Takht-e-Soleyman. Access to this area is by road from Takab through Shirmard, Zarshouran or Ghinarjeh

Geology: The predominant geological rock units in this area include micaschist, conglomerate, andesite, dolomite, limestone, travertine, dacite, komatite, tuff and gneiss (Fig 7.26b; extracted and GIS-ready from 1:100.000 geological map of Takht-e-Soleyman).

Structure: The major geological structural trend in this target area is NW-SE but the trends of minor faults are NE-SW and W-E (Fig. 7.26b).

Alteration and Mineralization: Argillic and sericitic altered rocks are exposed in different parts of this area (Fig. 7.26c) and the Zarshouran gold deposit (Fig. 7.26) is located in the northern part as a high priority of the fuzzy mineral potential map (Fig. 7.26d).

Samples Description: 13 samples (Ta_81-86, Ta_90, Ta_94-96 and Ta_122-124; Fig. 7.26) were taken from this target area. A part of this target area is shared with areas 4 and 5 of MVT Pb-Zn. Maximum values of gold belong to the samples Ta_82 and Ta_85 (10 ppb) (analysis results and coordinate of sampling places attached in appendices).

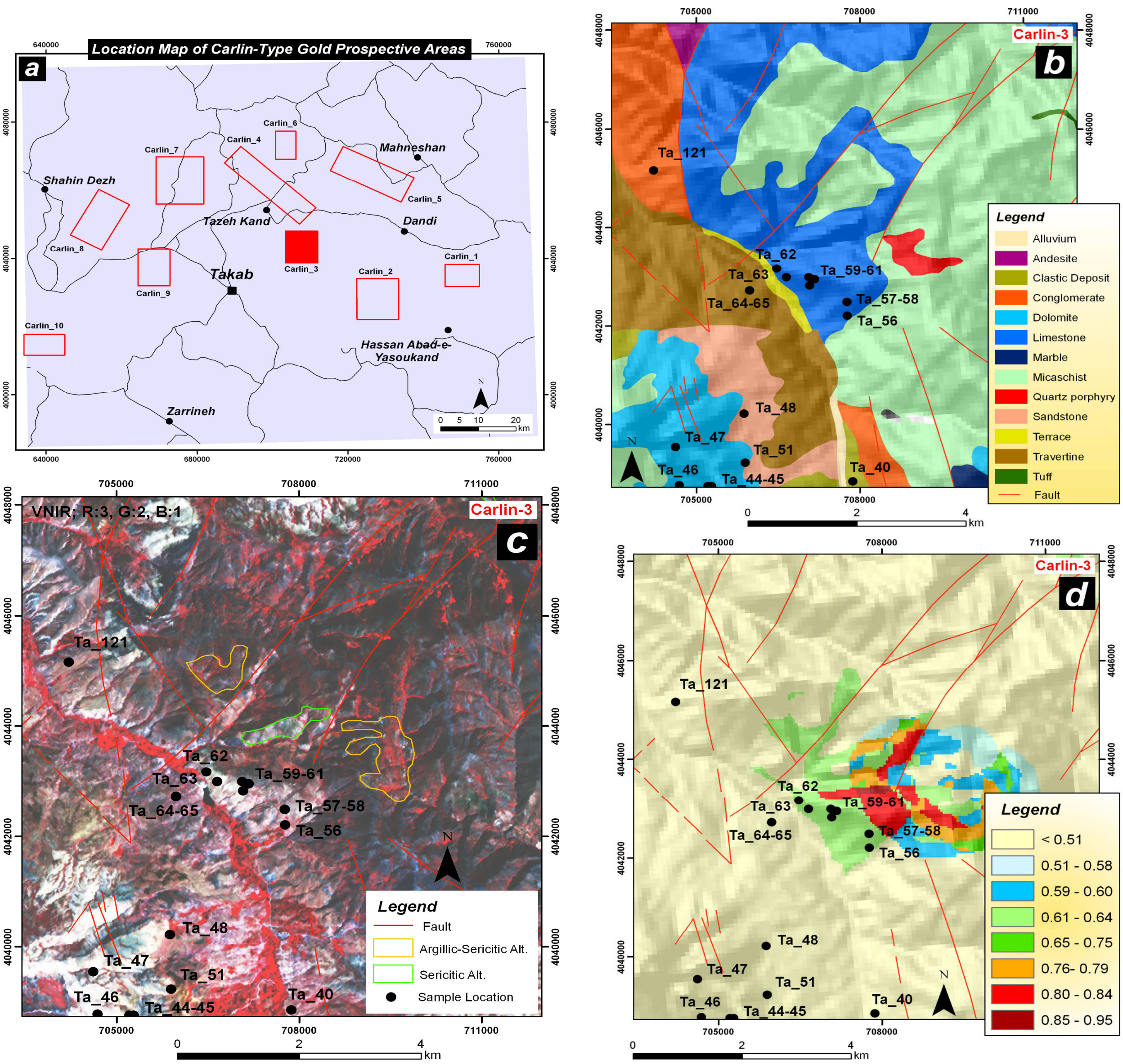

Fig. 7.25 **a** Location map of target area 3 (Carlin-type Au) in the study area; **b** Geological map of this area (extracted and GIS-ready from 1:100.000 geological maps of Takab and Takht-e-Soleyman); **c** Aster image (VNIR; R:3, G:2, B:1) and hydrothermally altered rocks (argillic and sericitic alteration) and **d** Fuzzy mineral potential map.

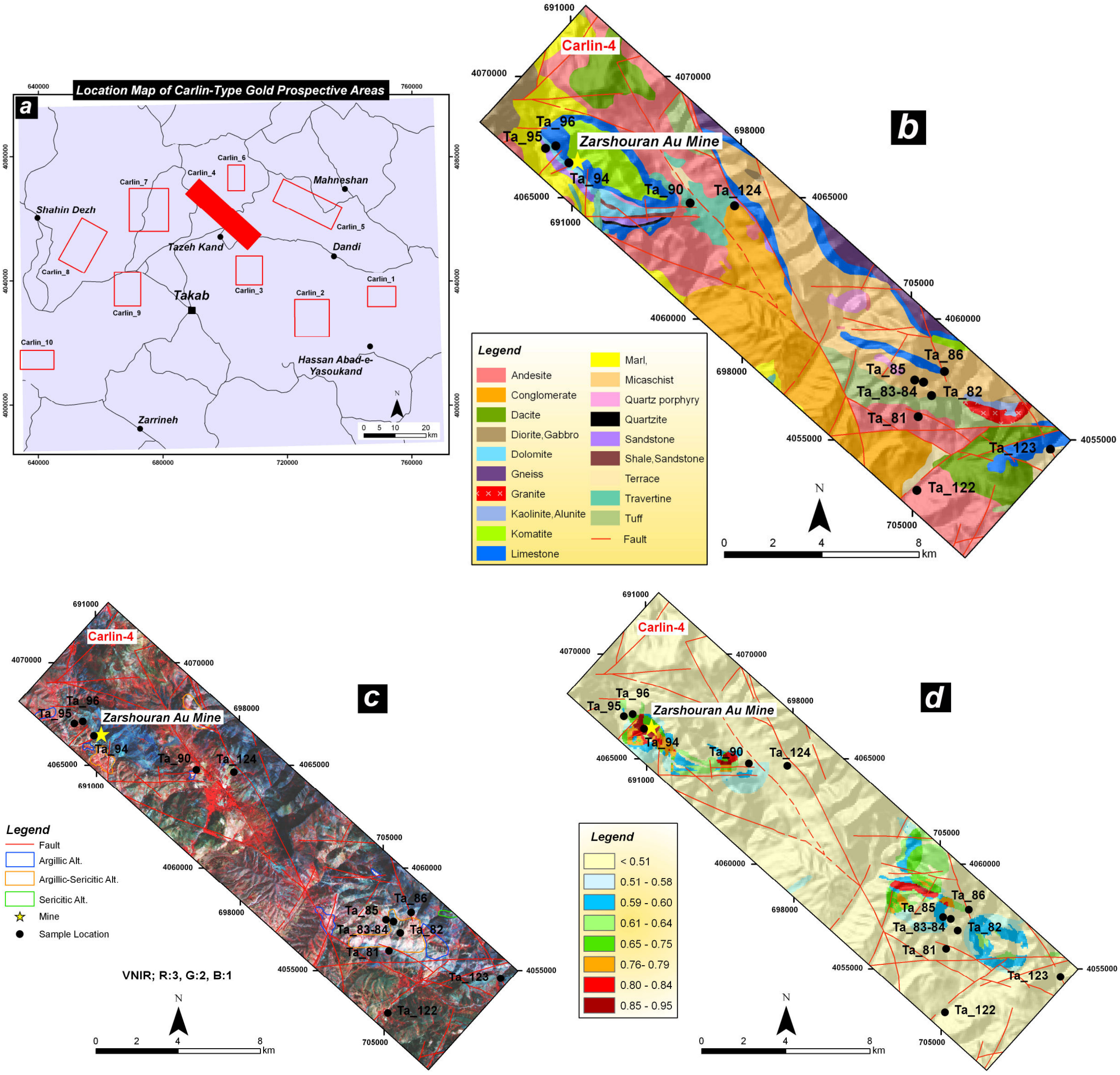

Fig. 7.26 **a** Location map of target area 4 (Carlin-type Au) in the study area; **b** Geological map of this area (extracted and GIS-ready from 1:100.000 geological map of Takht-e-Soleyman); **c** Aster image (VNIR; R:3, G:2, B:1) and hydrothermally altered rocks (argillic and sericitic alteration) and **d** Fuzzy mineral potential map and place of gold (Au) mineralization (the Zarshouran gold deposit is located in the high priority category of this map).

5- Area 5 (Carlin-type Au)

General Description: This target area is located in the central to northeastern part of the study area (Fig. 7.28a) covered by the 1:100.000 geological maps of Mahneshan and Takht-e-Soleyman. Access to this area is by road from Dandi through Khanik, Hajiaynak and Aqkand.

Geology: The predominant geological rock units in this area include granite, marble, limestone, dolomite, marl, amphibolites and gneiss (Fig 7.28b; extracted and GIS-ready from 1:100.000 geological maps of Mahneshan and Takht-e-Soleyman). Figure 7.27 shows the geological sketch map of the Aqkand sampling area.

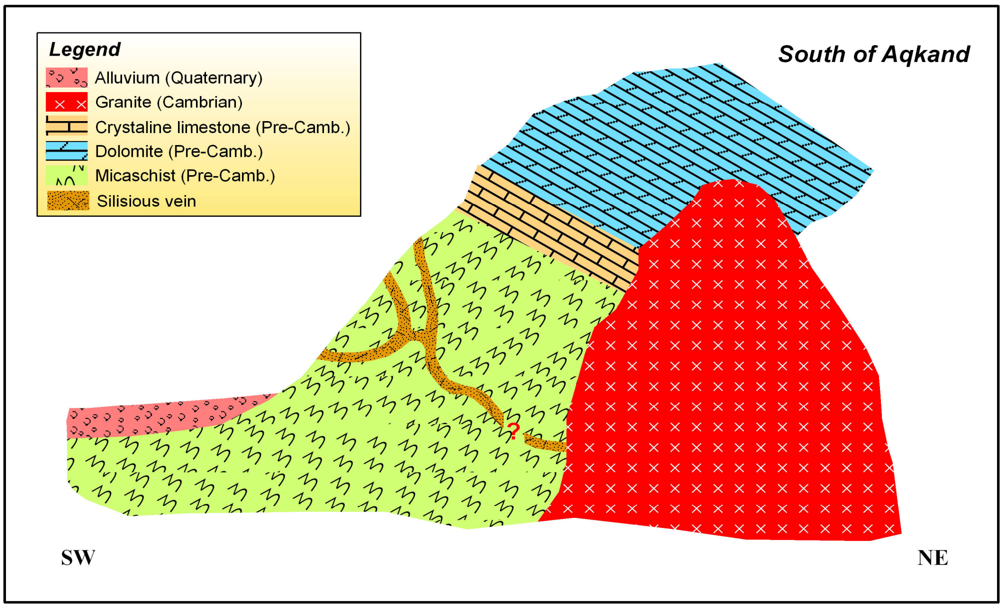

Fig. 7.27 Geological sketch map of the Aqkand sampling area. "n.b. schematic sketch map, not to scale".

Structure: The major geological structural trend in this target area is NW-SE (Fig. 7.28b).

Alteration and Mineralization: Argillic and sericitic altered rocks are exposed in different parts of this area (Fig. 7.28c) and the Ghuzlou Pb-Au and Pashtok Pb-Zn deposits and As (Arsenic) anomaly (Fig. 7.28) are located in the western part.

Samples Description: 13 samples (Ta_125-137; Fig. 7.28) were taken from this target area. Maximum value of gold is 1300 ppb (Ta_131) also the content of gold in sample Ta_128 is 360 ppb (analysis results and coordinate of sampling places attached in appendices).

6- Area 6 (Carlin-type Au)

General Description: This target area is located in the northern part of the study area (Fig. 7.29a) covered by the 1:100.000 geological map of Takht-e-Soleyman. Access to this area is by road from Takab through Shirmard, Zarshouran, Ghinarjeh, Alam Kandi and Chaigheshlagh.

Geology: The predominant geological rock units in this area include gneiss, marble, amphibolites, andesite, tuff and granodiorite (Fig 7.29b; extracted and GIS-ready from 1:100.000 geological map of Takht-e-Soleyman).

Structure: The major geological structural trends in this target area are almost W-E and N-S (Fig. 7.29b).

Alteration: Argillic and sericitic altered rocks are exposed in the central and western parts of this target area (Fig. 7.29c).

7- Area 7 (Carlin-type Au)

General Description: This target area is located in the central to northwestern part of the study area (Fig. 7.30a) covered by the 1:100.000 geological maps of Takht-e-Soleyman and Shahindezh. Access to this area is by road from Takab through Shirmard and Aqdarreh.

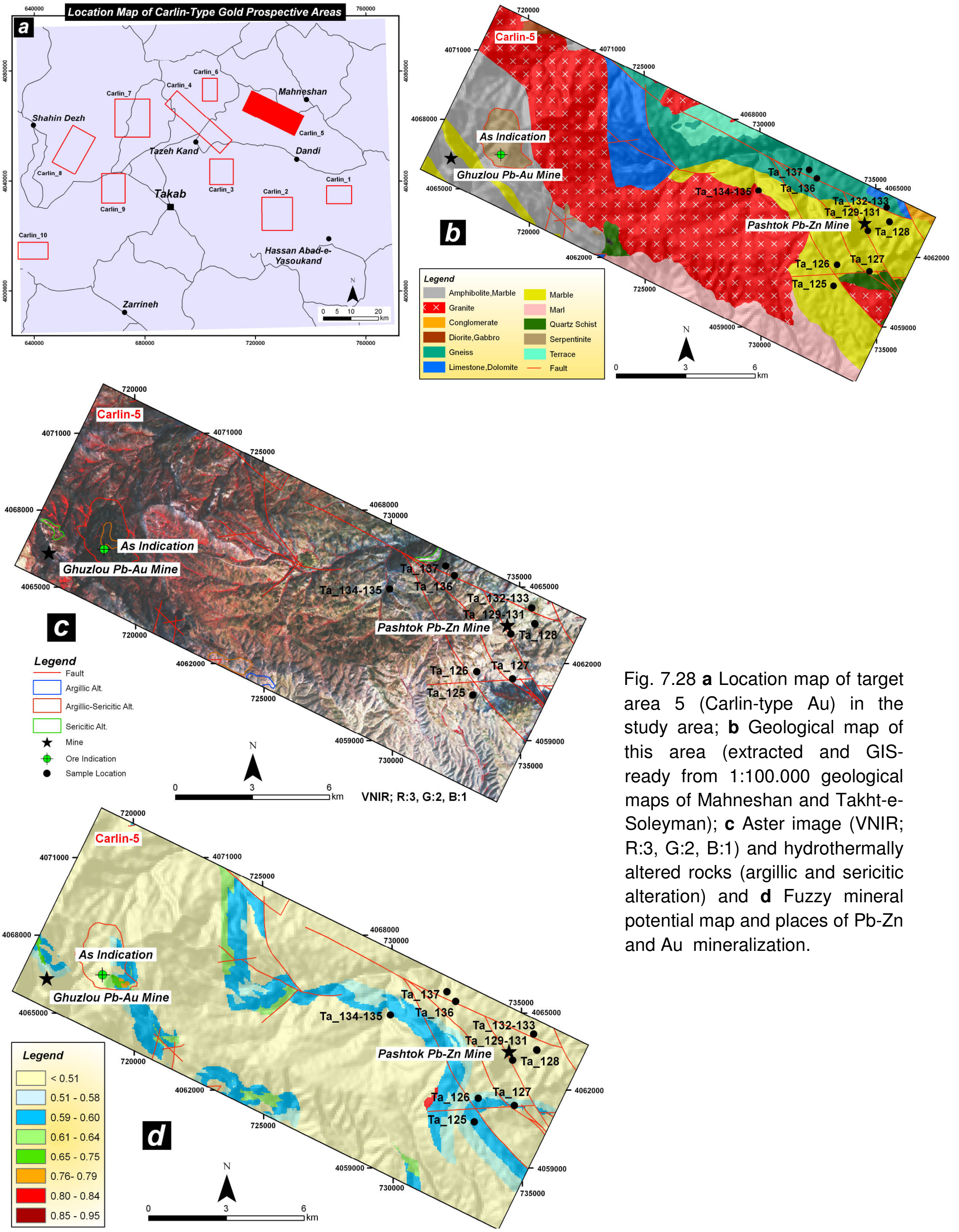

Fig. 7.28 **a** Location map of target area 5 (Carlin-type Au) in the study area; **b** Geological map of this area (extracted and GIS-ready from 1:100.000 geological maps of Mahneshan and Takht-e-Soleyman); **c** Aster image (VNIR; R:3, G:2, B:1) and hydrothermally altered rocks (argillic and sericitic alteration) and **d** Fuzzy mineral potential map and places of Pb-Zn and Au mineralization.

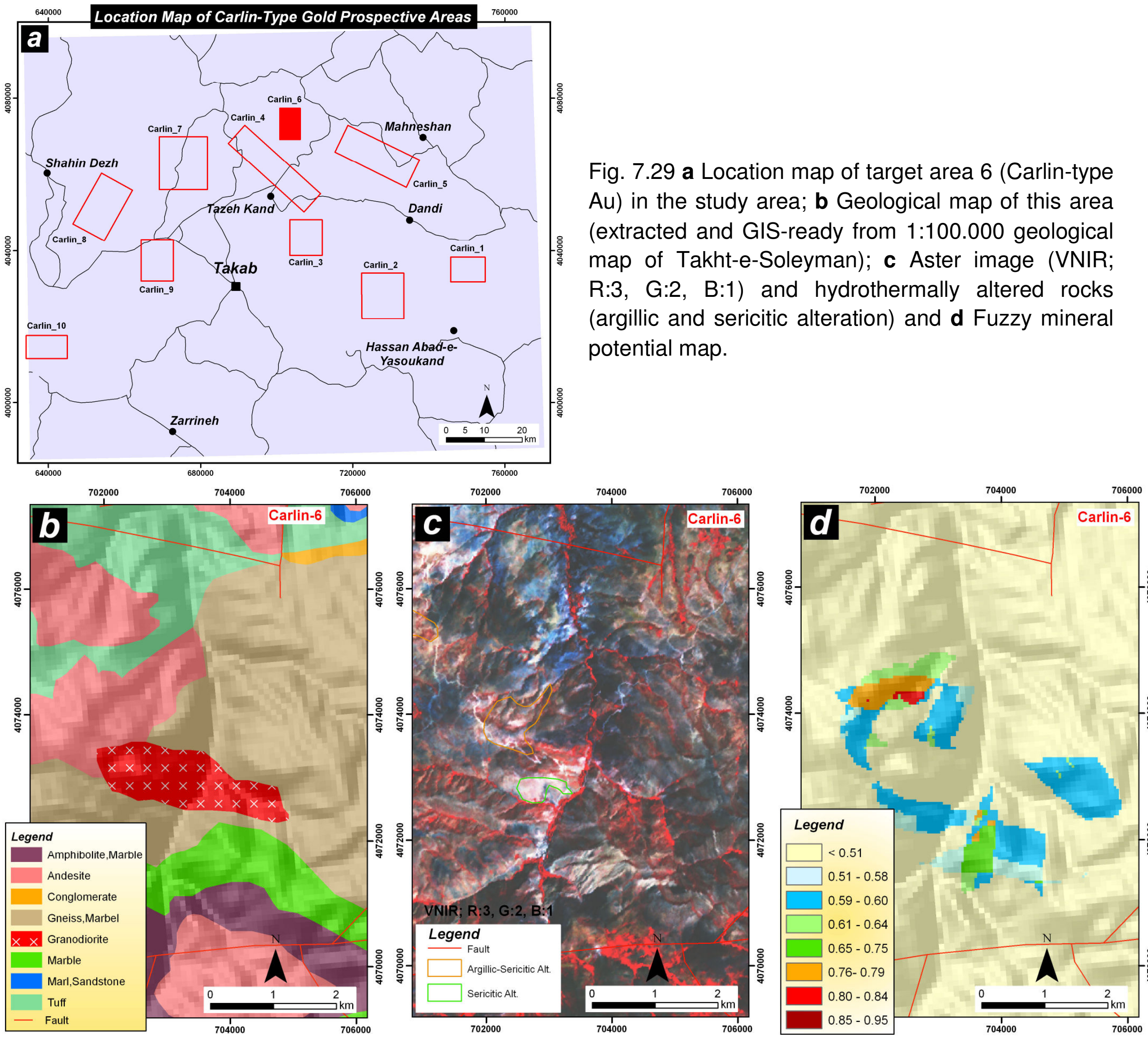

Fig. 7.29 **a** Location map of target area 6 (Carlin-type Au) in the study area; **b** Geological map of this area (extracted and GIS-ready from 1:100.000 geological map of Takht-e-Soleyman); **c** Aster image (VNIR; R:3, G:2, B:1) and hydrothermally altered rocks (argillic and sericitic alteration) and **d** Fuzzy mineral potential map.

Geology: The predominant geological rock units in this area include limestone, dolomite, marl, shale, conglomerate, quartz porphyry and granite (Fig 7.30b; extracted and GIS-ready from 1:100.000 geological map of Takht-e-Soleyman and Shahindezh).

Structure: The major geological structural trends in this target area are almost NW-SE and N-S and the trend of minor faults is NE-SW (Fig. 7.30b).

Alteration and Mineralization: Argillic and sericitic altered rocks are exposed in different parts of this area (Fig. 7.30c). The Aqdarreh gold (Au) deposit and Dashghiz Ghapan antimony (Sb) mine and also the Aqdarreh Sb and Shakh Shakh gold anomalies (Fig.7.30) are located in this target area.

Samples Description: 3 samples (Ta_138-140; Fig. 7.30) were taken from this target area. Maximum value of gold belongs to the sample Ta_139 (40 ppb) (analysis results and coordinate of sampling places attached in appendices).

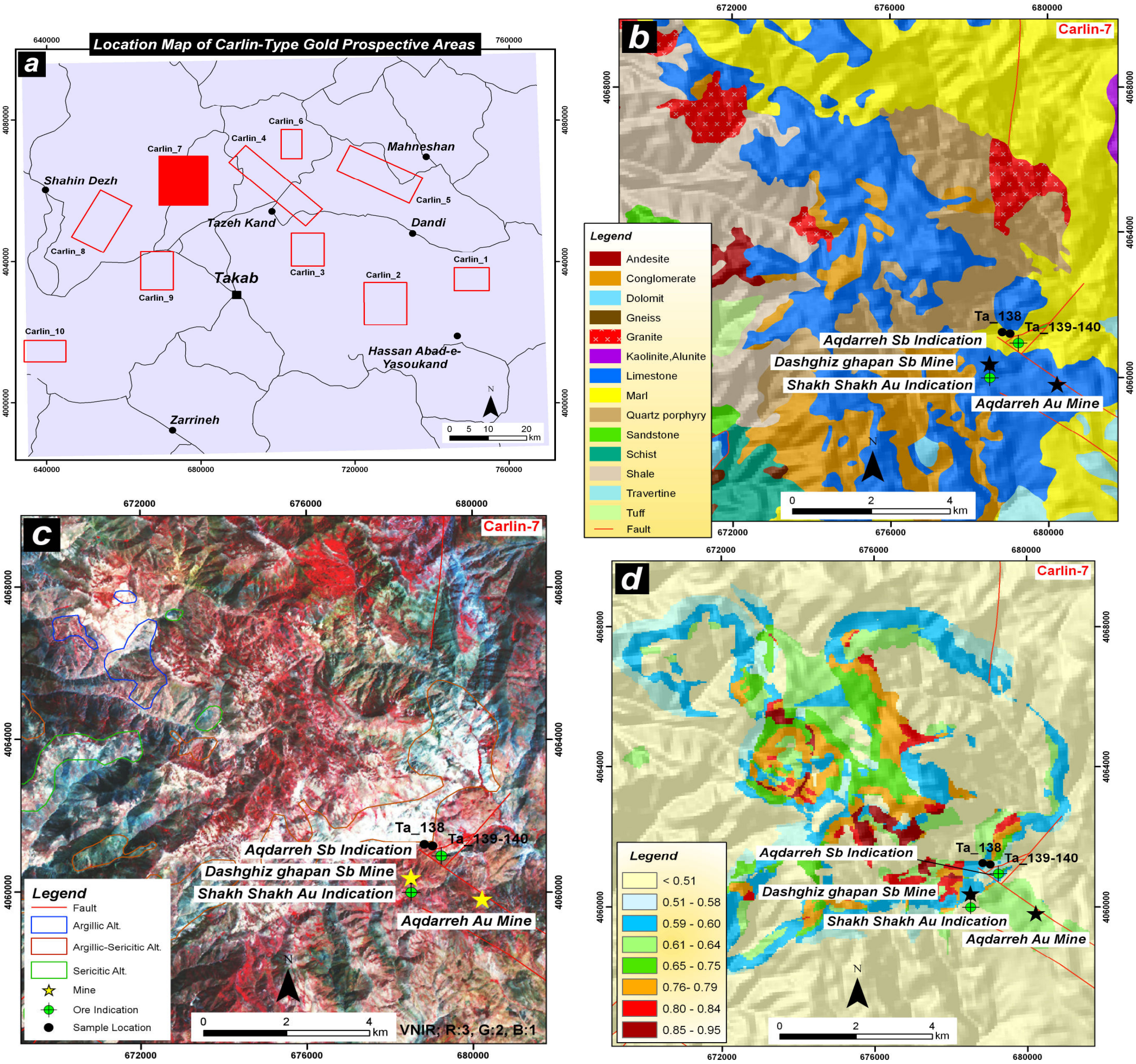

Fig. 7.30 **a** Location map of target area 7 (Carlin-type Au) in the study area; **b** Geological map of this area (extracted and GIS-ready from 1:100.000 geological maps of Takht-e-Soleyman and Shahindezh); **c** Aster image (VNIR; R:3, G:2, B:1) and hydrothermally altered rocks (argillic and sericitic alteration) and **d** Fuzzy mineral potential map and places of gold (Au) and antimony (Sb) mineralization.

8- Area 8 (Carlin-type Au)

General Description: This target area is located in the northern part of the study area (Fig. 7.31a) covered by the 1:100.000 geological map of Shahindezh. Access to this area is by road from Shahindezh through Hacheh Su and Kord Kandi.

Geology: The predominant geological rock units in this area include dolomite, limestone, sandstone, shale, schist, gneiss, granite and rhyolite (Fig 7.31b; extracted and GIS-ready from 1:100.000 geological map of Shahindezh).
Structure: The major geological structural trend in this target area is NW-SE (Fig. 7.31b).

Alteration: Argillic and sericitic altered rocks are exposed in different parts of this target area (Fig. 7.31c).

Samples Description: 3 samples (Ta_115-117; Fig. 7.31) were taken from this target area. A part of this target area is shared with area 10 of MVT Pb-Zn. Maximum value of gold belongs to the sample Ta_117 (5 ppb) (analysis results and coordinate of sampling places attached in appendices).

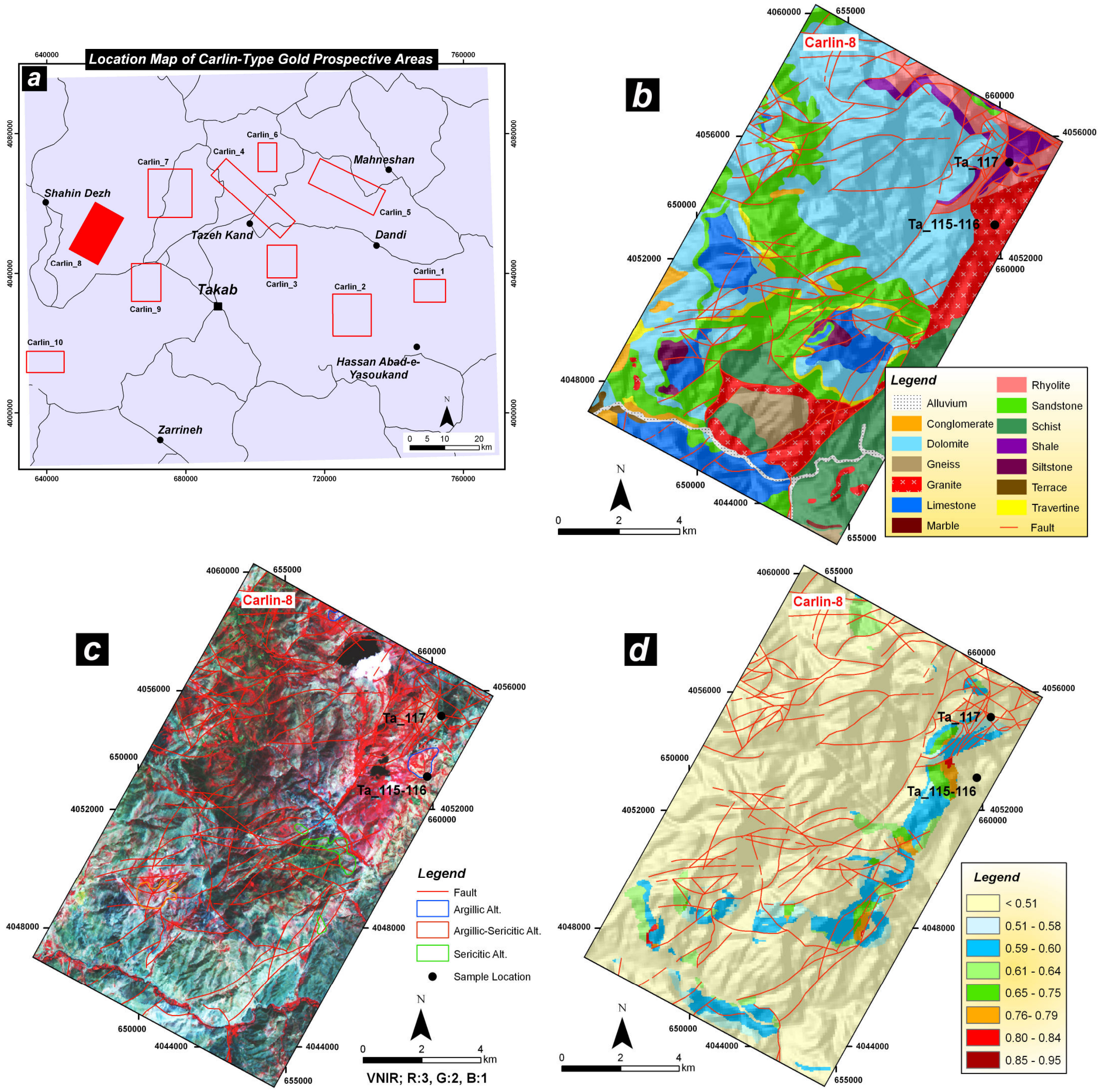

Fig. 7.31 **a** Location map of target area 8 (Carlin-type Au) in the study area; **b** Geological map of this area (extracted and GIS-ready from 1:100.000 geological map of Shahindezh); **c** Aster image (VNIR; R:3, G:2, B:1) and hydrothermally altered rocks (argillic and sericitic alteration) and **d** Fuzzy mineral potential map.

9- Area 9 (Carlin-type Au)

General Description: This target area is located in the western part of the study area (Fig. 7.32a) covered by the 1:100.000 geological maps of Shahindezh and Irankhah. Access to this area is by road from Takab (to Shahindezh) through Chopli, Goy Aghaj and Khar Khar.

Geology: The predominant geological rock units in this area include limestone, marl, conglomerate, gneiss, travertine and granite (Fig 7.32b; extracted and GIS-ready from 1:100.000 geological maps of Shahindezh and Irankhah).

Samples Description: 4 samples (Ta_141-144; Fig. 7.32) were taken from this target area (analysis results and coordinate of sampling places attached in appendices).

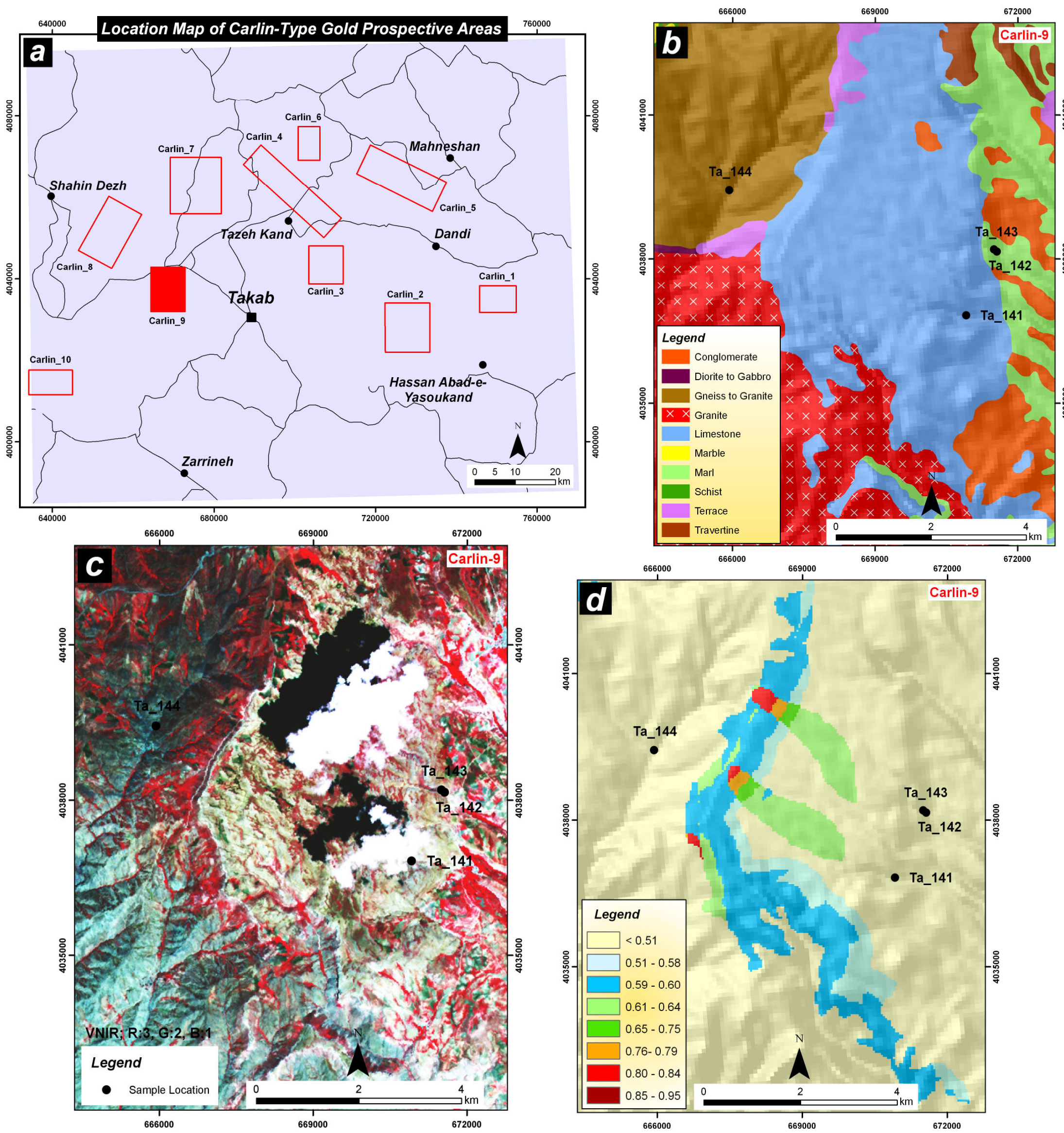

Fig. 7.32 **a** Location map of target area 9 (Carlin-type Au) in the study area; **b** Geological map of this area (extracted and GIS-ready from 1:100.000 geological maps of Shahindezh and Irankhah); **c** Aster image (VNIR; R:3, G:2, B:1) and **d** Fuzzy mineral potential map.

10- Area 10 (Carlin-type Au)

General Description: This target area is located in the south-east of the study area (Fig. 7.33a) covered by the 1:100.000 geological map of Irankhah. Access to this area is by road from Saqez through Saheb, Qaleh Kohneh, Chagharlu and Aliabad.

Geology: The predominant geological rock units in this area include dolomite, conglomerate, shale, andesite and granite (Fig 7.33b; extracted and GIS-ready from 1:100.000 geological map of Irankhah).

Structure: The major geological structural trend in this target area is NE-SW (Fig. 7.33b).

Alteration and Mineralization: Argillic-sericitic altered rocks are exposed in the central part of this area (Fig. 7.33c) and the Qaleh Kohneh and Yapesh Khan gold anomalies (Fig. 7.33) are located in this target area (Yapesh Khan gold anomaly is located in the high priority category of the fuzzy mineral potential map; Fig. 7.33d).

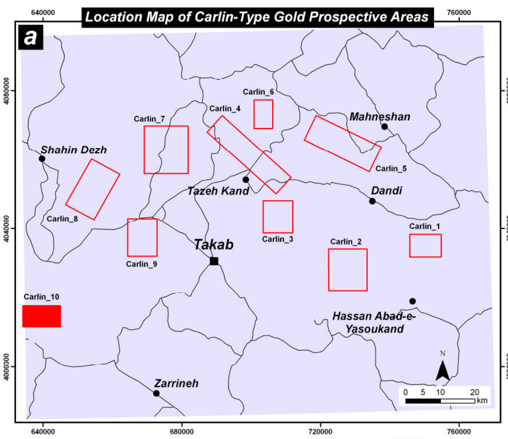

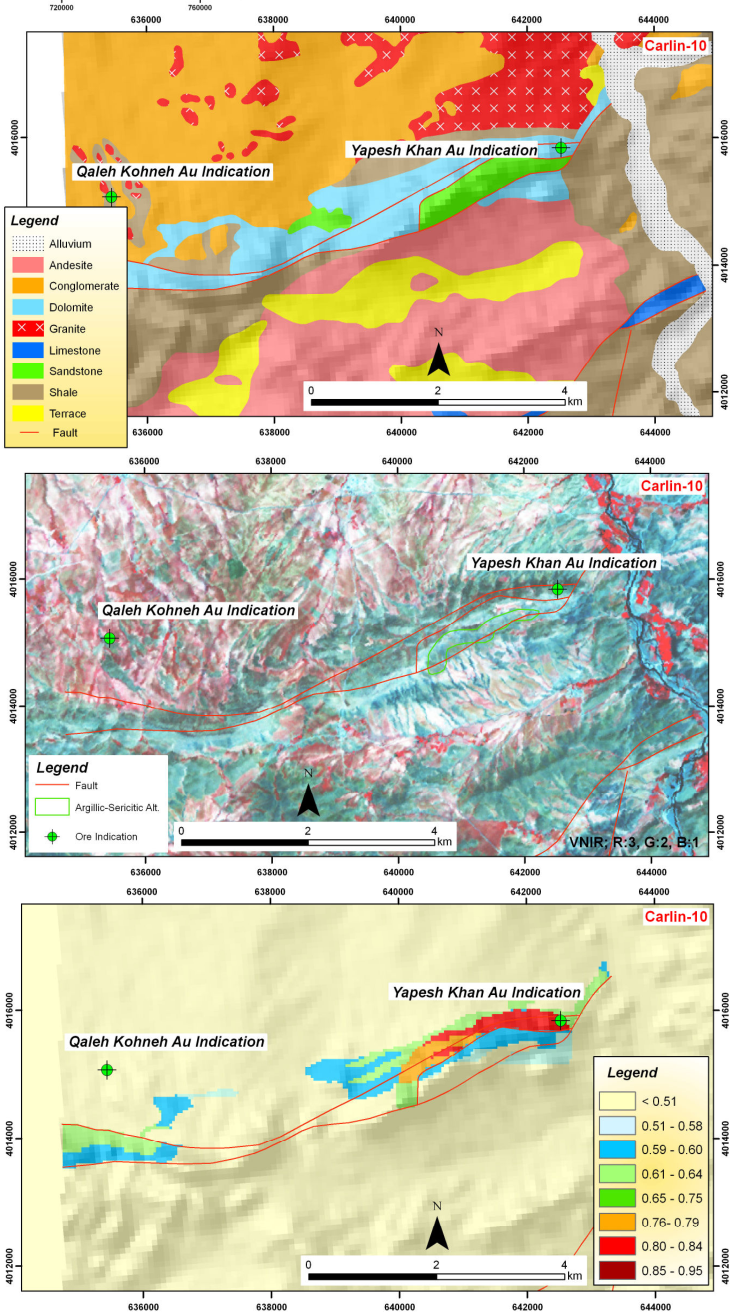

Fig. 7.33 **a** Location map of target area 10 (Carlin-type Au) in the study area; **b** Geological map of this area (extracted and GIS-ready from 1:100.000 geological map of Irankhah); **c** Aster image (VNIR; R:3, G:2, B:1) and hydrothermally altered rocks (argillic-sericitic alteration) and **d** Fuzzy mineral potential map and places of gold (Au) mineralization (the Yapesh Khan gold anomaly is located in the high priority category of this map).

Chapter 8 Conclusions

8.1 Introduction

GIS technology is valuable to all stages of mineral exploration and mineral potential mapping is an important task in regional exploration, as it is necessary at each stage to select the most promising areas on the basis of multiple sets of geo-exploration data (Pan et al., 2000).

Processing, analysis and integration of spatial data by GIS methods is useful in mineral potential mapping. As a consequence, the combination of metallogenetic modeling and modern GIS and remote sensing techniques provide powerful new tools for the identification of undiscovered mineral deposits.

The initial modeling program laid the foundation to establishing a process to use GIS methods to help guide regional exploration programs in Takab region. In reprocessing the geo-exploration datasets the results vary significantly from the first model. Knowledge about the spatial association between mineral deposits and structural features is important in mineral exploration. The structural model especially remote sensing structures needed to be simplified. The fuzzy mineral potential maps of MVT Pb-Zn and Carlin-type gold deposits were heavily influenced by the geochemical data, geological data (host rock or probable heat source) and structural data (remote sensing, geophysical and geological structural features).

8.2 Geotechnical Assessment of the Models

Fuzzy logic and index overlay methods comparison indicate some differences in the patterns but almost all of the most important deposits in the district are predicted satisfactorily (e.g. Angouran MVT Pb-Zn and Zarshouran Carlin-type gold deposits).

High probability areas in both models show differences in absolute values, according to the method, but generally predict the same regions. Additionally, there are some priorities for two types of mineralization in the predictive maps that can be considered in new regional explorations.

8.2.1 Comparison of Mineral Potential Maps

Comparing the results of mineral potential maps in two methods (fuzzy logic and index overlay) for both MVT Pb-Zn and Carlin-type gold mineralization shows that a number of the primary defined targets are eliminated and a number of new targets indicated. It must be recognized that these will need to be evaluated with care as it is possible that the modeling process has still not been thoroughly optimized and maybe a number of erroneous targets have been defined.

The fuzzy mineral potential map of MVT Pb-Zn in Takab region was divided into 5 mineralization blocks (Fig. 8.1) based on target areas for simple comparison. Additionally these blocks were plotted on the mineral potential map of MVT Pb-Zn with index overlay method (Fig. 8.2).

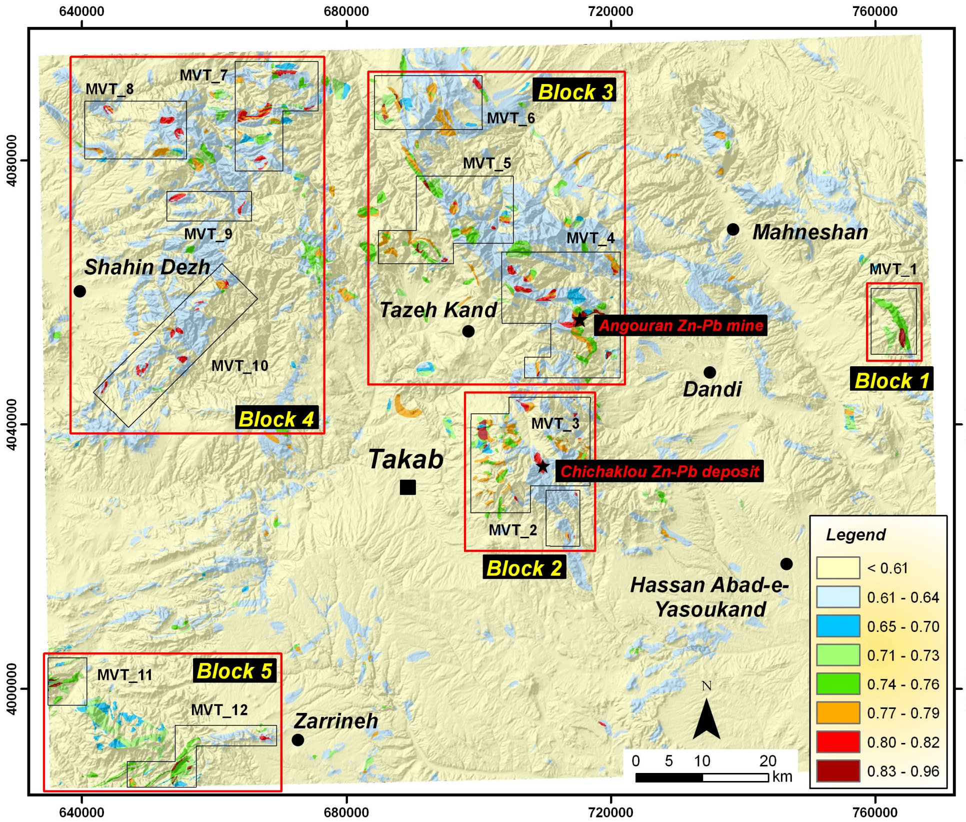

Fig. 8.1 Mineralization blocks in the mineral potential map of MVT Pb-Zn with fuzzy logic method.

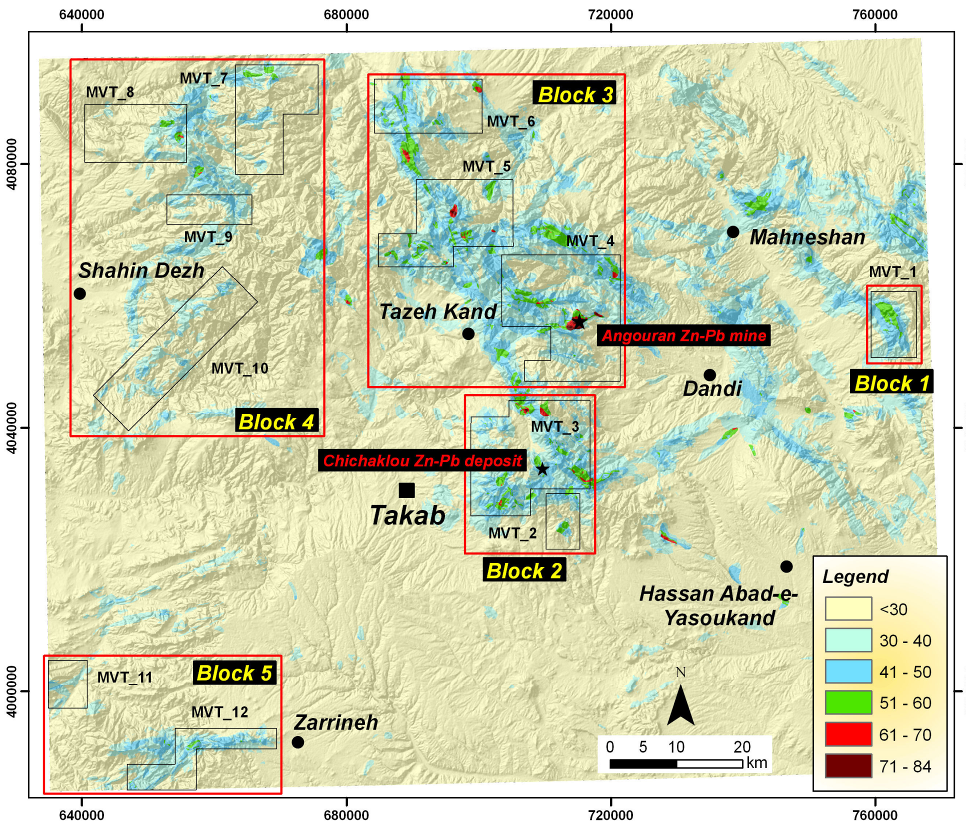

Fig. 8.2 Mineralization blocks in the mineral potential map of MVT Pb-Zn with index overlay method.

For example comparison of mineralization block 2 (Fig. 8.3) and block 3 (Fig. 8.4) on the mineral potential map of MVT Pb-Zn both with fuzzy logic and index overlay methods show some similarities and differences in the blocks 2 and 3 between two data integration methods but in general in the most parts the pattern of priorities of prospective areas are similar and differences occur only in the grade of these areas. The priorities associated with the prospective areas delineated through fuzzy logic integration method in the mineral potential map of MVT Pb-Zn are higher than those defined through index overlay method. The fuzzy logic integration method delineated larger favorable target areas than the index overlay method in this mineralization model (described in chapter 6). Almost two of the most important carbonate hosted Pb-Zn deposits in the district (Angouran and Chichaklou Zn-Pb deposits) are predicted satisfactorily specially in the fuzzy mineral potential map (Fig. 8.1 & 8.2).

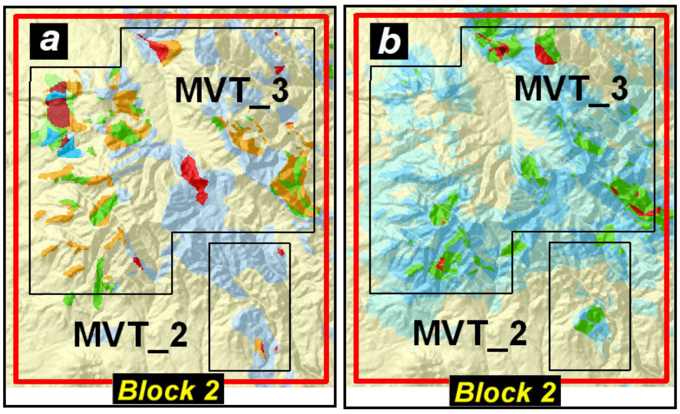

Fig. 8.3 Comparison of mineralization block 2 on the mineral potential map of MVT Pb-Zn with **a** Fuzzy logic and **b** Index overlay methods.

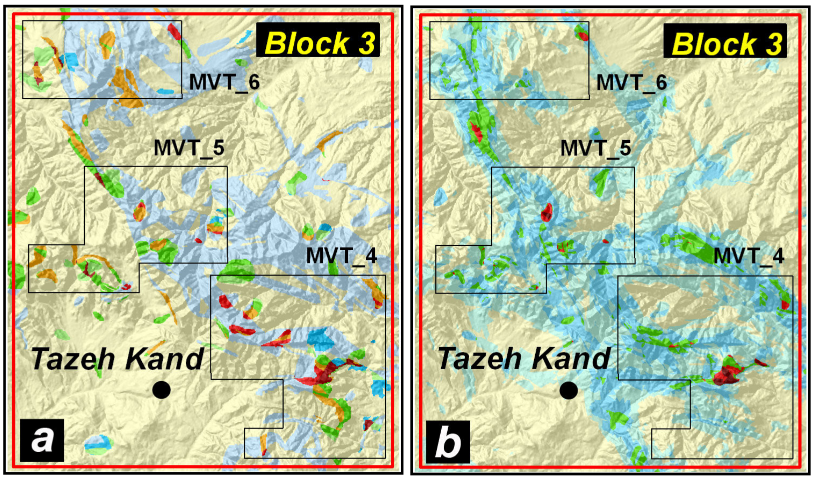

Fig. 8.4 Comparison of mineralization block 3 on the mineral potential map of MVT Pb-Zn with **a** Fuzzy logic and **b** Index overlay methods.

The fuzzy mineral potential map of Carlin-type gold in Takab region was divided to 5 mineralization blocks (Fig. 8.5) based on target areas. These blocks were plotted on the mineral potential map of Carlin-type gold with index overlay method (Fig. 8.6) for simple comparison. The similarities and differences in the blocks 3 of mineral potential map of Carlin-type gold between two data integration methods (fuzzy logic and index overlay) are seen in the figure 8.7. In this figure the similar mineralization pattern of favourable areas shows the similar places in two mineral potential maps but in index overlay method favorable areas are larger than fuzzy method. Also in this mineral potential map two of the most important Carlin-type gold deposits in the district (Zarshouran and Aqdarreh gold deposits) are predicted satisfactorily (Fig. 8.5 & 8.6).

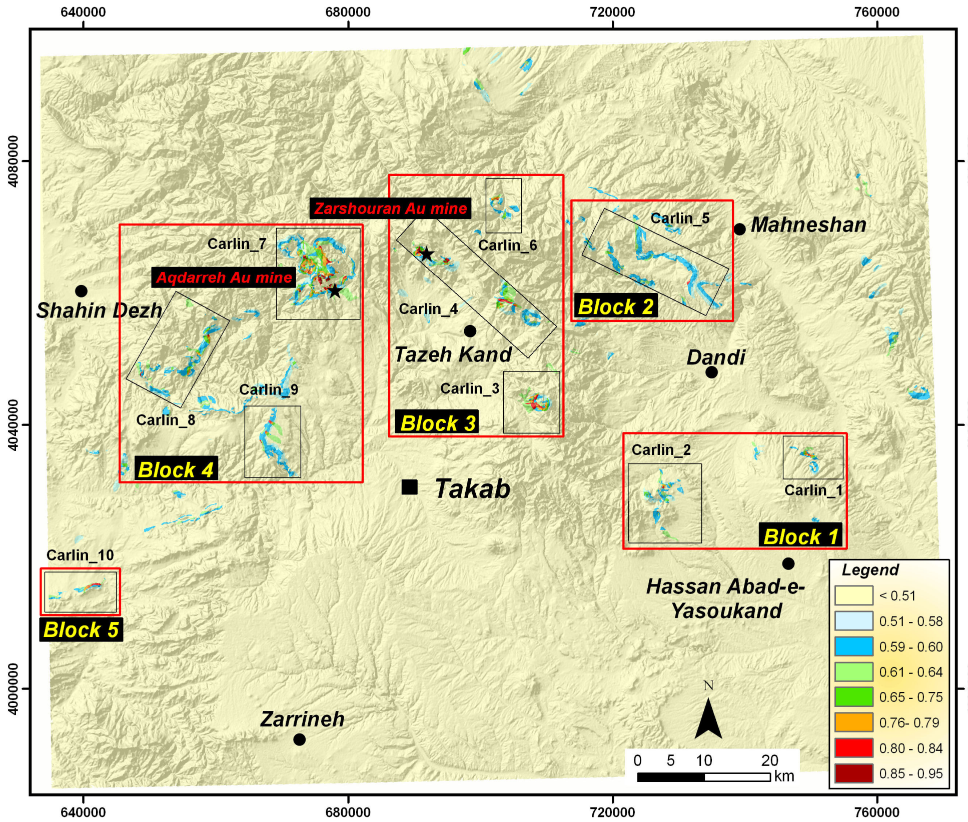

Fig. 8.5 Mineralization blocks in the mineral potential map of Carlin-type gold with fuzzy logic method.

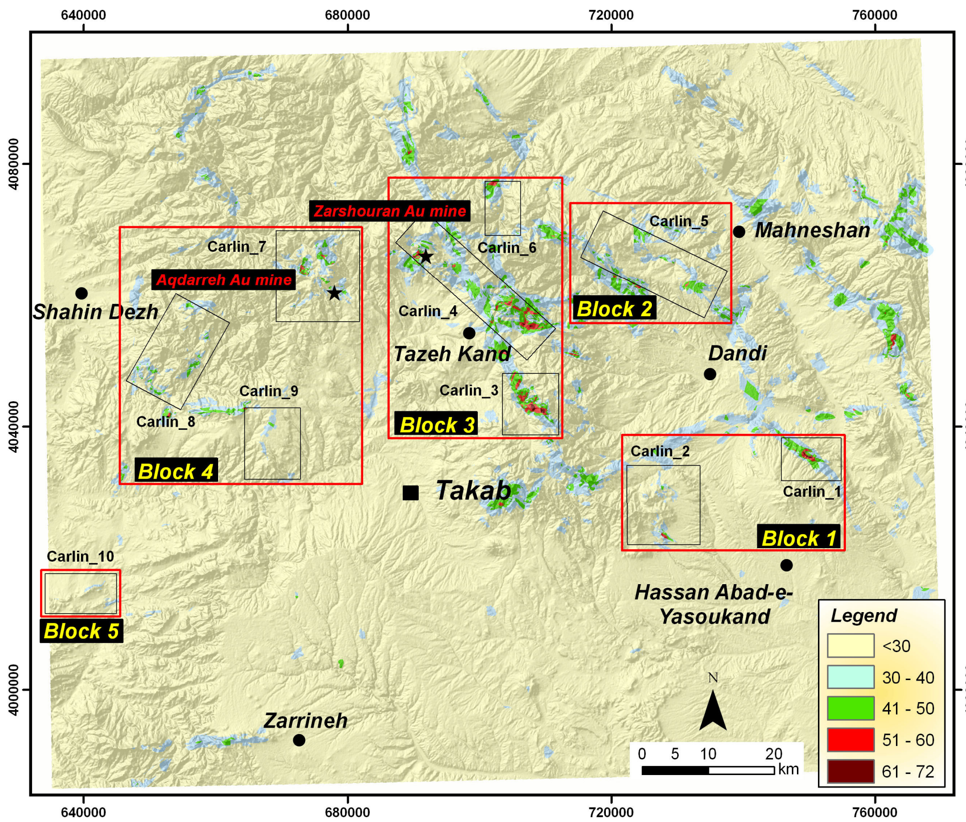

Fig. 8.6 Mineralization blocks in the mineral potential map of Carlin-type gold with index overlay method.

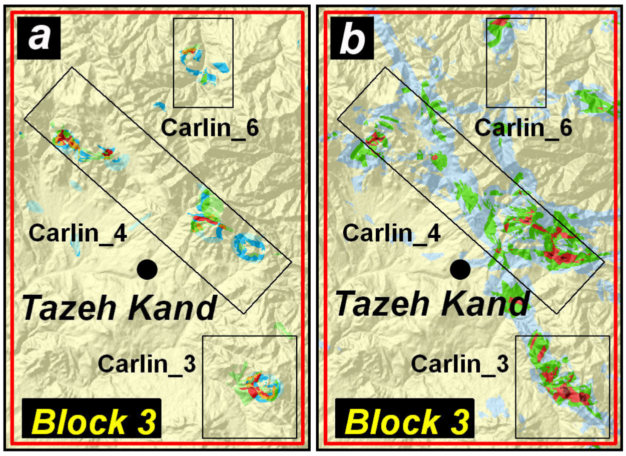

Fig. 8.7 Comparison of mineralization block 3 on the mineral potential map of Carlin-type gold with **a** Fuzzy logic and **b** Index overlay methods.

8.2.2 Comparative Analysis of the Favorability Targets

In mineral potential mapping, spatial analysis and integration of evidential maps by GIS modeling depends on the geo-exploration datasets, its spatial relationship between data layers and mineralization factors and selected ore deposit models in the study area. Generally for two of the above integration methods the geo-exploration datasets and the exploration models were the same. Both integration methods (fuzzy logic and index overlay) indicated a proper reliability in identifying of favorable prospective areas in Takab region. More target areas identified by the fuzzy method also were identified by the index overlay method for both mineralization models.

A measure of similarities and differences of the delineated favourable target areas between a pair of binary predictive potential maps by different integration methods is determined by calculating Jaccard's similarity coefficient (C_j) (Bonham-Carter, 1994), which is defined as:

$$C_j = \frac{T_{11}}{T_{12} + T_{21} + T_{11}} \tag{8.1}$$

Where T_{11} is the number of pixels of the 'positive overlap' of predicted favourable zones, T_{12} and T_{21} are number of pixels of mismatch (i.e., overlap of favourable zones in one map with unfavourable zones in the other map). Note that the 'negative overlap' of unfavourable zones is not considered, so the comparison is about the predicted favourable zones only. Jaccard's similarity coefficient ranges between zero (complete dissimilarity) and one (complete similarity).

A coefficient of at least 0.66 is here considered to represent good similarity, a coefficient of 0.33-0.66 is considered to represent fair similarity and a coefficient below 0.33 is considered to represent poor similarity (Carranza, 2002).

According to the equation 8.1, C_j (Jaccard's similarity coefficient) for the data of MVT potential maps is 579 / (801 + 286 + 579) = 0.347.

A similar similarity measure is the so-called simple matching coefficient, C_a, which is defined as the total area where the patterns match (positive and negative) divided by the total area (eq. 8.2). With areal data, this coefficient is known in the geographic literature as the coefficient of areal association, e.g.Taylor (1977). The coefficient ranges between 0 and 1, as before but the value is appreciably greater, due to the inclusion of negative matches in the expression. Notice that C_j and C_a are dimensionless and therefore independent of the units of areal measurement (Bonham-Carter, 1994).

$$C_a = \frac{T_{11} + T_{22}}{T_{12} + T_{21} + T_{11} + T_{22}} \qquad (8.2)$$

The area of negative match in the study area (T_{22}) is 13284 km^2. For comparison with Jaccard's coefficient, the areal coefficient of association for the data of MVT potential maps is (579 + 13284) / (801 + 286 + 579+ 13284) = 0.929.

Aforesaid analyses represent good similarity between two knowledge driven modeling methods (fuzzy logic and index overlay) also they almost show equivalent favorability targets in mineral potential maps.

8.3 Presentation of Preferable Target Areas

The highest zinc (Zn) value of 144 samples in the study area is 124900 ppm (about 12.5%) in a rock sample within the target area 3 in mineralization block 2 (Chichaklou Pb-Zn deposit).

Figure 8.8 shows the geochemical distribution map of Zn values in the samples of the study area. The highest lead (Pb) value of these samples is 105900 ppm (about 10.6%) in a rock sample from Pashtouk Pb-Zn deposit. Figure 8.9 shows the geochemical distribution map of Pb values in the samples of the study area.

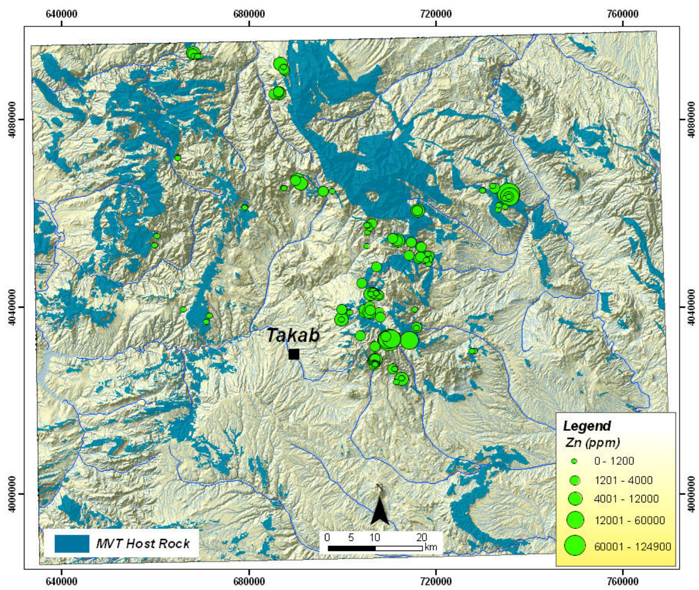

Fig. 8.8 Geochemical distribution map of Zinc (Zn) values in the samples of Takab region (Blue color shows the selected host rock for modeling of MVT Pb-Zn potential).

The highest gold (Au) value of field samples in the study area is 3914 ppb (about 4ppm) in a rock sample from Arabshah gold mineralization area. Figure 8.10 shows the geochemical distribution map of Au values in the samples of the study area.

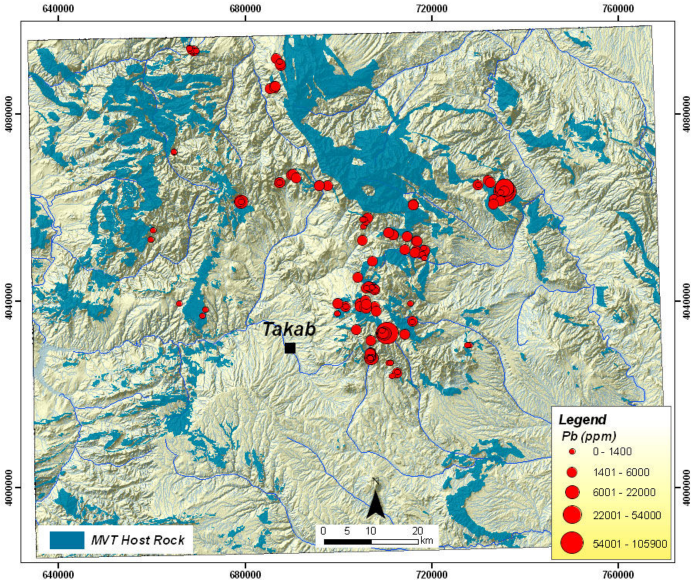

Fig. 8.9 Geochemical distribution map of lead (Pb) values in the samples of Takab region (Blue color shows the selected host rock for modeling of MVT Pb-Zn potential).

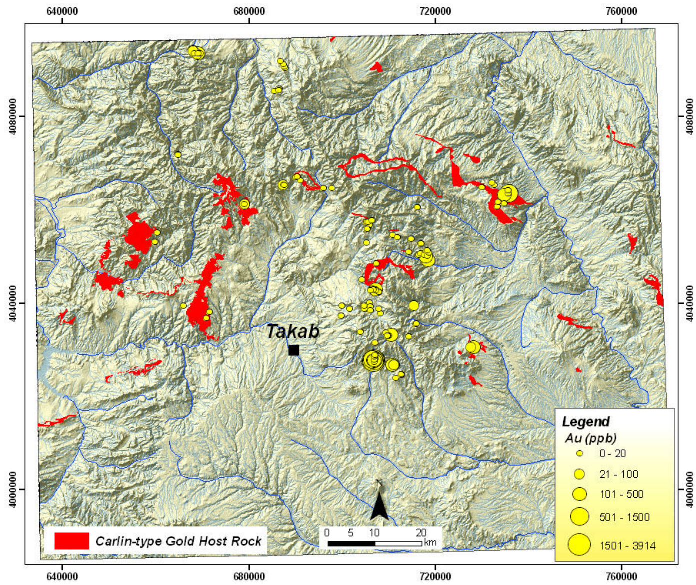

Fig. 8.10 Geochemical distribution map of gold (Au) values in the samples of Takab region (Red color shows the selected host rock for modeling of Carlin-type gold potential).

Geochemical analysis results of the samples show high values of Pb, Zn and Au in different parts of the study area that some of these favourable areas are covered by known deposits but there are some unknown targets that recommend for new exploration works. Figures 8.11 and 8.12 respectively show the susceptible areas for more exploration of Pb-Zn and Au. On figure 8.11, eight target areas have selected from preliminary targets of mineral potential map of MVT Pb-Zn (see fig. 8.1) based on field works and geochemical analysis of the samples. The results of Pb and Zn geochemical analysis are seen in table 8.1. Figure 8.12 and table 8.2 respectively show seven target areas of Carlin-type gold from preliminary targets of mineral potential map (see fig. 8.2) and the geochemical analysis results of gold.

These 15 target areas are recommended (8 target areas for MVT Pb-Zn and 7 target areas for Carlin-type gold) for new exploration works of carbonate hosted Pb-Zn and Au in Takab region.

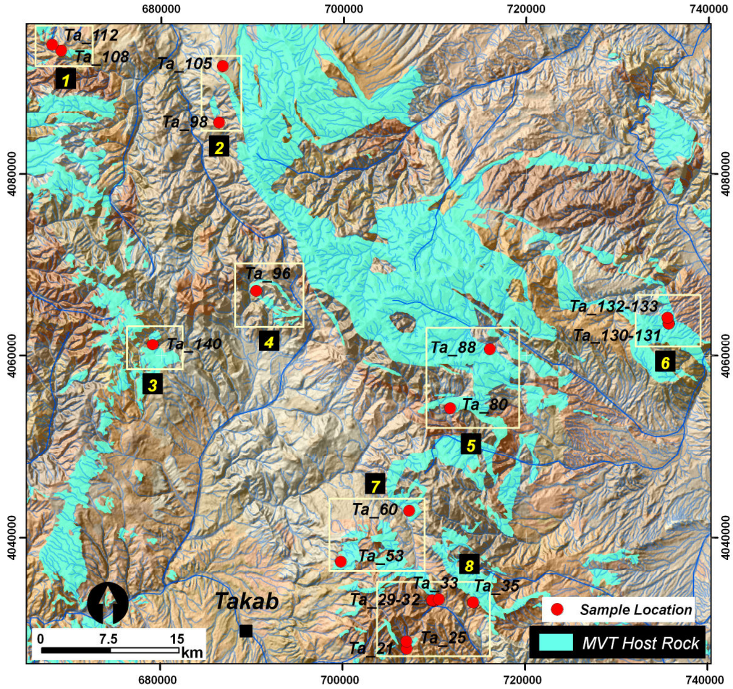

Fig. 8.11 Ultimate target areas of MVT Pb-Zn potential in the study area (blue color shows the selected host rock for modeling of MVT Pb-Zn potential).

Sample No.	X Coor.	Y Coor.	Type	Pb (ppm)	Zn (ppm)
Ta_21	706896	4027824	Rock	9600	0
Ta_25	706875	4028623	Rock	3000	7900
Ta_29	709866	4033014	Rock	3200	124900
Ta_30	709838	4033013	Rock	6100	43200
Ta_31	709685	4033043	Rock	2800	58200
Ta_32	709684	4033076	Soil	13000	26400
Ta_33	710405	4033172	Rock	54300	12450
Ta_35	714177	4032842	Rock	2200	26800
Ta_53	699677	4037344	Rock	0	5000
Ta_60	707176	4042950	Rock	5500	0
Ta_80	711686	4054218	Rock	2800	5600
Ta_88	715999	4060643	Rock	3300	6700
Ta_96	690394	4067129	Rock	2700	6000
Ta_98	686318	4085599	Rock	2400	5000
Ta_105	686724	4091869	Rock	2800	5400
Ta_108	669010	4093563	Rock	5921	113
Ta_112	668040	4094185	Rock	1386	6257
Ta_130	735598	4063569	Rock	38450	3400
Ta_131	735609	4063555	Rock	105900	60000
Ta_132	735483	4064177	Rock	22400	117900
Ta_133	735483	4064177	Rock	31800	109400
Ta_140	679056	4061201	Soil	9500	700

Tab. 8.1 Geochemical analysis results of Pb and Zn in the study area.

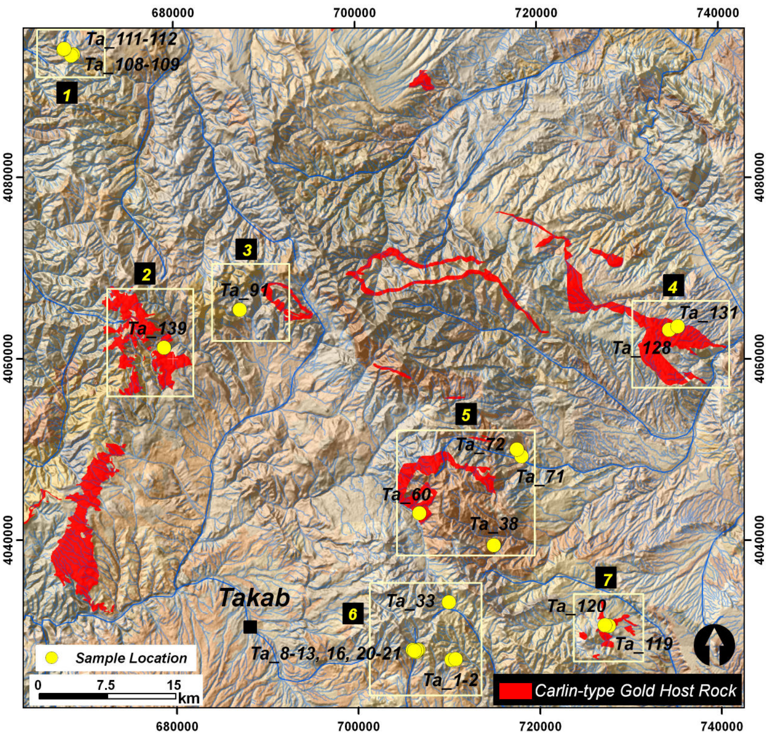

Fig. 8.12 Ultimate target areas of Carlin-type gold potential in the study area (red color shows the selected host rock for modeling of Carlin-type gold potential).

Sample No.	X Coor.	Y Coor.	Type	Au(ppb)
Ta_1	710714	4026790	Rock	136
Ta_2	711165	4026847	Rock	98
Ta_8	706435	4027856	Rock	899
Ta_9	706628	4027762	Rock	3914
Ta_10	706676	4027730	Rock	409
Ta_11	706786	4027668	Rock	1349
Ta_12	707075	4027874	Rock	403
Ta_13	706885	4027783	Rock	339
Ta_16	706779	4027755	Rock	2780
Ta_20	706789	4027654	Rock	450
Ta_21	706896	4027824	Rock	1500
Ta_33	710405	4033172	Rock	450
Ta_38	715369	4039421	Rock	29
Ta_60	707176	4042950	Rock	120
Ta_71	718402	4049238	Rock	400
Ta_72	717897	4050000	Rock	400
Ta_91	687361	4065377	Rock	35
Ta_108	669010	4093563	Rock	127
Ta_109	668809	4093439	Rock	30
Ta_111	667974	4094121	Rock	28
Ta_112	668040	4094185	Rock	31
Ta_119	728035	4030505	Rock	130
Ta_120	727583	4030596	Rock	25
Ta_128	734667	4063168	Rock	360
Ta_131	735609	4063555	Rock	1300
Ta_139	679056	4061201	Rock	40

Tab. 8.2 Geochemical analysis results of Au in the study area.

Based on the geochemical database, a distribution map of high geochemical anomalies was prepared that shows assemblage of stream sediment anomalies in the study area (Fig. 8.13). These anomalies indicate the geochemical targets in Takab region that can be also a beneficial guide for new exploration.

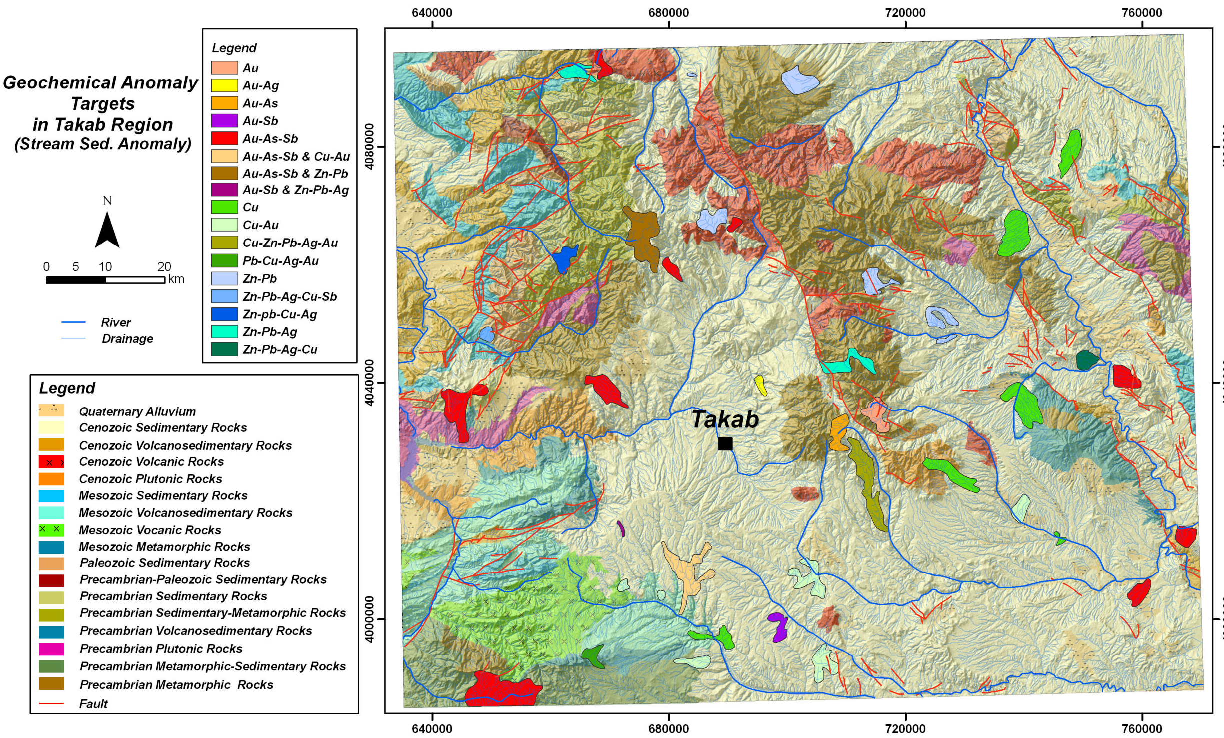

Fig. 8.13 Distribution map of high geochemical stream sediment anomalies based on geochemical database (assemblage of high geochemical stream sediment anomalies are seen on the simple 1:250.000 geological map; extracted and GIS-ready from 1:250.000 geological map, Geological Survey of Iran).

8.4 Structural Features, Magmatism and Mineralization Pattern

“Metallogeny is the study of the genesis and regional to global distribution of mineral deposits, with emphasis on their relationship in space and time to regional petrologic and tectonic features of the Earth's crust” (Guilbert and Park, 1986).

Ore deposit models are greatly used in mineral exploration as an important factor for predicting the mineral potential targets and metallogeny model of an area. The regional structural features (lineament and circular structure) are defined by remote sensing study, with additional evidence from integration and overlay of main structural zones, hydrothermally altered rocks, geophysics, geochemistry and geological datasets.

The main faults in the study area are divided to two sets (fig. 5.8): 1- Faults with NW-SE trend that are believed to form in Precambrian and can be followed out of the study area in forms of parallel and step and 2- Faults with NE-SW trend with Mesozoic age that are vertical on the first set. Tertiary metamorphism in Takab region has influenced from these fault sets and especially in the cross-cut of these faults (Ghorbani, 2002). The young big lineaments intersect these fault zones and are a susceptible place for displacement of ore minerals in the proper host rocks.

Regional structural pattern is represented by analysis of lineaments and circular structures as expression of magmatic activities. The structural study based on remote sensing technique indicated a new factor in identify of metallogeny model and spatial distribution of Au occurrences in the NW of Iran, also mineralization pattern of Au and Pb-Zn in the study area.

Regional structural zones are believed to represent the main tectonic and magmatism phases which control the spatial distribution of mineralization events. These structural systems are capable to activate again. In intersection of the lineaments with circular structures or minor fault zones can be made a favourable conduit for circulation of hydrothermally solutions and precipitation of ore mineral. Beside permeability of host rocks appears to be the main trap for hydrothermal fluids. Thus, the cross-cut of porose host rocks and large-scale structural zones are favourable geologic feature for the formation of ore deposits.

Generally large-scale structural features have important influence on the displacement of ore occurrences and may represent a significant evidence for exploration of different types of ore deposits.

Structural analysis of satellite data was concentrated upon lineaments and circular structures in the study area. The deep magmatic activities are reflected on the earth's surface by traces of circular structures. The large-scale circular structures are recognized by ridge forms and radial and ring drainage or river networks.

Several circular structures, kilometers in diameter, are extracted in Takab region. The diameter of main circular structure in this area is about 115 km. It consists of a drainage and river ring system. Figure 8.14 shows the trace of large ring structure by pattern of river and main drainage network. In the central part of this ring structure several plutonic rock units (Tertiary in age) have outcrop (1:250.000 geological map of Takab; Geological Survey of Iran). Some parts of this big circular structure were cut off by regional lineaments. Distribution of Au and Pb-Zn mineralization in this circular structure are seen in figure 8.15.

Analysis of Landsat 7 ETM$^+$ data in the NW of Iran indicated several regional lineaments. The rose diagram of aforesaid lineaments shows two main trends at NW-SE and NE SW directions. Large-scale lineaments appear to be the main spatial control on distribution pattern of Au, Cu and Pb-Zn mineralization (Fig. 8.20).

The Bayche Bagh, Zarshouran, Aqdarreh, Shakh Shakh, Ghozalbolagh, Yourgol, Yapesh Khan, Qaleh Kohneh, Kervian, Gholgholeh and Ghabagholoujeh gold mineralization have occurred along the big lineament with NE-SW trend in the study area (Fig. 8.16 to 8.19). Also the Sarikhanlou, Zaglik, Safikhanlou and Naghduz gold mineralization have situated along the other NE-SW large-scale lineament in the north of the study area (NW of Iran; Fig. 8.16 to 8.19).

Regional scale structural controls on magma emplacement are one of the factors that affect the potential to form several types of ore deposits. The locations of magmatic activity and hydrothermal systems can be related to the analyzed structural framework, and are seen to occur in the intersections of major structural features (linear or circular). Deeply magma and derived ore-bearing fluids flow across the channels and structural crushed zones of particular crustal weakness and control the localization of ore formation.

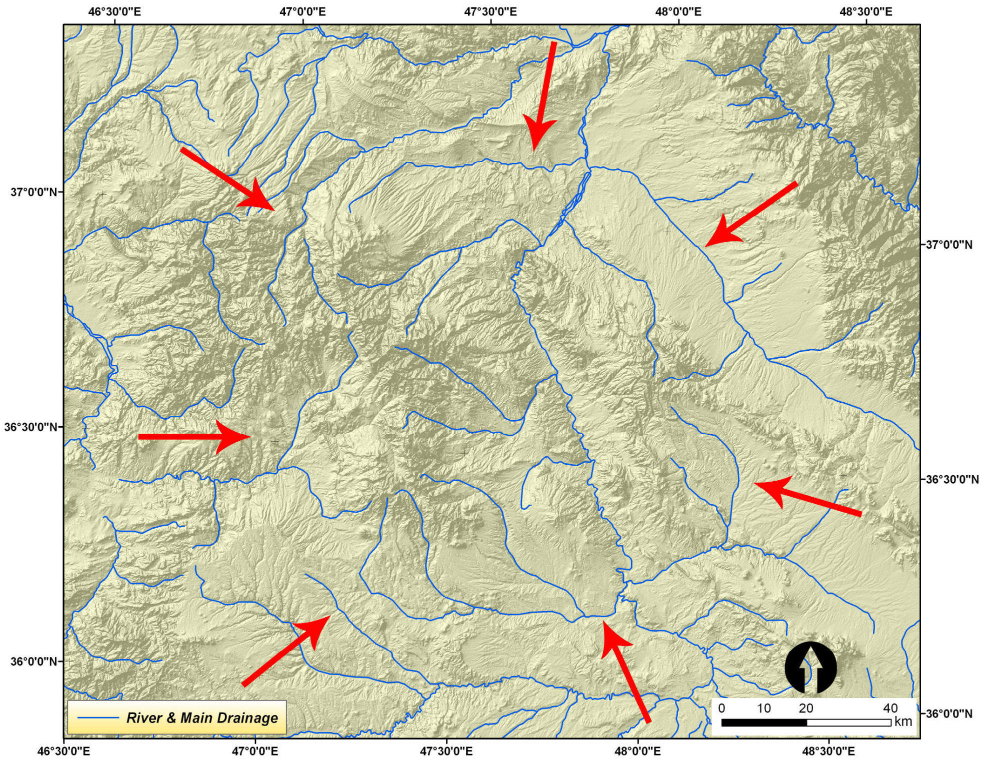

Fig. 8.14 Distribution map of river and main drainage network in Takab region shows the trace of large-scale circular structure (the diameter of this circular structure is about 115 km).

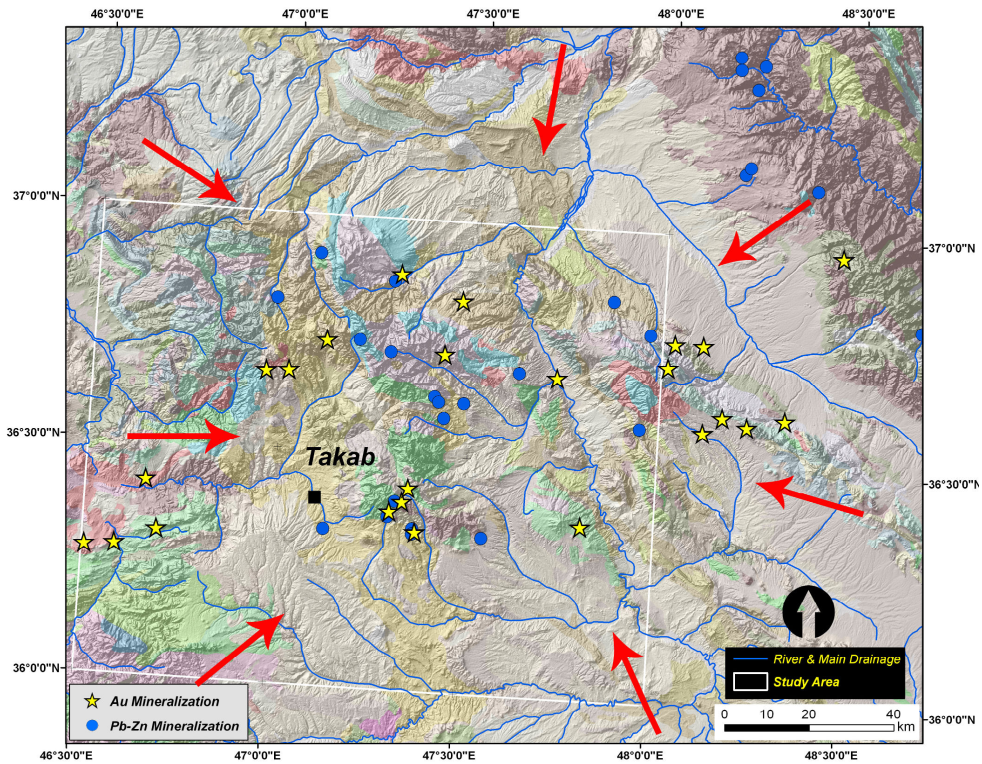

Fig. 8.15 Distribution map of Au and Pb-Zn ore occurrences and trace of the large –scale circular structure in Takab region.

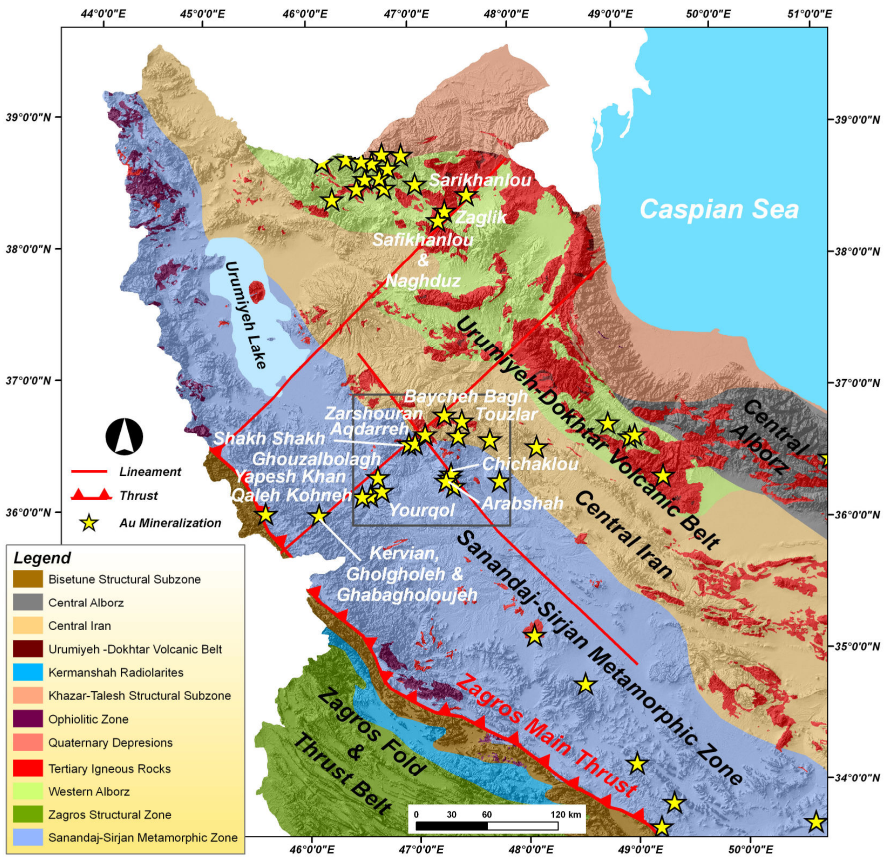

Fig. 8.16 Structural zones map of NW of Iran (modified after Sahandi et al., 2002) and three large-scale lineaments that appear to be the main spatial control on distribution pattern of Au mineralization in Takab region and in the North of the study area.

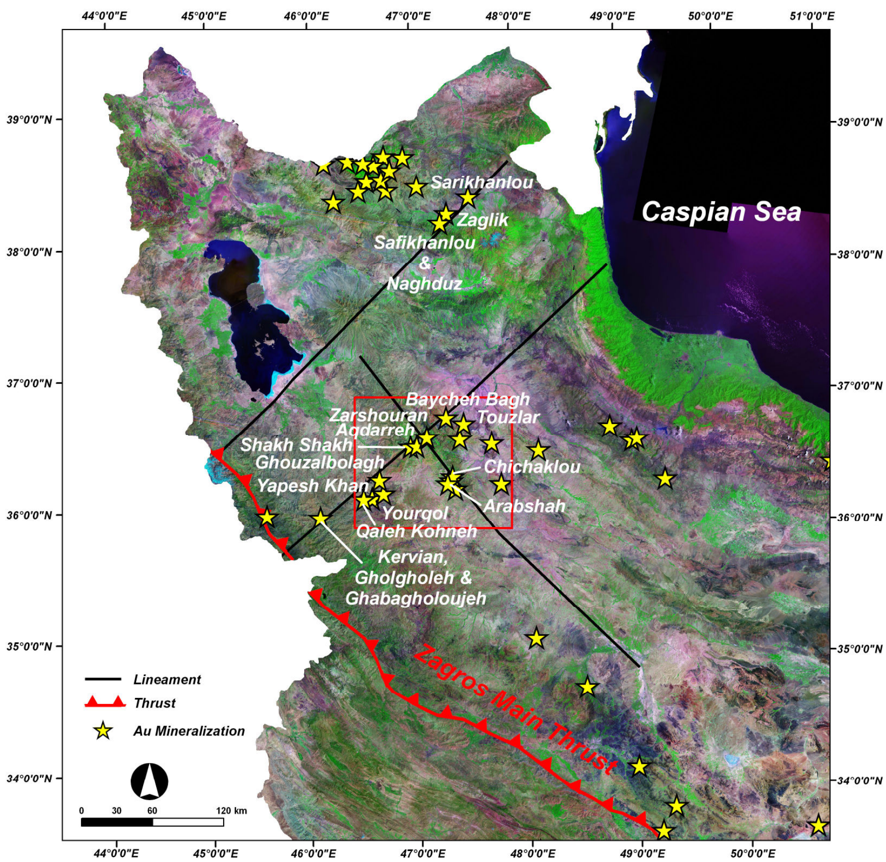

Fig. 8.17 Fig. 8.16 Landsat 7 ETM^{+} image (R: 7, G: 4, B: 2) of NW of Iran and distribution pattern of Au mineralization in Takab region and in the North of the study area.

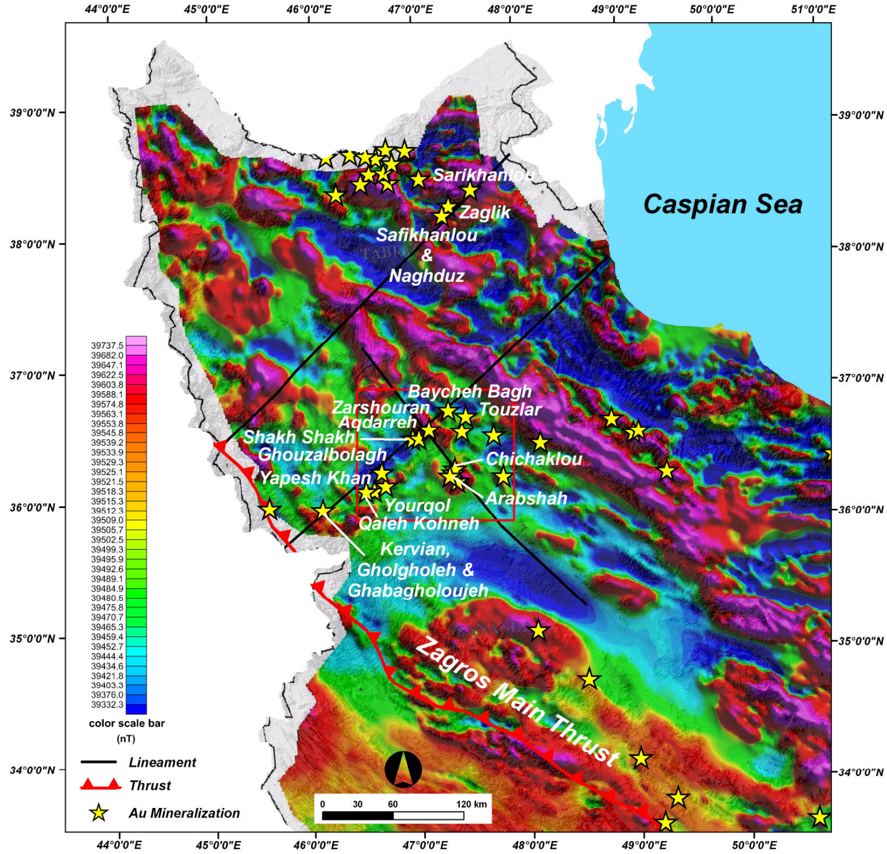

Fig. 8.18 Total magnetic intensity grid map (7.5 km line spacing; Geological Survey of Iran, 1978) of NW of Iran and distribution pattern of Au mineralization in Takab region and in the North of the study area.

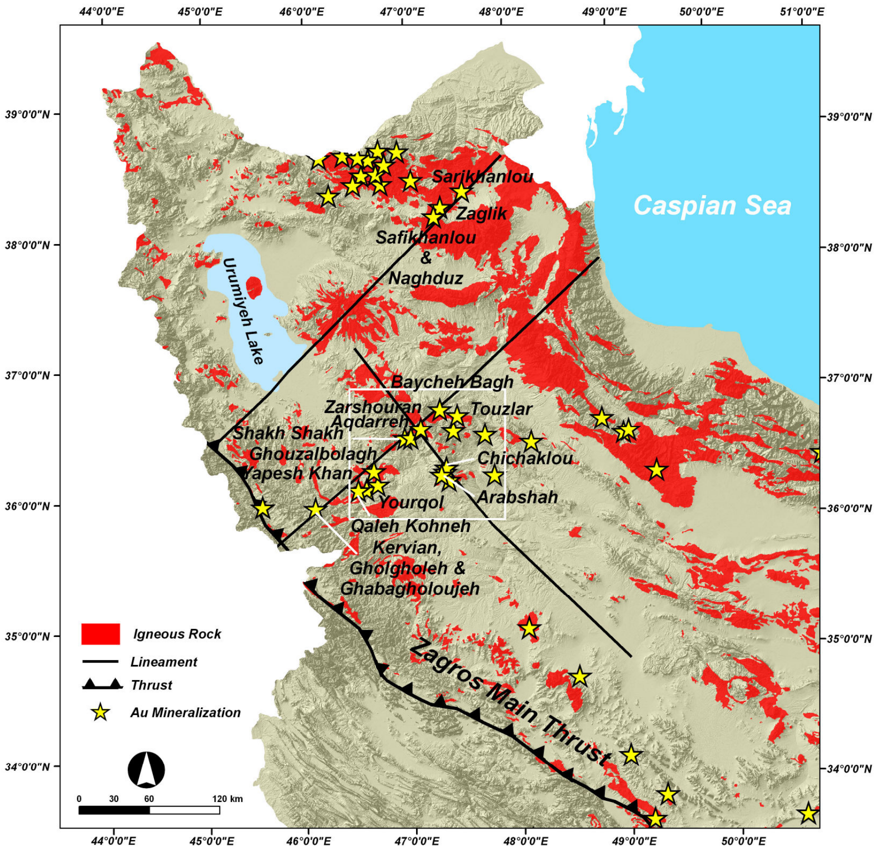

Fig. 8.19 Distribution map of igneous rocks in the NW of Iran (modified after Sahandi et al., 2002) and relationship between large-scale lineaments and mineralization pattern of Au in Takab region and in the north of the study area.

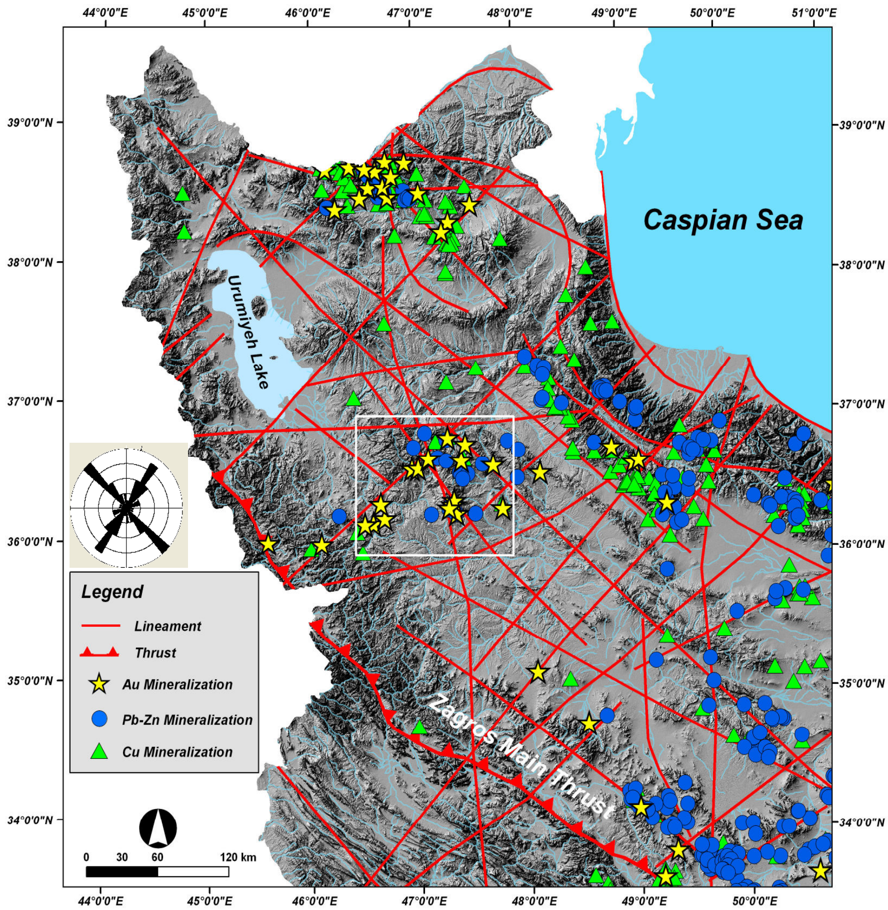

Fig. 8.20 Distribution map of structural features (large-scale lineaments) in the NW of Iran and mineralization pattern of Au, Pb-Zn and Cu. Two main trends of lineaments are seen (in NW-SE and NE-SW directions).

The Late Cenozoic magmatism (Pliocene and Quaternary; Fig 8.21a) and related hydrothermal activities, the distribution pattern of structural features and ore occurrences and especially gold mineralization in the NW of Iran demonstrate that mineralization events can occur along deep strike-slip faults. Figure 8.21b shows 3D map of the study area, exposure of the Quaternary basalts, places of three gold deposits and a probable deep strike-slip fault.

Quaternary basaltic and andesitic lavas from the NW Iran/eastern Turkey border area are related to the active Arabia–Eurasia collision (Kheirkhah et al., 2009). Aforesaid volcanism, generally oriented NW-SE to N-S appears to controlled by the regional deep strike-slip faults. Quaternary basalt flows occur along these faults in the NW of Iran and continue to Turkey and Armenia. These basaltic flows can be reached to the earth’s surface via deep faults. Detailed geological and geochemical investigation, remote sensing interpretation and structural analysis led to a better understanding of the regional structural controls of gold emplacement in the NW of Iran.

An investigation on the geophysical data in the study area and E, S and SE of it showed several large-scale structural features with NW-SE trends in this region (Fig. 8.22). Quaternary basalts have situated along a big structure that appear to be a probable deep strike-slip fault (Fig. 8.23). These faults are a proper environment for departure of hydrothermal solutions and formation of several types of ore deposits. In figure 8.23 places of three major gold deposits (Zarshouran, Aqdarreh and Dashkasan Au deposits) related to the large-scale structural features are seen.

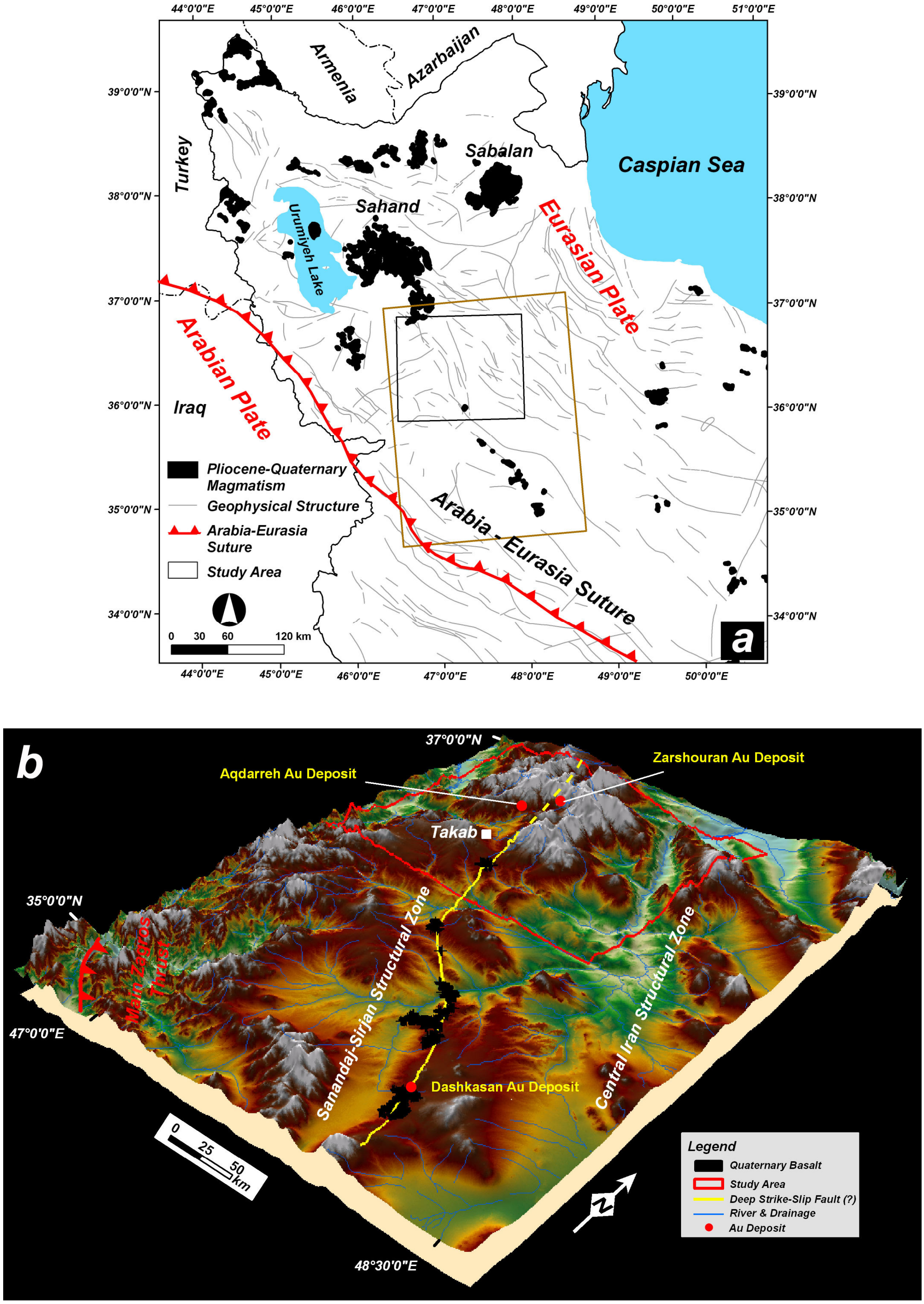

Fig. 8.21 **a** Distribution map of the Late Cenozoic magmatism in the NW of Iran (Quaternary basaltic and andesitic lavas) and **b** 3D map of the study area (based on digital elevation model) and exposure of Quaternary basalts in the E, S and SE of this region along a probable deep strike-slip fault?.

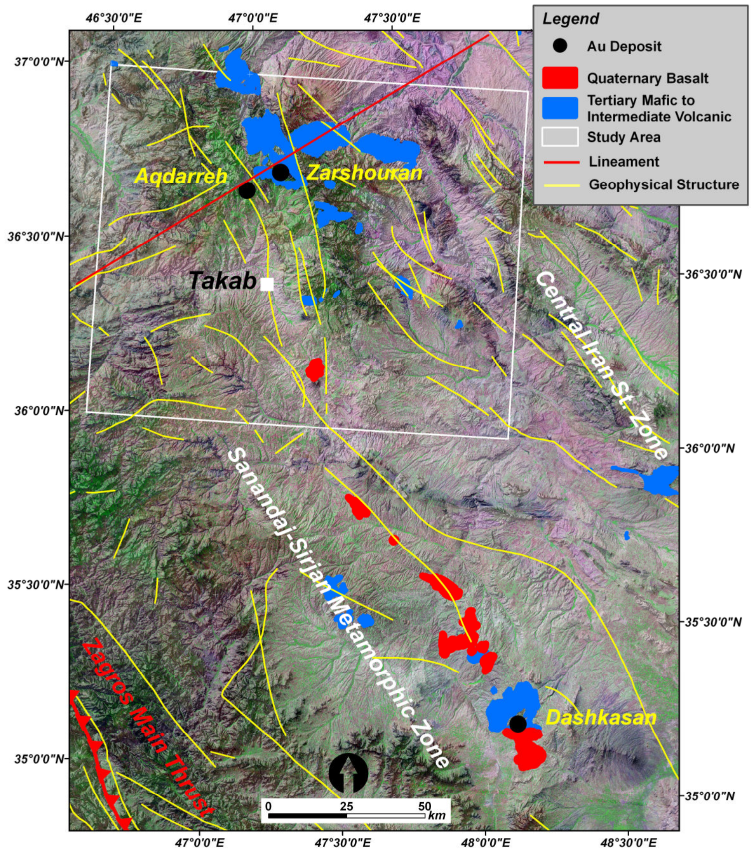

Fig. 8.22 Landsat 7 ETM+ image (R: 7, G: 4, B: 2) of the study area and E, S and SE of it. Exposure of Quaternary basalts and Tertiary mafic to intermediate volcanic rocks show some linear NW-SE trends. These probable deep faults can be a proper pathway for ore bearing fluids.

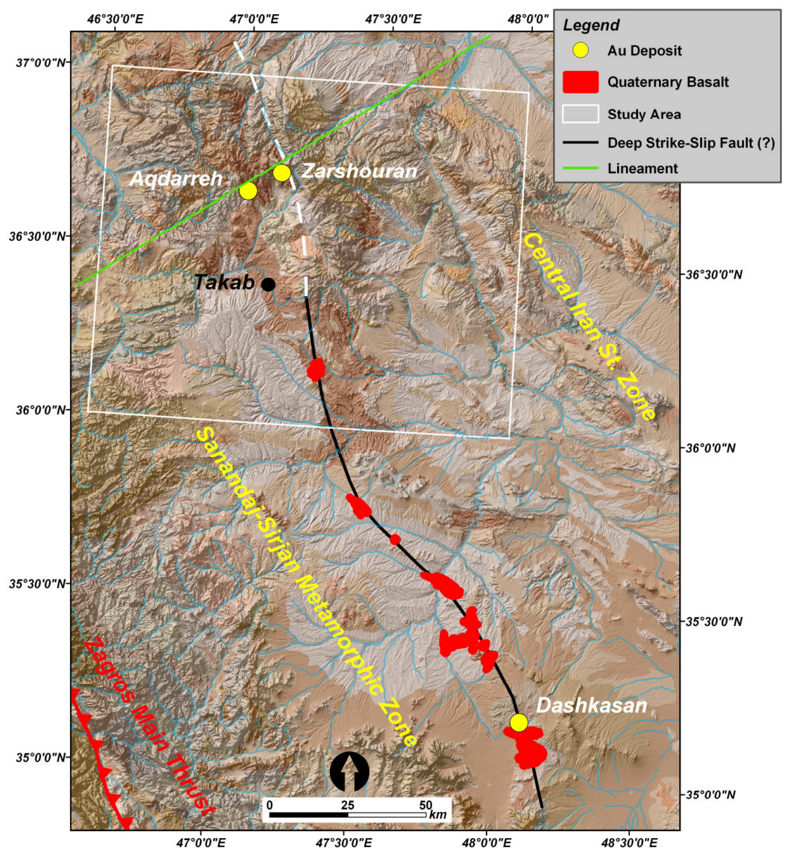

Fig. 8.23 Exposure of Quaternary basalts along a probable deep strike-slip fault and the places of three major gold deposits (Zarshouran, Aqdarreh and Dashkasan gold deposits).

The age of initial collision between the Arabian and Eurasian plates is disputed, with suggested ages ranging from~10–12 Ma (Late Miocene; McQuarrie et al., 2003) to ~35–40 Ma (Middle-Late Eocene; Hessami et al., 2001; Vincent et al., 2005). Early deformation and changing sedimentation patterns on both sides of the Arabia–Eurasia suture indicate a Late Eocene age (~35 Ma), consistent with a sharp reduction in magmatism between the Eocene and Oligocene (Allen and Armstrong, 2008).

The cause of melting on the regional scale in the NW of Iran and east of Turkey is related to either partial loss of the lower lithosphere, slab break-off of Tethyan oceanic lithosphere, or a combination of the two but the nature and origins of this Late Cenozoic magmatism are still debated (Kheirkhah et al., 2009).

With attention to the initial collision age between the Arabian and Eurasian plates and completion of it in about 5 Ma, even if these Quaternary basaltic and andesitic flows show the subduction evidence, reason of this event because of its large extension has a question mark and it is unknown yet and It may be presumed that it related to deep strike-slip faults (?). Only an accurate and detailed petrological and geochemical studies and isotropic evidence of these young magmatism and specification of their geodynamic situations can help to answer this question. NW of Iran has a complex geodynamic environment and different types of mineral potential could be formed in this tectonic process. Different types of gold mineralization in the Tethyan Metallogenic Belt of the NW Iran including Carlin-type gold, epithermal gold, porphyry copper/gold and carbonate-replacement gold. These types of deposits are related to different tectonic situations such as subduction, collision zone, post-collision and rifting stages.

8.5 Recommendations

1- For future exploration of carbonate replacement deposits (CRD) of Pb-Zn and Au in Takab region and with respect to field work and geochemical results of sample analysis and presentation of preferable promising areas (Fig 8.11 and 8.12), detailed geological mapping, geochemistry (stream sediment and heavy mineral) and rock sampling and processing of structural features in the target areas and interpretation of tectonic evolution related to the geodynamic environments in the study area are recommended.

2- Due to the known major Pb-Zn and Au deposits has been occurred as a high priority in the fuzzy mineral potential maps, also modeling by index overlay method confirmed it and whereas some high priorities of promising areas haven't checked in this research therefore, they should be traversed on a reconnaissance prospecting and sampling work will be required to evaluate these targets for their economic potential.

3- In some targets the geochemical analysis results of rock or stream sediment samples show high content of Pb, Zn or Au. For these final targets (see chapter 7 and fig 8.11 and 8.12) more detail exploration is recommended.

4- An integration of geo-exploration datasets based on new information in GIS environment also, interpretation of high resolution satellite images by new remote sensing technique is necessary.

References

Abdelhamid, G. and Rabba, I., 1994, An investigation of mineralized zones revealed during geological mapping, Jabal Hamra Faddan-Wadi Araba, Jordan, using Landsat TM data. Int. J. Remote Sensing, 15, 7, 1495-1506.

Abrams, J.M., 1983, Remote sensing for porphyry copper deposits in southern Arizona. Economic Geology, 78, 591-604.

Agard, P., Omrani, J., Jolivet, L. and Mouthereau, F., 2005, Convergence history across Zagros (Iran): constraints from collisional and earlier deformation. International Journal of Earth Sciences (Geol Rundsch), 94, 401-419.

Ahadjie, J., 2003, Spatial data integration for classification of stream sediment geochemical anomalies in Masbate island, the Philippines. M.Sc. thesis, International Institute for Geo-Information Science and Earth Observation, Enschede, The Netherlands, 79 p.

Akhavi, M.S., Webster, T.L. and Raymond, D.A., 2001, RADARSAT-1 imagery and GIS modeling for mineral exploration in Nova Scotia, Canada. Geocarto. International, 16, 55-61.

Alavi, M., 1994, Tectonics of the Zagros Orogenic belt of Iran: new data and interpretations. Tectonophysics, 229, 211-238.

Alavi, M., Hajian, J., Amidi, M. and Bolourchi, H., 1982, Geology of Takab-Saein-Qal'eh, 1:250.000. Geological Survey of Iran, Report 50.

Alavi, M., Amidi, M., 1968, Geology of western part of Takab quadrangle. Geological Survey of Iran, Report 49 (unpublished).

Allen, M.B. and Armstrong, H.A., 2008, Arabia–Eurasia collision and the forcing of mid Cenozoic global cooling. Palaeogeography Palaeoclimatology Palaeoecology 265, 52-58, doi:10.1016/j.palaeo.2008.04.021.

Allison, I., de Pao,r D.G., Haszeldine, S., Bowman, A., and Maguire, M., 1997, Cryptic structural trends in basement revealed by Patterson diagrams: Examples from the Scottish and Irish Caledonian Orogen. In: Sengupta S. (Ed.), Evolution of Geological Structures in Micro to Macro-Scales. London, Chapman and Hall, p. 487-495.

Alvarez, M.G., 2000, Neuro-fuzzy modeling in engineering geology: applications to mechanical rock excavation, rock strength estimation, and geological mapping, 244 p.

Annels, A.E., O'Donovan, G. and Bowles, M., 2003, New ideas concerning the genesis of the Angouran Zn-Pb deposit, NW Iran. 26th Mineral Deposits Studies Group, Abstracts, University of Leicester (UK), 11-12 January.

Arehart, G.B., 2003, Giant Carlin-type gold deposits: characteristics, origins and exploration methodology. Department of Geological Sciences, Mackay School of Mines, University of Nevada, Reno, NV 89557, U.S.A.

Arehart, G.B., Chakurian, A.M., Tretbar, D.R., Christensen, J.N., McInnes, B.A. and Donelick, R.A., 2003, Evaluation of radioisotope dating of Carlin-type deposits in the Great Basin, Western North America, and Implications for deposit genesis. Economic Geology, 98, 235-248.

Arehart, G.B., 1996, Characteristics and origin of sediment-hosted disseminated gold deposits: A review. Ore Geology Reviews, 11, 383-403.

Arellano, P., 2003, Missing information in remote sensing: Wavelet approach to detect and remove clouds and their shadows. M.Sc. thesis, International Institute for Geo-Information Science and Earth Observation, Enschede, The Netherlands, 58 p.

Asadi, H.H., 2000, The Zarshuran gold deposit model applied in a mineral exploration GIS in Iran, PhD Thesis, Delft University of Technology, The Netherlands, 190 p.

Asadi H.H., Voncken J.H.L., Kuhnel R.A. and Hale, M., 2000, Petrography, mineralogy and geochemistry of the Zarshuran Carlin-like gold deposit. Mineralium Deposita, 35, 672-682.

Aster User's Guide, 2007, Part II, level 1 data products, (Ver.5.1), ERSDAC: Earth Remote Sensing Data Analysis Center.

Babakhani, A.R. and Ghalamghash, J., 1990, Geological map of Takht-e-Soleyman, 1:100.000. Geological Survey of Iran, Tehran.

Berberian, F. and Berberian, M., 1981, Tectono-plutonic episodes in Iran. American Geophysical Union, Geodynamic Series, 3, 5-32.

Berberian, M. and King, G.C.P., 1981, Towards a paleogeography and tectonic evolution of Iran. Canadian Journal of Earth Sciences, 18, 210-265.

Bonham-Carter, G.F., 1997. GIS methods for integrating exploration data sets. In: A.G. Gubins (Ed.), Proceedings of Exploration 97: 4th Decennial International Conference on Mineral Exploration, Toronto, Canada, 14-18 September 1997, pp. 59-64.

Bonham-Carter, G. F., 1994, Geographic information systems for geoscientists, modeling with GIS. Ontario, Pergamon, 398p.

Bonham-Carter, G.F., Agterberg, F.P. and Wright, D.F., 1988, Integration of geological data sets for gold exploration in Nova Scotia. Photogrammetric Engineering and Remote Sensing, 54, 1585-1592.

Boni, M., Gilg, H.A., Balassone, G., Schneider, J., Allen, C.R. and Moore, F., 2007, Hypogene Zn carbonate ores in the Angouran deposit, NW Iran. Mineralium Deposita, DOI 10.1007/s00126-007-0144-4, p. 799-820.

Borg, G., 2005, Geological and economical significance of supergene nonsulphide zinc deposits in Iran and their exploration potential. In: Geological Survey of Iran (Ed.) Mining and Sustainable Development. 20th World Mining Congress, 7-11 November 2005, Tehran, Iran, 385-390.

Borg, G. and Daliran, F., 2004, Hypogene and supergene formation of sulphides and non-sulphides at the Angouran high-grade zinc deposit, NW-Iran. In: Abstract volume of Geoscience Africa, University of the Witwatersrand, Johannesburg, 69-70.

Bradley, D.C., and Leach, D.L., 2003, Tectonic controls of Mississippi Valley- type lead-zinc mineralization in orogenic forelands. Mineralium Deposita, 38, 652-667.

Braun, J.J., Pagel, M., Herbillon, A. and Rocin, C., 1993, Mobilization and redistribution of REEs and thorium in a syenitic lateritic profile: A mass balance study. Geochimica et Cosmochimica Acta, 57, 4419-4434.

Budkewitsch, P., Newton, G. and Hynes, A.J., 1994, Characterization and extraction of linear features from digital images. Canadian Journal of Remote Sensing, 20, 268-279.

Carballo, E.L., 1998, Integration of aeromagnetic, thematic mapper and geochemical data for mineral exploration in the Makonde District, Zimbabwe.

Carranza, E.J.M., 2002, Geologically-constrained mineral potential mapping: examples from the Philippines. Ph.D. thesis, Delft University of Technology, The Netherlands, 480 p.

Chen, S. and Zhou, Y., 2005, Classifying depth-layered geological structures on Landsat TM images by gravity data: a case study of the western slope of Songliao Basin, northeast China. International Journal of Remote Sensing, 26, 13, 2741-2754.

Chikambwe, E.M., 2002, GIS-based predictive mapping for aquamarine-bearing pegmatites, Lundazi area, northeast Zambia. M.Sc. thesis, International Institute for Geo-Information Science and Earth Observation, Enschede, The Netherlands.

Chica-Olmo M. and Abarca F., 2002, Development of a decision support system based on remote sensing and GIS techniques for gold-rich area identification in SE Spain. International Journal of Remote Sensing, 23, 22, 4801-4814.

Chinn, G.T. and Ascough, G.L., 1997, Mineral potential mapping using an expert system and GIS. In: A.G. Gubins (Ed.), Proceedings of Exploration 97, 4th Decennial International Conference on Mineral Exploration, Toronto, Canada, 14-18 September 1997, 105-114.

Choi, S., Moon, W.M. and Choi, S.G., 2000, Fuzzy logic fusion of W-Mo exploration data from Seobyeog-ri, Korea. Geosciences Journal, 4, 2, 43-52.

Chung, C.F. and Agterberg, F.P., 1980, Regression models for estimating mineral resources from geological map data. Math. Geology, 12, 473-488.

Clarke, D.S. and Govett, G.J.S., 1990, Southwest Pacific epithermal gold: a rock geochemistry perspective. In: J.W. Hedenquist, N.C. White and G. Siddeley (Eds.), Epithermal Gold Mineralization of the Circum-Pacific: Geology, Geochemistry, Origin and Exploration. Journal of Geochemical Exploration, 35, 225-240.

Crowley, J.K., Brickey, D.W. and Rowan, L.C., 1989, Airborne imaging spectrometer data of the Ruby Mountains, Montana; mineral discrimination using relative absorption band-depth images. Remote Sensing of Environment, 29, 2, 121-134.

Cox, M.R., Evans, K.R. and Krizanich, G.W., 2007, GIS-based geologic mapping of the Vista quadrangle, west-central Missouri [abs.]. Geological Society of America, 39, 3, p. 25.

D’ercole, C., Groves, D.I. and Knox-Robinson, C.M., 2000, Using fuzzy logic within a GIS-environment to enhance conceptually based prospectivity analysis of MVT mineralisation. Australian Journal of Earth Sciences, 47, 913-927.

Daliran, F., Borg, G., Armstrong, R., Walther, J., Vennemann, T., Friese, K., Sadeghi, M. and Woodhead, J.D., 2009, Nonsulphide Zinc Deposits, Iran- The Hypogene Emplacement and Supergene Modification History of the Angouran Zinc Deposit, NW-Iran. Berichte zur Lagerstätten und Rohstoffforschung, 57, 75 p., Bundesanstalt für Geowissenschaften und Rohstoffe, Hannover.

Daliran, F., 2007, The carbonate rock-hosted epithermal gold deposit of Agdarreh, Takab geothermal field, NW Iran-hydrothermal alteration and mineralization. Mineralium deposita, DOI 10.1007/s00126-007-0167-x.

Daliran, F. and Borg, G., 2005a, Genetic aspects of the Angouran nonsulphide zinc ore deposit, NW-Iran, as an exploration guide for nonsulphide zinc. In: Geological Survey of Iran (Ed.), Mining and Sustainable Development. 20th World Mining Congress, 7-11 November 2005, Tehran, Iran, 433-437.

Daliran, F. and Borg, G., 2005b, Characterisation of the nonsulphide zinc ore at Angouran, Northwestern Iran, and its genetic aspects. In: Mao, J. and Bierlein, F.P. (Eds.), Mineral Deposit Research, Meeting the Global Challenge, 2, 913-916.

Daliran, F., Hofstra, A.H., Walther, J. and Stüben, D., 2002, Agdarreh & Zarshuran SRHDG deposits, Takab region, NW-Iran. Geological Society of America, annual meeting, 34, 6, 141.

Daneshfar, B., Desrochers, A. and Budkewitsch, P., 2006, Mineral-potential mapping for MVT deposits with limited data sets using Landsat data and geological evidence in the Borden Basin, Northern Baffin Island, Nunavut, Canada. Natural Resources Research, 15, 3, 129-149.

DoE (Department of the Environment), 1987, Handling Geographic Information, HMSO, London.

Eggers, A.J., 1979, Large-scale circular features in North Westland and West Nelson, New Zealand: Possible structural control for porphyry molybdenum-copper mineralization?. Economic Geology, 74, 6, 1490-1494.

Emsbo, P., Groves, D.I., Hofstra, A.H. and Bierlein, F.P., 2006, The giant Carlin gold province: a protracted interplay of orogenic, basinal, and hydrothermal processes above a lithospheric boundary. Mineralium Deposita, 41, 517-525.

Evans, A.M., 1993, Ore geology and industrial minerals: An introduction. Blackwell Scientific Publications, 390 p.

ENVI User's Guide. Research Systems, Inc., 1999.

Fabris, A.J., Keeling, J.L. and Fidler, R.W., 2006, A comparison of geochemical exploration techniques: Curnamona province. Regolith, Consolidation and Dispersion of Ideas.

Fonoudi, M., 1998, Geological map of Takab, 1:100.000. Geological Survey of Iran, Tehran.

Fonoudi, M., 2000, Geological map of Yasoukand (Ghodjour), 1:100.000. Geological Survey of Iran, Tehran.

Fonoudi, M. and Sadeghi, M., 2001, Exploration project of Zn-Pb Angouran type mineralization in the 4000 km^2. Taskmaster: Iran Zink Mines Development Company (IZMDC), Executor: Geological Survey of Iran, Supervisor: Babakhani, A., in Farsi.

Fry, N., 1979, Random point distributions and strain measurement in rocks. Tectonophysvics, 60, 89-105.

Galbraith, J.H. and Saunders, D.F., 1983, Rock classification by characteristics of aerial gamma-ray measurements. Journal of Geochemical Exploration, 18, 49-73.

Gazanfari, F., 1991, Metamorphic and igneous petrogenesis in NE of Takab with special regard to zinc mineralization in the Angouran mine. Unpubl. Master's thesis, University of Teheran (in Farsi).

Ghasemi, A. and Talbot, C.J., 2005, A new tectonic scenario for the Sanandaj–Sirjan Zone (Iran). Journal of Asian Earth Sciences, 26, 683-693.

Ghorbani, M., 2002, Introduction to the economic geology of Iran. National Geosciences Database of Iran (NGDIR), 854 p.

Gilg, H.A., Boni, M., Balassone, G., Allen, C.R., Banks, D. and Moore, F., 2006, Marble-hosted sulfide ores in the Angouran Zn-(Pb-Ag) deposit, NW Iran: interaction of sedimentary brines with a metamorphic core complex. Mineralium Deposita, 31, 1, 1-16.

Guilbert, J.M. and Park, C.F., 1996, The geology of ore deposits. New York, W.H. Freeman and Company, 985 p.

Guilbert, J.M. and Park, C.F., 1986, The geology of ore deposits, Chapter 21, Freeman, ISBN 0-7167-1456-6.

Hamdi, B., 1995, Precambrian-Cambrian deposits in Iran. In: Hushmandzadeh, A. (ed) Treatise of the geology of Iran, vol 20. Geological Survey of Iran, Tehran, 1535.

Harris, J.R., Lemkow, D., Jefferson, C., Wright, D. and Falck, H., 2008, Mineral potential modelling for the Greater Nahanni Ecosystem using GIS based analytical methods. Natural Resources Research, 17, 2, 51-78.

Harris, M.C., Cassidy, J., Locke, C.A., Mauk, J.L., Stevens, M., and Vidanovich, P., 2005, Geophysical characteristics of the Karangahake epithermal deposit, Hauraki Goldfield, New Zealand. Proceedings of the 2005 New Zealand Minerals Conference, 115-124.

Harris, J.R., Wilkinson, L. and Grunsky, E.C., 2000, Effective use and interpretation of lithogeochemical data in regional exploration programs. Ore Geol. Rev., 16, 107-143.

Harris, J.R., 1991, Mapping of regional structures of eastern Nova Scotia using remotely sensed images: implications for regional tectonics and gold exploration. Canadian Journal of Remote Sensing, 17, 122-135.

Harris, J.R., 1989, Data integration for gold exploration in eastern Nova Scotia using a GIS. In: Remote Sensing for Exploration Geology, Proc. Calgary, Alberta, 233-249.

Hassanipak, A.A., Shojaat, B., 2000, Ore deposit modeling (Metallic & Nonmetallic) with exploration approach. Tehran University (in Farsi).

Herrmann, W., Blake, M. and Doyle, M., 2001, Short wavelength infrared (SWIR) spectral analysis of hydrothermal alteration zones associated with base metal sulfide deposits at Rosebery and Western Tharsis, Tasmania, and Highway-Reward, Queensland. Economic Geology, 96, 5, 939-955.

Hessami, K., Koyi, H.A., Talbot, C.J., Tabasi, H. and Shabanian, E., 2001, Progressive unconformities within an evolving foreland fold-thrust belt, Zagros Mountains. Journal of the Geological Society, London 158, 969-981.

Hofstra, A.H., 2002, Diverse origins of sedimentary rock-hosted disseminated gold deposits worldwide: overview. GSA Annual Meeting, Abstr with Prog, Session 63-1.

Hofstra, A.H., and Cline, J.S., 2000, Characteristics and models for Carlin-type gold deposits. Reviews in Economic Geology, 13, 163-220.

Jafarzadeh, A., Ghorbani, M. and Pezeshkpour, M., 1995, Geology of Iran: Iron deposits. Geological Survey of Iran, Tehran (in Farsi).

Jingyuan Y. and Xucman W., 1991, The application of remote sensing techniques for gold prospecting in the north Fujian Province. Proceedings of 8th Thematic Conference on Geologic Remote Sensing, Denver, Colorado, USA, April 29-May 2, 1991.

Junek, P., 2004, Preliminary results of geological mapping in the Cheleken Peninsula, Turkmenistan area using Advanced Spaceborne Thermal Emission and Reflection Radiometer (ASTER) data. Laboratory of Remote Sensing, Faculty of Civil Engineering, CTU Prague Thákurova 7, 166 29 Praha 6, Czech Republic.

Kalinowski, A. and Oliver, S., 2004, ASTER mineral index processing manual, Remote Sensing Applications, Geoscience Australia.

Karimi, M. and Valadan Zoej, M.J., 2004, Mineral Potential Mapping of Copper Minerals with GIS. XXth ISPRS Congress, 12-23 July 2004 Istanbul, Turkey.

Karnieli, A., Meisels, A., Fisher, L. and Arkin, Y., 1996, Automatic extraction and evaluation of geological linear features from digital remote sensing data using a Hough transform. Photogrammetric Engeneering and Remote Sensing, 62, 525-531.

Kesler, S.E., Riciputi, L.C. and Ye, Z., 2005, Evidence for a magmatic origin for Carlin-type gold deposits: isotopic composition of sulfur in the Betze–Post–Screamer deposit, Nevada, USA. Mineralium Deposita, 40, 127-136.

Kesler, S.E., 1994, Mineral Resources, economics and the environment. Macmillan, New York, 394 p.

Kheirkhah, M., Allen, M.B. and Emami, M., 2009, Quaternary syn-collision magmatism from the Iran/Turkey borderlands, Journal of Volcanology and Geothermal Research, 182, 1-12.

Kholghi Khasraghi, M.H., 1999, Geological map of Irankhah, 1:100.000. Geological Survey of Iran, Tehran.

Kholghi Khasraghi, M.H., 1994, Geological map of Shahindezh, 1:100.000. Geological Survey of Iran, Tehran.

Knox-Robinson, C.M., 2000, Vertical fuzzy logic: a novel technique for enhanced mineral prospectivity mapping, with reference to the orogenic gold mineralization potential of the Kalgoorlie Terrane, Western Australia. Australian Journal of Earth Sciences, 47, 929-941.

Kouda, R. and Koide, H., 1978, Ring structures, Resurgent cauldron, and ore deposits in the Hokuroku Volcanic Field, Northern Akita, Japan. Mining Geology, 28, 233-244.

Leach, D.L., Sangster, D.F., Kelley, K.D., Large, R.R., Garven, G., Allen, C.R., Gutzmer, J. and Walters, S., 2005, Sediment-hosted lead-zinc deposits: A global perspective. Society of Economic Geologists, Inc., Economic Geology 100th Anniversary Volume, pp. 561-607.

Leach, D.L., Viets, J.B., Foley-Ayuso, N., and Klein, D.P., 1995, Mississippi Valley-type Pb-Zn Deposits (Models 32a, b; Briskey, 1986a,b), in Du Bray, E.A., ed., Preliminary compilation of descriptive geoenvironmental mineral deposit models: U.S. Government Consulting Group. Open File Report 95-831, p. 234-243.

Lepage, R., Rouhana, R. G., St-Onge, B., Noumeir, R. and Desjardins, R., 2000, Cellular neural network for automated detection of geological lineaments on Radarsat images. IEEE Transactions on Geoscience and Remote Sensing, 38, 1224-1233.

Liu, D.S., 1994, The Carlin-type gold deposits in China. Nanjing University Press, Nanjing, pp. 414.

Liu, C.C., Sousa Jr., M.A. and Gopinath, T.R., 2000, Regional structural analysis by remote sensing for mineral exploration, Paraiba state, Northeast Brazil. Geocarto. International, 15, 69-75.

Longhi, I., Sgavetti, M., Chiari, R. and Mazzoli, C., 2001, Spectral analysis and classification of metamorphic rocks from laboratory reflectance spectra in the 0.4-2.5 micrometer interval: a tool for hyperspectral data integration. International Journal of Remote Sensing, 22, 18, 3763-3782.

Lotfi , M., 2001, Geological map of Mahneshan, 1:100.000. Geological Survey of Iran, Tehran.

Lotfi, M. and Karimi, M., 2004, Mineralogy and ore genesis of Bayche-Bagh five element (Ag-Ni-Co-As-Bi) vein deposit (NW Zanjan, Iran). Scientific quarterly journal geosciences, 12, 53, 40-45 (in Farsi).

Lowell, J.D., 1991, The discovery of the La Escondida Orebody. In: R.W. Hutchinson and R.I. Grauch (Eds.), Historical perspectives of genetic concepts and case histories of famous discoveries. Economic Geology Monograph 8, Economic Geology Publishing Company, 300-313.

Ludington, S., Barton Jr., P.B. and Johnson, K.M., 1985, Mineral deposit models: theory and practice (a modified version of a speech given at the first McKelvey Forum on Mineral Resources. February 6, 1985): US Geological Survey, Open-File Report 85-391, p.18.

Madani, A.A., 2001, Selection of the optimum Landsat Thematic Mapper bands for automatic lineaments extraction, Wadi Natash area, South Eastern Desert, Egypt. 22nd Asian Conference on Remote Sensing, Singapore, 5-9 November 2001.

Mars, J.C. and Rowan, L. C., 2007, Mapping phyllic and argillic-altered rocks in southeastern Afghanistan using Aadvanced Spaceborne Thermal Emission and Reflection Radiometer (Aster) data. U.S. Geological Survey open-file report 1055, http://pubs.usgs.gov/of/2007/1005/.

Mars, J.C. and Rowan, L. C., 2006, Regional mapping of phyllic and argillic altered rocks in the Zagros magmatic arc, Iran, using Advanced Spaceborne Thermal Emission and Reflection Radiometer (ASTER) data and logical operator algorithms. Geosphere, 2, 3, 161-186.

McQuarrie, N., Stock, J.M., Verdel, C. and Wernicke, B., 2003, Cenozoic evolution of Neotethys and implications for the causes of plate motions. Geophysical Research Letters 30. doi:10.1029/2003GL017992 art. no. 2036.

Mehrabi, B., Yardley, B.W.D. and Komninue, A., 2003, Modelling the Au-As association in hedrothermal gold mineralization: Example of Zarshouran deposit, NW Iran. Journal of Sciences, Islamic Republic of Iran, 14, 1, 37-52.

Mehrabi, B., Yardley, B.W.D. and Cann, J.R., 1999, Sediment-hosted disseminated gold mineralization at Zarshuran, NW Iran. Mineralium Deposita, 34, 673-696.

Miyatake, S., 2002, Regional lineament analysis and alteration mineral mapping for intrusive-related copper exploration in the Myanmar central volcanic belt. Tokyo, Japan, Metal Mining Agency of Japan, p. 1-4.

Modabberi, S. and Moore, F., 2004, Environmental geochemistry of Zarshuran Au-As deposit, NW Iran. Environmental Geology, 46, 796-807.

Mohajer, G., Parsaei, H., Fallah, N. and Ma'dani, F., 1989, Mercury exploration in the Saein Dezh-Takab area. Tehran, Ministry of Mines and Metals of Iran (in Farsi).

Mohajjel, M. and Fergusson, C.L., 2000, Dextral transpression in Late Cretaceous continental collision, Sanandaj–Sirjan zone, Western Iran. Journal of Structural Geology, 22, 1125-1139.

Moon, W.M., Chung, C.F. and An, P., 1991, Representation and integration of geological, geophysical and remote sensing data. Geoinformatics, 2, 177-182.

Mukhopadhyay, B., Hazra, N., Sengupta, S.R. and Kumar Das, S., 2002, Mineral potential map by a knowledge driven GIS modelling: An example from Singhbhum copper belt, Jharkhand. Map India, 6-8 February 2002, Taj Palace Hotel, New Delhi, India.

Nabavi, M.H., 1976, An introduction to Iranian geology. 110 pp (in Farsi).

Neawsuparp, K., Charusiri, P. and Meyers, J., 2005, New processing of airborne magnetic and electromagnetic data and interpretation for subsurface structures in the Loei Area, Northeastern Thailand. ScienceAsia 31, 283-298.

Neville, R.A., Levesque, J., Staenz, K., Nadeau, C., Hauff, P. and Borstad, G.A., 2003, Spectral unmixing of hyperspectral imagery for mineral exploration: comparision of results from SFSI and AVIRIS. Canadian Journal of Remote Sensing, 29, 99-110.

O'Leary, D., Friedman, J. and Pohn, H., 1976, Lineament, linear, lineation: some proposed new standards for old terms. Geological Society of American Bulletin, 87, 1463-1469.

Ouattara, T., Couture, R., Bobrowsky, P.T. and Moore, A., 2004, Remote sensing and geosciences. Geological Survey of Canada, open file 4542.

Palomera, R.P.A., 2004, Application of remote sensing and geographic information systems for mineral predictive mapping, Deseado Massif, southern Argentina. M.Sc. thesis, International Institute for geo-information science and earth observation enschede, the Netherlands, 68 p.

Pan, G.C. and Harris, D.P., 2000. Information synthesis for mineral exploration. Oxford University Press, Inc., New York, 461 pp.

Pelissier, G. and Bolourchi, M.H., 1967, East Takab metamorphic complex, Geological Survey of Iran, (unpublished).

Peters, S.G., Ludington, S.D., Orris, G.J., Sutphin, D.M. and …, 2007, Preliminary non-fuel mineral resource assessment of afghanistan. U.S. Department of the Interior and U.S. Geological Survey, USGS Open-File Report 2007-1214.

Pirajno, F., 1992. Hydrothermal mineral deposits, principles and fundamental concepts for the exploration geologists. Springer-Verlag, Berlin, 709 pp.

Podwysocki, M.H., Segal, D.B. and Abrams, M.J., 1983, Use of multispectral scanner images for assessment of hydrothermal alteration in the Marysvale, Utah, mining area. Economic Geology, 78, 675-687.

Portnov, A.M., 1987, Specialization of rocks toward potassium and thorium in relation to mineralization. International Geology Review, 29, 326-344.

Porwal, A.K., 2006, Mineral potential mapping with mathematical geological models. Ph.D. thesis, ITC, The Netherlands, 289 p.

Porwal, A., Carranza, E.J.M. and Hale, M., 2004, A hybrid neuro-fuzzy model for mineral potential mapping. Mathematical Geology, 36, 7, 803-826.

Porwal, A., Carranza, E.J.M. and Hale, M., 2003, Knowledge-driven and data-driven fuzzy models for predictive mineral potential mapping. Natural Resources Research, 12, 1, 1-25.

Radtke, A.S., 1985, Geology of the Carlin gold deposit, Nevada. U.S. Geological Survey, Professional Paper 1267, 124 p.

Radtke, A.S., Rye, R.O. and Dickson, F.W., 1980, Geology and stable isotope studies of the Carlin gold deposit, Nevada. Economic Geology, 75, 641-672.

Raines, G.L., 1999, Evaluation of weights of evidence to predict epithermal gold deposits in the Great Basin of the western United States. Natural Resources Research, 8, 257-276.

Raines, G.L., 1997, Data, evidence, and the silver bullet. In: A.G. Gubins (Ed.), Proceedings of Exploration 97, 4th Decennial International Conference on Mineral Exploration, Toronto, Canada, 14-18 September 1997, pp. 87-88.

Rajesh, H.M., 2004, Application of remote sensing and GIS in mineral resource mapping- An overview. Journal of Mineralogical and Petrological Sciences, 99, 83-103.

Raupa, B., Kaab, A., Kargelc, J. S., Bishopd, M. P., Hamiltone, G., Leef, E., Paulb, F., Raug, F., Solteszf, D., Khalsaa, S.J.S., Beedlea, M. and Helma, C., 2007, Remote sensing and GIS technology in the Global Land Ice Measurements from Space (GLIMS) Project. Computers & Geosciences, 33, 104-125.

Reeves, C.V., Westerhof, A.B., Botman, L.G., Dessauvagie, T.F.J. and Dijkstra, S., 1990, Systematic mineral resource development in the '90s and the next century: new techniques, old challenges. ITC Journal 1990-2, pp. 92-101.

Rein, B. and Kaupfmann, H., 2003, Exploration for gold using panchromatic stereoscopic intelligence satellite photographs and Landsat TM data in Hebei area, China. International Journal of Remote Sensing, 24, 2427–2438.

Rencz, A.N., Harris, J.R., Watson, G.P. and Murphy, B., 1994, Data integration for mineral exploration in the Antigonish Highlands, NovaScotia. Canadian Journal Remote Sensing, 20, 258-267.

Ressel, M.W., Noble, D.C. and Henry, C.D., 2000, Dike-hosted ores of the Beast deposit and the importance of Eocene magmatism in gold mineralization of the Carlin trend. Economic Geology, 95, 1417-1444.

Richards, J.P., 2000, Lineaments revisited. Society of Economic Geologists Newsletter, 42, 14-20.

Robert, F., Poulsen, K.H. and Dube, B., 1997, Gold deposits and their Geological classification. In Proceedings of Exploration 97, Edited by Gubins, A.G, Fourth Decennial International Conference on Mineral Exploration, Toronto, 209-219.

Rock, N.M.S., 1988, Numerical Geology: a source guide, glossary, and selected bibliography to geological issues of computers & statistics. Lecture Notes in Earth Sciences 18. Springer Verlag, New York.

Rojas, A.S., 2003, Predictive mapping of massive sulphide potential in the western part of the Escambray Terrain, Cuba. M.Sc. thesis, International Institute for geo-information science and earth observation enschede, the Netherlands, 62 p.

Rokos, D., Mavrantza, R., Vamvoukakis, C., St-Seymour, K., Kouli, M., Karfakis, I. and Denes, D., 2000, Localization of alteration zoning for the detection of epithermal gold by integration of remote sensing and geo chemical techniques: Lesvos Island, Aegean Sea, Hellas. Proceedings of the Fourteenth International Conference on Applied Geologic Remote Sensing, Las Vegas Nevada, p. 161-168.

Rose, A.W., Hawkes, H.E. and Webb, J.S., 1979, Geochemistry in Mineral Exploration. 2nd Ed., Academic Press, London, 657 pp.

Rothery, D.A., 1987, Improved discrimination of rock units using Landsat Thematic Mapper imagery of the Oman ophiolite. Journal of the Geological Society, London, 144, 587-597.

Rowan, L.C., Mars, J.C. and Simpson, S.J., 2005, Lithologic mapping of the Mordor, Northern Territory, Australia, ultramafi c complex by using the Advanced Spaceborne Thermal Emission and Refl ection Radiometer (ASTER).Remote Sensing of Environment, 99, 105-126.

Rowan, L.C. and Mars, J.C., 2003, Lithologic mapping in the Mountain Pass, California, area using Advanced Spaceborne Thermal Emission and Refl ection Radiometer (ASTER) data. Remote Sensing of Environment, 84, 3, 350-366.

Sabins, F.F., 1999, Remote sensing for mineral exploration. Ore Geology Reviews, 14, 157-183.

Sadeghi, M., Borg, G. and Glaesser, C., 2008a, Application of GIS and remote sensing in metallogenic modeling & mineral potential mapping in the Takab District, NW Iran. 28. Wissenschaftlich-Technische Jahrestagung der DGPF, 23-26 April 2008, in Oldenburg, Germany (present with poster).

Sadeghi, M., Borg, G. and Glaesser, C., 2008b, Relationship between large-scale ring structures and lineaments with big porphyry copper deposits in Iran. 28. Wissenschaftlich-Technische Jahrestagung der DGPF, 23-26 April 2008, in Oldenburg, Germany (present with poster).

Sahandi, M.R., Soheily, M., Sadeghi, M., Delavar, S.T. and Jafari Rad, A., 2002, Geological map of Iran, 1:1000.000. Geological Survey of Iran, Tehran, Unpublished.

Saul, J.M., 1978, Circular structures of large scale and great age on the Earth's surface. Nature, 271, 345-349.

Sengör, A.M.C., Altmer, D., Cin, A., Ustaomer, T. and Hsu, K.J., 1988, Origin and assembly of the Tethyside orogenic collage at the ex- pense of Gondwana Land. In: Audley-Charles, M.G., Hallam, A. (Eds.), Gondwana and Tethys. Geological Society of London, Special Publication 37, 119-181.

Sheikholeslami, R., Bellon, H., Emami, H., Sabzehei, M. and Pique, A., 2003, New structural and ^{40}K / ^{40}Ar data for metamorphic rocks from the Neyriz region, Sanandaj-Sirjan Zone, southern Iran; their interest in an overview of the Neo-Tethyan domain in the Middle East. Geoscience, 335, 13, 981-991.

Sillitoe, R.H. and Bonham, H.F., 1990, Sediment-hosted gold deposits; distal products of magmatic–hydrothermal systems. Geology, 18, 157-161.

Singhroy, V., Nebert, D. and Johnson, A.L., 1996, Remote sensing and GIS for site characterization: Applications and standards. Published by ASTM International, 177 p.

Spray, J.G., 2002, Planetary science: Impacts in the round. Nature, 418, 487-488.

Stockli, D.F., Hassanzadeh, J., Stockli, L.D., Axen, G., Walker, J.D. and Dewane, T.J., 2004, Structural and geochronological evidence for Oligo-Miocene intra-arc low-angle detachment faulting in the Takab-Zanjan area, NW Iran. Abstr Programs Geol Soc Am 36, 5, p. 319.

Stöcklin, J., 1968, Structural history and tectonics of Iran: A review. American Association of Petroleum Geologists Bulletin, 52, 1229-1258.

Tangestani, M.H. and Moore, F., 2003, Mapping porphyry copper potential with a fuzzy model,northern Shahr-e-Babak, Iran. Australian Journal of Earth Sciences, 50, 311-317.

Tangestani, M.H. and Moore, F., 2002, Porphyry copper alteration mapping at the Meiduk area, Iran. International Journal of Remote Sensing, 23, 4815-4825.

Teal, L. and Jackson, M., 2002, Geologic overview of the Carlin Trend gold deposits. Nevada
Bureau of Mines and Geology, Bulletin 111: Gold Deposits of the Carlin Trend, 9-19.

Vearncombe, J. and Vearncombe, S., 1999, The spatial distribution of mineralization: Applications of Fry analysis. Geology, 94, 475-486.

Vincent, S.J., Allen, M.B., Ismail-Zadeh, A.D., Flecker, R., Foland, K.A. and Simmons, M.D., 2005, Insights from the Talysh of Azerbaijan into the Paleogene evolution of the South Caspian region. Bulletin of the Geological Society of America 117, 1513-1533.

Wang, K.R., Zhou, Y.Q., Sun, L.G. and Ren, C.G., 1994, Study on the gold occurrence from several typical Carlin-type gold deposits in China. Publishing House of University of Science & Technology of China, Hefei.

Weese, A., 2002, The integration of remote sensing data into Geographic Information Systems. George Mason University, (http://www.aubreyrhea.com/bookbag/geog553/index.htm).

Wilford, J., 2002, Airborne gamma-ray spectrometry. In: Papp E, ed. Geophysical and remote sensing methods for regolith exploration. Canberra: CRC LEME, open-file report 144, 46-52.

Witschard, F., 1984, Large-magnitude ring structures on the Baltic Shield; metallogenic significance. Economic Geology, 79, 1400-1405.

Wright, D.F. and Bonham-Carter, G.F., 1996, VHMS favourability mapping with GIS-based integration models, Chisel Lake-Anderson Lake Area. In: G.F. Bonham-Carter, A.G. Galley, G.E.M. Hall (eds.) EXTECH I: A Multidisciplinary Approach to Massive Sulphide Research in the Rusty Lake-Snow Lake Greenstone Belts, Manitoba. Geol. Survey Canada Bull, 426, 339-376.

Yaghubpur, A. and Hassannejad, A.A., 2006, The spatial distribution of some chromite deposits in Iran, using Fry analysis. Journal of Sciences, Islamic Republic of Iran, University of Tehran 17, 2, 147-152.

Yetkin, E., 2003, Alteration mapping by remote sensing: Application to Hasandag-Melendiz volcanic complex. M.Sc. thesis, Middle East technical university, Graduate school of natural and applied sciences, 114 p.

Zadeh, L.A., 1965, Fuzzy sets. Institute of electrical and electronic engineering information and control, 8, 338-353.

Zimmermann, H.J. and Zysno, P., 1980, Latent Connectives in Human Decision Making. Fuzzy Sets and Systems, 4, 37–51.

Appendix 1

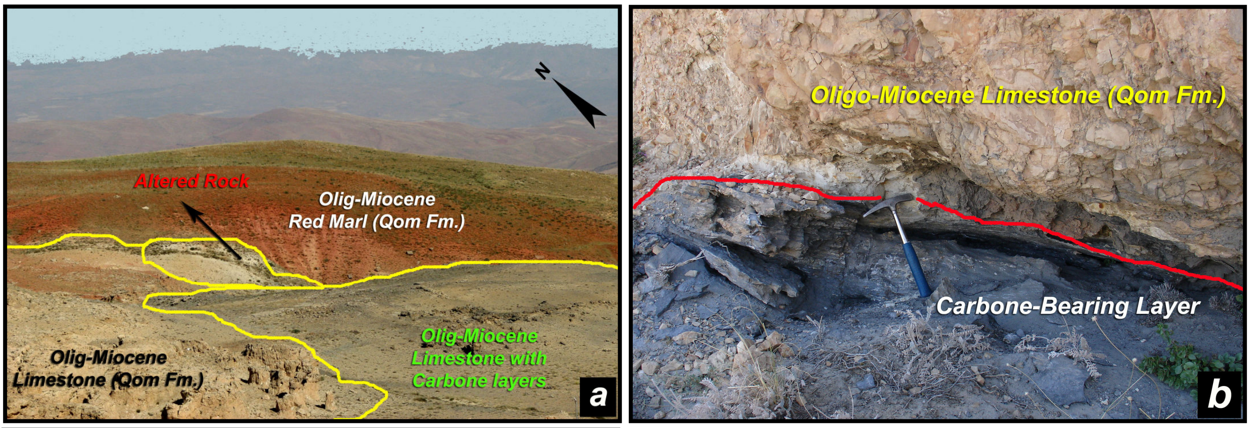

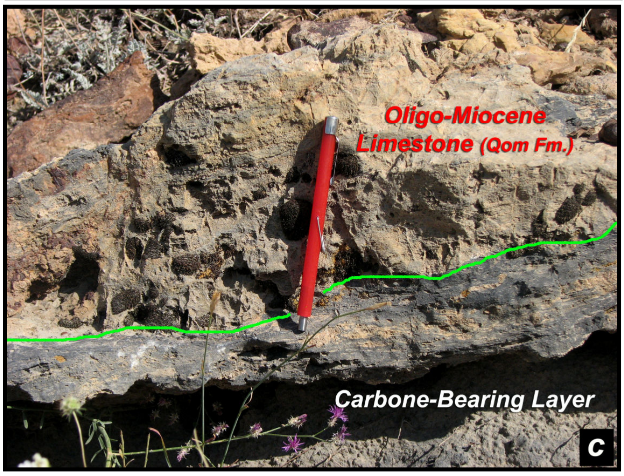

Fig. 1 **a** A part of target area 3 (MVT Pb-Zn) in the east of Takab and **b & c** Carbonate rocks in the contact of Carbone-bearing layer and iron oxide (sampling place of Ta_52 and Ta_53).

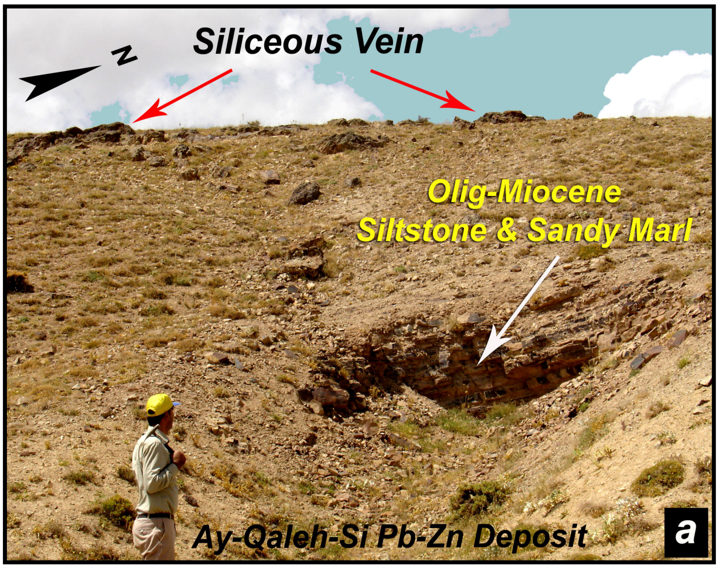

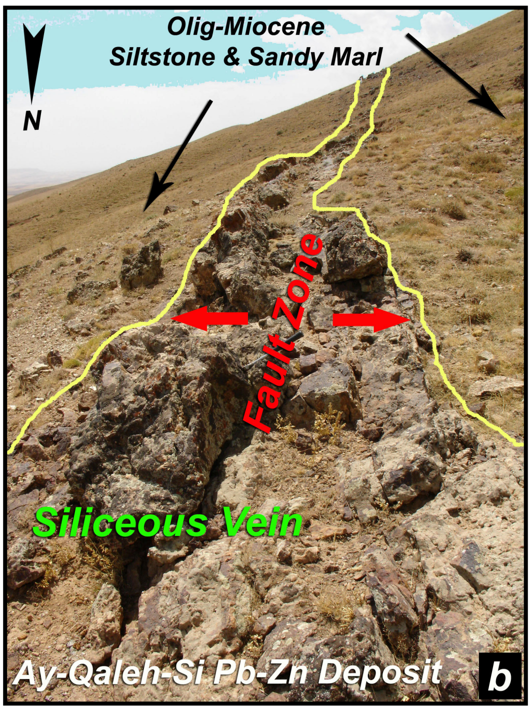

Fig. 2 **a** A view of siliceous vein and Oligo-Miocene sedimentary sequence in the Ay-Qaleh-Si Pb-Zn deposit in the target area 2 (MVT Pb-Zn) and **b** Siliceous vein with N35E trend (in a fault zone) and about 1 km length inclusive Pb and Zn minerals (sampling place of Ta_5-7).

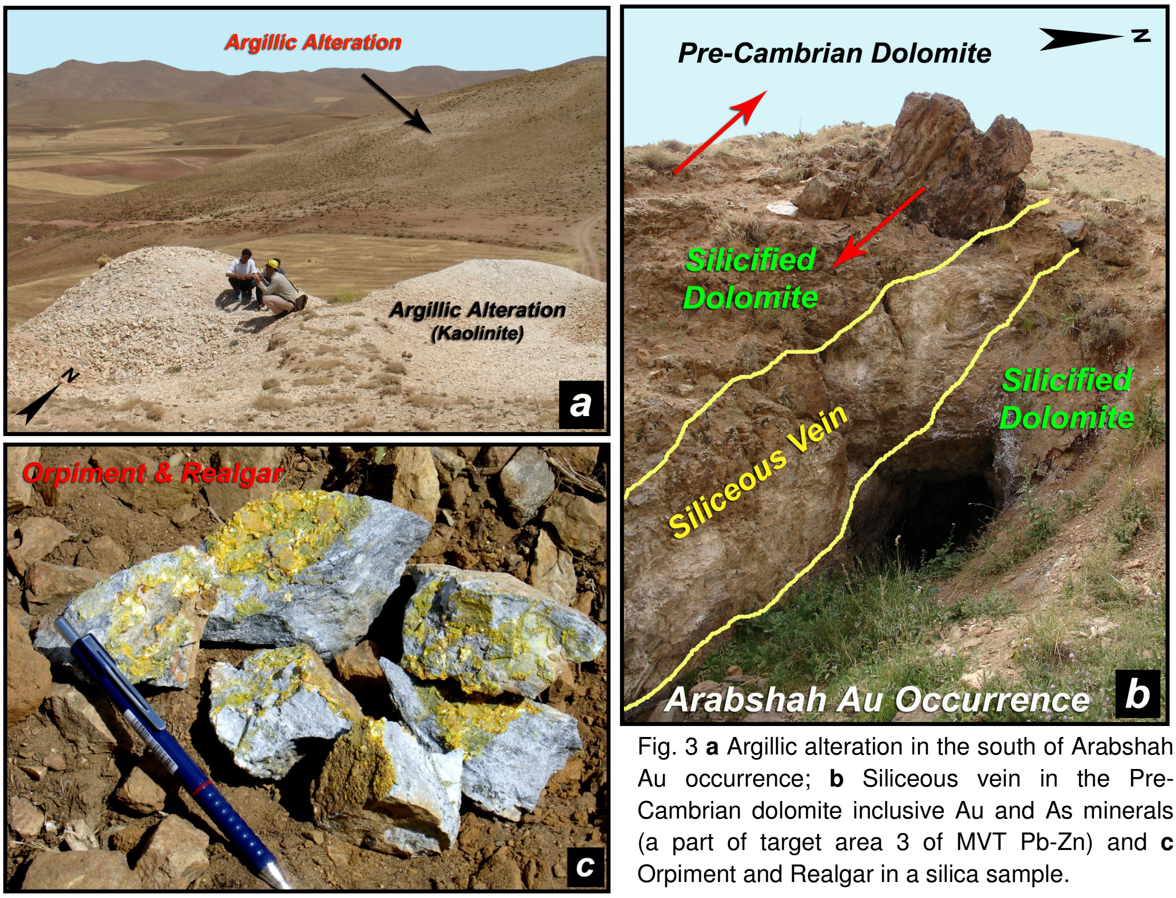

Fig. 3 **a** Argillic alteration in the south of Arabshah Au occurrence; **b** Siliceous vein in the Pre-Cambrian dolomite inclusive Au and As minerals (a part of target area 3 of MVT Pb-Zn) and **c** Orpiment and Realgar in a silica sample.

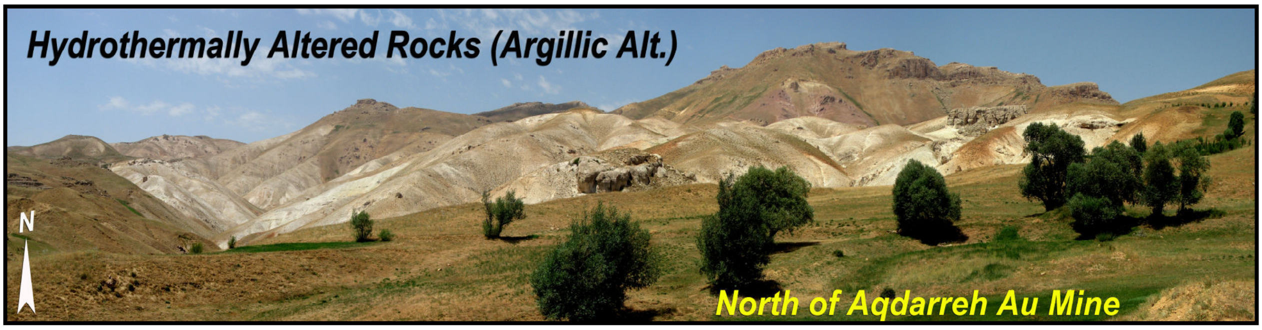

Fig. 4 Panoramic view of hydrothermally altered rocks (argillic alt.) in the north of Aqdarreh Au mine (a part of target area 7 of Carlin-type gold).

Fig. 5 Quaternary travertine in the south of Chahar Tagh (NE of Takab). A part of target area 3 (MVT Pb-Zn).

Fig. 6 **a** Panoramic view of Karaftoo cave (ancient carbonate cave) in Oligo-Miocene carbonate rock and **b** A view from inside of Caraftoo cave (formed by chemical solution in carbonate rock).

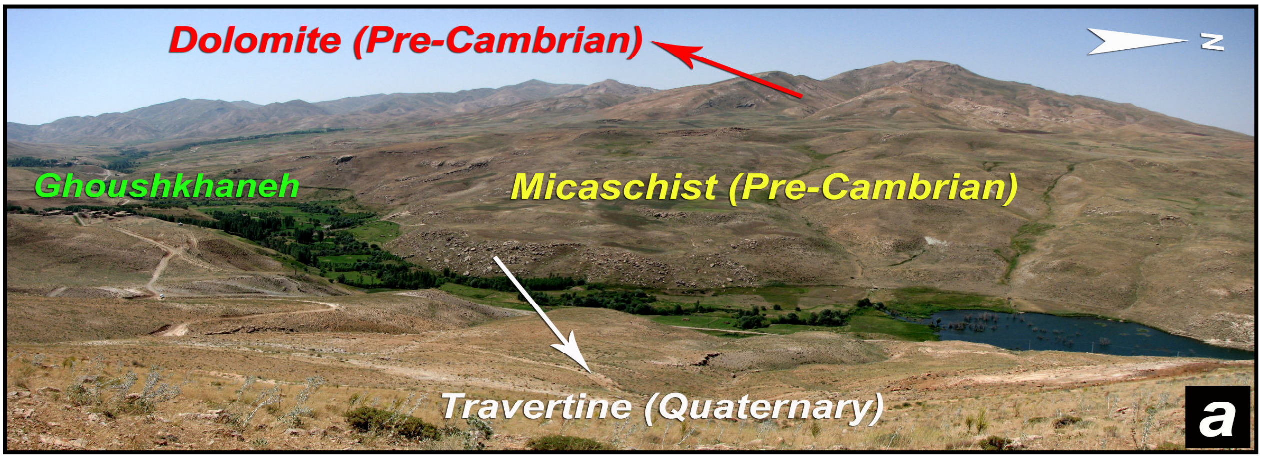

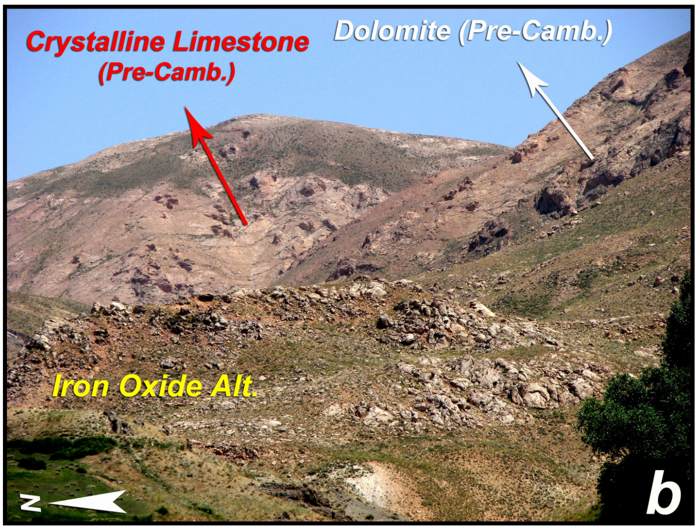

Fig. 7 **a** Panoramic view of Pre-Cambrian rocks (dolomite and micaschist) and Quarternary travertine in the north of Ghoushkhaneh and **b** A view of Pre-Cambrian carbonate rocks and iron oxide alteration in this area (a part of target area 3 of MVT Pb-Zn and target area 3 of Carlin-type gold).

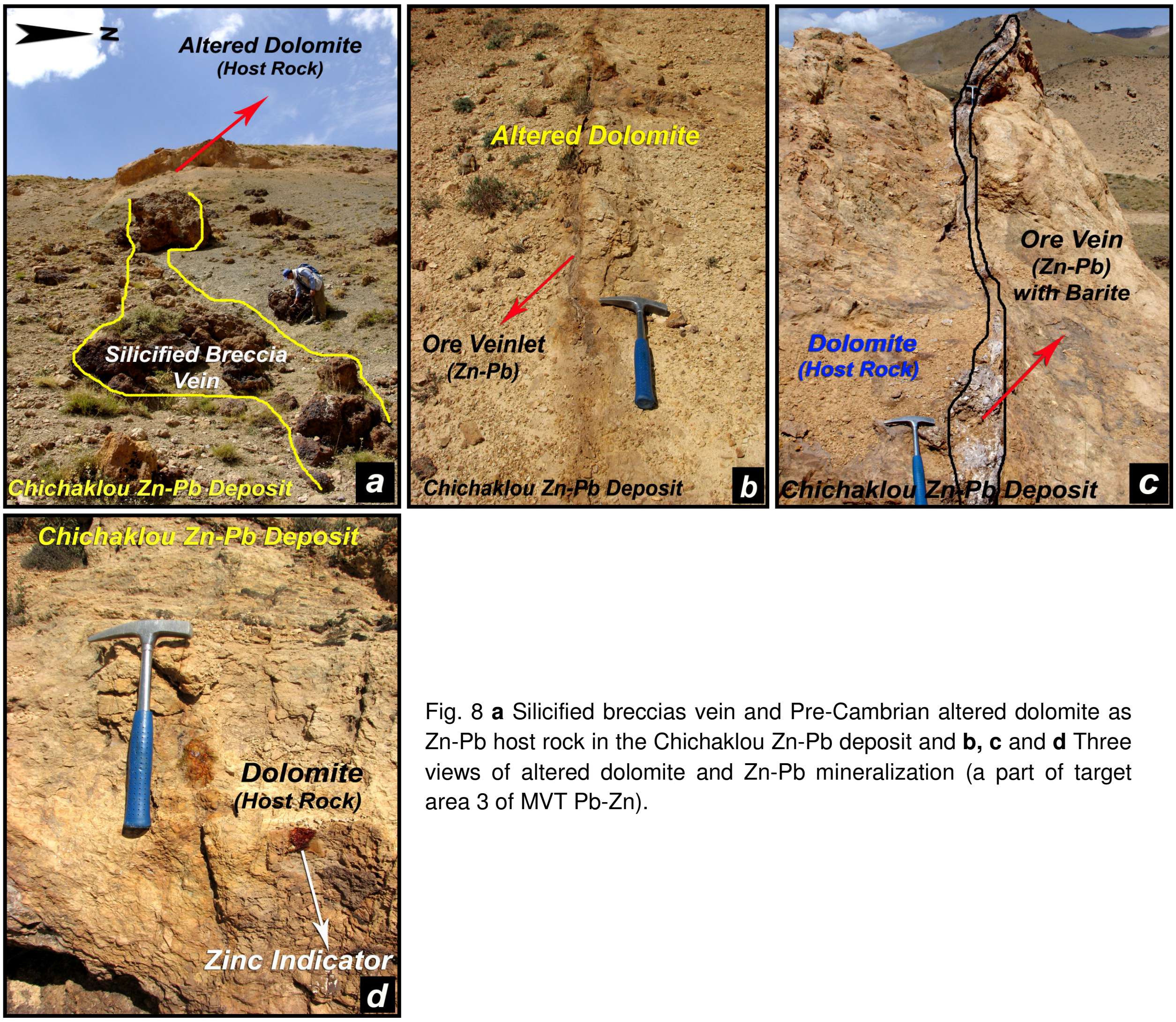

Fig. 8 **a** Silicified breccias vein and Pre-Cambrian altered dolomite as Zn-Pb host rock in the Chichaklou Zn-Pb deposit and **b, c** and **d** Three views of altered dolomite and Zn-Pb mineralization (a part of target area 3 of MVT Pb-Zn).

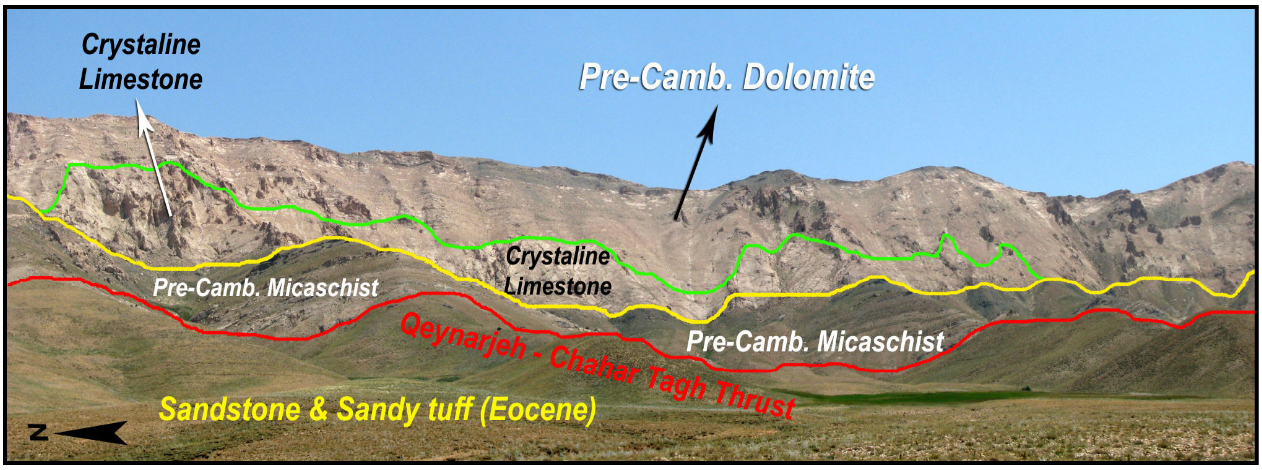

Fig. 9 Panoramic view of Pre-Cambrian rocks and Eocene sandstone in the Chahar Tagh - Chichaklou road. The Qeynarjeh – Chahar Tagh thrust fault has laied Eocene sedimentary layers against the Pre-Cambrian rocks (a part of target area 3 of MVT Pb-Zn).

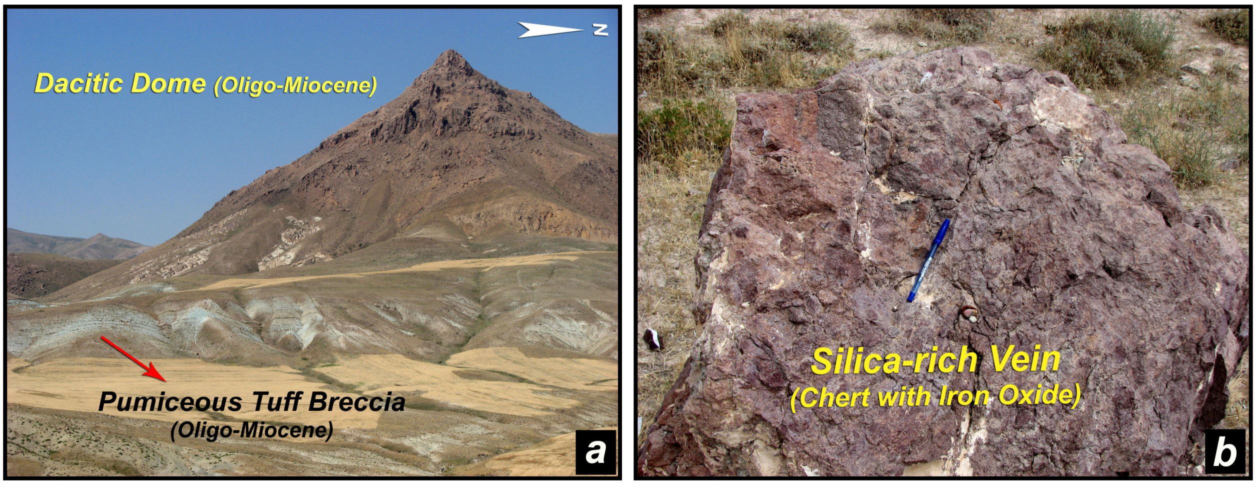

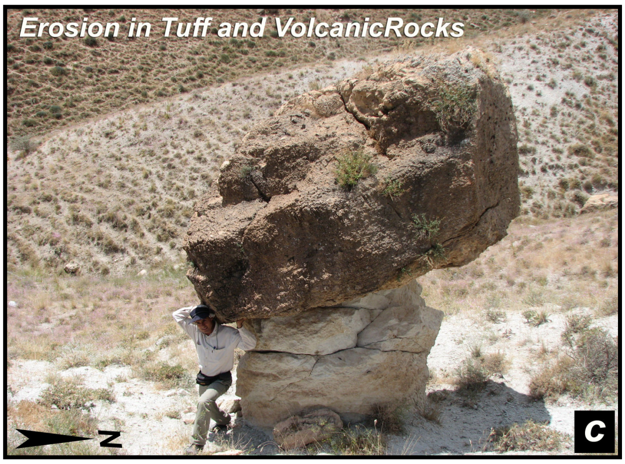

Fig. 10 **a** A view of Oligi-Miocene volcanic rocks and tuff in the south of Angouran mine (a part of target area 4 of MVT Pb-Zn); **b** Chert with iron oxide (sampling place of Ta_71) and **c** Erosion in Oligi-Miocene volcanic rocks.

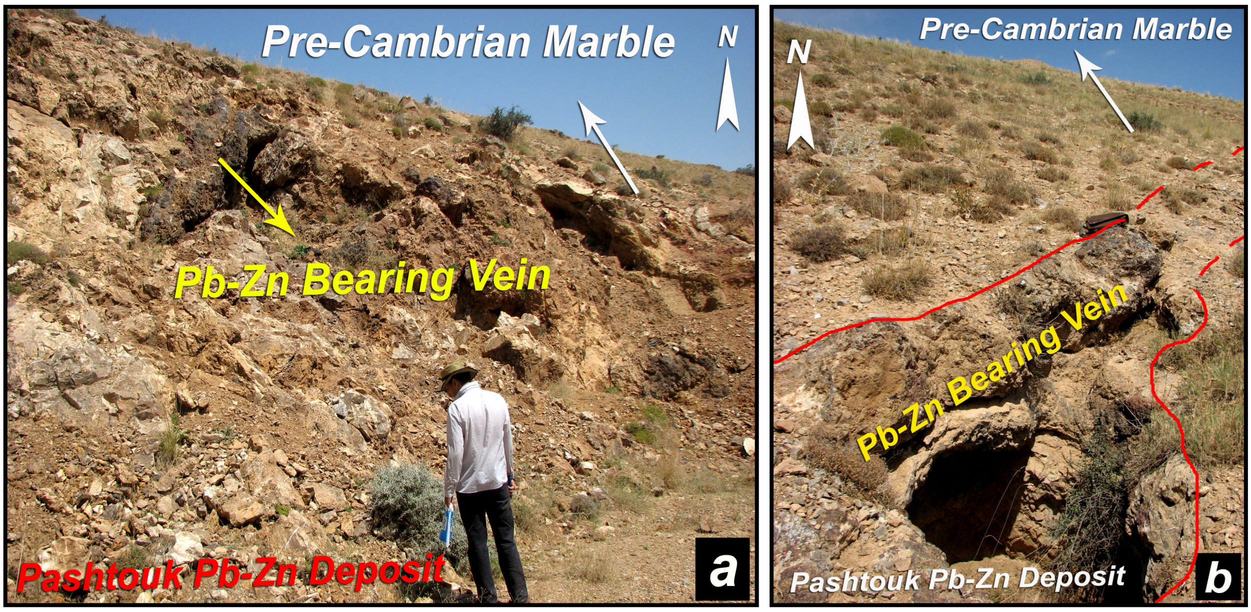

Fig. 11 **a** A view of Pre-Cambrian Marble (host rock) and Pb-Zn bearing vein in the Pashtouk Pb-Zn deposit and **b** An ancient exploration tunnel under the ore vein (a part of target area 5 of Carlin-type gold).

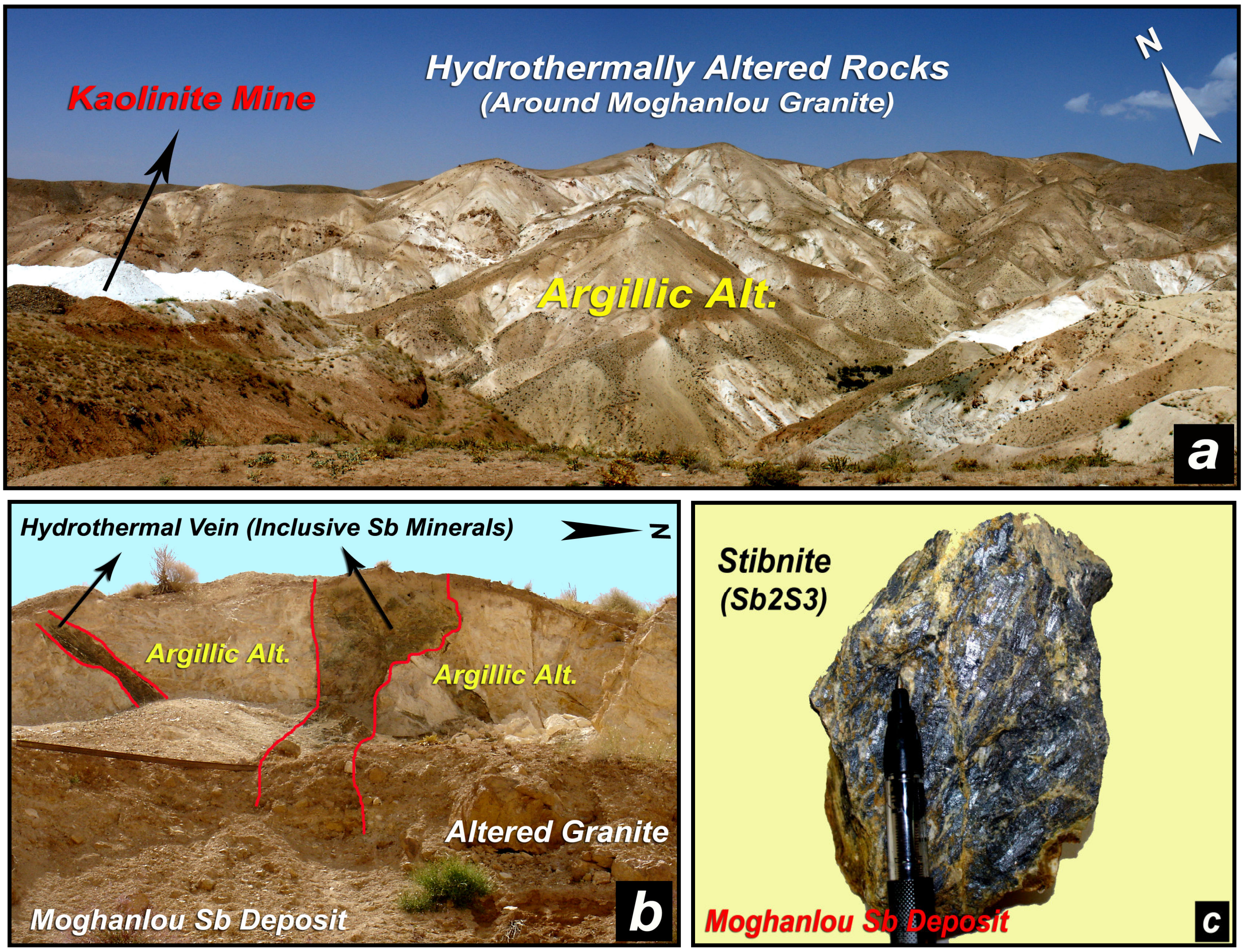

Fig. 12 **a** Panoramic view of hydrothermally altered rocks (argillic alt.) in the SW of Moghanlou granite (a part of target area 1 of MVT Pb-Zn); **b** A view of hydrothermal vein (inclusive Sb minerals) in Moghanlou abandoned Sb mine and **c** A rock sample including Stibnite (Sb_2S_3) from Moghanlou Sb mine.

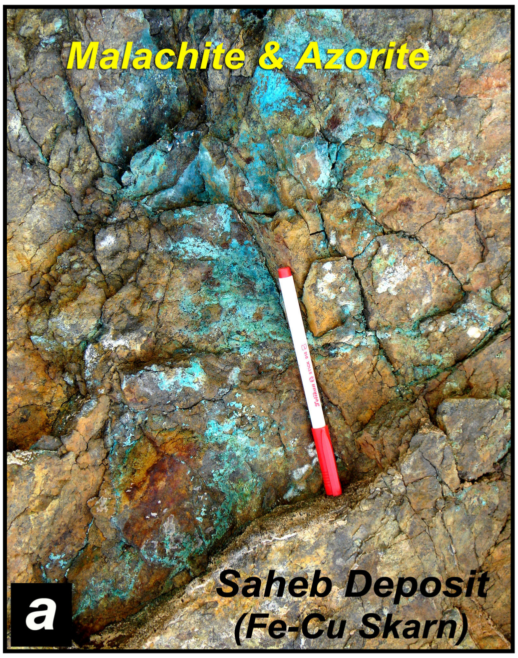

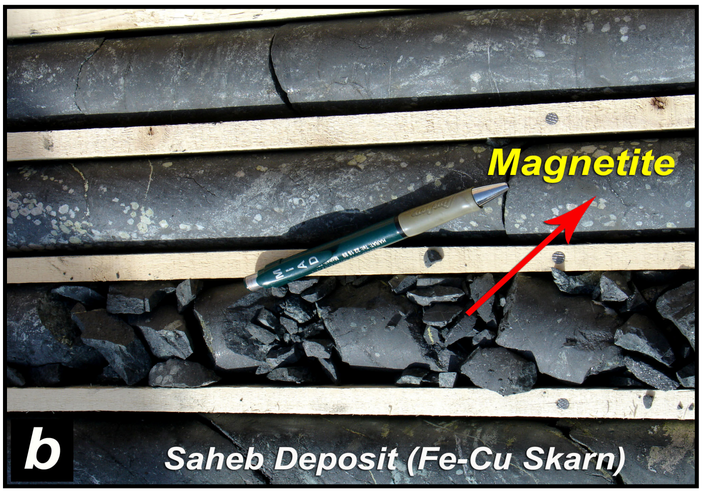

Fig. 13 **a** Malachite and Azurite in the Saheb Fe-Cu skarn deposit (a part of target area 10 of Carlin-type gold) and **b** Magnetite in drill core of an exploration borehole in deposit area.

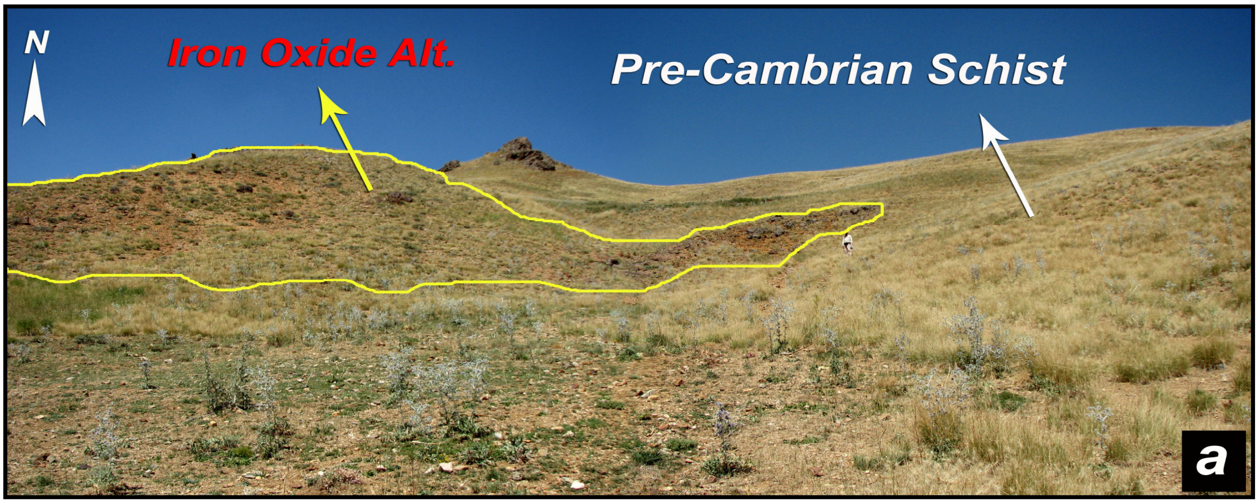

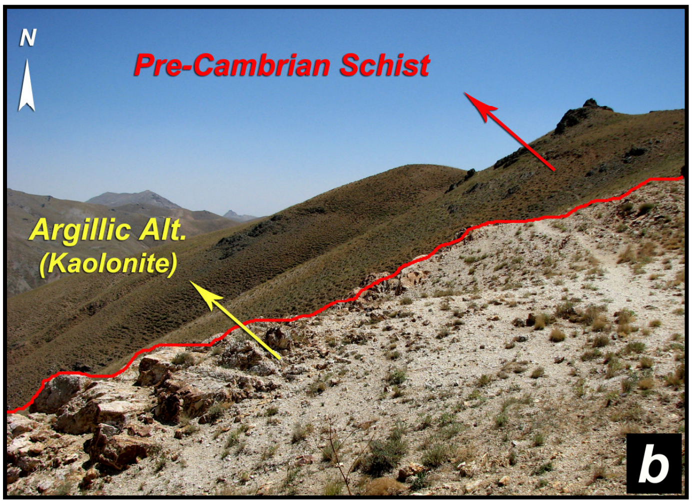

Fig. 14 **a** Panoramic view of iron oxide alteration in Pre-Cambrian schist in the east of Angouran mine (a part of target area 4 of MVT Pb-Zn and target area 4 of Carlin-type gold) and **b** Boundary of argillic alteration and Pre-Cambrian rocks in this area.

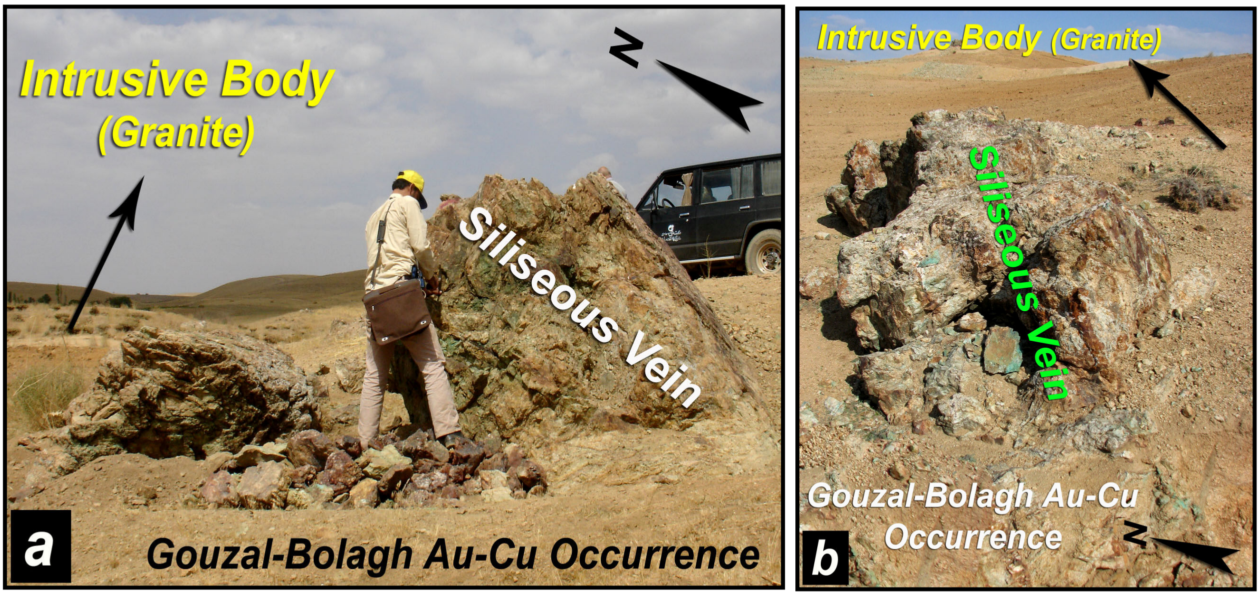

Fig. 15 **a** A view of siliceous vein in a granite body in the Ghozal-Bolagh Au-Cu occurrence (in the east of the study area) and **b** Another view of siliceous vein with NE-SW trend and intrusive body (granite) in this ore occurrence.

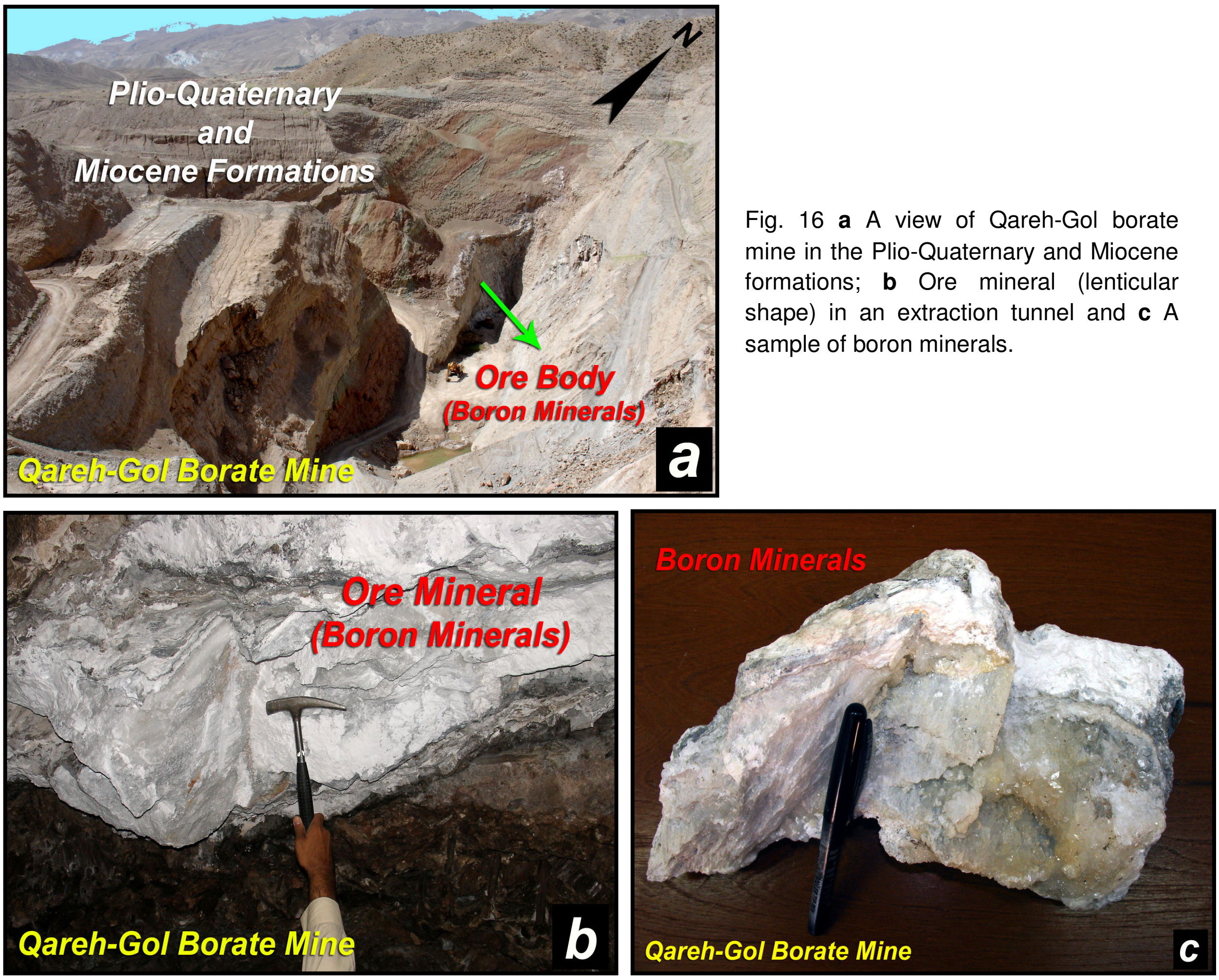

Fig. 16 **a** A view of Qareh-Gol borate mine in the Plio-Quaternary and Miocene formations; **b** Ore mineral (lenticular shape) in an extraction tunnel and **c** A sample of boron minerals.

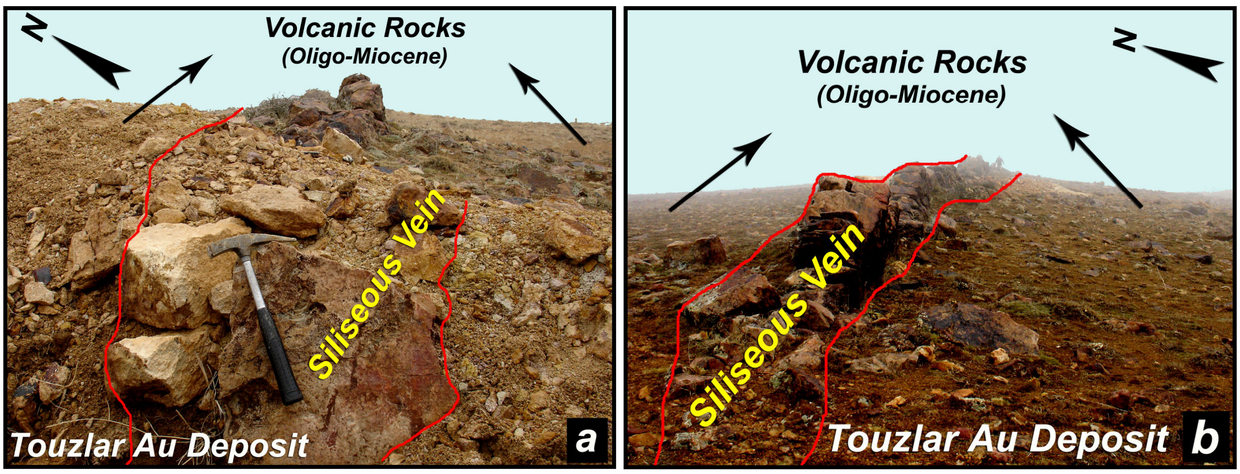

Fig. 17 **a** Siliceous vein with W-E trend in Oligo-Miocene volcanic rocks in the Touzlar Au deposit and **b** Another view of siliceous vein in Touzlar Au deposit.

Appendix 2

Sample_No.	X_Coor.	Y_Coor.	Type	Description	Pb(ppm)	Zn(ppm)	Au(ppb)
Ta_1	710714	4026790	Rock	Quartz, limonite, gossan along NNW, dipping 70, NE fault at dacitic tuff/marl, sandstone contact, XRF analysis.	62	1558	136
Ta_2	711165	4026847	Rock	Quartz-FeOxide vein with sugary quartz texture, hosted in qtzartz, clay, sericite, altered dacite, XRF analysis.	105	891	98
Ta_3	711168	4026846	Rock	Quartz, clay, sericite, altered dacite with stringer and disseminated jarosite, XRF analysis.	15	73	24
Ta_4	711503	4024017	Soil	Quartz, biotite, chlorite, XRD analysis.			
Ta_5	712510	4024685	Rock	Pb and Zn analysis with wet chemichal method (after Fonoudi & Sadeghi, 2001).	3400	4500	
Ta_6	712662	4024722	Rock	Galena, sphalerite, serussite, quartz, XRD analysis.			
Ta_7	712662	4024722	Soil	Galena, sphalerite, biotite, illite, kaolonite, quartz, XRD analysis.			
Ta_8	706435	4027856	Rock	Jasperoid E-W, dipping 75 N, chrysocolla & mallachite incrustations, length is about 50m.	755	887	899
Ta_9	706628	4027762	Rock	Brecciated gossanous jasperoid, (Hem, Lim) +marble, about 15m width.	381	1090	3914
Ta_10	706676	4027730	Rock	Light grey-beige jasperoid, 15x30m along E-W, dipping 70 N fault, breccia texture, about 2m width.	531	139	409
Ta_11	706786	4027668	Rock	Black jasperoid veins in orange-black sanded marble, the sample collected from a trench.	23	725	1349
Ta_12	707075	4027874	Rock	2x50m jasperoid +/- limonite along E-NE fault, dipping 80 N, about 2m width.	119	156	403
Ta_13	706885	4027783	Rock	Silicified marble with orpiment along fractures, disseminated pyrite & minor reargar, beside an old adit.	10	13	339
Ta_14	706787	4027422	Rock	Siliceous vein, Arabshah, gold analysis.			5
Ta_15	706779	4027755	Rock	Siliceous vein, Arabshah, gold analysis.			9
Ta_16	706779	4027755	Rock	Siliceous vein, Arabshah, gold analysis.			2780
Ta_17	706942	4028070	Rock	Pb and Zn analysis with wet chemichal method (after Fonoudi & Sadeghi, 2001), Arabshah.	2500	2100	
Ta_18	706942	4028070	Rock	Pb and Zn analysis with wet chemichal method (after Fonoudi & Sadeghi, 2001), Arabshah.	3100	2500	
Ta_19	706891	4027947	Rock	Pb and Zn analysis with wet chemichal method (after Fonoudi & Sadeghi, 2001), Arabshah.	2800	3800	
Ta_20	706789	4027654	Rock	Arabshah gold anomaly (As-Au).	1000	1300	450
Ta_21	706896	4027824	Rock	Arabshah gold anomaly (As-Au).	9600		1500
Ta_22	706873	4028690	Soil	Pb and Zn analysis with wet chemichal method (after Fonoudi & Sadeghi, 2001), Arabshah.	1800	2700	
Ta_23	706900	4028690	Rock	Altered dolomite, Pb and Zn analysis with wet chemichal method (after Fonoudi & Sadeghi, 2001), Arabshah.	2200	4300	
Ta_24	706875	4028623	Soil	Pb and Zn analysis with wet chemichal method (after Fonoudi & Sadeghi, 2001), Arabshah.	1900	3000	
Ta_25	706875	4028623	Rock	Pb and Zn analysis with wet chemichal method (after Fonoudi & Sadeghi, 2001), Arabshah.	3000	7900	
Ta_26	707019	4028971	Rock	Pb and Zn analysis with wet chemichal method (after Fonoudi & Sadeghi, 2001), Arabshah.	2400	1600	
Ta_27	707028	4031591	Rock	Pb and Zn analysis with wet chemichal method (after Fonoudi & Sadeghi, 2001), Arabshah.	2000	2800	
Ta_28	703787	4033945	Soil	Pb and Zn analysis with wet chemichal method (after Fonoudi & Sadeghi, 2001), Arabshah.	1900	1500	
Ta_29	709866	4033014	Rock	Altered dolomite, Pb and Zn analysis with wet chemichal method (after Fonoudi & Sadeghi, 2001), Chichaklou.	3200	124900	
Ta_30	709838	4033013	Rock	Altered dolomite, Pb and Zn analysis with wet chemichal method (after Fonoudi & Sadeghi, 2001), Chichaklou.	6100	43200	
Ta_31	709685	4033043	Rock	Altered dolomite, Pb and Zn analysis with wet chemichal method (after Fonoudi & Sadeghi, 2001), Chichaklou.	2800	58200	
Ta_32	709684	4033076	Soil	Altered dolomite, Pb and Zn analysis with wet chemichal method (after Fonoudi & Sadeghi, 2001), Chichaklou.	13000	26400	
Ta_33	710405	4033172	Rock	Altered dolomite, Chichaklou Zn-Pb deposit.	54300	12450	450
Ta_34	709277	4033713	Rock	Altered dolomite, Chichaklou Zn-Pb deposit.	923	1500	17
Ta_35	714177	4032842	Rock	Altered dolomite, Pb and Zn analysis with wet chemichal method (after Fonoudi & Sadeghi, 2001), Chichaklou.	2200	26800	
Ta-36	715857	4035626	Soil	Pb and Zn analysis with wet chemichal method (after Fonoudi & Sadeghi, 2001), Ghouzijagh.	2600	1300	
Ta_37	715769	4035555	Rock	Stone Mine (Marble)(None Active).	986		<1
Ta_38	715369	4039421	Rock	Yellow-brown fault breccia, quartz & schist, intense silicification, disseminated jarosite.	366	353	29
Ta_39	708177	4037902	Soil	Dolomite, Pb and Zn analysis with wet chemichal method (after Fonoudi & Sadeghi, 2001), Chichaklou.	1700	2200	
Ta_40	707877	4038860	Soil	Dolomite, Pb and Zn analysis with wet chemichal method (after Fonoudi & Sadeghi, 2001), Chichaklou.	2100	3300	
Ta_41	705947	4038559	Soil	Pb and Zn analysis with wet chemichal method (after Fonoudi & Sadeghi, 2001), Badrlou.	2100	3200	
Ta-42	705947	4038559	Rock	Pb and Zn analysis with wet chemichal method (after Fonoudi & Sadeghi, 2001), Badrlou.	2000	2800	
Ta_43	705668	4038586	Rock	Pb and Zn analysis with wet chemichal method (after Fonoudi & Sadeghi, 2001), Badrlou.	2000	2200	
Ta_44	705216	4038763	Rock	Pb and Zn analysis with wet chemichal method (after Fonoudi & Sadeghi, 2001), Badrlou.	2400	3400	
Ta_45	705288	4038765	Soil	Pb and Zn analysis with wet chemichal method (after Fonoudi & Sadeghi, 2001), Badrlou.	2200	2800	
Ta_46	704695	4038784	Soil	Pb and Zn analysis with wet chemichal method (after Fonoudi & Sadeghi, 2001), Badrlou.	2200	3400	
Ta_47	704623	4039549	Rock	Pb and Zn analysis with wet chemichal method (after Fonoudi & Sadeghi, 2001), Badrlou.	2500	3200	
Ta_48	705880	4040222	Soil	Pb and Zn analysis with wet chemichal method (after Fonoudi & Sadeghi, 2001), Badrlou.	1800	2200	

Sample_No.	X_Coor.	Y_Coor.	Type	Description	Pb(ppm)	Zn(ppm)	Au(ppb)
Ta_49	701567	4038805	Rock	Siliceous vein, gold analysis.			3
Ta_50	701567	4038805	Rock	Siliceous vein with iron oxide.	2400		3
Ta_51	705904	4039235	Soil	Pb and Zn analysis with wet chemichal method (after Fonoudi & Sadeghi, 2001), Badrlou.	1800	2200	
Ta_52	699677	4037344	Rock	Carbonate rock, partly including sulphide minerals, 50x70 m.			<1
Ta_53	699677	4037344	Rock	Iron oxide with jasper.		5000	2
Ta_54	699892	4039471	Soil	Pb and Zn analysis with wet chemichal method (after Fonoudi & Sadeghi, 2001), Badrlou.	1900	3000	
Ta_55	699892	4039471	Rock	Pb and Zn analysis with wet chemichal method (after Fonoudi & Sadeghi, 2001), Badrlou.	2300	2800	
Ta_56	707778	4042211	Rock	Hampa, gold analysis.			4
Ta_57	707771	4042488	Rock	Pb and Zn analysis with wet chemichal method (after Fonoudi & Sadeghi, 2001), Hampa.	2600	2600	
Ta_58	707771	4042488	Rock	Pb and Zn analysis with wet chemichal method (after Fonoudi & Sadeghi, 2001), Hampa.	2900	1500	
Ta_59	707072	4042992	Rock	Carbonate rock (Dolomite) with iron oxide, gold analysis.			2
Ta_60	707176	4042950	Rock	Siliceous vein with iron oxide.	5500		120
Ta_61	707087	4042824	Rock	Carbonate rock with iron oxide and silicca.	1200	1800	<1
Ta_62	706482	4043168	Rock	Pb and Zn analysis with wet chemichal method (after Fonoudi & Sadeghi, 2001), Hampa.	2500	3200	
Ta_63	706657	4042994	Soil	Pb and Zn analysis with wet chemichal method (after Fonoudi & Sadeghi, 2001), Hampa.	2600	1400	
Ta_64	705982	4042723	Rock	Hampa, gold analysis.			3
Ta_65	705982	4042723	Rock	Pb and Zn analysis with wet chemichal method (after Fonoudi & Sadeghi, 2001), Hampa.	2800	4400	
Ta_66	707267	4048606	Soil	Pb and Zn analysis with wet chemichal method (after Fonoudi & Sadeghi, 2001), Hampa.	2500	2600	
Ta_67	714173	4051038	Soil	Pb and Zn analysis with wet chemichal method (after Fonoudi & Sadeghi, 2001), Hampa.	2600	2700	
Ta_68	716354	4050449	Soil	Pb and Zn analysis with wet chemichal method (after Fonoudi & Sadeghi, 2001), Hampa.	2600	2500	
Ta_69	716769	4050704	Soil	Pb and Zn analysis with wet chemichal method (after Fonoudi & Sadeghi, 2001), Hampa.	2700	1500	
Ta_70	717504	4050322	Soil	Pb and Zn analysis with wet chemichal method (after Fonoudi & Sadeghi, 2001), Hampa.	3000	1900	
Ta_71	718402	4049238	Rock	Sedimentary silica (chert) with iron oxide, gold analysis.			400
Ta_72	717897	4050000	Rock	Carbonate rock with iron oxide and silicca.	700		400
Ta_73	718152	4050183	Soil	Pb and Zn analysis with wet chemichal method (after Fonoudi & Sadeghi, 2001), Hampa	3400	2200	
Ta_74	718555	4050904	Soil	Pb and Zn analysis with wet chemichal method (after Fonoudi & Sadeghi, 2001), Hampa	2400	2900	
Ta_75	718196	4051367	Rock	Carbonate rock, in some part brown with tiny veinlet, XRF analysis, gold analysis.			<1
Ta_76	716743	4052801	Rock	Pb and Zn analysis with wet chemichal method (after Fonoudi & Sadeghi, 2001), Tozlou.	2500	4000	
Ta_77	716813	4052858	Soil	Pb and Zn analysis with wet chemichal method (after Fonoudi & Sadeghi, 2001), Tozlou.	2000	2100	
Ta_78	714756	4053861	Soil	Pb and Zn analysis with wet chemichal method (after Fonoudi & Sadeghi, 2001), near Angouran mine.	2500	1300	
Ta_79	711686	4054218	Soil	Pb and Zn analysis with wet chemichal method (after Fonoudi & Sadeghi, 2001), near Angouran mine.	2700	2800	
Ta_80	711686	4054218	Rock	Pb and Zn analysis with wet chemichal method (after Fonoudi & Sadeghi, 2001), near Angouran mine.	2800	5600	
Ta_81	705280	4055967	Rock	Altered rock (kaolinite) with siliceous carbonate vein, Gharavol Khaneh, gold analysis.			1
Ta_82	705831	4056833	Rock	Iron oxid (magnetite, hamatite), Gharavol Khaneh, gold analysis.			10
Ta_83	705500	4057383	Rock	Altered rock (kaolinite) with iron oxide, Gharavol Khaneh, gold analysis.			<1
Ta_84	705500	4057383	Rock	Altered rock (kaolinite) with iron oxide, Gharavol Khaneh, for spectrometry.			
Ta_85	705139	4057469	Rock	Siliceous schist, Gharavol Khaneh, gold analysis.			10
Ta_86	706354	4057819	Soil	Pb and Zn analysis with wet chemichal method (after Fonoudi & Sadeghi, 2001), Hampa.	2400	2300	
Ta_87	715999	4060643	Soil	Pb and Zn analysis with wet chemichal method (after Fonoudi & Sadeghi, 2001), Yasti Qale.	2200	1300	
Ta_88	715999	4060643	Rock	Pb and Zn analysis with wet chemichal method (after Fonoudi & Sadeghi, 2001), Yasti Qale.	3300	6700	
Ta_89	715999	4060643	Rock	Pb and Zn analysis with wet chemichal method (after Fonoudi & Sadeghi, 2001), Yasti Qale.	2000	1700	
Ta_90	695907	4064789	Soil	Pb and Zn analysis with wet chemichal method (after Fonoudi & Sadeghi, 2001), Zarshouran	2500	1300	
Ta_91	687361	4065377	Rock	Siliceous vein with iron oxide.	1200		35
Ta_92	687358	4065343	Rock	Siliceous vein with iron oxide.	2400		5
Ta_93	687536	4065361	Rock	Altered siliceous vein with iron oxide.	2200		2
Ta_94	690928	4066431	Rock	Pb and Zn analysis with wet chemichal method (after Fonoudi & Sadeghi, 2001), near Zarshouran mine.	2600	4700	
Ta_95	689976	4067031	Soil	Pb and Zn analysis with wet chemichal method (after Fonoudi & Sadeghi, 2001), near Zarshouran mine.	2700	1400	
Ta_96	690394	4067129	Rock	Pb and Zn analysis with wet chemichal method (after Fonoudi & Sadeghi, 2001), near Zarshouran mine.	2700	6000	
Ta_97	685303	4085544	Rock	Pb and Zn analysis with wet chemichal method (after Fonoudi & Sadeghi, 2001), Chogati.	2600	3100	
Ta_98	686318	4085599	Rock	Pb and Zn analysis with wet chemichal method (after Fonoudi & Sadeghi, 2001), Chogati.	2400	5000	

Sample_No.	X_Coor.	Y_Coor.	Type	Description	Pb(ppm)	Zn(ppm)	Au(ppb)
Ta_99	686318	4085599	Rock	Pb and Zn analysis with wet chemichal method (after Fonoudi & Sadeghi, 2001), Chogati.	2500	1900	
Ta_100	686451	4086035	Rock	Pb and Zn analysis with wet chemichal method (after Fonoudi & Sadeghi, 2001), Chogati.	2200	1700	
Ta_101	686407	4086001	Soil	Pb and Zn analysis with wet chemichal method (after Fonoudi & Sadeghi, 2001), Chogati.	2400	1500	
Ta_102	687619	4090468	Rock	Pb and Zn analysis with wet chemichal method (after Fonoudi & Sadeghi, 2001), Chogati.	2300	3200	
Ta_103	687559	4090777	Soil	Pb and Zn analysis with wet chemichal method (after Fonoudi & Sadeghi, 2001), Chogati.	2200	1300	
Ta_104	687323	4091360	Rock	Pb and Zn analysis with wet chemichal method (after Fonoudi & Sadeghi, 2001), Chogati.			
Ta_105	686724	4091869	Rock	Pb and Zn analysis with wet chemichal method (after Fonoudi & Sadeghi, 2001), Chogati.	2800	5400	
Ta_106	669501	4093567	Rock	Outcrop 10x15m, dark grey strongly silicified conglomerate.	77	51	16
Ta_107	669005	4093557	Rock	Strongly siliciated conglomerate.	326	38	9
Ta_108	669010	4093563	Rock	Outcrop: 20cm wide, NNE strike, dark grey silica vein with disseminated pyrite.	5921	113	127
Ta_109	668809	4093439	Rock	Outcrop: 250x30, dark grey strongly silicified conglomerate.	933	55	30
Ta_110	668202	4093663	Rock	Outcrop: 200x90 WE, dark brown Lim-goethite gossan, Hosted in conglomerate.	688	966	19
Ta_111	667974	4094121	Rock	Outcrop: 25x50, dark brown iron oxide-smithsonite? siliceous gossan breccia, silicified clast, hosted in conglomerate	203	2715	28
Ta_112	668040	4094185	Rock	Outcrop: NNE strike, dipping 70 SSE, dark brown iron oxide, siliceous gossan breccia.	1386	6257	31
Ta_113	664818	4071803	Soil	Stream sediment sample, basement is schist, meta acidic volcanics ,floats have some Si vein.	122	132	8
Ta_114	664771	4072017	Soil	Stream sediment sample, basement is meta acidic volcanics.	32	140	9
Ta_115	659846	4053097	Rock	Brecciated Qtz., sulfidies vein with pyrite in the matrix, thickness is 1m,N10W.	11	15	
Ta_116	659848	4053101	Rock	Sample from granite as hostrock with sulfide veinlet.	7	16	
Ta_117	660322	4055155	Rock	Sample from limestone including siliceous veinlet with iron oxide, gold analysis.			5
Ta_118	654871	3989148	Rock	Outcrop 100x3 NNE, Qtz+/-Ep zone hosted at dolomite/chl. Schist.	7	114	
Ta_119	728035	4030505	Rock	Granodiorite with silica, gold analysis.			130
Ta_120	727583	4030596	Rock	Carbonate rock (Dolomite) with silica, gold analysis.			25
Ta_121	704222	4045156	Soil	Pb and Zn analysis with wet chemichal method (after Fonoudi & Sadeghi, 2001), Hampa.	2400	2700	
Ta_122	705226	4052933	Rock	Siliceous vein near Aghbolagh village, XRD analysis.	2600		3
Ta_123	710709	4054616	Soil	Pb and Zn analysis with wet chemichal method (after Fonoudi & Sadeghi, 2001), near Angouran mine.	2600	1400	
Ta_124	697742	4064676	Soil	Pb and Zn analysis with wet chemichal method (after Fonoudi & Sadeghi, 2001), near Zarshouran mine.	2700	1200	
Ta_125	733188	4060783	Soil	Pb and Zn analysis with wet chemichal method (after Fonoudi & Sadeghi, 2001), Aghkand.	2600	0	
Ta_126	733342	4061686	Soil	Pb and Zn analysis with wet chemichal method (after Fonoudi & Sadeghi, 2001), Aghkand.	3300	0	
Ta_127	734736	4061413	Soil	Pb and Zn analysis with wet chemichal method (after Fonoudi & Sadeghi, 2001), Aghkand.	2700	0	
Ta_128	734667	4063168	Rock	Iron oxide, XRF, gold analysis.			360
Ta_129	735598	4063569	Rock	Pb and Zn analysis with wet chemichal method (after Fonoudi & Sadeghi, 2001),Pashtok.	1900	0	
Ta_130	735598	4063569	Rock	Pb and Zn analysis with wet chemichal method (after Fonoudi & Sadeghi, 2001),Pashtok.	384500	3400	
Ta_131	735609	4063555	Rock	Carbonate rock with silica, XRF analysis.	105900	60000	1300
Ta_132	735483	4064177	Rock	Pb and Zn analysis with wet chemichal method (after Fonoudi & Sadeghi, 2001),Pashtok.	22400	117900	
Ta_133	735483	4064177	Rock	Pb and Zn analysis with wet chemichal method (after Fonoudi & Sadeghi, 2001),Pashtok.	31800	109400	
Ta_134	729946	4064926	Rock	Aghkand, gold analysis.			4
Ta_135	729946	4064926	Soil	Pb and Zn analysis with wet chemichal method (after Fonoudi & Sadeghi, 2001), Aghkand.	2700	1100	
Ta_136	732471	4065449	Soil	Pb and Zn analysis with wet chemichal method (after Fonoudi & Sadeghi, 2001), Aghkand.	2700	1400	
Ta_137	732130	4065818	Soil	Pb and Zn analysis with wet chemichal method (after Fonoudi & Sadeghi, 2001), Aghkand.	2900	1100	
Ta_138	678863	4061244	Rock	Brecciation siliceous rock with iron oxide, Aqdarreh, XRD analysis.	2000		5
Ta_139	679056	4061201	Rock	Siliceous vein with organic material, Aqdarreh.			40
Ta_140	679056	4061201	Soil	Iron oxide soil, Aqdarreh.	9500	700	22
Ta_141	670920	4036816	Rock	Carbonate rock (Qom Fm.).		300	
Ta_142	671567	4038153	Soil	Thinly-moderately bedded limestone (Qom Fm.).	24	82	<1
Ta_143	671506	4038199	Rock	Carbonate rock (Qom Fm.).			<1
Ta_144	665936	4039425	Soil	Stream sediment in the granite rocks, gold analysis.			1